UNIVERSITAT POLITÈCNICA
DE CATALUNYA
BARCELONATECH

Study of ice content and hydro-mechanical behavior of frozen soils

Yanxin Mao

ADVERTIMENT La consulta d'aquesta tesi queda condicionada a l'acceptació de les següents condicions d'ús: La difusió d'aquesta tesi per mitjà del repositori institucional UPCommons (http://upcommons.upc.edu/tesis) i el repositori cooperatiu TDX (http://www.tdx.cat/) ha estat autoritzada pels titulars dels drets de propietat intel·lectual **únicament per a usos privats** emmarcats en activitats d'investigació i docència. No s'autoritza la seva reproducció amb finalitats de lucre ni la seva difusió i posada a disposició des d'un lloc aliè al servei UPCommons o TDX. No s'autoritza la presentació del seu contingut en una finestra o marc aliè a UPCommons (*framing*). Aquesta reserva de drets afecta tant al resum de presentació de la tesi com als seus continguts. En la utilització o cita de parts de la tesi és obligat indicar el nom de la persona autora.

ADVERTENCIA La consulta de esta tesis queda condicionada a la aceptación de las siguientes condiciones de uso: La difusión de esta tesis por medio del repositorio institucional UPCommons (http://upcommons.upc.edu/tesis) y el repositorio cooperativo TDR (http://www.tdx.cat/?locale-attribute=es) ha sido autorizada por los titulares de los derechos de propiedad intelectual **únicamente para usos privados enmarcados** en actividades de investigación y docencia. No se autoriza su reproducción con finalidades de lucro ni su difusión y puesta a disposición desde un sitio ajeno al servicio UPCommons No se autoriza la presentación de su contenido en una ventana o marco ajeno a UPCommons (*framing*). Esta reserva de derechos afecta tanto al resumen de presentación de la tesis como a sus contenidos. En la utilización o cita de partes de la tesis es obligado indicar el nombre de la persona autora.

WARNING On having consulted this thesis you're accepting the following use conditions: Spreading this thesis by the institutional repository UPCommons (http://upcommons.upc.edu/tesis) and the cooperative repository TDX (http://www.tdx.cat/?locale-attribute=en) has been authorized by the titular of the intellectual property rights **only for private uses** placed in investigation and teaching activities. Reproduction with lucrative aims is not authorized neither its spreading nor availability from a site foreign to the UPCommons service. Introducing its content in a window or frame foreign to the UPCommons service is not authorized (framing). These rights affect to the presentation summary of the thesis as well as to its contents. In the using or citation of parts of the thesis it's obliged to indicate the name of the author.

UNIVERSITAT POLITÈCNICA DE CATALUNYA

DOCTORAL THESIS

Study of Ice Content and Hydro-Mechanical Behaviour of Frozen Soils

By

YANXIN MAO

A thesis submitted in fulfillment of the requirements
for the degree of Doctor of Philosophy

in the

Division of Geotechnical Engineering
Department of Civil and Environmental Engineering
E.T.S.C.C.P.B., L'Escola Tècnica Superior d'Enginyers de Camins, Canals i Ports
UPC, Universitat Politècnica de Catalunya, BARCELONATECH

Supervisors:

Prof. Antonio Gens Solé
Prof. Enrique Romero Morales

June 11, 2018

To my whole family

Acknowledgments

I would like to take this opportunity to acknowledge all the persons who contributed to the accomplishment of this work and without whom this Ph.D. experience would never have been one of the best experiences in my life.

I would start by thanking the Prof. Antonio Gens Solé and Prof. Enrique Romero Morales. Thank you for giving me this opportunity to participate in this Ph.D. program. I want to say "thank you" to them, for their patient guiding and unreserved help throughout my whole Ph.D. study.

I would like to thank all the technicians in the lab of Geotechnical engineering UPC, including José, Tomás, Mercedes, Rodrigo, Víctor and the technician Gianpierro in Politecnico di Torino as well. Thank you so much for their kind help for designing set-ups, purchasing necessary experimental materials, performing experiments and giving some important advice.

I want to thank my colleagues in UPC, including Dr. Laura, Dr. Sajjad, Dr. Mauricio, Dr. Clara and many Ph.D. students including Núria, Dani, Rodrigo Weber, Alessandro, Erdem, Saeed, Arisleidy, etc. Thanks for their care and help both in study and in life. All these memories will keep in my mind forever and hope one day we can meet in China.

Thanks to my friends in Barcelona, He Lu, Xiao Lin, Xiao Dou, Jia Kong, Jun Lei, Ningning Zhang, Boyi Ye, Chen Jin, Heng Yang, Heping Shu, Yang Lu, Zhongbo Hu, Jianlin Chen, Tian Peng, Deniz, Nitin, Dalila, Joseph, Ali, Jue, Manuel etc. Because of you, I never feel lonely in Barcelona.

I also want to thank Barcelona, an amazing city with so many unforgettable memories that she gave me. I can never forget the nights we enjoyed with friends on the Barcelona beach. I can never forget the birthday parties my friends gave me, and I can never forget the memories of I met my wife here. I even cannot say goodbye to Barcelona.

I appreciate the financial support from Joint Scholarship between China Scholarship Council (CSC) and Universitat Politècnica de Catalunya (UPC). I also appreciate the funding support from my supervisor Antonio Gens, Enrique Romero, without their support, it is impossible to finish my Ph.D. research.

Lastly, I would like to express my gratitude to my parents, my elder brother, my younger sister, my sister in law, my nephew, my niece and all my family for their endless support in spirit. I also want to give my special thanks to my beloved wife for loving me and supporting me all the time and I am so lucky to have the best girl to be my wife and forever.

Abstract

The hydro-mechanical behaviour of soils during freezing and thawing is a coupled multi-physics process that has important practical applications. To cite but a few examples, on artificial ground freezing –to provide structural support and exclude the groundwater from underground constructions–, on seasonal variations of permafrost soils and their consequences on infrastructures, on geocomposite capillary barriers used to reduce frost heave in soils, and on engineered barriers subjected to freezing and thawing processes. Despite this importance, ice content and its migration process, as well as the coupled hydro-mechanical behaviour have not been extensively studied in partially saturated frozen soils. In these soils, ice formation increases the number of phases and the complexity of the experimental studies.

In this thesis, the unfrozen liquid saturation and the hydro-mechanical behaviour of two frozen soils (Barcelona clayey silt and fine sand) have been investigated at different initial degrees of saturation. A series of experimental setups have been designed and built to perform the tests (oedometer cell installed in a freezing/thawing chamber to control the temperature up to -15 °C; setup for freezing cylindrical samples in an electrical resistivity tomography ERT cell with 16 lateral electrodes).

Different methods have been considered and several models proposed in the thesis to indirectly determine the unfrozen liquid saturation of compacted soils at different temperatures, porosities and initial degrees of saturation. The methods rely on measurements during transient freezing of the bulk electrical conductivity EC, relative dielectric permittivity, and thermal conductivity. In the case of EC tests, the unfrozen liquid saturation results have been interpreted with a modified Archie's law and compared to the electrical conductivity of the pore liquid. The soil freezing retention curve (unfrozen liquid saturation vs temperature) has been also estimated by combining the Clausius-Clapeyron equation with water retention data on drying, as well as with a capillary bundle model with mercury

intrusion porosimetry MIP results. A very good agreement has been found between the proposed approach using bulk EC measurements and the water retention and porosimetry results, which validated the proposed models.

The EC model has been used to interpret the transient freezing of cylindrical homogeneous samples that have been exposed to very low temperatures at its central axis (-15°C) and with adiabatic conditions imposed at the external boundaries. A 2D ERT setup is used to monitor the phase change and the migration of pore liquid. Reconstructed maps of EC have been translated into images of temperature and unfrozen liquid saturation at different elapsed times. The reconstructed temperature field showed good agreement with direct temperature measurements using inserted thermocouples. The ERT tests have been also performed on homogeneous samples with inclusions (low electrical conductive or high electrical conductive zones), which indicated that the ERT system could perfectly detect the effects of these anomalies on a transient freezing process.

The volume change behaviour on freezing/thawing has been investigated on saturated samples using temperature controlled oedometer cells under different constant vertical stresses. A small irreversible compression has been systematically detected after a freezing/thawing cycle on different soils, which depended on the current stress state. The microstructural changes of the compacted samples after freezing/thawing paths have been also explored using MIP and field emission scanning electron microscopy FESEM observations, which have been analysed using PCAS image processing software. MIP results have indicated that the freezing/thawing process might have decreased the macropore volume (between aggregates) and enlarge some micropore volume.

Key Words: unsaturated frozen soil, ice content, electrical conductivity, relative dielectric permittivity, thermal conductivity, electrical resistivity tomography, temperature controlled oedometer, microstructure changes, THM coupling

Resumen

El comportamiento hidromecánico de los suelos durante la congelación y descongelación es un proceso multifísico acoplado que tiene importantes aplicaciones prácticas. Por ejemplo, en la congelamiento artificial del terreno -para dar soporte estructural y evitar el agua en construcciones subterráneas-, en las variaciones estacionales de suelos permafrost y sus efectos sobre las infraestructuras, en las barreras capilares utilizadas para reducir los efectos de heladas, y en barreras de ingeniería sometidas a ciclos de congelación/descongelación. A pesar de esta importancia, el contenido de hielo y su proceso de migración, así como el comportamiento hidromecánico acoplado, no se han estudiado en forma extensa en los suelos parcialmente saturados. En estos suelos, la formación de hielo aumenta el número de fases y la complejidad de los estudios experimentales.

Se han estudiado el grado de saturación de líquido descongelado y el comportamiento hidromecánico de dos suelos congelados (limo arcilloso de Barcelona y arena fina) a diferentes grados de saturación iniciales. Se han diseñado y construido una serie de equipos experimentales para realizar los ensayos (célula edométrica en una cámara de congelación/descongelación para controlar la temperatura hasta -15 °C; equipo para congelar muestras cilíndricas en una célula de tomografía de resistividad eléctrica ERT con 16 electrodos laterales).

Se han utilizado diferentes métodos y se han propuesto modelos para determinar indirectamente la saturación de líquido descongelado en suelos compactados a diferentes temperaturas, porosidades y grados de saturación iniciales. Los métodos se basan en mediciones de la conductividad eléctrica del suelo EC, la permitividad dieléctrica relativa y la conductividad térmica. En el caso de los ensayos de EC, los resultados se han interpretado con una ley de Archie modificada y se han comparado con la conductividad eléctrica del líquido intersticial. La curva de retención de congelación del suelo (grado de saturación de líquido descongelado frente a temperatura) se estimó combinando la ecuación de Clausius-Clapeyron con los datos de retención al agua durante el secado, así como con un modelo capilar utilizando porosimetría de intrusión de mercurio MIP. Los resultados de las mediciones de EC, así como de retención al agua y porosimetría, han sido muy consistentes lo que ha permitido validar al modelo.

El modelo EC se ha utilizado para interpretar la etapa transitoria de congelación de muestras cilíndricas, que han estado expuestas a temperaturas muy bajas en su eje central (-15 °C) y con condiciones adiabáticas en los contornos. Se utiliza ERT 2D para controlar el cambio de

fase y la migración del líquido de poro. Los mapas reconstruidos de EC se han convertido en mapas de temperatura y de saturación de líquido descongelado a lo largo del tiempo. El dominio reconstruido de temperatura resultó ser consistente con las medidas directas de temperatura con termopares. Los ensayos ERT también se realizaron sobre muestras con inclusiones (zonas de alta o baja conductividad eléctrica), que han evidenciado la utilidad de este método para detectar los efectos de estas anomalías durante una congelación.

Los cambios de volumen durante un ciclo de congelación/descongelación se han investigado sobre muestras saturadas a diferentes tensiones verticales constantes utilizando células edométricas de temperatura controlada. Se ha detectado una pequeña compresión irreversible después de la congelación/descongelación, que depende del estado tensional. También se han estudiado los cambios microestructurales generados después de un ciclo de congelación/descongelación utilizando MIP e imágenes de microscopía electrónica FESEM analizadas mediante tratamiento de imágenes PCAS. Los resultados de MIP han indicado que el ciclo de congelación/descongelación podría haber disminuido el volumen de macroporos (entre agregados) y aumentado el volumen de microporos.

Palabras clave: suelo congelado parcialmente saturado, contenido de hielo, conductividad eléctrica, permitividad dieléctrica relativa, conductividad térmica, tomografía de resistividad eléctrica, edómetro con control de temperatura, cambios de microestructura, acoplamiento THM

Table of Contents

List of Figures

List of Tables

Chapter 1 Introduction

1.1 Background and motivation

Frozen ground is soil or rock with a temperature below the freezing point of water. The definition is based completely on temperature and is independent of the water and ice content of the soil or rock (Andersland and Ladanyi, 2004). The freezing process occurs naturally in many areas of the globe, such as elevated plateaus and mountains, the two poles and the northern latitudes. The ground in the polar region is frozen all year round, and this is known as permafrost. Compared with permafrost, most natural ground freeze and thaw in a seasonal way. Ice lens formation during freezing (frost heave) and settlement during thawing could be harmful to the engineering performance of roads, pavements, and civil infrastructures. The pictures of damage associated with frost heave and settlement on thawing are plotted in Figure 1.1.

(a) (b)

Figure 1.1 (a) Freeze-thaw damage on pavements (http://www.pavementinteractive.org/frost-action/); (b) Thaw settlement of building at Nain, Labrador (https://ipa.arcticportal.org/news/)

On the other hand, the increase of ice content in the soil as the temperature decreases will increase soil hear strength and decrease the permeability. There are advantages to man-made freezing; since it can be easily controlled. It has been used by civil and mining engineers to temporarily stabilise the surrounding soil and rock during an excavation. The process has become known as artificial ground freezing (AGF), which is done to provide structural support and/or to exclude the groundwater from openings until construction of a final lining provides permanent security (Harris, 1995; Casini et al., 2014; Russo et al., 2015). Being a temporary process with a low environmental impact, freezing does not affect the level of the water table or the quality of the groundwater. The initial cost may be higher than other temporary support techniques, but if the risk and final costs are considered in total, the method has frequently been shown to be the most cost-effective (Harris, 1995).

In the last two decades, an increase in applications of AGF in underground constructions (see Figure 1.2) has been observed. There are many recent examples reported in the literature on structures such as railway station tunnels, passageways and shafts that have been successfully completed using AGF under very diverse geotechnical conditions all over the world (Ping et al., 2003; Colombo et al., 2008; Chang and Lacy, 2008; Russo et al., 2015). Besides protecting excavations, AGF can be used to stabilise slopes, retrieve undisturbed samples of coarse-grained soils, construct temporary access roads and maintain permafrost below pipeline foundations and heated buildings (Sego et al., 1994; Harris, 1995). Laboratory and full field experiments have also demonstrated the effectiveness of AGF for the containment of subsurface hazardous and radioactive waste (Dash et al., 1997). The US Department of Energy has designated frozen ground barriers as one of its top ten remediation technologies and the technique has been considered as a possible solution for the radioactive contamination of the water surrounding the compromised Fukushima nuclear power plant.

Meanwhile, climate change has caused public concern over the last several decades and greater attention has been given to its impact on the cryosphere (Nelson, 2003; Barnett et al., 2005; Cheng and Wu, 2007). As a main component of the cryosphere, permafrost is extremely vulnerable to climate change at different spatial and temporal scales. Permafrost

degradation may affect local hydrology, ecology, engineering infrastructure, and even the climate (Cheng and Zhao, 2000; Nelson et al., 2001; Zhang et al., 2005; Zimov et al., 2006).

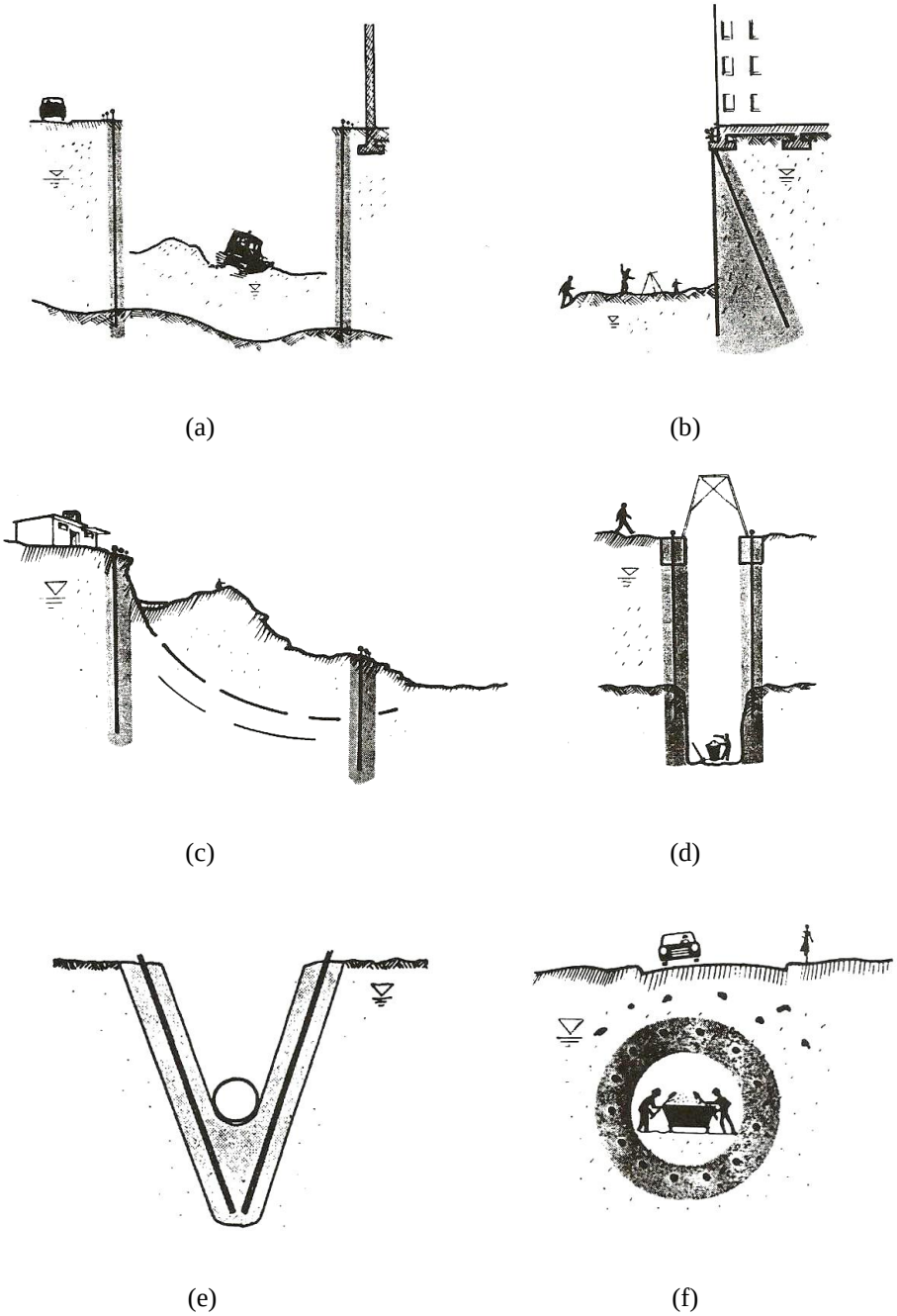

Figure 1.2 Ground freezing applications: (a) deep excavations; (b) underpinning; (c) landslides; (d) shafts; (e) deep trenches and (f) tunnels. (Andersland and Ladanyi, 2004)

Moreover, winter conditions associated with freezing, thawing and soil moisture changes are important factors for a wide range of agricultural applications. Extreme soil temperatures and soil ice affect winter survival of crops, as well as pests. Runoff and soil water transfer are important concerns for the analysis of soil erosion and for spring soil moisture reserves in dryland areas (Hayhoe, 1994).

The frozen soils in all above-mentioned cases (natural or artificial) are not always saturated. In fact, geocomposite capillary barriers used to reduce frost heave in soils, as well as engineered barriers subjected to freezing and thawing processes, are some examples in which partially saturated soils may be found. Therefore, a deep understanding of partially saturated and fully saturated frozen soils is very important and necessary to all the applications and for avoiding damage to some infrastructures. Despite this importance, ice content and its migration process, as well as the coupled hydro-mechanical behaviour have not been extensively studied in partially saturated frozen soils. In these soils, ice formation increases the number of phases and the complexity of the experimental studies.

1.2 Objectives

The main goal of this thesis is to explore and better understand the freezing-thawing process in soils from a fundamental physical perspective, under both saturated and partially saturated conditions.

To achieve this main goal, the following objectives have been addressed:

- To develop and calibrate different cells to perform the freezing/thawing experiments (oedometer cell installed in a freezing/thawing chamber to control the temperature up to -15°C, set up for freezing cylindrical samples in an electrical resistivity tomography ERT cell).
- To calibrate different techniques to estimate the unfrozen liquid saturation under partially saturated and saturated conditions using non-destructive methods (bulk

electrical conductivity EC, relative dielectric permittivity and thermal conductivity measurements).

- To propose an EC model based on a modified Archie's law to indirectly estimate the unfrozen liquid saturation at different soil temperatures, porosities and initial degrees of saturation.
- To validate the EC model results with soil freezing retention curves obtained by combing the Clausius-Clapeyron equation with water retention data on drying, as well as with a capillary bundle model with mercury intrusion porosimetry MIP results.
- To monitor the temporal and spatial evolution of freezing processes in soils (homogeneous soils and soils with inclusions) in an electrical resistivity tomography ERT cell, in which reconstructed maps of EC have been translated into images of temperature and unfrozen liquid saturation at different elapsed times.
- To study the volume change behaviour of different soils and the corresponding microstructural changes (using MIP and image analyses of FESEM observations) along different stress and temperature paths (freezing/thawing cycle).

1.3 Methodology

The thesis follows and experimental methodology, in which two soils (Castelldefels fine sand and Barcelona clayey silt) have been studied at different freezing temperatures, porosities and initial degrees of saturation. The methodology involved the following tasks.

To begin with, the ice content (or unfrozen liquid saturation) in frozen soil has been explored using different techniques (bulk electrical conductivity EC, relative dielectric permittivity, and thermal conductivity). At a first stage of the research, a commercial frequency domain reflectometry FDR probe has been used for EC and relative dielectric permittivity measurements. At a more advanced stage of the research, a small cell with plate and needle electrodes and thermocouples has been improved to better assess EC by applying a uniform

flow of electric current to a partially saturated soil at different temperatures. The thermal conductivity of the soil has been determined using an existing setup that has been modified to conduct the tests under unfrozen and maximum frozen states.

Efforts have been dedicated to proposing an EC model based on a modified Archie's law to indirectly estimate the unfrozen liquid saturation at the different soil states. The model predictions at different temperatures have been compared to soil freezing retention curves obtained by different methods (Clausius-Clapeyron equation with water retention data on drying, and with a capillary bundle model with mercury intrusion porosimetry MIP data).

The EC model has been also used to interpret the temporal and spatial evolution of unfrozen liquid saturation and temperature using a new setup for freezing cylindrical samples in an electrical tomography ERT cell. The ERT system has been used to track the soil freezing process of partially saturated and saturated states, in which homogeneous samples and samples with high and low conductivity inclusions have been analysed.

Finally, the volume change behaviour and microstructure changes of clayey silt samples have been investigated along different stress and temperature paths (loading/unloading at constant temperature and freezing/thawing cycle at constant vertical stress). A temperature-controlled oedometer cell using a freezing/thawing chamber has been updated and calibrated. MIP and electron microscopy FESEM tests with image analyses using PCAS software have been used to study the microstructural changes.

The following papers stem from the research done along the thesis:

Mao Y., Romero E. and Gens A. (2016). Exploring ice content on partially saturated frozen soils using dielectric permittivity and bulk electrical conductivity measurements. In: 3rd European Conference on Unsaturated Soils, Paris, France, pp.1-6.

Mao Y., Romero E., and Gens A. (2018) Ice formation in unsaturated frozen soils. In: 7th International Conference on Unsaturated Soils, Hong Kong, China, August 2018 (accepted contribution).

Mao Y., Romero E., Musso G. and Gens A. (2018) Exploring ice formation and migration in frozen soils. In: International Symposium on Energy Geotechnics, Lausanne, Switzerland, September 2018 (accepted contribution).

Mao Y., Romero E., Gens A. and Musso G. (2018). Freezing retention behaviour of a partially saturated clayey silt. Géotechnique Letters (submitted).

Mao Y., Romero E., Musso G. and Gens A. (2018). Temporal and spatial monitoring of soil freezing using electrical resistivity tomography. Géotechnique (in preparation).

Mao Y., Romero E., Gens A. and Casini F. (2018). Volume change behaviour and microstructural changes undergone by soils submitted to freezing/thawing. Canadian Geotechnical Journal (in preparation).

1.4 Layout of thesis

The layout of the thesis includes:

Chapter 1: **Introduction.** The first chapter introduces different geotechnical applications and highlights the need for further hydro-mechanical studies on partially saturated soils subjected to freezing/thawing cycles. The objectives, methodology followed, and layout of the thesis are presented.

Chapter 2: **Literature review**. The chapter presents a literature review on different techniques to indirectly determine the ice content. It also describes details on soil freezing retention curves based on semi-empirical models and on models that use the Clausius-Clapeyron equation combined with water retention curves, aspects of ERT in soils are also described, as well as behavioural and microstructural features on frozen soils.

Chapter 3: **Experimental program and equipment.** The experimental program, the properties of the tested materials and all the equipment used in the tests are

introduced. Details on new designs, modifications, and calibrations of the set-up are presented.

Chapter 4: **Exploring ice formation and migration in partially frozen soils.** Measurements of bulk EC, dielectric permittivity and thermal conductivity for fine sand and clayey silt samples at different initial states (temperature, porosity, and degree of saturation) are presented. The results can be used to obtain the parameters in Archie's second law, alpha model, and geometric mean expression, respectively. The obtained expressions will be compared and used to determine the ice content of soils at the given temperature and initial conditions (porosity and degree of saturation). Two soil freezing retention curve models are proposed and compared with bulk EC data.

Chapter 5: **ERT monitoring of soil freezing.** Several freezing ERT tests are described: (a) homogeneous samples at different initial degrees of water saturation (including full saturation); (b) homogeneous samples with inclusions (low and high conductivity inclusions); (c) samples during several freezing-thawing cycles. ERT results are discussed and reconstructed by the proposed model to display the temporal and spatial evolutions of temperature and ice content. Numerical modelling is used to back-analyse selected soil properties (for example, retention curve) during the test by comparing measured and computed variables (for example, unfrozen liquid content) in space and time.

Chapter 6: **Volume change behaviour and microstructural changes on a freezing/thawing cycle.** The oedometer test results on clayey silt, Pozzolana and Yellow tuff samples following different stress and temperature paths are presented and discussed. The volume change behaviour and microstructural changes are analysed and discussed.

Chapter 7: **Conclusions and future works.** The general concluding remarks and highlights are presented, and future works proposed.

Chapter 2 Literature review

2.1 Preface

This chapter presents a literature review of some issues discussed when describing soil freezing-thawing behaviour, such as ice content, soil freezing retention curve and macro and microstructure changes after stress and temperature paths. For determining ice content of frozen soils, different measurements such as electrical conductivity, relative dielectric permittivity, thermal conductivity and corresponding theoretical and empirical models are reviewed. Secondly, several soil freezing retention curves proposed by different authors are reviewed, including semi-empirical models and models based on SWCC equation combined with Clausius-Clapeyron equation. Thirdly, the development of ERT techniques in the soil are generally investigated and especially the applications of ERT technique in frozen soils. Lastly, the volume change behaviour of frozen soils and their microstructure changes are studied.

2.2 Measurement of ice (or unfrozen water) content

Ice content and its migration process have not been extensively studied in partially saturated soils (Liu and Si, 2011; Zhou et al., 2014), despite having important practical applications for the geocomposite capillary barriers used to reduce frost heaving in soils, for AGF in partially saturated soils and for engineered barriers that are subjected to the freezing and thawing process.

When dealing with the modelling of THM coupled processes induced by the freezing of saturated and unsaturated soils, an important issue is the definition of the freezing retention

model, which links the saturation degree of the liquid phase (unfrozen water) to the temperature of the soil. The Clausius-Clapeyron equation, which governs the condition for equilibrium between the coexisting liquid water and ice phases, together with a modified form of the van Genuchten equation to consider the liquid-ice surface tension is usually adopted to represent this freezing retention model (see for instance, Nishimura et al., 2009; Gens, 2010; Casini et al., 2013 and Casini et al., 2014).

To experimentally validate coupled THM models for frozen soils, cryogenic suction, together with ice content, are important stress and state variables to determine. Nevertheless, as cryogenic suction is usually difficult to measure directly, experimental efforts have been mainly concentrated on estimating ice content (or unfrozen water content) indirectly by many measurements such as bulk electrical conductivity EC, relative dielectric permittivity, thermal conductivity and other workable measurements. The detailed literature studies of exploring ice content are summarised below.

2.2.1 Electrical conductivity

Electrical conductivity measurements have been used in the past decades to characterize the state of soil samples with success because of its non-destructive properties. The determination of soil water content (Rhoades et al., 1976; Kalinshi and Kelly, 1993; Muñoz-Castellblanco et al., 2012), salinity (Rhoades et al., 1989; Rhoades and Schilfgaarde, 1976; Comina et al., 2011), porosity (Lovell, 1985), degree of water saturation (Mao et al., 2016), degree of compaction (McCarter, 1984; Abu-Hassanein et al., 1996), liquefaction potential (Erchul and Gularte, 1982; Arulmoli et al., 1985), consolidation (Roberts and Schwartz 1985; Orru et al., 2009), and permeability (Kelly, 1977; Lovell, 1985; Avellaneda and Toroquato, 1991; Liang et al., 2000) by electrical conductivity have been investigated.

These investigations indicate that the contributions of soil bulk electrical conductivity include the particle conductivity σ_p, the pore water conductivity σ_w, and the surface conductivity σ_s. According to these constituents of soil, several mixing models have been developed and

proposed by different researchers, to determine the bulk electrical conductivity σ of the saturated porous media. These models are summarised in Table 2.1.

Table 2.1 Various mixing models used for predicting electrical conductivity of the soil

Name	Equation
Parallel model (Rhoades et al., 1976)	$\sigma = (1-n)\sigma_p + n\sigma_w$
Series model (Shang et al., 1995)	$\frac{1}{\sigma} = \frac{1-n}{\sigma_p} + \frac{n}{\sigma_w}$
Logarithmic model (McLachlan et al., 1990)	$\sigma^{\alpha} = (1-n)\sigma_p{}^{\alpha} + n\sigma_w{}^{\alpha}$
General effective medium model (McLachlan et al., 1990)	$\frac{(1-n)\left(\sigma_p{}^{1/t} - \sigma^{1/t}\right)}{\sigma_p{}^{1/t} + X\sigma^{1/t}} + \frac{n\left(\sigma_w{}^{1/t} - \sigma^{1/t}\right)}{\sigma_w{}^{1/t} + X\sigma^{1/t}} = 0$
Maxwell model (Maxwell, 1881)	$\frac{\sigma}{\sigma_w} = \frac{2\sigma_w + \sigma_p - 2(1-n)(\sigma_w - \sigma_p)}{2\sigma_w - \sigma_p + (1-n)(\sigma_w - \sigma_p)}$
Archie's law (Archie, 1942)	$\sigma = c\sigma_w n^p$
Modified Archie's law (Glover et al., 2000)	$\sigma = \sigma_p (1-n)^k + \sigma_w n^s,\ k = \log(1-n^s)/\log(1-n)$

Key factors: n is porosity, α, t, p, k, s are fitted model parameters.

For the unsaturated soils, Archie's law (Archie, 1942) can be expressed as

$$\sigma = c\sigma_w n^p S_r^q \tag{2.1}$$

where c is a fitting parameter, and p is the cementation factor, which is related to the tortuosity and interconnectivity of the pore network (usually between 1.4 and 2.0). These parameters help in incorporating the influence of tortuosity and interconnectivity of pores and make Archie's law more versatile in nature. S_r is the degree of saturation and q is a saturation exponent, typically around 2.0.

Kalinski and Kelly (1993) proposed a method for estimating water content of soils from electrical conductivity, which is presented as

$$\sigma_0 = a\sigma_w\theta^2 + b\sigma_w\theta + \sigma_s \tag{2.2}$$

where σ_w is the pore-water electrical conductivity, dS/m, σ_s is the apparent soil-particle electrical conductivity, dS/m and a, b are material constants (Rhoades et al., 1976).

Fukue et al. (1999) proposed a structural model consisting of serial and parallel parts with three phase components, solid, liquid and gas, which was developed to give information on soil structures. The structure model is characterized by the ratio of the serial and parallel parts, which have different electrical conductivities at given directions. The ratio is expressed by a structural factor, F. The value of Γ defined by $\sigma_w/(1\text{-}F)$ is used and examined to characterize the clay structure, where σ_w is the apparent resistivity of pore water. The structural model of the soil is presented in Figure 2.1.

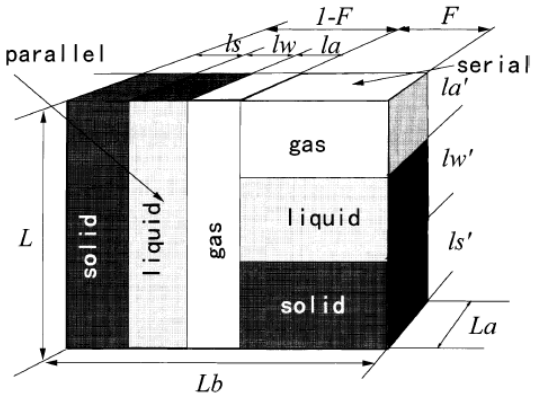

Figure 2.1 Structural model of soil (Fukue et al., 1999)

Chen et al. (2007) established a 2-D empirical model of resistivity changing with the water saturation in expansive soil. For a given soil body, ignoring the change in porosity caused by the change of saturation, the model is presented as

$$\begin{cases} \rho_1 \approx \dfrac{\rho}{S_r \times n} + c_1 \\ \rho_2 \approx \alpha \times \dfrac{\rho}{S_r \times n} + c_2 \end{cases} \tag{2.3}$$

where ρ_1 is the resistivity of the soil, given that its liquid consists largely of free water, ρ_2 is the resistivity of the soil given that the liquid in the soil consists largely of bound water, α is

the structural factor, S_r is the degree of saturation, n is the porosity and c_1 and c_2 are the constants of integration.

The bulk electrical conductivity of unsaturated soil comprises particle conductivity, surface conductivity, and interstitial water conductivity. The particle conductivity and surface conductivity are quite low compared to interstitial water, particularly in soils with the moderate specific surface. Therefore, the particle conductivity and surface conductivity can be ignored compared with the higher electrical conductivity of interstitial water especially when interstitial water is a saline solution. This assumption is applied to all three unsaturated models mentioned above. Due to the fact that ice has similar electrical conductivity property to soil solids, then the above models could possibly to be used to predict the amount of unfrozen water at different temperatures. It is important to remark that soil bulk electrical conductivity has a strong temperature-dependence. Soil EC above freezing decreases with the decrease of temperature (Bai et al., 2013), associated with the decrease of the mobility of the ions dissolved in the liquid phase.

2.2.2 Relative dielectric permittivity

Besides electrical conductivity, relative dielectric permittivity is another independent physical property that can be used to characterize the behaviour of soil when excited by electromagnetic field (Porretta and Bianchi, 2016). The dielectric constant of a material describes its ability to store electrical potential energy in response to an applied electric field. The large contrast between the dielectric constant of water (~80) and that of air (1), ice (~4) and soil minerals (~4) can be used to determine the unfrozen water content accurately in many soils (Jones and Or, 2003). Time domain reflectometry (TDR) and frequency domain reflectometry (FDR) have been widely used to determine unfrozen water content in frozen soils for their accuracy, fast response and automation capability (Hayhoe et al., 1983; Spaans and Baker, 1995; Seyfried and Murdock, 1996; Boike and Roth, 1997; Stahli and Stadler, 1997; Flerchinger et al., 2006; Watanabe and Wake, 2009; He and Dyck, 2013; Zhou et al., 2014; Mao et al., 2016). The nuclear magnetic resonance (NMR) method has also been used

to measure unfrozen water content in frozen soil (Tice et al., 1982; Ishizaki et al., 1996; Watanabe and Mizoguchi, 2002; Watanabe and Wake, 2009; Zhou et al., 2014).

For calibrating the measured ε, Patterson and Smith (1981) found that replacing air with ice at constant volumetric water content θ increased the soil dielectric permittivity ε slightly, but the increase was insignificant compared to their overall variation in ε determination. They concluded that the same calibration equation is applicable to both frozen and unfrozen soils. Topp et al. (1980) proposed a third-order polynomial relationship to calibrate ε

$$\theta = -0.053 + 0.29\varepsilon - 5.5\times10^{-4}\varepsilon^2 + 4.3\times10^{-6}\varepsilon^3 \tag{2.4}$$

Smith and Tice (1988) calibrated TDR for frozen soil in small, saturated samples using NMR to determine θ and found that

$$\theta = -1.458\times10^{-1} + 3.858\times10^{-2}\varepsilon - 8.502\times10^{-4}\varepsilon^2 + 9.920\times10^{-6}\varepsilon^3 \tag{2.5}$$

The composite dielectric approach used by Roth et al. (1990) describes the soil as a three-phase medium consisting of the solid, liquid and gaseous phases and the mixing model for water content is

$$\varepsilon_c = \left[\theta\varepsilon_w^{\alpha} + (1-n)\varepsilon_s^{\alpha} + (n-\theta)\varepsilon_a^{\alpha}\right]^{1/\alpha} \tag{2.6}$$

where ε_c is the composite dielectric constant, and ε_s, ε_w, and ε_a are the dielectric constants of soil particles, water, and air, respectively. θ, $1-n$, and $\theta-n$ are the volume fractions of water, soil particles, and air, respectively. n is the soil porosity, α is the geometric factor of the probe. The above equation can be rearranged to the following one:

$$\theta = \frac{\varepsilon_c^{\alpha} - (1-n)\varepsilon_s^{\alpha} - n\varepsilon_a^{\alpha}}{\varepsilon_w^{\alpha} - \varepsilon_a^{\alpha}} \tag{2.7}$$

For frozen soil consisting of unfrozen water, ice, soil particles, and air, the mixing model can be written as (Seyfried and Murdock, 1996; Stahli and Stadler, 1997; Watanabe and Wake, 2009; Zhou et al., 2014):

$$\varepsilon_c = \left[\theta_u \varepsilon_w^\alpha + \theta_i \varepsilon_i^\alpha + (1-n)\varepsilon_s^\alpha + (n-\theta_t)\varepsilon_a^\alpha\right]^{1/\alpha} \tag{2.8}$$

where θ_u is the unfrozen water content in frozen soil, θ_i is the ice content, ε_i is the dielectric constant of ice, and θ_t is equal to $\theta_u + \theta_i$. Considering the total water content ($\theta_t = \theta_w + \frac{\rho_i}{\rho_w}\theta_i$), equation (2.7) can be rewritten as

$$\theta_u = \frac{\varepsilon_c^\alpha - (1-n)\varepsilon_s^\alpha - \left(n - \frac{\rho_w}{\rho_i}\cdot\theta_{total}\right) - \frac{\rho_w}{\rho_i}\cdot\theta_{total}\varepsilon_i^\alpha}{\varepsilon_w^\alpha - \frac{\rho_w}{\rho_i}\cdot\varepsilon_i^\alpha + \left(\frac{\rho_w}{\rho_i} - 1\right)\cdot\varepsilon_a^\alpha} \tag{2.9}$$

In addition, the influence of temperature T on the dielectric constant of water is considered as follows (Weast, 1986):

$$\varepsilon_w(T) = 78.54\left[1 - 4.579\times10^{-3}(T-25) + 1.19\times10^{-5}(T-25)^2 - 2.8\times10^{-8}(T-25)^3\right] \tag{2.10}$$

The temperature and frequency have strong effects on the dielectric constant of water. Figure 2.2 shows the real dielectric constants ε of liquid water and ice against the frequency f of the exciting electrical field for various values of the temperature.

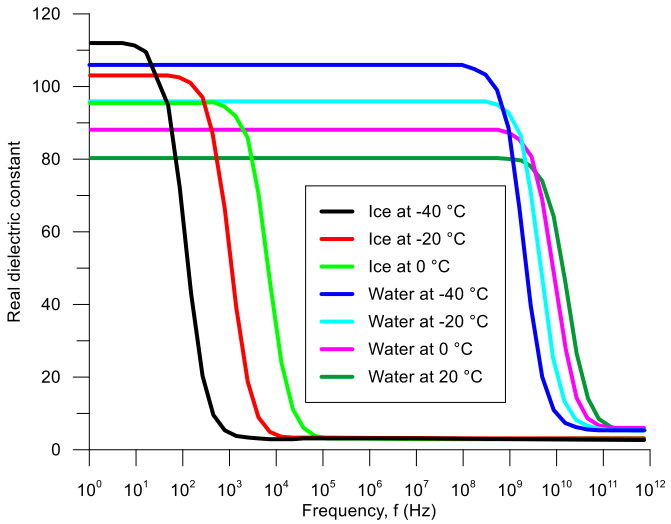

Figure 2.2 Frequency dispersion of water and ice real dielectric constants at different temperatures. (Fabbri et al., 2006)

Aside from the effect from the temperature, the EC of interstitial water also relates to the real dielectric constant at different frequencies. The figure 2.3 shows that at a given frequency, ion-dipole polarization is more evident as the EC increases. Typically, the frequency range for dielectric measurements is 50 MHz to 1 GHz. In this frequency range, salinity effects are not a factor if the EC is less than 1 dS/m. However, for salinities greater than 1 dS/m, salinity effects begin to manifest due to an increase in the dielectric constant which is a result of the onset of ion-dipole polarization.

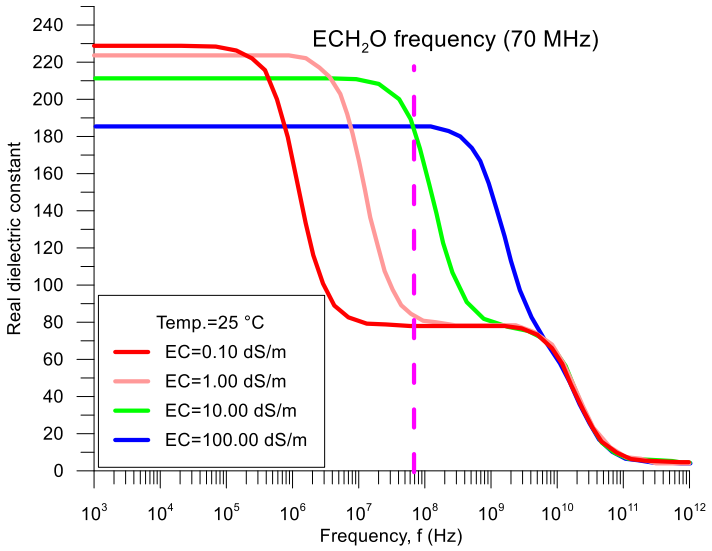

Figure 2.3 Electrical conductivity (EC) dependence of real dielectric constant (Buehler et al., 2011)

Therefore, when applying dielectric permittivity to explore the unfrozen water content in frozen soils, the temperature and concentration of pore-water effects on dielectric permittivity should be considered.

2.2.3 Thermal conductivity

The soil is a multi-phase material consisting of solid particles, gas and/or liquid. Thermal properties of soils are not only determined by the intrinsic physical properties of each phase but also affected by variation of each phase. The thermal conductivity λ of different soil phases varies over two orders of magnitude (e.g., thermal conductivity of mineral particles $\lambda_{mineral} > 3$ W/m·K, thermal conductivity of water $\lambda_{water} = 0.56$ W/m·K (at 0°C), and thermal

conductivity of air λ_{air} = 0.026 W/m K) (Mitchell and Soga, 2005; Yun and Santamarina, 2008). However, the thermal conductivity of dry soil λ_{dry_soil} is almost one order of magnitude lower than that of the pure mineral solids, in most cases λ_{dry_soil} < 0.5 W/m·K, depending on mineral composition and packing density (Farouki, 1981). This implies that the air obstructs heat conduction and heat conduction primarily occurs through the particle contacts in dry soil. At the other end, the thermal conductivity of water-saturated soil is between that of the pure mineral and that of water, implying that replacement of air with water provides a significant improvement in the heat conduction through the soil mixture. The ordered sequence of typical thermal conductivity values is $\lambda_{air} < \lambda_{dry\_soil} < \lambda_{water} < \lambda_{saturated\_soil} < \lambda_{mineral}$. These observations and many experimental studies (Brandon and Mitchell 1989; Farouki 1981; Smits et al. 2010) confirm that the varying water saturation in the soil mixture system plays an important role in determining the bulk thermal properties. Some typical values of thermal parameters of selected materials are shown in Table 2.2.

Table 2.1 Typical values of thermal parameters of selected materials (Harris, 1995)

Material	Thermal conductivity W/mK	Volumetric heat capacity: MJ/m^{3}K	Thermal diffusivity: m^2/s·10^{-7}
Water	0.602	4.18	1.45
Ice	2.22	1.93	11.5
Air	0.024	0.00126	190
Quartz	8.4	1.9	44
Many soil minerals	2.9		
Organic soil	0.25	2.5	1
Limestone	1.7-2.9	2.4-4.2	4-12
Dolomite	5.02	2.51	2
Sandstone	1.8-4.2	2.51	7-16.7
Shale	1.5	1.84	8.2
Quartzite	4.5-7.1		
Concrete	1.3-1.7		

The accurate prediction of the thermal conductivity of composite materials comprises a significant portion of the literature about heat transfer in porous media, and a large number of effective thermal conductivity models have been proposed. New models for thermal

conductivity of soils are emerging, suggesting that, to-date, a unified model or prediction procedure has not been found with universal applicability. In this section, several existing models have been reviewed and categorized into the following three groups based upon their principles:

- *Mixing models.* This type of model conceptualizes the multi-phase soil system as a certain combination of series and parallel solid, air and/or water blocks in the cubic cell or representative elementary volume; and the effective thermal conductivity of the bulk medium is calculated by mixing those blocks (see Table 2.3).
- *Mathematical models.* These models were adopted from predictive models of other physical properties, such as dielectric permittivity, magnetic permeability, electrical conductivity, and hydraulic conductivity; which are calculated by certain mathematical algorithm given the thermal conductivity of each component and their volume fractions (see Table 2.3).
- *Empirical models.* This group of models builds the relationship between relative thermal conductivity and degree of saturation or water content, by normalizing the effective thermal conductivity or Kersten number over the difference between saturated state thermal conductivity λ_{sat} and dry state λ_{dry} (see Table 2.4).

Table 2.3 Selected mixing and mathematic models for the effective thermal conductivity of unsaturated frozen soils (Dong et al., 2015)

Models	Equations
Series	$\frac{1}{\lambda_{eff}} = \sum_{i=1}^{4} n_i \cdot \frac{1}{\lambda_i}$
Parallel	$\lambda_{eff} = \sum_{i=1}^{4} n_i \lambda_i$
Geometric mean	$\lambda_{eff} = \prod_{i=1}^{4} \lambda_i^{n_i}$
Quadratic parallel	$\lambda_{eff} = \left(\sum_{i=1}^{4} n_i \cdot \sqrt{\lambda_i} \right)^2$
Effective medium	$\sum_{i=1}^{4} \left(n_i \frac{\lambda_i - \lambda_{eff}}{\lambda_i + 2\lambda_{eff}} \right) = 0$
Self-consistent	$k_{eff} = \frac{1}{3} \left(\sum_{i=1}^{4} \frac{n_i}{\lambda_i + 2\lambda_{eff}} \right) = 0$

De Vries (1963)	$k_{eff} = \frac{\sum_{i=1}^{4} F_i n_i \lambda_i}{\sum_{i=1}^{4} F_i n_i}$	F_i and g_i are weight and shape factors

Key factors: n_i are volume fraction of each phase; i can be *a* (air), *w* (water), *i* (ice) and *s* (soild), [-]; λ_i are the thermal conductivity of each phase, (λ_a =0.56, λ_w =0.026, λ_i =2.20), (W/ m·K)

Table 2.4 Selected empirical models for the effective thermal conductivity of soils

Models	Parameters			Equations
	λ_i	λ_e , λ_{dry} , λ_{sat}	others	
Kersten (1949)	-	-	-	$\lambda_e = 0.14\left(\log\theta - 0.2\right)\cdot 10^{0.62\cdot\gamma_{dry}}$
Johansen (1975)	$\lambda_s = \lambda_q^q \lambda_o^{(1-q)}$	$\lambda_{sat} = \lambda_s^{(1-n)}\lambda_w^n$ $\lambda_{dry} = \frac{0.135\gamma_{dry} + 64.7}{2700 - 0.947\gamma_{dry}}$	-	Coarse sand: $k_e = 0.7\log S + 1.0$ Fine soil: $k_e = \log S + 1.0$
Donazzi (1977)	-	-	-	$\lambda_e = \lambda_w^n \lambda_s^{1-n}\exp\left[3.08n\left(1-S_r\right)\right]$
Cote and Konrad (2005)	$\lambda_s = \lambda_q^q \lambda_o^{(1-q)}$	$\lambda_{sat} = \lambda_s^{(1-n)}\lambda_w^n$ $\lambda_{dry} = \chi\times 10^{-\eta\cdot n}$	χ	$k_e = \frac{\kappa S}{1+(\kappa-1)S}$
Lu et al. (2007)	$\lambda_s = \lambda_q^q \lambda_o^{(1-q)}$	-	α	$k_e = \exp\left[\alpha\left(1-S^{\alpha-1.33}\right)\right]$
Chen (2008)	-	-	b , c	$\lambda_e = \lambda_s^{1-n}\lambda_w^n n\left[\left(1-b\right)S + b\right]^{cn}$

Key parameters: S is degree of saturation, $S = n_w / \left(1-n_s\right)$, (-); θ is volumetric water content, $\theta = nS$, (-); n is porosity, $n = 1-n_s$, (-); γ_{dry} is dry bulk density, $\gamma_{dry} = G_s\left(1-n\right)$, (kg/m^3); λ_q is thermal conductivity of quartz and q is the quartz content, (W/m·K); λ_o is thermal conductivity of other materials, (W/m·K); k_e is Kersten number, $k_e = (\lambda_e - \lambda_{dry})/(\lambda_{sat} - \lambda_{dry})$, (-). Empirical parameters: α, χ, b, c are fitted parameter for different materials.

A comparison of a set of measured thermal conductivity values for Bonny silt and the calculated thermal conductivity by different models is shown in Figure 2.4 a (Dong et al., 2015). Evidently, the parallel/series and HS upper/lower bounds set the upper and lower limits of the thermal conductivity values. The geometric mean model has the right rend but concaves to an opposite direction to the experimental data. SCM model has ‘‘quasi-linear’’ projections and higher predictions over all the saturation range. De Vries (1963) model has close results at mediate saturation range 0.2–0.6. Empirical models fit quite well with the experimental data points. Nevertheless, only Lu et al.’s (2007) model captures the characteristic “flat-tail” behaviour of thermal conductivity of silt at low degrees of saturation with a slightly shift. Also, Johansen’s and Lu et al.’s models underestimate the thermal conductivity at lower saturation and overestimate at higher saturation. Cote’s model has the best fit with experimental data but fails to simulate the behaviour of thermal conductivity of silt at low degrees of saturation.

Figure 2.4 b shows the 1:1 diagonal comparison. By the above comparison, the empirical models work better than mixing and mathematic models, which use certain mathematical functions to fit the experimental results and then determine the parameters in these functions to match with the certain type of soil.

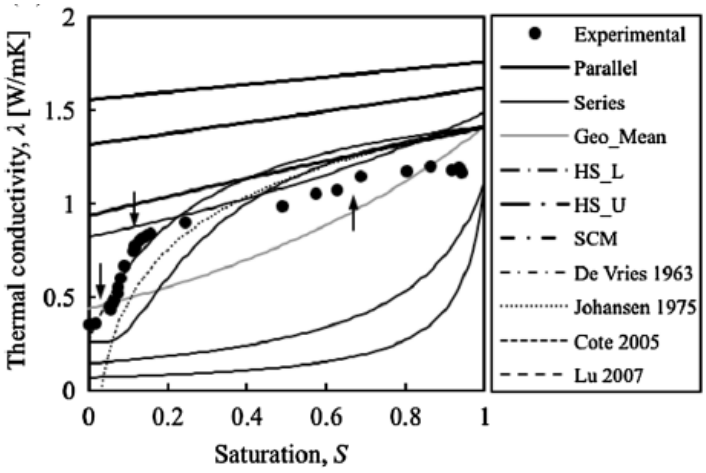

(a)

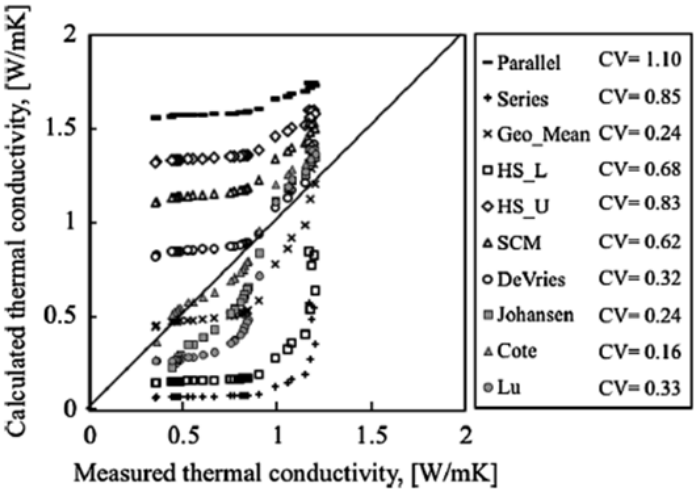

(b)

Figure 2.4 Comparison of thermal conductivity model simulation and the experimental data of silt: (a) effective thermal conductivity vs degree of saturation; (b) 1:1 comparison space for predicted measured values (Dong et al., 2015)

2.2.4 Other workable methods

NMR is one of another popular method for measuring unfrozen water content (Tice et al., 1978; Ishizaki et al., 1996; Yoshikawa and Overduin, 2005; Watanabe and Wake, 2009). The nuclei of some atoms including hydrogen resemble miniature bar magnets that will align a strong magnetic field. When ratio frequency is applied, the atoms will absorb energy to realign to another stable position within the magnetic field (Tice et al., 1978). If the frozen soil is placed in a pulsed NMR analyser and a radio frequency pulse is applied, voltage (which corresponds to the amount of absorbing energy) is induced in a receiver. The NMR analyser detects the voltage and the magnitude of the voltage is related to the amount of the unfrozen water in the mixture. Therefore, the NMR readings could be used to indirectly detect unfrozen water in the frozen soil.

Although the NMR is a widely used method for determining unfrozen water content, it has several drawbacks during the measurement (Spanns and Baker, 1995). (1) the use of NMR is restricted to the laboratory (Yoshikawa and Overduin, 2005). It is not suitable for in situ measurements because of the complicated equipment. (2) Magnetic particles in the soil

interfere with the measurements. (3) It cannot be automated. (4) The equipment is expensive. Furthermore, the stress state cannot be applied to the soil specimen during the determination of unfrozen water content using NMR (Mu, 2017).

Depending on the different properties of the specific heat capacity of water and ice, Williams (1964) proposed a method of measuring the unfrozen water content of frozen soils and soil moisture suction using a calorimeter. Liu and Si (2011) also proposed a technique using a heat pulse probe method to measure the ice content in frozen soils.

2.3 SFRC models

2.3.1 Semi-empirical models

Soil freezing retention curve (SFRC) models are necessary for predicting frost heave and thawing settlement (Nishimura et al., 2009; Sheng et al., 2014; Zhang et al., 2015) as well as water and solute transport in frozen soil (Stahli and stadler, 1997; Kurylyk and Wantanabe, 2013). So far, many models were proposed to formulate the SFCC. Table 1.1 summarizes some of the existing SFCC equations in the literature. According to Kurylyk and Wantanabe (2013), the existing SFCC models in the literature could be mainly divided into two categories: (a) semi-empirical models and (b) the models which are derived from soil water retention curve (SWRC) combing with the Clausius-Clapeyron equation. For the semi-empirical models, Anderson and Tice (1972) proposed a power equation for the SFCC as follows:

$$\theta_w = \frac{p_d\left(1-\theta_s\right)}{100\,p_w}\alpha\left(-T\right)^{\beta} \tag{2.11}$$

Where θ_w is the unfrozen volumetric water content; T is the soil temperature (°C); α and β are fitting parameters which are related to soil specific surface area; p_d and p_w are the soil dry density and water density, respectively and θ_s is the saturated volumetric water content. It should be noted that equation 2.9 is formulated on the assumption that adsorptive forces

rather than capillary force govern the freezing process. On the other hand, the exponential equation was also widely used for the SFCC (Michalowski, 1993; Zhang et al., 2015).

$$\theta_w = \theta_{res} + (\theta_s - \theta_{res}) \exp(\alpha_1 T) \tag{2.12}$$

Where θ_{res} represents the residual volumetric water content; α1 is a fitting parameter defining the rate of decrease in unfrozen water content with decreasing temperature. In this model, only the freezing of capillary water was considered and the phase change in the residual water was ignored. In addition, other semi-empirical models such as the linear equation (Dillon and Anderson, 1966) and piecewise linear equation (McKenzie et al., 2008) were also proposed for the SFCC.

2.3.2 SWCC equations combined with Clausius-Clapeyron equation

The SFCC could also be formulated trough a SWRC equation combining with the Clausius-Clapeyron equation. The SWRC equation proposed by van-Genuchten (1980) was widely used for the SFCC (Nishimura et al., 2009)

$$\theta_w = \left[1 + \left(\frac{\lambda \ln(T + 273.15) / 273.15}{\alpha_0} \right)^{n_0} \right]^{-m_0} \tag{2.13}$$

Where α_0, n_0, and m_0 are fitting parameters and λ is the latent heat of fusion of water (333.7 kJ kg^{-1} at 0 °C). In addition, the Brooks-Corey equation (Sheshukov and Nieber, 2011) and Fredlund and Xing (Azmatch et al., 2012) were also adopted to formulate the SFCC. However, these semi-empirical and SWRC-derived models may not give a good calculation for the SFCC over a wide temperature range as they lack considering of both capillarity and adsorption meachnisms. For solute-free soil, the capillarity and adsorption are the two distinct physical mechanisms controlling the entire freezing process of pore water (Lebeau and Konard, 2012; Kurylyk and Watanabe, 2013). Furthermore, effects of initial soil void ratio, which significantly influences the capillarity, on the SFCC was not explicitly considered in these models.

Table 2.5 Existing models for soil freezing characteristic curve

Category	No.	Citations	Equations	Number of fitting parameters
Empirical equations	1	Dillon and Anderson (1966)	$\theta_w = \frac{2.8\cdot10^{-7} p_d S}{p_w A_c}\frac{T}{T_0}$	1 (A_c)
	2	Anderson and Tice (1972)	$\theta_w = \frac{p_d(1-\theta_s)}{100 p_w}\alpha(-T)^{\beta}$	2 (α and β)
	3	Gilpin (1980) and Cahn (1992)	$\theta_w = \kappa(-T)^{-1/3}$	1 (κ)
	4	McKenzie et al. (2008)	$\theta_w = m(T-T_0)+\theta_s \quad T > B_T$ $\theta_w = \theta_{res} \quad T < B_T$	2 (m and θ_{res})
	5	Ge et al. (2011) and Zhang et al. (2015)	$\theta_w = \theta_{res} + (\theta_s - \theta_{res})\exp\left(-\left(\frac{T-T_0}{w}\right)^2\right)$ or $\theta_w = \theta_{res} + (\theta_s - \theta_{res})\exp(\alpha_1(T-T_0))$	1 (w or α_1)
SWCC equations combined with the Clausius-Clapeyron equation	7	Sheshukov and Nieber (2011)	$\theta_w = \theta_{res} + (\theta_s - \theta_{res})\left(\frac{p_w \lambda T}{T_0}\right)^{-1/b}$	2 (b and θ_{res})
	8	Nishimura et al. (2009) and Liu and Yu (2013)	$\theta_w = \left[1+\left(\frac{\lambda l_w \ln(T/T_0)}{\alpha_0}\right)^{n_0}\right]^{-m_0}$	3 (α_0, n_0 and m_0)
	9	Watanabe (2011)	$\frac{\theta_w-\theta_{res}}{\theta_s-\theta_{res}} = (1-w)\left[1+\alpha_1 p_w \lambda \ln\left(\frac{T-T_0}{T_0}\right)^{n_1}\right]^{-m_1} + w\left[1+\alpha_2 p_w \lambda \ln\left(\frac{T-T_0}{T_0}\right)^{n_2}\right]^{-m_2}$	7 (α_1, α_2, m_1, m_2, n_1, n_2 and w)
	10	Azmatch et al. (2012)	$\theta_w = \theta_S\left[1-\left(\frac{\ln(1+\lambda\ln(T/T_0))/C_r}{\ln(1+1000000/C_r)}\right)\right]/\left(\ln\left(2.718+(\lambda\ln(T/T_0)/\alpha_2)^{n_2}\right)\right)^{m_2}$	4 (C_r, α_2, m_2 and n_2)
	11	Qingyi (2017)	$\theta = (\theta_s - \theta_{a\max})\left[\frac{1}{1+\left(m_0 e^{m_1} p_w \lambda \ln((T+273.17)/273.15)\right)^{m_2}}\right]^{m_3} + \theta_{a\max}\left\{1-\left[\exp\left(\frac{T-T_{\min}}{T+T_c}\right)\right]^k\right\}$	6 (m_0, m_1, m_2, m_3, k and $\theta_{a\max}$)

2.4 Application of ERT techniques in soils

ERT aims at imaging the electrical conductivity distribution of the subsurface. Using petrophysical relationships such as Archie's law, one may recover indirect parameters such as saturation, water electrical conductivity or total dissolved solid content.

Imaging techniques developed rapidly in the past decades, it can provide two- or three-dimensional representations of the investigated soil volume at different times. Being non-invasive, they do not disturb flow patterns and soil structure. Electrical resistivity tomography (ERT) allows the distribution of the electrical conductivity of an investigated domain to be inferred. ERT has two main advantages: cost effectiveness and suitability for a wide range of scales, both in the laboratory and in situ (Comina et al., 2011). Geotechnical laboratory cells with ERT capabilities have been described by Comina et al., (2008). ERT images have been used to locate heterogeneities (Borsic et al., 2005), to visualize liquefaction (Jinguuji et al., 2007) and to monitor salt diffusion (Comina et al., 2005; Damasceno et al., 2009). There are however no publications related to ice formation using 2D or 3D ERT images.

2.5 Volume change behaviour of soils

Geotechnical investigations on the behaviour of frozen soils have received particular attention for the last six decades. Because permafrost covers about 24% of the exposed Northern hemisphere landmass any major engineering works in the form of either resource or transport development in these areas requires a clear understanding of frozen soils. Engineering problems often faced include, freezing of foundations; thawing settlement/distress of buildings, roads, rail lines and pipelines carrying essential commodities. Predicting the behaviour of these soils is paramount in lieu of effects of global warming which could potentially alter regions that were once permanently frozen.

Before the 1930's, the volumetric changes occurring in frozen soils were understood to be a consequence of the expansion caused due to phase transformation of water to ice. However when a considerable difference was noticed in the observed volumetric change and theoretical

changes due to phase change, the presence of unfrozen water below the freezing point of water was conceived (Taber, 1929). This was later quantified by Beskow (1935) and Everett (1961) and experimentally proved by Tice et al. (1988) using the pulse nuclear magnetic resonance technique. Several effects including frost heave and the formation of ice lens in soil were attributed to movement of this unfrozen water. It is also seen to a have major influence on the thermal and hydraulic behaviour of the frozen soil. Therefore, studying this migration of unfrozen water forms an essential component in understanding frozen soil behaviour. Fundamental aspects related to the effect of freezing temperature on soils have been largely studied in the literature (e.g. Miller et al., 1978; Konrad and Shen, 1996; Chamberlain and Gow, 1979). Among these works, particular interest for this research are the studies focused on the presences of unfrozen water in frozen soils and the associated cryogenic suction (e.g. Williams, 1964; Tice et al., 1989; Hohmann, 1996; Fakuda, 1983). Recent studies in this area have focused on the effect of pore size distribution on unfrozen water (e.g. Coussy, 2005; Multon et al., 2011). Other approaches include: the rigid ice model (e.g. Miller, 1978; Gilpin, 1980; O'Neill and Miller, 1985); hydrodynamic models (e.g. Jame and Norum, 1980; Harlan, 1973; Newman and Wilson, 1997); and the segregation potential model (e.g. Konrad and Shen, 1996; Konrad and Morgenstern, 1980, 1981, 1984).

The interaction between the phases of (unfrozen) unsaturated soils was observed to be similar to the interaction between the frozen and unfrozen components. The representation of the three phases for the unfrozen unsaturated soils and frozen soil is shown in Fig 2.5a and Fig 2.5b respectively. A coupled thermo-hydro mechanical (THM) framework for frozen soils based on the behaviour of unsaturated soils was proposed by Nishimura et al. (2008). Previous studies (Thomas et al., 2009, Nishimura et al., 2008) mainly focused on systems which had (unlimited) access to free water (open system). There is limited information about systems which do not have the access to free water (closed system). The current work focuses on the movement of unfrozen water in frozen soils in a closed system. The numerical code CODE_BRIGHT (Olivella et al., 1996) has been modified to deal with the presence of ice and unfrozen water in porous media.

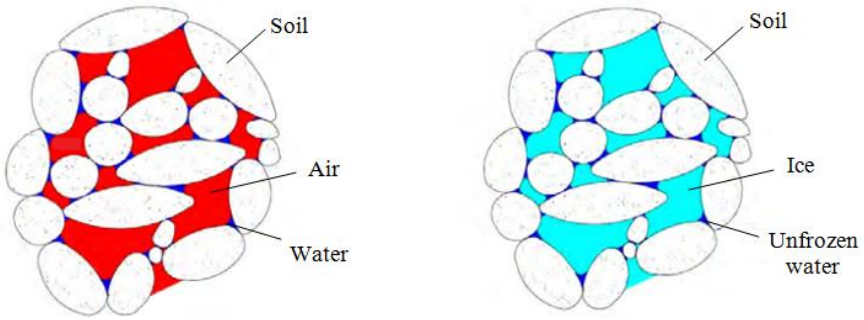

(a) (b)

Figure 2.5 Cryogenic suction in a) Unfrozen unsaturated soils and b) Frozen soils

2.5.1 Microstructure changes

There are still no direct measurement results of cryogenic suction in the frozen soil published. Shastri et al. (2012) explored the capabilities of a mechanical model for unsaturated soils to describe the behaviour of frozen soils including the effect of the cryogenic suction and temperature. The cryogenic suction, calculated from Clausius-Clapeyron equation, increases with a decrease in temperature under conditions of constant liquid pressure. There are other works incorporating the concept of cryogenic suction (e.g. Nishimura et al., 2009; Thomas et al., 2009), which is associated with the potential which develops between the ice and the liquid water phases in frozen soils.

2.6 Summary

In summary, the experimental results for frozen soil behaviour are still scarce currently and the testing techniques for the cryogenic environment are still under development, particularly under partially saturated conditions. Moreover, the increasing development of numerical modelling could contribute to the interpretation of frozen soil tests to some extent.

Chapter 3 Experimental set-up and program

3.1 Preface

This chapter presents the basic properties of the soil materials (Castelldefels fine sand and Barcelona clayey silt) and interstitial water (5% NaCl solution) that are tested in this thesis. Furthermore, the main equipment, set up, data acquisition system and other techniques are introduced, especially their improvement and modification. Finally, all the experimental programs are presented.

The main experiments in this thesis include: (1) determining the ice content of partially saturated frozen soils using bulk electrical conductivity EC, relative dielectric permittivity and thermal conductivity; (2) ERT monitoring of saturated and unsaturated soil freezing; (3) conducting temperature-controlled oedometer tests under different stress and temperature paths; and (4) investigating the microstructure changes of clayey silt samples at different stress and temperature paths using the MIP and FESEM methods. The Particle (Pore) and Cracks Analysis System (PCAS) is used to analyse the images of FESEM.

3.2 Materials

3.2.1 Properties of tested soils

Uniform fine sand from Castelldefels, Barcelona, and Barcelona clayey silt are studied in this thesis. Hereinafter, the Castelldefels fine sand will be shortened to fine sand and Barcelona clayey silt will be shortened to clayey silt. The particle size distribution of fine sand and clayey silt is presented in Figure 3.1. Modified clayey silt is no larger than 2 mm to meet the

requirement of the experimental set-up used (Cardenas et al., 2014). The solid densities of the fine sand and the clayey silts are 2.65 Mg/m^3 and 2.67 Mg/m^3, respectively.

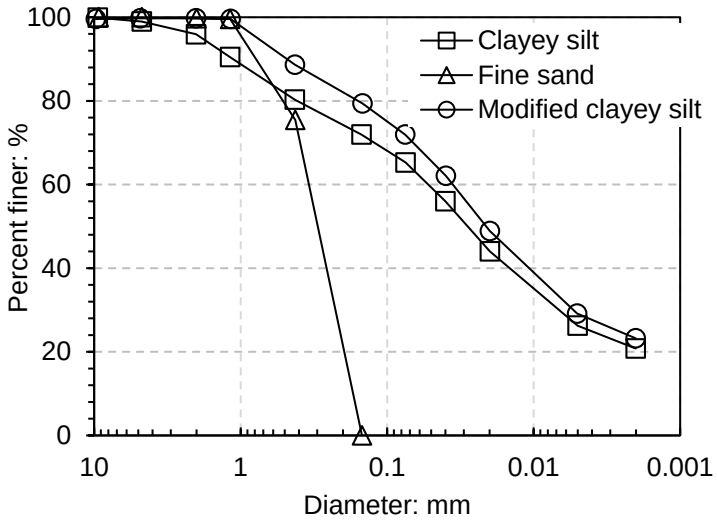

Figure 3.1 Particle size distribution curve (Cardenas et al., 2014)

Figure 3.2 (Alonso and Romero, 2003) shows the density function of the fine sand particle size distribution; the grains vary in size between 75 and 500 µm, exhibiting a dominant particle size of around 270 µm. The photomicrograph shown in Figure 3.3 complements the information concerning the dimensions and shapes of the sand grains.

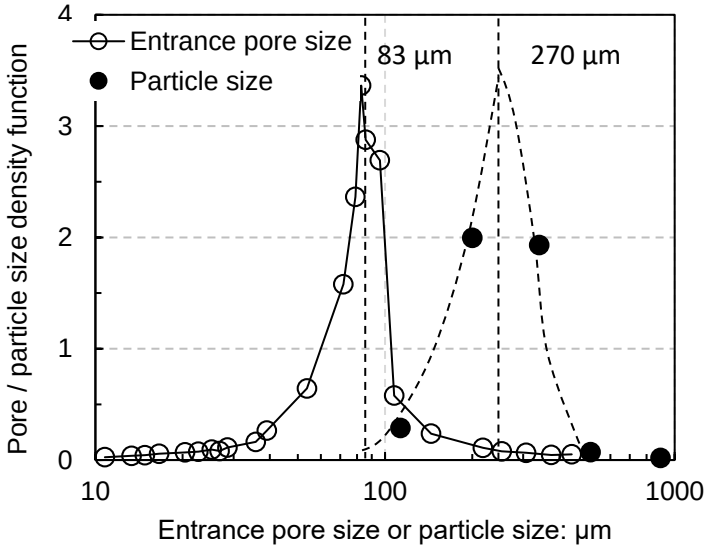

Figure 3.2 Pore and particle size density functions (Alonso and Romero, 2003)

The clayey silt has a liquid limit of 28–31%, a plastic limit of 19%, a clay-size fraction of ≤ 2 μm of 13–19% and a silty fraction between 2 and 75 μm of 40–46%. The dominant mineral of the clayey fraction is illite (Barrera, 2002). Pore size distributions of statically compacted clayey silt (see Figure 3.4; Buenfil et al., 2005) are obtained using mercury intrusion porosimetry MIP to examine the fabric of the soil. As shown in Figure 3.4 (Buenfil et al., 2005), the clayey silt with two different dry densities (1.49 Mg/m^3 and 16.9–17.1 Mg/m^3, respectively) are tested.

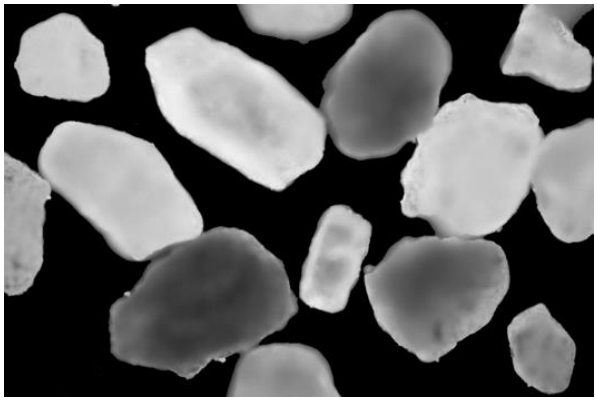

Figure 3.3 Photomicrograph of the sand grains. Background area is 1.5×1.0 mm. (Alonso and Romero, 2003)

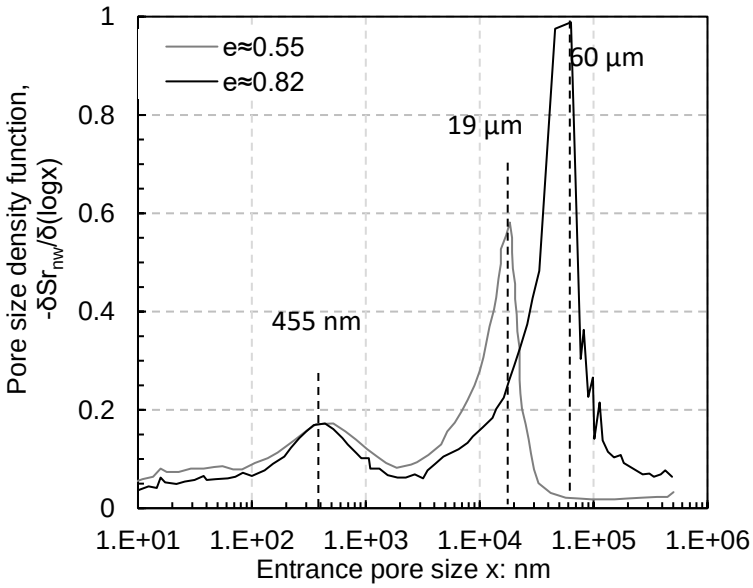

Figure 3.4 Pore size distributions of two clayey silt samples from MIP results (Buenfil et al., 2005)

Figure 3.5 shows the FESEM microphotographs of the samples corresponding to the two packing soils as mentioned above. In the photograph of the low-density soil (Figure 3.5 (a)), it is possible to detect large inter-aggregate pores with dimensions between 20 μm and 100 μm, which are consistent with the large pore mode obtained using MIP test. In the photograph of the high-density soil (Figure 3.5 (b)), a significant decrease in the size of the inter-aggregate pores, which display diameters smaller than 30 μm, can be observed. The intra-aggregate pores that are visible at the magnification used in the figure present similar sizes for the two packing soils investigated.

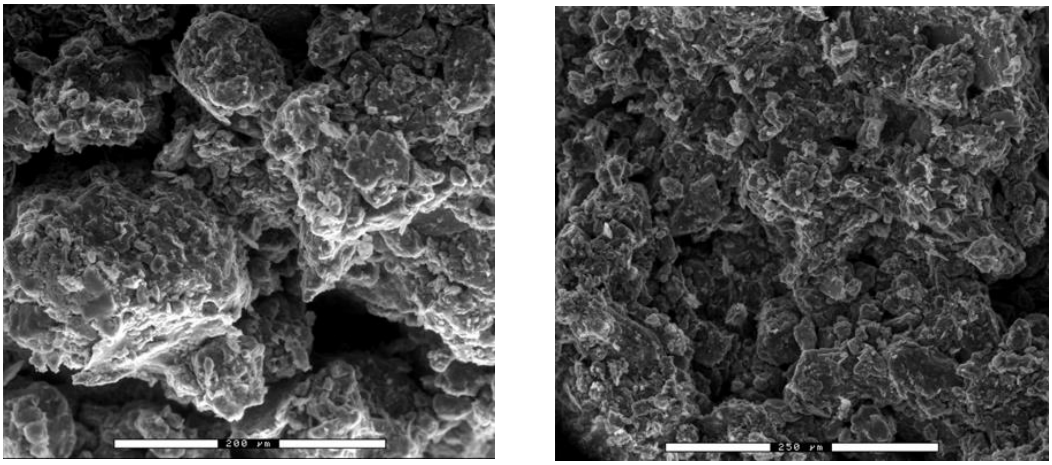

(a) (b)

Figure 3.5 Scanning electron micrographs of the compacted silt at (a) lower packing e=0.82 and (b) higher packing e=0.55 (Buenfil et al. 2005)

The water retention curves of the two soils on the drying path and in terms of degree of water saturation are plotted in Figure 3.6. The van Genuchten (1980) expression is used to fit the experimental results,

$$S_r = \left[1 + \left(\frac{s}{P} \right)^{\frac{1}{1-\lambda}} \right]^{-\lambda} \tag{3.1}$$

where s is the suction, λ is the material constant and P is associated with the air entry value.

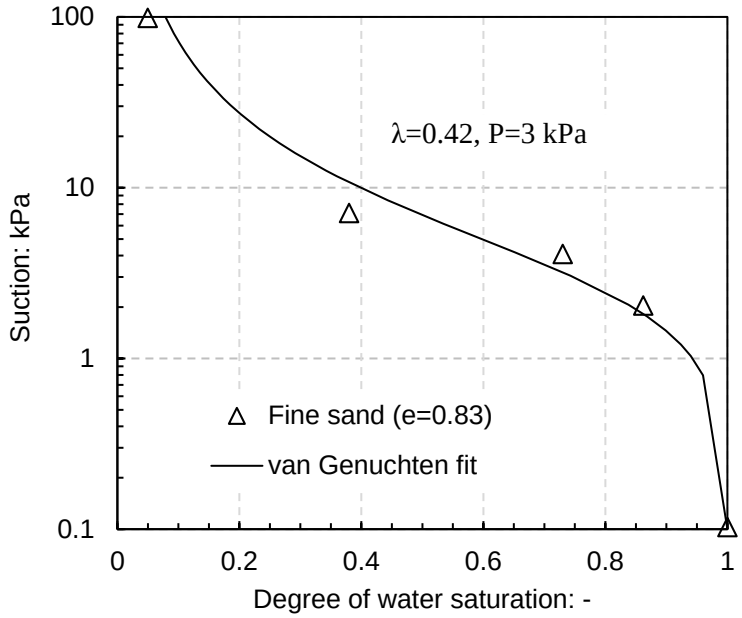

(a)

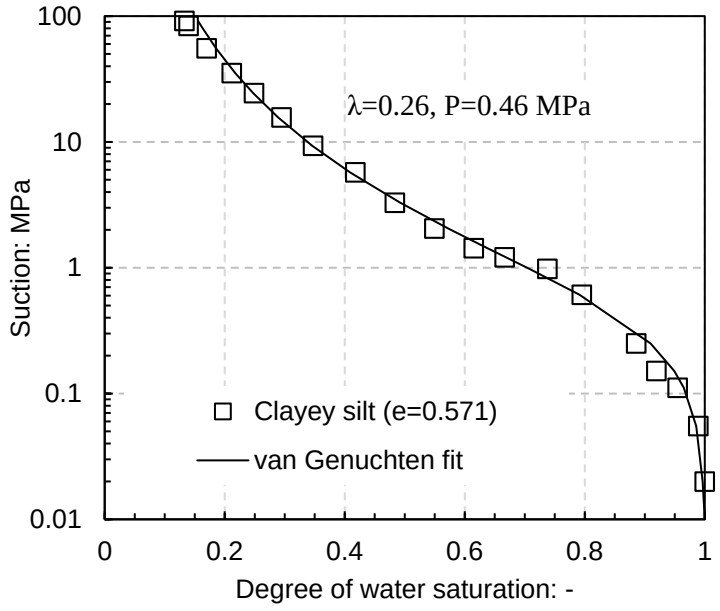

(b)

Figure 3.6 Water retention curves of (a) fine sand (adapted from results by Cardenes et al., 2014) and (b) clayey silt (adapted from results by Mora 2016) on drying path

3.2.2 Properties of interstitial water

A 5% NaCl solution (mass basis) is used as interstitial water instead of pure water to better discriminate between the EC values of ice and unfrozen water. Figure 3.7 shows the EC readings of the solution along temperature decrease and freezing paths. A clear dependence on temperature is observed because of changes in ionic mobility and solution viscosity. The relationship between EC and temperature in the unfrozen state (without phase change) is linear; it changes to non-linear below the freezing point because of ice generation.

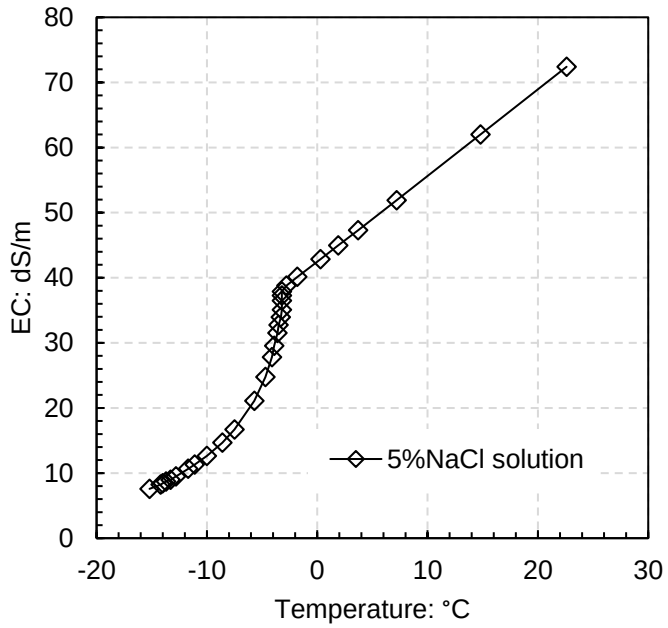

Figure 3.7 EC values of 5% NaCl solution along temperature decrease and freezing paths

The freezing point of the solution changes depending on the concentration of solute. If the solution is treated as an ideal solution, a simple linear relationship with the cryoscopic constant (Blagden's law) can be used to estimate the freezing point of the solution. The formula is

$$\Delta T_f = iK_f m \tag{3.2}$$

where ΔT_f is the freezing point depression, defined as T_f (pure solvent) − T_f (solution), i is the van's Hoff factor (number of ion particles per individual molecule of solute, e.g., i=2 for NaCl, i=3 for $BaCl_2$) and K_f is the cryoscopic constant, which is dependent on the properties

of the solvent, not the solute. For water, K_f is 1.86 °C·kg/mol. And m is the molality of the solution (moles solute per kilogram of solvent). The calculation procedure is as follows:

Moles of NaCl=5g NaCl*1 mol NaCl/58.5g NaCl=0.0855 mol NaCl

Mass of water =0.10 kg H_2O

m=moles of NaCl/kilograms of water =0.0855 mol/0.10 kg=0.86 mol/kg

ΔT_f=2*1.86 °C·kg/mol*0.86 mol/kg=3.20 °C

Therefore, the freezing point of the 5% NaCl solution is -3.2 °C. It is assumed that only the liquid phase is contributing to EC since this value in ice is approximately three orders of magnitude lower than liquid water (ionic mobility is restricted by the ice lattice). Other research also illustrates that the concentration of solution not only affects the freezing point of the soil but also the soil freezing process (for instance, Watanabe and Mizoguchi, 2002; Xiao et al., 2018).

3.3 Measurement of ice content

3.3.1 FDR sensor

The equipment for measuring bulk EC and relative dielectric permittivity is the commercial frequency domain reflectometry (FDR) sensor 5TE (Decagon Devices, 2015). As shown in Figure 3.8, the two small screws were used to measure EC and the dielectric constant was measured using capacitance/frequency domain technology. To minimise the effects of soil texture and salinity, a 70 MHz frequency was used. The accuracy of apparent dielectric permittivity (ε_a) is ±1 ε_a (unitless) from 1–40 (soil range) and ±15% from 40–80. The accuracy of EC is ±10% from 0 to 7 dS/m and user calibration is required above 7 dS/m. The accuracy of temperature is ±1 °C. The required measurement volume of the Decagon 5TE sensor is shown in Figure 3.9.

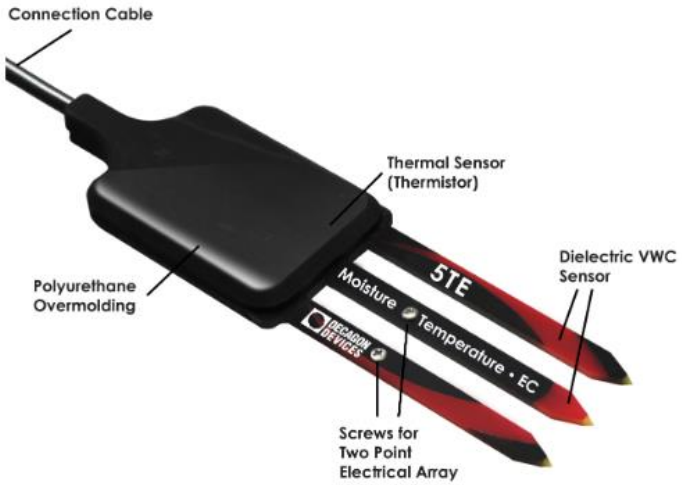

Figure 3.8 FDR 5TE components

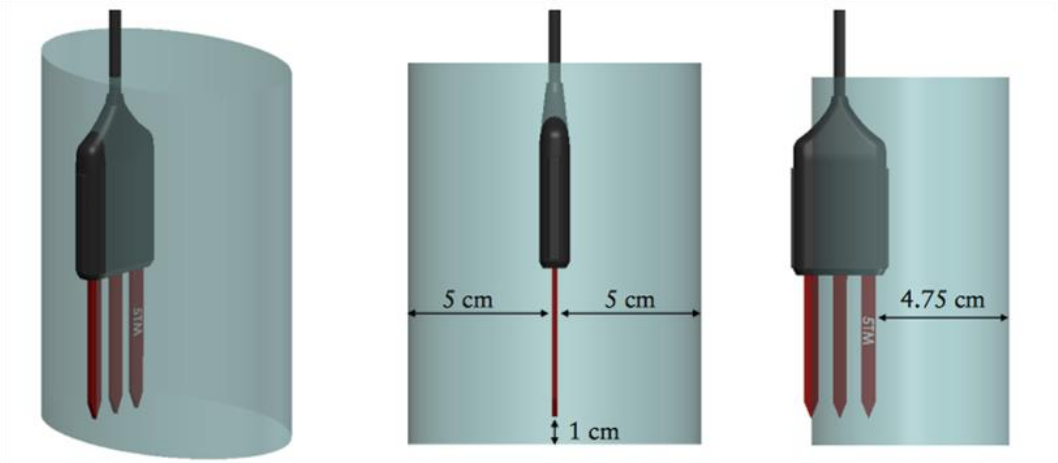

Figure 3.9 Ideal measurement volume of the 5TE sensor

The data acquisition equipment for FDR data is a commercial Decagon Em50 data logger, as shown in Figure 3.10. There are five channels in both the hardware and software. When connecting to the data logger, the software can acquire the voltage signals of the FDR sensor and then translate them to temperature, bulk EC, and dielectric permittivity values. The frequency of data acquisition can be set as the requirement of each test.

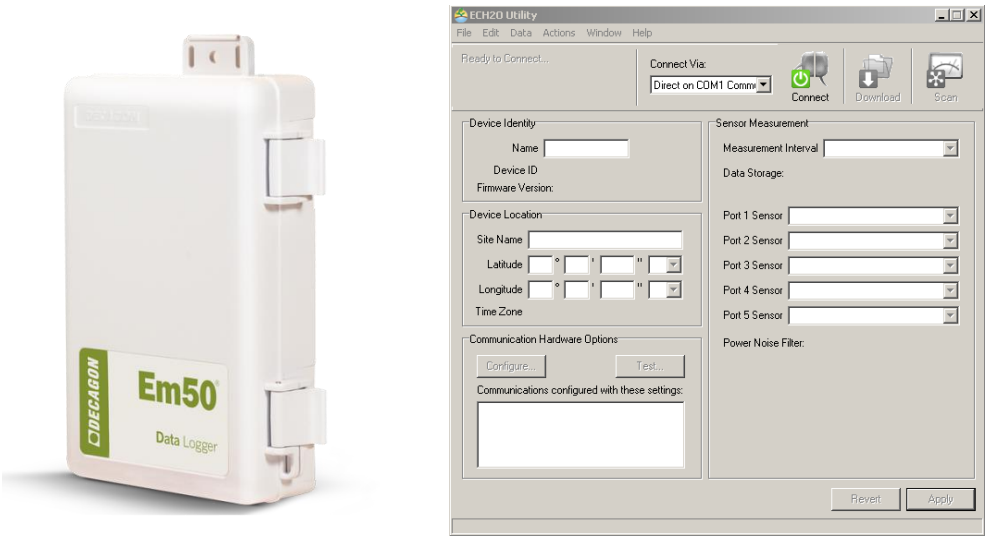

(a) (b)

Figure 3.10 (a) Em50 box and (b) FDR data acquisition software interface

3.3.2 Modification of thermocouples

Temperature information is very important for all types of experiments in this thesis, which means precise temperature measurements are required. Temperature is monitored by T-type thermocouples using a hardware and software system developed with the Labview package (National Instruments Spain SL, Madrid) for automation of thermal process control. The previous data acquisition box has only three channels for connecting the thermocouples, but four thermocouples are needed for conducting the thermal conductivity test.

In order to match the requirement of the test, another two thermocouple channels were built by hand. Two same SENICA cards (UK) were bought and connected to National Instrument. Two holes were made to install the joints for the thermocouples. The working principle of a thermocouple is that the voltage difference between the two alloys of the thermocouple can be acquired and then translated transfer to temperature values using calibrated relations. The inside view of the data acquisition hardware is presented in Figure 3.11.

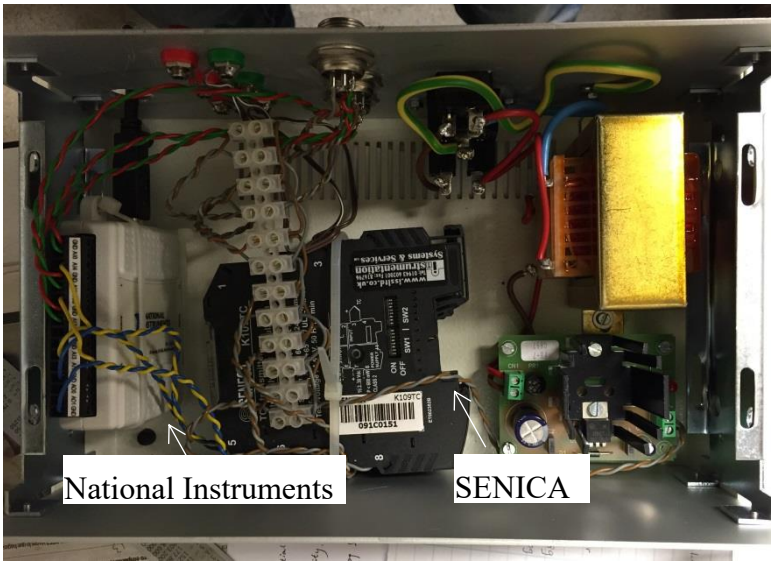

Figure 3.11 Internal of data acquisition hardware

3.3.3 Modification of refrigerator set-up

The cooling system mainly includes a cooling bath manufactured by Heto Lab Equipment A/S (Type: Hetofrig CB 23-45) in Denmark. There are two separate components in the tank: a refrigerator and a heater. The continuous liquid nitrogen is controlled with a constant pressure valve, which is significant for controlling the temperature of freezing. The power of the refrigerator is 830 W. The refrigerator coil in the vessel walls is for better contacting with the antifreeze liquid. The thermostat is a system that includes a heater, a thermocouple, and a stirrer. The heater is used for heating the antifreeze liquid. The thermocouple can measure the temperature of the liquid, which is an indicator for the heater to switch on and off. The stirrer is used to circulate the antifreeze liquid in the bath to keep uniform temperature. The thermostat and refrigerator work together to control the temperature as the requirement of the experimental program. The previous thermostat has already been broken. A new thermostat is instilled instead of the old one. A new calibration is performed. The temperature range of the new modified cooling bath is from 20 °C to -15 °C. The configuration of the old cooling system is presented in Figure 3.12.

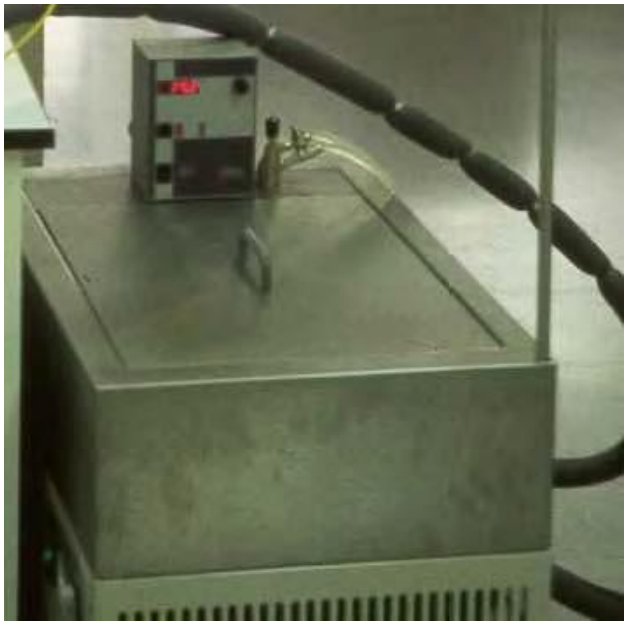

Figure 3.12 Refrigerator HETOFRIG, type CB 23-45. Geotechnical Laboratory, UPC.

In order to mitigate the effects of condensation of water vapour produced by the air-saturated environment and to avoid the appearance of masses of ice on the surface of the cell cover and the contact point of the piston LVDT rod, it is necessary to build an airtight insulation structure for the upper perimeter of the heat bath, which would generate a sort of microclimate inside the equipment. There is a considerable difference in temperature between the heat bath and the top of the oedometer cell.

The above mentioned enclosure is made of reticulated polyethylene with L-type polyvinyl chloride (PVC) profiles, which is contributing to the stiffness of the structure, and the high-performance tape was used for connection between materials. A small methacrylate viewer, with 100 mm×150 mm dimensions, is built on the top of the refrigerator; it can be used for checking the status of the cell top and the temperature on the digital regulator of the refrigerator (see Figure 3.13).

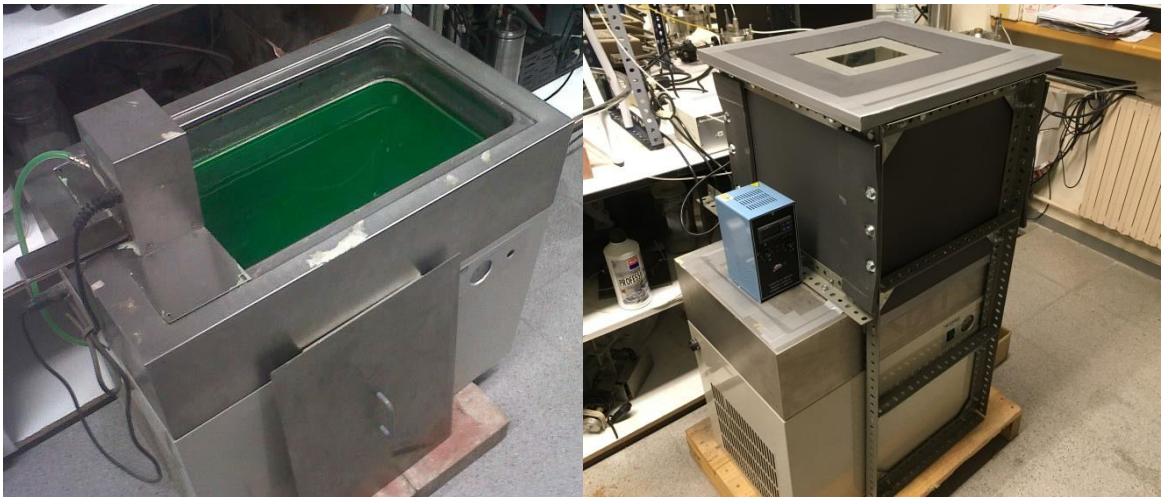

(a) (b)

Figure 3.13 (a) Refrigerator before modification and (b) refrigerator with the structure of polyethylene insulation

3.3.4 Set-up of measuring thermal conductivity

The set-up for measuring thermal conductivity using a steady-state method at room temperature is described in Barry-Macaulay et al. (2013) and Romero et al. (2016). It is designed to apply a high temperature (around 30 °C) at the top of cylindrical soil specimen (38 mm in diameter and 40 mm in height). In order to prepare the fine sand as a cylindrical specimen, a PVC tube (38 mm in diameter), which has a lower thermal conductivity (0.2 W/m·K) compared with fine sand, is used. A membrane is also used to constrain the soil specimen, heat flux and caps from outside. The heaters in the top and bottom caps are regulated using thermostats that switch electrical resistances off at the desired set point based on values measured by the thermocouples placed inside the top and bottom caps. Figure 3.14 (a) shows the cross-section of the set-up for measuring unfrozen soil and Figure 3.15 presents a set of pictures of different components of the set-up.

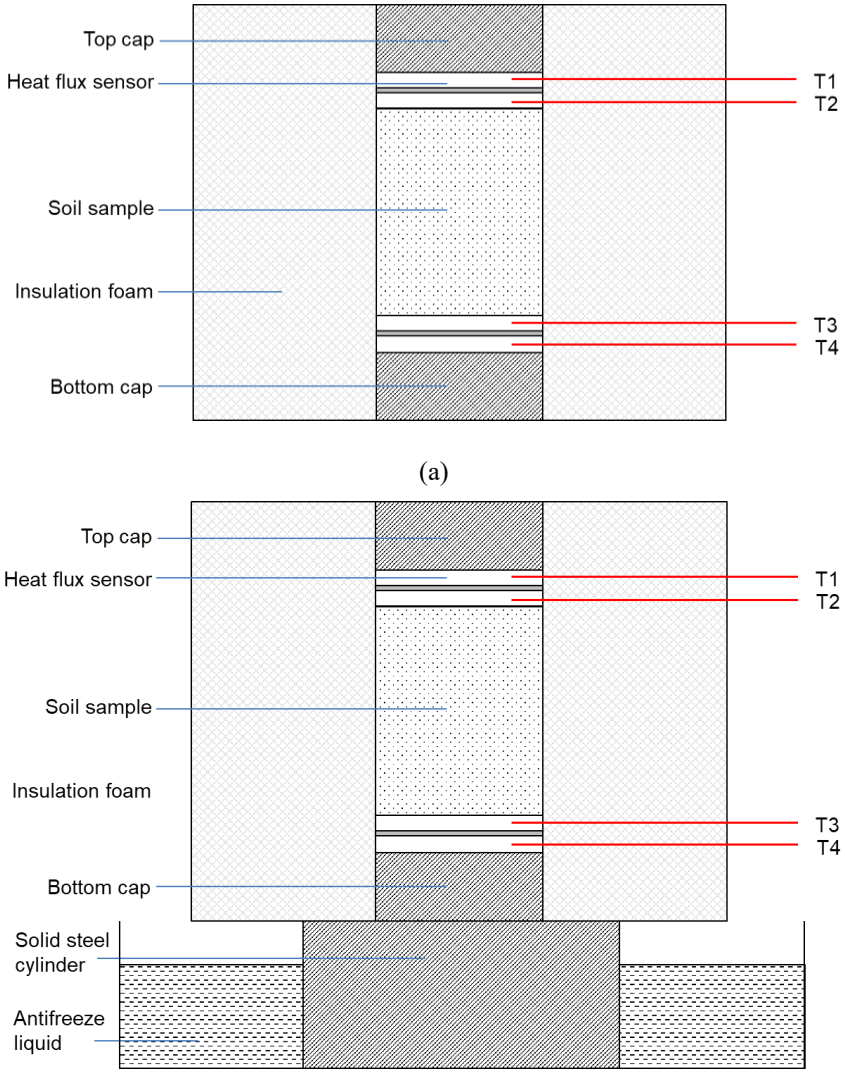

Figure 3.14 Schematic of thermal conductivity test for (a) unfrozen soil and (b) full frozen state

The interstitial water used in the thermal conductivity tests is tap water, not saline water, with a freezing point around 0 °C. When testing unfrozen soil, the samples are prepared at room temperature and the set-up is also placed outside at room temperature (20 °C ± 1 °C). When testing the full frozen soil, the soil samples are first surrounded with waterproof plastic bag and then immersed in antifreeze liquid of cooling bath to freeze at -15 °C up to three hours. The frozen samples are then installed in set-up shown in Figure 3.14 (b). This set-up is similar to the one for unfrozen soil but placeed inside the cooling bath. A solid steel cylinder is placed in the antifreeze liquid and the set-up is placed on it. Due to the good conduction

performance (around 80 W/m·K) of steel, the set-up can be frozen from the bottom and the heaters in the top and bottom caps are both switched off.

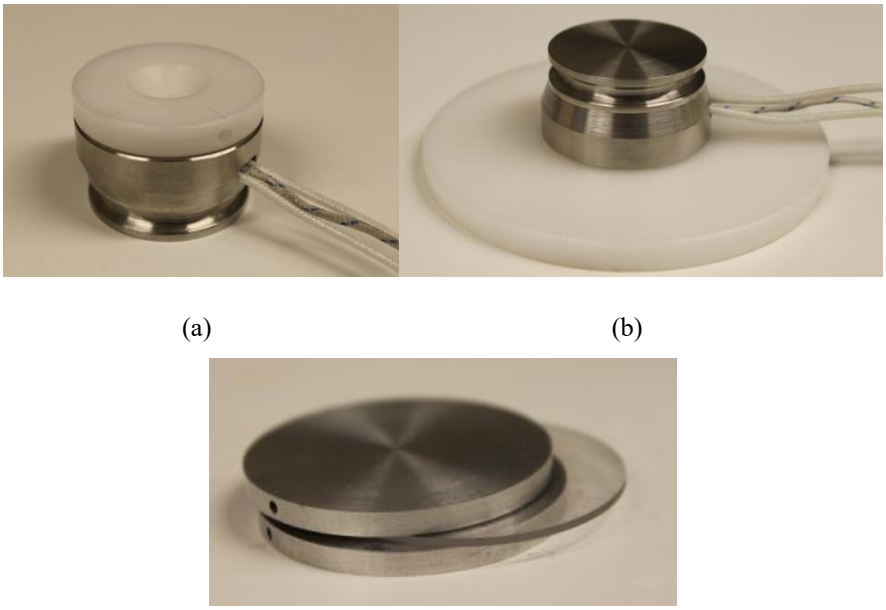

(a) (b)

(c)

Figure 3.15 Components of thermal conductivity set-up: (a) top heating cap, (b) bottom heating cap and (c) heat flux sensor (Romero et al., 2016; Romero and Sau, 2016)

The schematic and size of heat flux sensor are shown in Figure 3.16. The polycarbonate disc (1 mm) is between two aluminium discs (3 mm), of which thermal conductivities are 0.2 W/(m·K) and 209 W/(m·K), respectively.

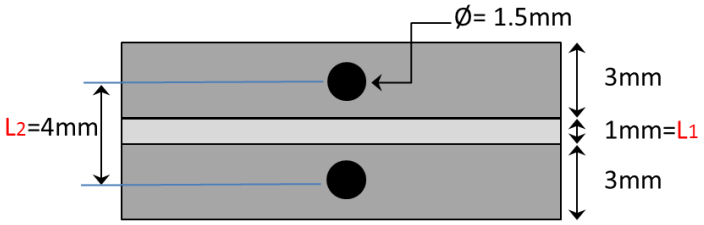

Figure 3.16 Schematic and size of heat flux sensor

There two methods to determine the heat flux (q), the first method is (Romero and Sau, 2016)

$$q = \frac{\lambda_{polycarbonate} \cdot \Delta T}{L_1} \tag{3.3}$$

The second method is

$$\frac{L_2}{\lambda_{equivalent}} = \frac{1.5\,mm}{\lambda_{alu\,\min uim}} + \frac{1\,mm}{\lambda_{polycarbonate}} + \frac{1.5\,mm}{\lambda_{alu\,\min ium}} \tag{3.4}$$

$$q = \frac{\lambda_{equivalent} \cdot \Delta T}{L_2} \tag{3.5}$$

Depending on the equation, $\lambda_{equivalent} = 0.798$ W/(mK). Here, the second method is used. The expression for heat flux input, output and average are

$$q_{in} = \frac{\lambda_{equivalent} \cdot \Delta T_{top}}{L_2} \tag{3.6}$$

$$q_{out} = \frac{\lambda_{equivalent} \cdot \Delta T_{bottom}}{L_2} \tag{3.7}$$

$$q_{average} = \frac{q_{in} + q_{out}}{2} \tag{3.8}$$

where $\Delta T_{top} = T_1 - T_2, \Delta T_{bottom} = T_3 - T_4$.

The thermal conductivity of the sample is

$$\lambda_{sample} = \frac{q_{average} \cdot L_{sample}}{\Delta T} \tag{3.9}$$

where $\Delta T = T_2 - T_3$.

3.3.5 Modification of data acquisition system

The original version of data acquisition system for LVDT and thermocouples is shown in Figure 3.17; it is the SoftLabGeo program developed at the Geotechnical Laboratory. It has some disadvantages; for instance, it is inconvenient for calibrating several thermocouples at

the same time and it does not have enough channels for measuring temperature. Therefore, the new LabVIEW data acquisition system was developed to solve these problems.

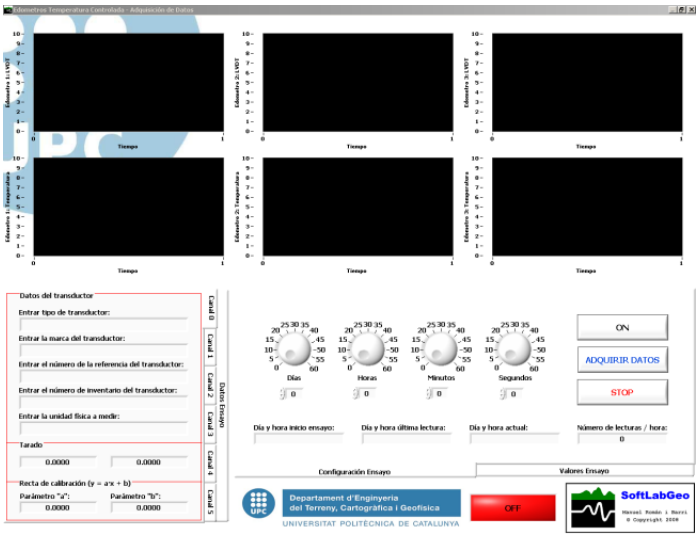

Figure 3.17 UI of Soft LabGeo program

Figure 3.18 shows some interfaces of LabVIEW data acquisition system, there are some advantages compared with the original one: (a) eight thermocouples or LVDTs can be calibrated at the same time; (b) there are 8 acquisition channels in total, each one can be used for both thermocouple and LVDT; (c) each channel can download its own calibration data, which makes the measurement more precisely; (d) the frequency of data acquisition can be set separately in different time intervals; (e) it is an open system that can add more channels depending on the requirement of hardware.

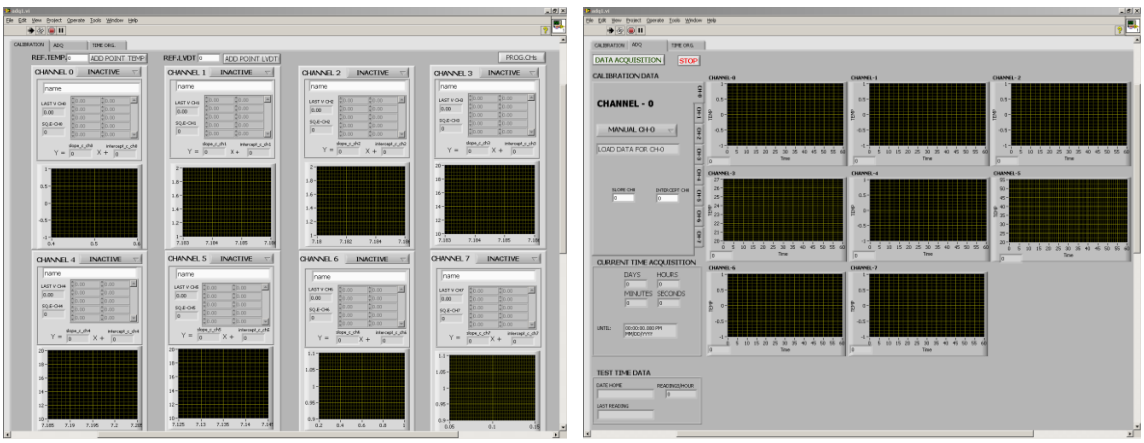

(a) (b)

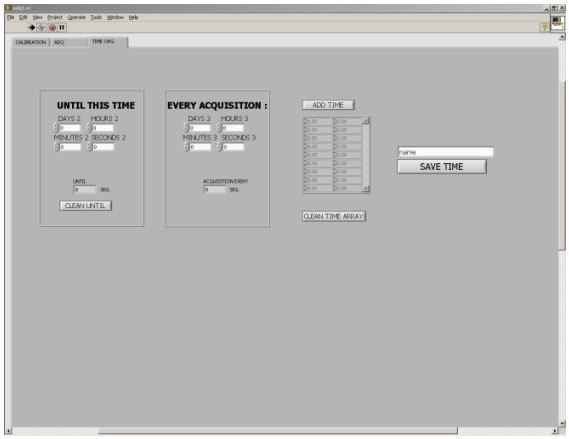

(c)

Figure 3.18 UI of LabVIEW data acquisition system: (a) calibration interface, (b) acquisition interface, and (c) time setting interface

After the new data acquisition program has been developed, all the thermocouples and LVDTs required in the following experiments have been calibrated with the results presented in Figures 3.19 and 3.20, respectively. Both the thermocouples and LVDTs have good linear performance and the coefficient of determination R squared are all more than 0.999.

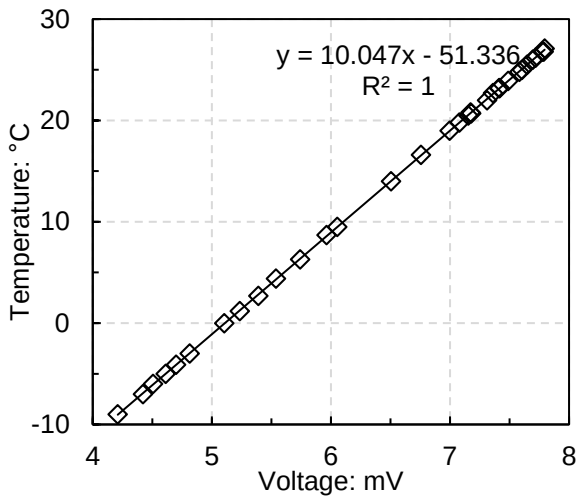

(a)

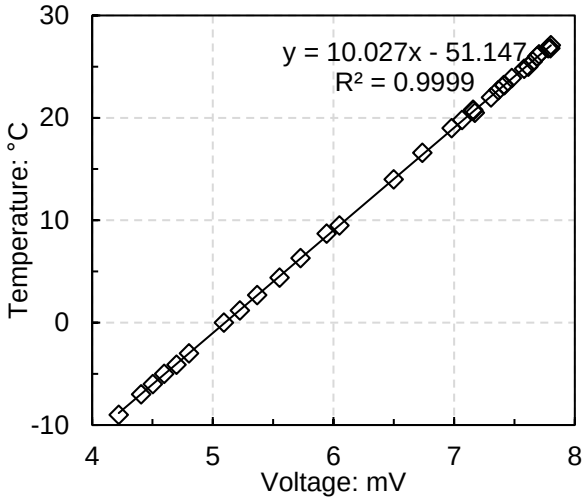

(b)

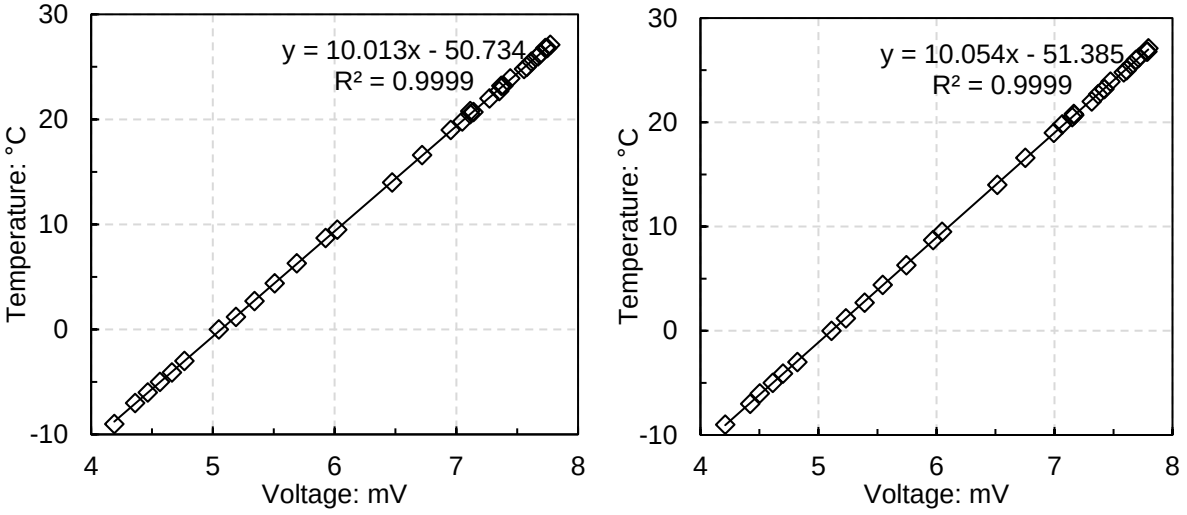

(c) (d)

Figure 3.19 Calibration of thermocouples: (a) TC 1, (b) TC 2, (c) TC 3 and (c) TC 4

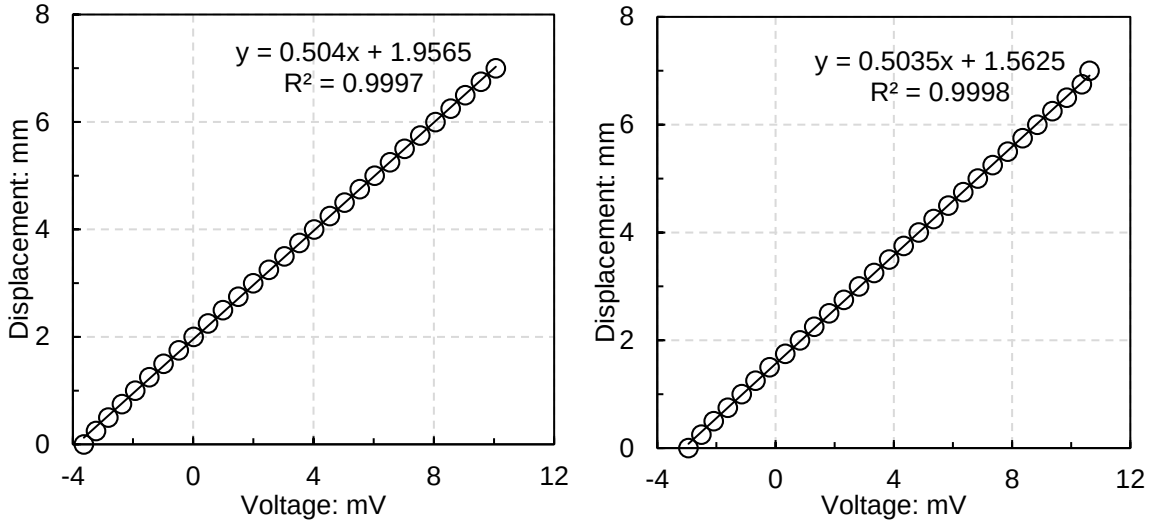

(a) (b)

Figure 3.20 Calibration of LVDTs: (a) LVDT 1 and (b) LVDT 2

3.3.6 Experimental program

For measuring the bulk EC and relative dielectric permittivity of fine sand and clayey silt, a cylindrical PVC container, which is 109 mm in height and 110 mm in diameter, is used. The soils with different known degrees of saturation are prepared to fill the PVC container. The FDR sensor is installed as described in Section3.3.1. Except for the FDR component, three

additional thermocouples are added at different positions inside the soil to make the measurements accurately. The PVC container with soil and sensors is then immersed into antifreeze liquid inside the cooling bath. The liquid level is a little bit lower than the surface of PVC container in case that antifreeze liquid flows into the soil sample. The bare soil surface is covered by a film in case any condensed vapour flows into the soil. The freezing-thawing experiment is then performed with a temperature range from 20 °C to -15 °C. The data for EC and dielectric permittivity are thus obtained at different temperature stages. The set-up of the experiments is plotted in Figure 3.21.

The bulk EC and dielectric permittivity initially would decrease during freezing, and finally, they reach a constant value that indicates the maximum ice stage has been reached. The bulk EC and dielectric permittivity in full liquid state at the critical freezing point and in maximum ice state will be recorded and used for analysis.

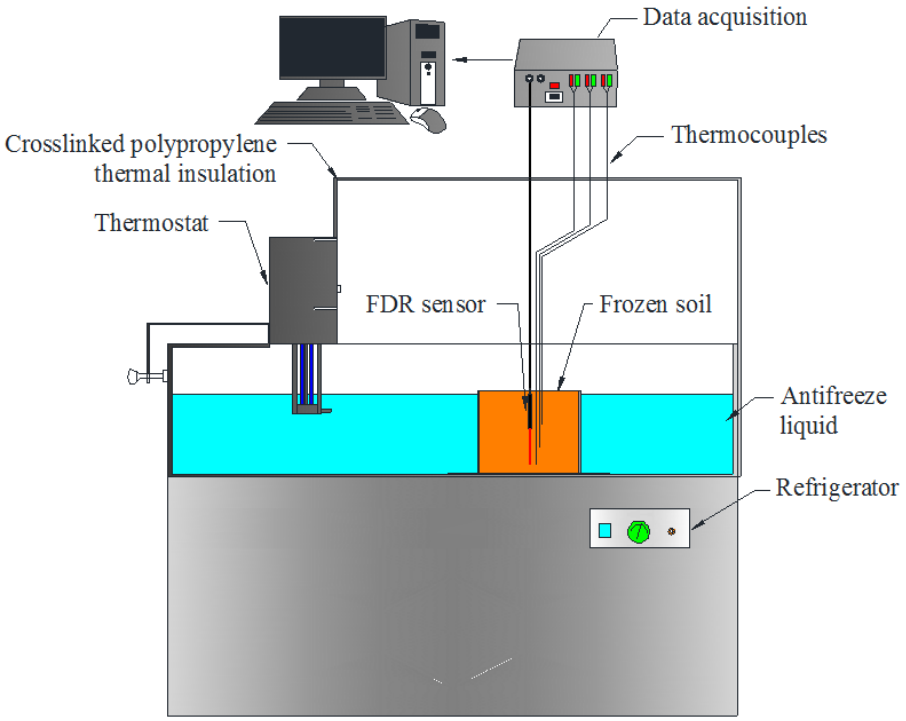

Figure 3.21 Set-up of temperature-controlled EC and permittivity test

3.4 ERT monitoring of frozen soils

3.4.1 Electrical resistivity tomography (ERT) system

Electrical resistivity tomography (ERT) is a technique that allows determination of the spatial distribution of the EC within an object from resistivity measurements at its boundary. Several electrodes are applied to the surface of the object, and known currents are then imposed on some of them. The electric potentials resulting from the application of such currents are then measured on the rest of electrodes. As the collected measurements are linked to the object conductivity by known physical laws, the distribution of conductivity within the sample can be estimated. Such an estimation process is called tomographic reconstruction.

3.4.1.1 Forward model

The solution of the forward problem links the voltage measurements to the object conductivity. It is assumed that the object under measurement has a conductivity σ that is isotropic and that the electric and magnetic fields are slowly varying, the electric potential u inside the body Ω is governed by the stationary form of Maxwell's equations:

$$\nabla\left(\sigma\nabla u\right)=0 \tag{3.10}$$

The presence of the electrodes is considered via appropriate boundary conditions. One model for electrodes, which provides accurate predictions at least for laboratory experiments (Borsic, 2002; 2005), is the complete electrode model proposed by Somersalo et al. (1992). The model assumes that electrodes are good conductors and therefore that the electric potential of each electrode is constant over its entire surface. Moreover, the model assumes that there is contact impedance at the interface between the electrode and the object under measurement. Under these assumptions, the following relation holds for each electrode, $l=1,\cdots,L$:

$$V_l = u + z_l\sigma\frac{\partial u}{\partial \vec{n}} \text{ on } \partial\Omega_l, \quad l=1,\cdots,L \tag{3.11}$$

where V_l is the potential of the l th electrode, z_l is the contact impedance of the l th electrode, u and σ are the object potential and conductivity, $\vec{n}$ is the outwards normal to $\partial\Omega$, and $\partial\Omega_l$ is the portion of $\partial\Omega$ underneath electrode l.

Stimuli are accounted for by specifying for each electrode that

$$\int \sigma \frac{\partial u}{\partial \vec{n}} = I_l \quad \text{on} \quad \partial\Omega_l, \quad l = 1, \cdots, L \tag{3.12}$$

where I_l is the current injected into the l th electrode. Equations (2) and (3) apply to the portions of $\partial\Omega$ that falls underneath each electrode. To the remaining parts of $\partial\Omega$ (inter-electrode gaps), the following relationship applies:

$$\sigma = \frac{\partial u}{\partial \vec{n}} = 0 \tag{3.13}$$

as no current density is crossing the free surface of the object under measurement. Equations (3.11)–(3.13) specify the model for the electrode; voltages on the electrodes are, however, specified to within an arbitrary additive constant, as no reference potential has been specified. As this is an arbitrary choice, usually the model is complemented with the additional condition

$$\sum_{l=0}^{L} V_l = 0 \tag{3.14}$$

which allows the unique determination of all V_l.

3.4.1.2 Reconstruction

The inverse operator, which given the measurements would return the conductivity, is not known in the general case. Hence, reconstruction algorithms make use of a forward model, and the reconstruction is formulated as a non-linear least-squares problem, where the conductivity of the forward model is varied until a satisfactory match between the

measurements simulated by the forward model and the real measurements is met. Most reconstruction codes implement the forward model with a finite element solver (Paulson et al., 1992; Vauhkonen, 1997; Borsic, 2002; Polydorides and Lionheart, 2002; Borsic et al., 2005), discretising both the domain Ω and the conductivity distribution. The reconstruction problem is therefore stated as

$$\mathrm{s}_{rec} = \arg\min \left\| h(\mathrm{s}) - \mathrm{v} \right\|_2^2 \tag{3.15}$$

where **v** is the vector of measured voltages, **s** is the discrete conductivity, ***h*** is the non-linear forward operator from model space to measurements space and $\left\| \cdots \right\|_2^2$ indicates the squared 2-norm. The reconstruction problem, both in its continuous form and in its discrete form as expressed by Equation (6), is *ill* posed in the sense that small perturbations in the measured data can cause arbitrarily large errors in the estimated conductivity (Calderon, 1980; Sylvester and Uhlman, 1987). Given the *ill*-posed nature of the inverse problem, reconstruction algorithms adopt regularisation techniques in order to obtain a stable solution. In practical terms, such ill conditioning arises from certain patterns of conductivity for which the corresponding measurements are extremely small (Breckon, 1990; Borsic, 2002), and which are therefore affected by measurement noise.

Such patterns of conductivity, for which the observations are unreliable, corrupt the reconstruction. Regularisation techniques are adopted to prevent such problems. Equation (6) is commonly solved using the Tikhonov regularisation, formulating the reconstruction as

$$\mathrm{s}_{rec} = \arg\min \left\| h(\mathrm{s}) - \mathrm{v} \right\|_2^2 + \alpha F(\mathrm{s}) \tag{3.16}$$

where $F(\mathrm{s}) \geq 0$ is the regularisation function and α is a positive scalar called the Tikhonov factor. Specifically, F acts as a penalty term by taking large values corresponding to the distribution **s** that is to be prevented in the reconstructed profile. The effect of F on the reconstructions can be adjusted by varying the value of α. As the conductivity is discrete, the regularisation function is usually expressed as $F(\mathrm{s}) = \left\| Ls \right\|_2^2$, where L is the regularisation matrix. The reconstruction is therefore formulated as

$$\mathrm{s}_{rec} = \arg\min \left\| h(\mathrm{s}) - \mathrm{v} \right\|_2^2 + \alpha \left\| L\mathrm{s} \right\|_2^2 . \qquad (3.17)$$

As anticipated, the role of the regularisation function is to penalise the presence in the reconstructed image of conductivity distributions for which observations are exceedingly small compared with the noise in the measurements. Thorough discussions on the choice of α and on regularisation techniques in ERT can be found in Kolehmainen (2001) and Borsic et al. (2002). The classical choice for the matrix *L* is the identity matrix. A similar choice is made in the NOSER algorithm (Cheney et al., 1990), which uses a positive diagonal matrix. Matrices that approximate first- and second-order differential operators have also been proposed (Hua et al., 1988). All these regularisation methods achieve the stability of the inversion by penalising sudden variations in the conductivity and hence offering a trade-off between the stability of the reconstruction and the sharpness of the image.

3.4.2 Previous 2D experimental set-up

The two-dimensional ERT system used in this thesis is from the Geotechnical Engineering Laboratory in Politecnico di Torino, Italy. The detailed description of the whole system can be found in Borsic et al. (2005).

Experiments have been performed on a cylindrical Perspex cell, with an internal diameter of 130 mm and a height of 100 mm (Borsic et al. 2005). Sixteen electrodes (thin silver plates, 5 mm × 80 mm × 0.1 mm) are applied on the lateral surface of the soil sample with constant spacing (see Figure 3.22). The shape and position of the electrodes have been chosen to realistically reproduce a 2D propagation of electric currents inside the sample. The decision to use 16 electrodes is a compromise between simplicity of design and resolution. In ERT, the resolution is determined by the number of electrodes and by the signal-to-noise ratio of the measurements. Industrial and medical applications of ERT on round or ‘almost round’ objects show that the use of 32 electrodes only marginally improves the resolution compared to the 16-electrode configuration (Holder, 2004).

Figure 3.22 Measurement set-up: (1) personal computer; (2) data acquisition system; (3) inverter and (4) measuring cell (Borsic et al., 2005)

Electrodes are connected to the data acquisition system using silver wires welded to their back and protruding outside the cell through thin holes (1 mm in diameter). A silicone injection in these holes prevents leakage of the interstitial fluid from the cell. For the same reason, the base of the cell is equipped with an O-ring, providing a watertight contact.

The data acquisition system is the Complex Impedance Tomography (CIT) Mark I, a prototype designed by Iridium Italia s.a.s. in collaboration with the Applied Geophysics Section of Politecnico di Torino (Sambuelli et al., 2002). The main characteristics of the instrument are reported in Table 3.1. The instrument is a single current source tomography.

Table 3.1 Characteristics of the complex impedance tomography (Bena, 2003)

Parameters	value
Maximum output current: A	0.25
Maximum output voltage: V	40
Operative frequencies	12 steps from 0.488 to 976 Hz
Acquisition channels	16
Resolution on phase angles: mrad	≈1
Resolution on voltage: μV	100
Resolution on current: μA	10
Input impedance: MΩ	200

A digital direct synthesiser is used for the generation of the AC waveform, which is then fed to a voltage-controlled current source and applied via a multiplexer to the pair of driving electrodes. The output impedance of the current source is estimated to be in the range of 200 MΩ, making it possible to drive currents in very resistive media. The injected current intensity is measured on a shunt resistor in series with the driving pair, which ensures accurate measurement of the applied current. A second multiplexer connects the electrodes to an analogue to digital converter for voltage measurement. The output signals are processed by an on-board digital signal processor, which separates in-phase and out-of-phase components (Bena, 2003). The instrument is controlled by a PC to implement the measurement scheme and to gather the results.

The experimental data have been collected using the 'opposite' measurement protocol (Hua et al., 1988; Lionheart et al., 2001), in which currents are injected by diametrical electrodes and potential differences are measured for all possible pairs of the remaining electrodes. Switching the input pair, 96 linearly independent measurements can be collected over the 16 electrodes of the cell. This protocol is preferred to the adjacent measurement method because it offers a better resolution, as the current travels with greater uniformity inside the sample (Lionheart et al., 2001).

Tomographic inversions have been performed with a commercial ERT toolbox (SC-AIP, 2004). The reconstruction is formulated as in Equation (3.15), and the forward model is a finite element implementation of Equations (3.10) to (3.14). The cell layout and the sample geometry are such that a 2D model can be used. The regularisation matrix L of Equation (3.15) is chosen to be a discrete representation of the Laplacian. The toolbox uses a double mesh: a coarse mesh is used to represent the discrete conductivity, and a second, finer mesh is used to represent the electric potential. The number of elements of the coarse mesh coincides with the number of unknowns of the reconstruction process; hence, it must be chosen with care, considering the number of available measurements in light of sensitivity and non-uniqueness issues. For the interpretation of the tests reported in the present paper, there are 812 triangular elements in the coarse mesh (degrees of freedom of the conductivity) and the mesh is illustrated in Figure 3.23. As such, a mesh is not appropriate as an accurate solution

for the forward problem; a second and finer mesh is used for the computation of simulated voltages at the electrodes. The fine mesh, shown in Figure 3.24, is obtained by adaptive refinement of the coarse mesh. The forward solver projects the conductivity from the coarse mesh to the fine one each time a forward solution is needed, and the FEM stiffness matrix is assembled for the fine mesh. The refinement of the mesh allows good accuracy in the approximation of the electric potential, especially in the proximity of the electrodes, where it varies rapidly owing to the injected currents (Vauhkonen, 1997; Borsic, 2002).

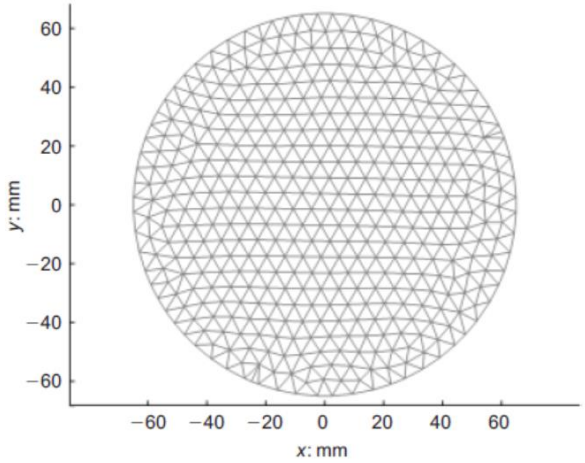

Figure 3.23 Coarse finite element mesh

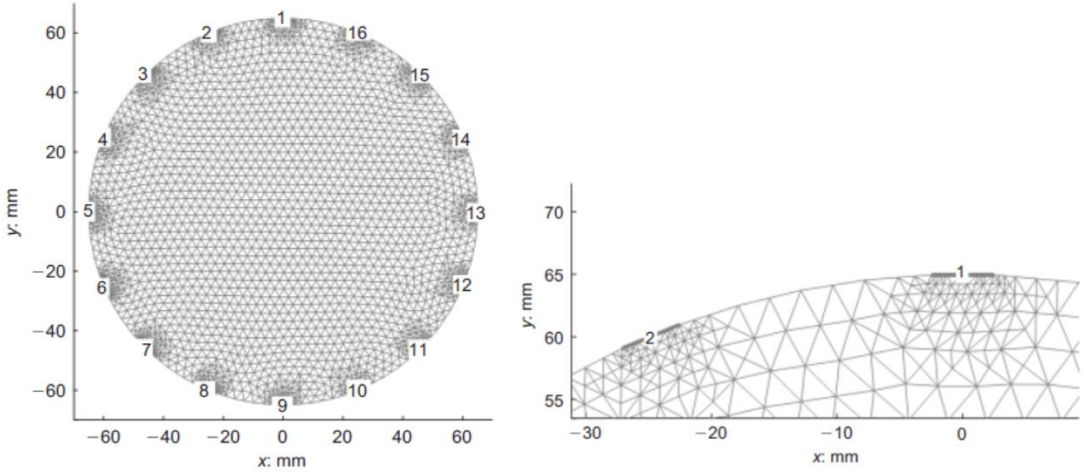

(a) (b)

Figure 3.24 Fine finite element mesh: (a) global view and (b) close-up view near electrodes 1 and 2

3.4.3 Modification of cylindrical freezing cell

In this thesis, a modified cell with ERT system is developed to monitor spatial and temporal bulk EC under controlled temperature (ranging from 22 °C to -15 °C). The cell has an internal diameter of 80 mm and can accommodate samples with heights of up to 50 mm. The thickness of the cell is 20 mm with 16 electrodes on its sidewall. The top and bottom plates are all 10 mm thick. The electrode is a silver foil (5×35×0.1 mm) connected with a metal bar. A 15-mm thick polyurethane foam with thermal conductivity λ=0.022–0.033 W/m·K is used for thermal insulation.

A 10-mm aluminium alloy tube with waterproof insulating tape is placed in the centre of the cell to allow the antifreeze liquid to flow through it. The reason for this setup is that soil is frozen from the centre instead of from the outside. Thus, ice generation is avoided on the surface of the electrodes, which could affect the electrical conduction between the electrodes and soil sample. The waterproof tape wrapped around the tube is implemented to increase its electrical resistivity. A cooling bath is used to cool the antifreeze liquid to the target temperature.

During ERT measurements, electrical current is applied with two electrodes, and other pairs of electrodes register the induced electrical potential differences. The experimental data are then used to reconstruct the EC field using a least-square inversion algorithm with Tikhonov regularisation (Borsic et al., 2005; Comina et al., 2008). The soil is modelled with a finite-element mesh, and the bulk EC of each element -assumed to be isotropic- is estimated. The details of the ERT instrumentation and its reconstruction software were described in Comina et al. (2008; 2010). The modification and manufacture of the new cell are presented in Figure 3.25.

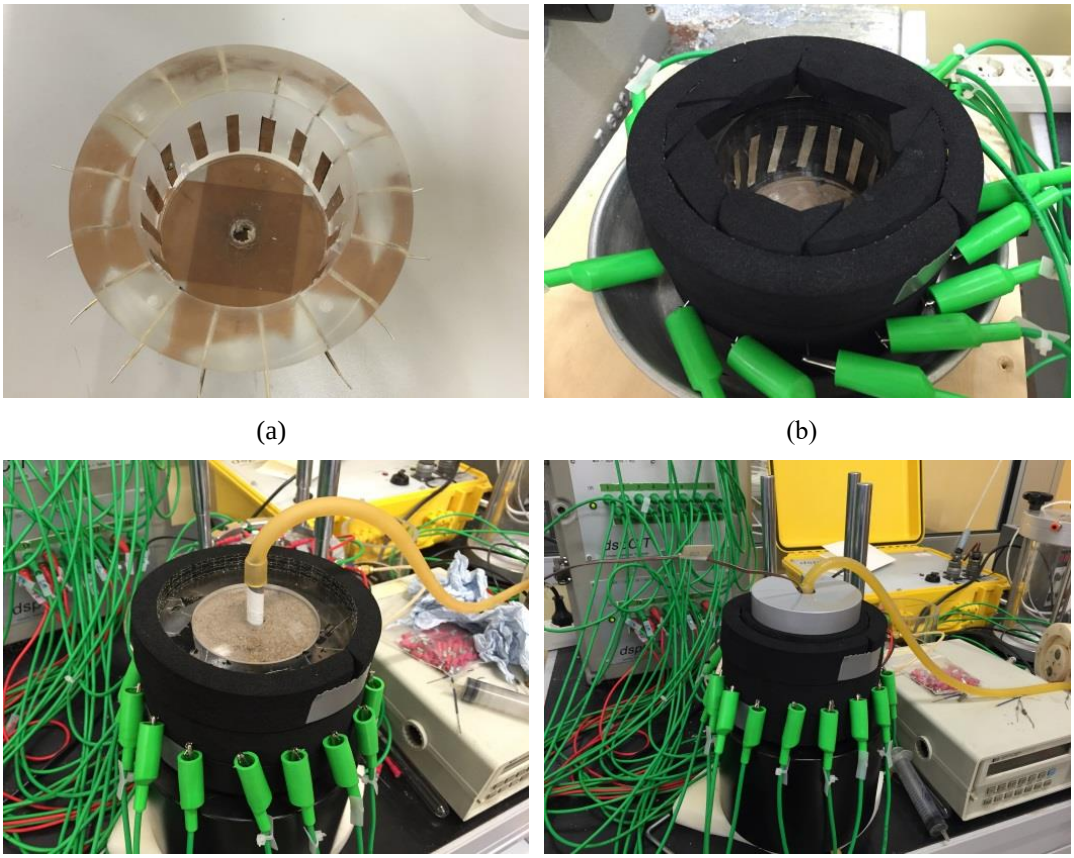

(a) (b)

(c) (d)

Figure 3.25 ERT oedometer cell: (a) ERT cell with electrodes; (b) ERT cell with thermal isolation; (c) complete ERT cell with samples; (d) overall view of freezing ERT test.

3.4.4 Calibration of ERT system

A small cell presented in Figure 3.26 (a) is used to calibrate the ERT system, which has a very precise measurement performance. The electrical current is applied to the two plate electrodes at the ends, so measurements can be done using the parallel pair of electrodes in the middle of the sample. The small cell displayed consistent values compared to an independent electrical conductometer shown in Figure 3.26 (c). Moreover, this small cell can be also used to explore the relationship between bulk EC and temperature on different soils with different initial porosities and degrees of water saturation (Mao et al., 2018).

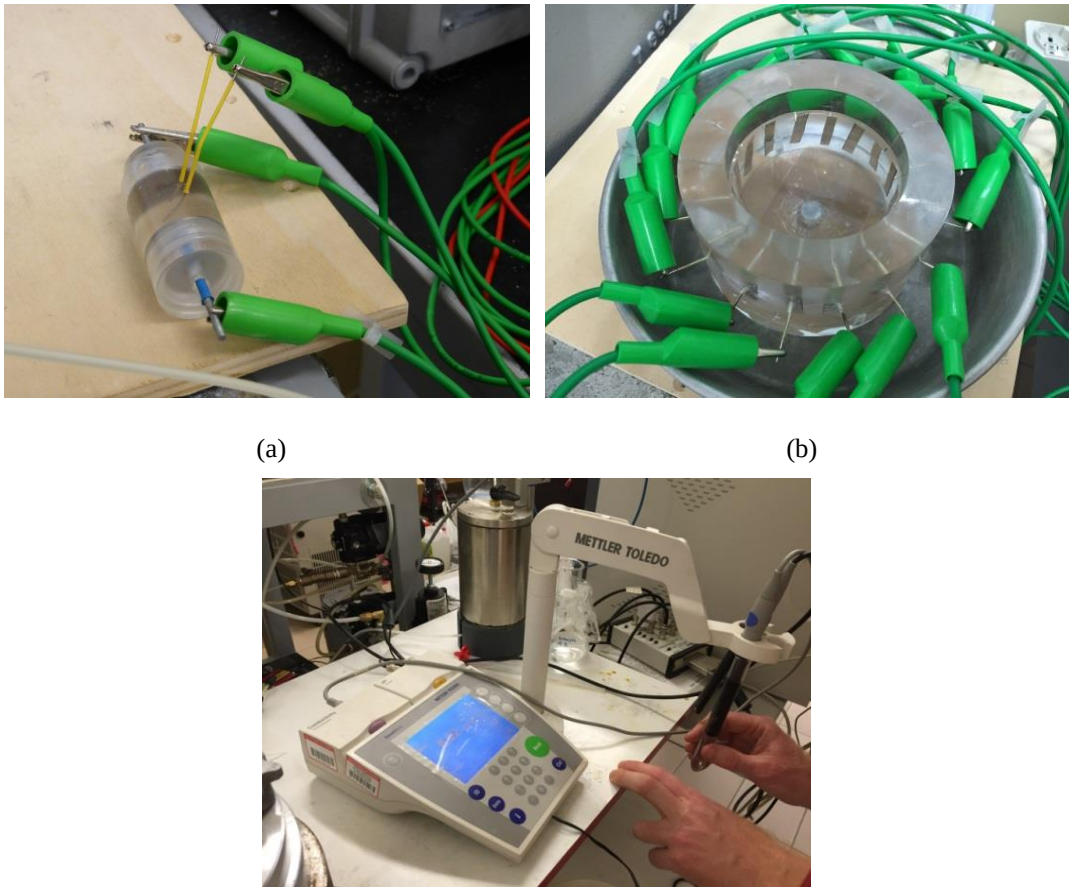

(a) (b)

(c)

Figure 3.26 (a) Small cell of measuring soil EC, (b) new modified ERT cell and (c) electrical conductometer.

The calibration of the new modified ERT cell is presented in Figure 3.26 (b). Preliminary tests are performed to examine and calibrate the reconstruction process by imaging some uniform samples. The cell filled with pure water solutions with different concentrations of KCl and NaCl has been measured and reconstructed. Figure 3.27 shows the image of the ERT reconstruction of the 1-mol KCl solution, which gives a uniform EC distribution. Other salt concentrations also give similar uniform images with different EC scales. These tests give confidence to the reconstruction process for the specific experimental set-up.

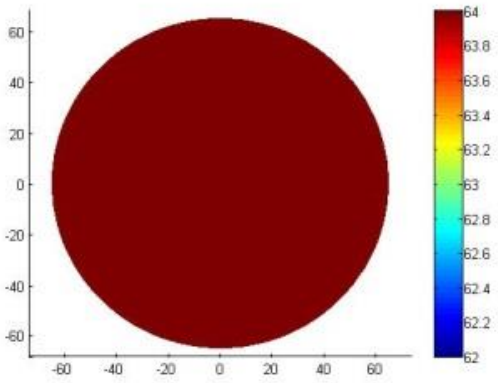

Figure 3.27 ERT reconstruction of a 1-mol KCl solution

The mean values of the reconstructed results are then compared with the independent measurements by an electrical conductometer, which gives an average ratio of 1.72. All calibration data is listed in Table 3.2. The maximum variation is 3% and is due to some small deviations in the proximity of electrodes.

Table 3.2 Calibration of different water solutions

Number	Conductometer/ dS/m	ERT reconstruction/ dS/m	Ratio of Cond./ERT
0.05 mol KCl	7.90	4.74	1.78
0.2 mol KCl	26.00	15.17	1.71
1 mol KCl	117.00	65.80	1.67
5% NaCl	79.70	46.37	1.72
Average			1.72

3.4.5 Experimental program

The set-up of the ERT system for monitoring the soil freezing process is shown in Figure 3.28. When a soil sample is prepared and installed in the cell, two latex tubes are connected to both ends of the aluminium freezing tube, which is placed in the centre of the sample. The electrodes are connected to green cables with numbers. The cooling bath is first switched on and frozen antifreeze liquid is brought to the target temperature (-15 °C in these experiments). Then the antifreeze liquid is pumped to flow through the freezing tube and the ERT is switched on at the same time. In order to keep a constant flow in the tube (axisymmetric

freezing can be obtained), the flow direction should be from the bottom upward. The time intervals for data acquisition can be set and automatically logged.

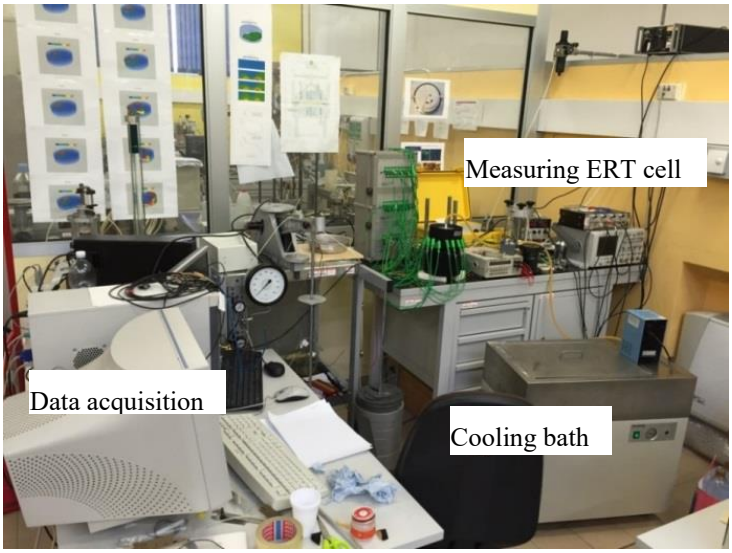

Figure 3.28 Set-up of frozen soil ERT system

A set of experiments have been carried out to explore the behaviour of the soil freezing process by setting a series of benchmark tests: homogeneous unsaturated/saturated fine sand, homogeneous unsaturated/saturated clayey silt, sand inclusion within homogeneous clayey silt and a hole inside the homogeneous fine sand. A 5% NaCl solution (mass basis) is used instead of tap water as the interstitial water in the tests with the aim of being better able to distinguish between the EC of ice and that of unfrozen water. The pictures of the prepared samples are presented in Figure 3.29. The initial physical properties of prepared samples are listed in Table 3.3.

(a) (b)

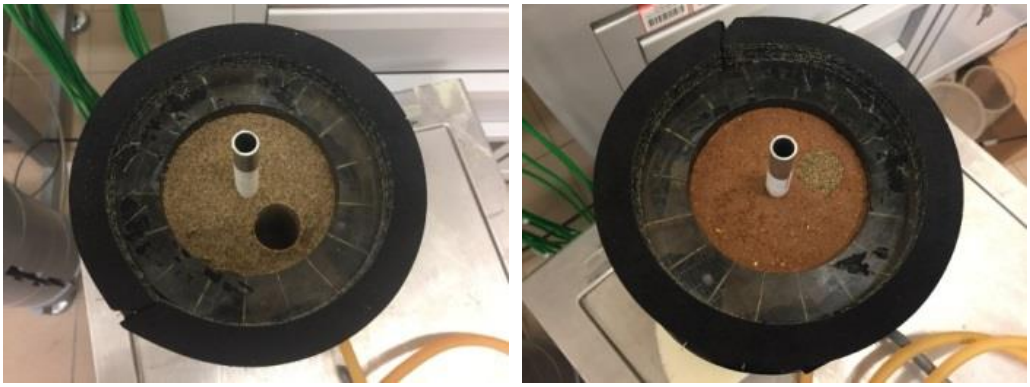

(c) (d)

Figure 3.29 Prepared soil samples: (a) homogeneous fine sand; (b) homogeneous clayey silt; (c) a hole inside the homogeneous sand and (d) sand inclusion within the homogeneous clayey silt

Table 3.3 Initial properties of soil specimens in freezing ERT tests

Sample		Porosity, n	Degree of water saturation, S_r	Volumetric water content, θ
Homogeneous sand	1	0.38	0.91	0.35
	2	0.38	0.55	0.21
	3	0.37	0.70	0.26
Homogeneous silt	1	0.26	1.00	0.26
	2	0.36	0.52	0.19
	3	0.30	0.84	0.25
Sand with an opening		0.40	0.67	0.27
Silt with sand inclusion	Silt	0.30	0.81	0.24
	Sand inclusion	0.40	0.67	0.27

Notes: From Figure 3.6, the suction of sand inclusion at S_r=0.67 and silt at S_r=0.81 can be estimated, which are around 3kPa and 790 kPa, respectively. The suction difference between silt and sand inclusion would probably induce the water migration, as shown in ERT results.

3.5 Temperature-controlled oedometer test

3.5.1 Previous oedometer cell

The previous oedometer equipment is a suction-controlled oedometer cell developed at the Geotechnical Laboratory of the UPC; it has a ring size of 50 mm in diameter and 20 mm in height (Peláez, 2013). Figure 3.30 shows the design drawing of the previous oedometer cell,

which is a rigid metal group consisting of five main components: ① the base, ② sample holding ring, ③ the central body, ④ the top and ⑤ the load shaft sealing membrane and piston.

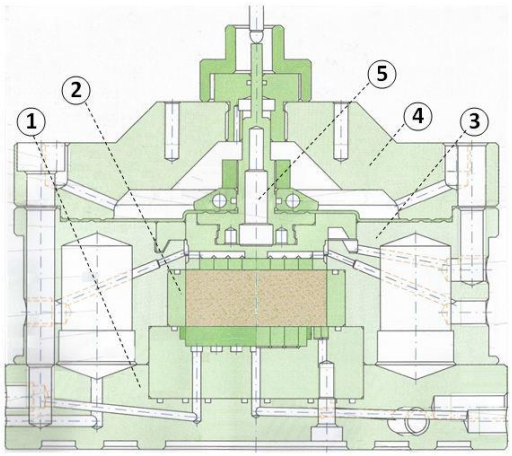

Figure 3.30 Schematic of the oedometer cell used. Geotechnical Laboratory, UPC.

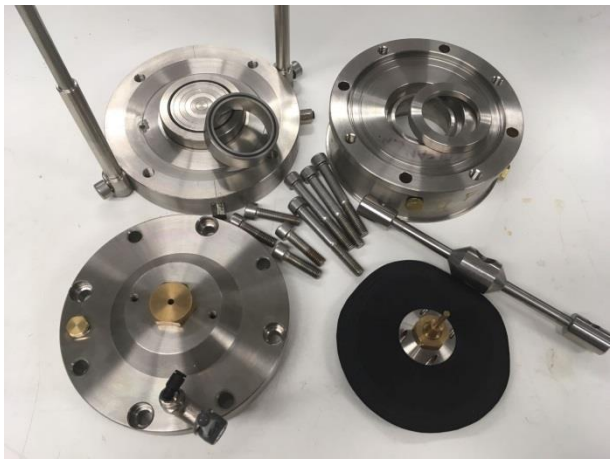

Figure 3.31 Components of the oedometer cell. Geotechnical Laboratory, UPC.

The physical components are shown in Figure 3.31. The base consists of two parts, a base plate, and sample support. The valves are housed in the base plate and used to connect water and/or air. The sample support is interchangeable depending on the type of test (suction controlled or not). For performing this test, a series of metal rings, with dimensions of 50 mm in diameter and 7.15 mm in thickness, are used. The ring holder is supported concentrically with the base support and allows testing specimens with variable heights between 10 mm and

20 mm. The central body contains the sample ring that restricts horizontal movement and connections for valves and air/water circulation.

3.5.2 Modification of oedometer cell

3.5.2.1 Measuring temperature inside the oedometer cell

To measure the temperature of the tested sample more precisely, a small hole was made on the lateral part of the main body. The thermocouple can be inserted into the hole so that it is very close to the soil sample. Silicone is used for fixing the thermocouple and sealing the hole to prevent the entry of antifreeze liquid into the hole. The modification can be seen in Figure 3.32.

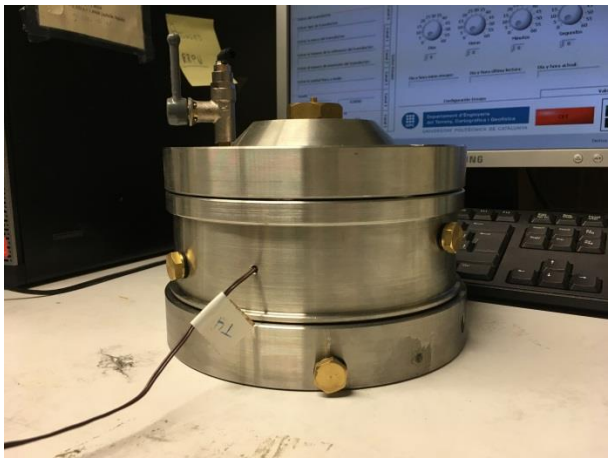

Figure 3.32 Thermocouple stretches into oedometer cell

3.5.2.2 Isolation of contact area of piston rod LVDT

When conducting the temperature-controlled oedometer test, the oedometer cell is immersed in the antifreeze liquid and the top part is exposed to air. Due to the high thermal conductivity of this metal material (81 to 116 W/m·K), the condensed water vapour on the top area quickly changes to ice and extends over the entire surface area exposed to air. It will affect the contact point of the LVDT and piston rod; it may even freeze the entire system so that the piston cannot be shifted up and down (see Figure 3.33).

(a) (b)

Figure 3.33 Insulation contact area of the piston-rod LVDT with section PVC and polyethylene lining

(a) (b)

Figure 3.34 Freezing state situation: (a) without insulation and (b) with PVC insulation

To prevent the ice mass from reaching the point of contact, a section of PVC pipe, 100 mm in inner diameter and 100 mm in length, was placed on the top of the cell; it was internally coated with crosslinked polyethylene to isolate the contact point (rod-LVDT). In Figure 3.34 (a), a detail of the pieces placed in order is shown. The significant effect of PVC isolation can be seen in Figure 3.34 (b).

3.5.2.3 Air Drying Chamber

The formation of ice can be found inside the loading chamber after the freezing test; see Figure 3.35 (a). Obviously, the moisture in the air will be deposited on the piston rod under

pressure and subsequently freeze and affect the vertical movement of the piston. It is deemed necessary to design a system that flows air through a drying system to reduce its relative humidity (HR ≤ 10%).

The drying process is performed by passing the pressurised air through a chamber (no membrane) with lithium chloride (LiCl) inside and out of the other valve to the oedometer cell. Lithium chloride is used as a dehydrating agent to reduce the moisture to lower than the dew point when the temperature approaches the freezing point. In Figure 3.35 (b), the chambers with lithium chloride therein are presented.

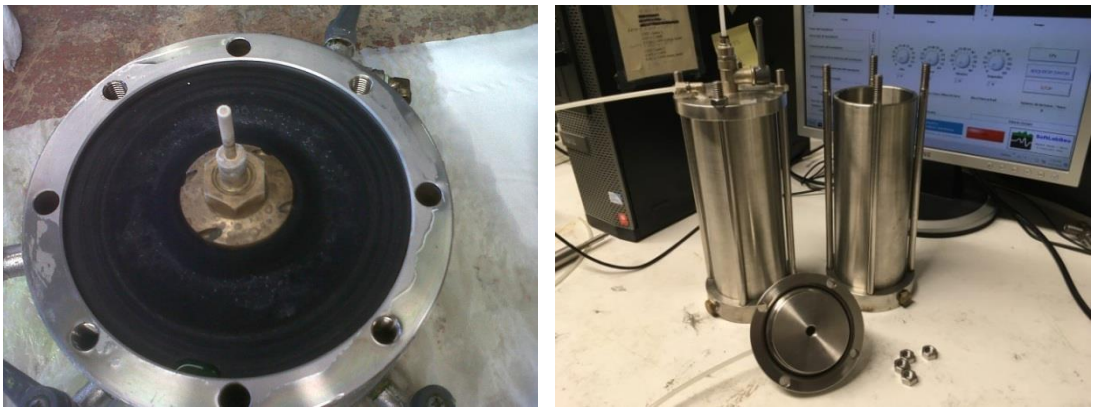

(a) (b)

Figure 3.35 (a) Formation of frost on the part of the piston rod and (b) air drying chamber

3.5.3 Final experimental set up

After all modifications of the cooling bath, data acquisition, thermocouples, and oedometer cell were completed, the final experimental set-up is ready to perform temperature-controlled (from 20 °C to -15 °C) oedometer tests. The external device configuration is presented in Figure 3.36. To observe the coupling phenomenon of the various parts, the test soil is placed in the oedometer cells, which is then put inside the refrigerator bath and consolidated by the pressurised air. During the consolidation stage, the cooling system stays off and there is not antifreeze liquid inside the bath; see Figure 3.37 (a). During the thermal stage (freezing-thawing path), the whole bath is filled with the antifreeze liquid below the top level of oedometer and then both the refrigerator and its internal thermostat are turned on (Figure 3.37 (b)).

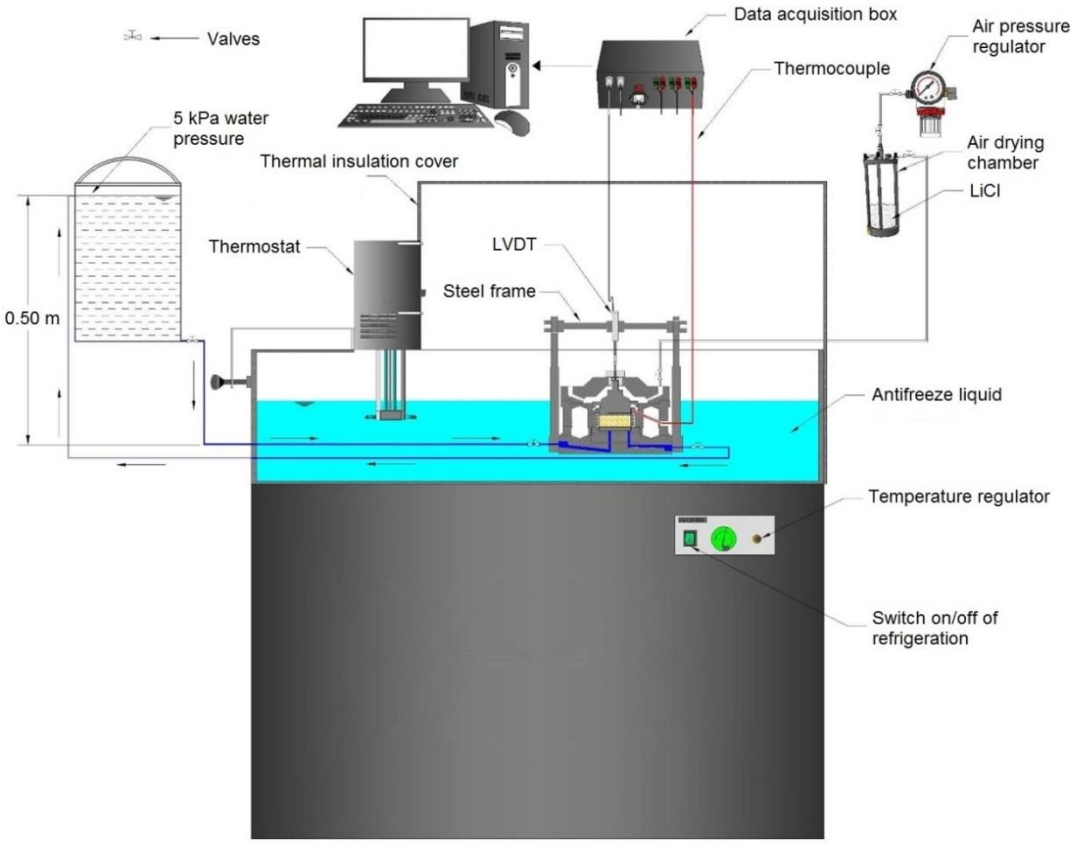

Figure 3.36 Schematic of temperature-controlled oedometer test set-up

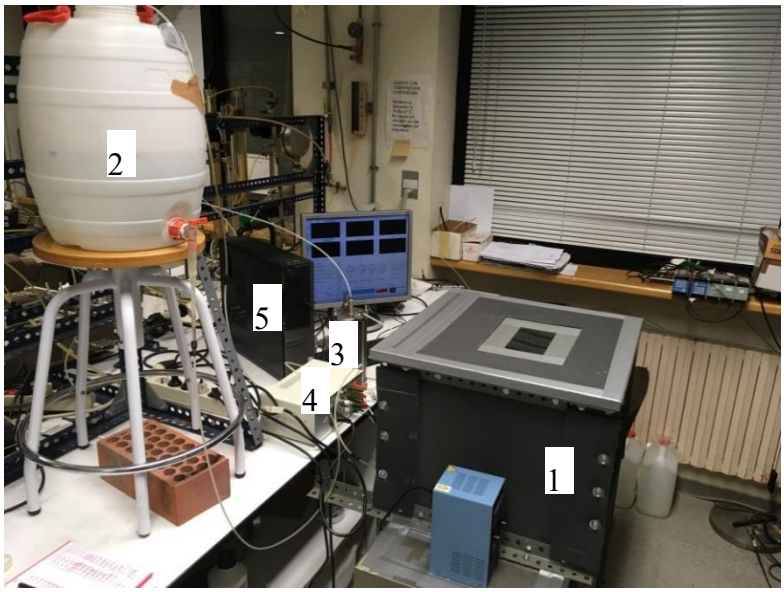

(a)

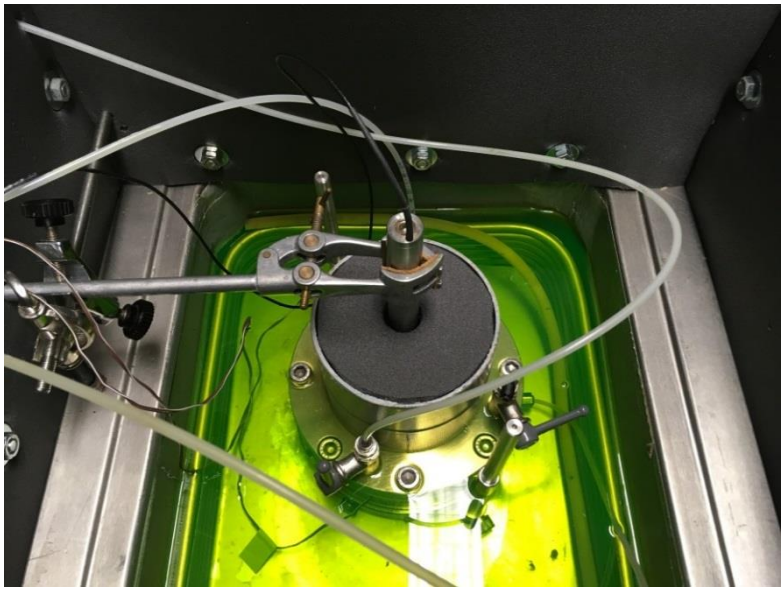

(b)

Figure 3.37 Set-up of temperature-controlled oedometer test (a) external: (1) cooling bath with oedometer; (2) water pressure around 10 kPa (1 meter of water); (3) air-dry chamber; (4) data acquisition box; (5) computer data collection; (b) internal of cooling bath.

3.5.4 Experimental program

The experimental program of the temperature-controlled oedometer test is designed to explore the behaviour of consolidation and thermal effects on Barcelona clayey silt. Two types of tests will be performed, one only for consolidation and the other for both consolidation and thermal path. For the first type of test, pressurised air is applied to the oedometer cell for the vertical stress steps (20kPa→ 50kPa→ 100kPa→ 200kPa→ 400kPa→ 600kPa). Each stress stage is kept for 24 hours. After loading to the maximum stress (600 kPa), the unloading path will be performed using the same procedure.

For the second type of test, in the consolidation stage (loading), the pressurised air is applied to the oedometer cell using the following vertical stress steps (20kPa→ 50kPa→ 100kPa→ 200kPa→ 400kPa→ 600kPa). When the consolidation stage is completed, the oedometer cells are put inside the refrigerator bath, which is filled with antifreeze coolant, to start the thermal stage (freezing-thawing path). This liquid allows applying temperature changes that are controlled by a regulator (thermostat). Once the temperature is achieved, it is maintained for 24 hours, and then returned to the starting point. The whole procedure is executed using

staggered temperature steps (20 ºC →0 ºC→-5 ºC→-10 ºC→-5 ºC→0 ºC→20 ºC). The stress and temperature paths followed by two samples of Barcelona clayey silt are presented in Figure 3.38.

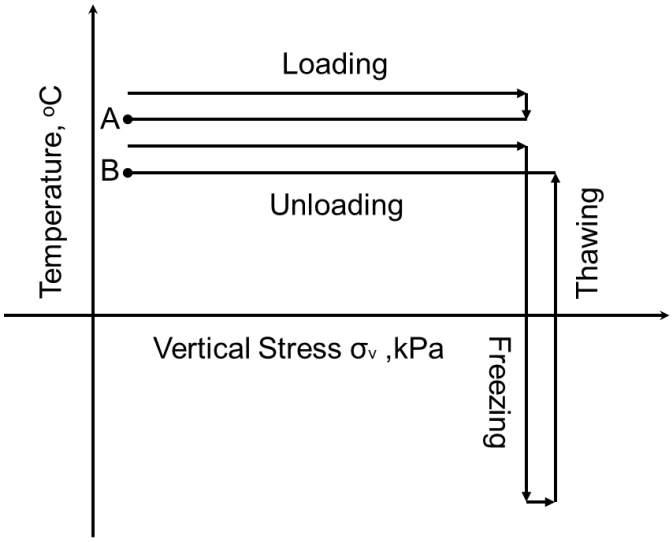

Figure 3.38 Stress and temperature paths followed on two samples of Barcelona clayey silt (stress path: 0–600kPa, thermal path: 20 °C~-15 °C)

3.6 Microstructure investigation of clayey silt

3.6.1 Mercury Intrusion Porosimetry (MIP)

3.6.1.1 Description of MIP

Mercury intrusion porosimetry (MIP) in the geotechnical field allows for a good estimate of the size distribution of the pores that are interconnected within a material. This is done by applying an absolute pressure while a sample is immersed in mercury. The applied absolute pressure causes the mercury to fill the pores, the larger ones first and then the smaller ones.

The basic principle of the MIP technique is based on the Washburn equation (Equation 3.18) in which an absolute pressure p_{Hg} is applied to a non-wetting liquid (mercury) to force it to

enter the empty pores. The equation, which applies to pores of cylindrical shape and parallel infinite plates (Webb, 2001), is

$$p_{Hg} = -\frac{n\sigma_{Hg}\cos\theta_{Hg}}{x} \tag{3.18}$$

where σ_{Hg} is the surface tension of mercury (σ_{Hg}=0.484 N/m at 25 °C), θ_{Hg} is the contact angle between the mercury and the pore wall and x is either the entrance or throat pore diameter (n=4) or the entrance width between parallel plates (n=2). The value n=4 is often used in MIP. The contact angle, which is very sensitive to surface roughness, is usually between 139° and 147° for clay minerals.

The mercury intrusion procedure can be used to obtain data on the retention behaviour of the soil. It can become assimilated to drying path of the soil moisture characteristic curve by applying increasing external air pressure (non-wetting fluid) to an initial saturated sample to gradually dry the soil (Romero, 1999). Thus, the injection of non-wetting mercury with a contact angle of θ_{nw} is equivalent to the ejection of water from the pores (desorption curve) by the non-wetting front advance of air with θ_{nw}=180° for the same diameter of pores being intruded. Therefore, the volume of pores not intruded by mercury could be used to evaluate the water content or degree of saturation corresponding to the equivalent applied air overpressure. The relationship between the equilibrium mercury intrusion pressure p_{Hg} and air overpressure or matric suction (u_a-u_w) can be obtained by applying Equation (3.19) for the same diameter x of pores being intruded:

$$\left(u_a - u_w\right) = \frac{4\sigma_w\cos\theta_w}{x} \quad \text{and} \quad p_{Hg} = -\frac{4\sigma_{Hg}\cos\theta_{nw}}{x} \tag{3.19}$$

$$\left(u_a - u_w\right) = -\frac{\sigma_w\cos\theta_w}{\sigma_{Hg}\cos\theta_{nw}}\,p_{Hg} \approx 0.196\,p_{Hg} \tag{3.20}$$

where σ is the surface tension and $\cos\theta_w$ =1 is the wetting coefficient for the air-water interface.

The corresponding water content (w) can be estimated by means of the following expressions (3.21):

$$S_{rnw} + S_r = 1;\ S_r \cdot e = G_s \cdot w;\ w = \frac{e}{G_s}\left(1 - S_{r_{nw}}\right) = w_{sat}\left(1 - S_{r_{nw}}\right) \tag{3.21}$$

where S_r is the degree of water saturation, S_{rnw} is the degree of saturation of the non-wetting mercury, w_{sat} is the water content at S_r =1, e is the void ratio and G_s is the specific gravity of the soil grains.

Romero and Simms (2008) presented the main limitations of MIP: (a) isolated pores enclosed by surrounding solids are not measured—this enclosed porosity is not significant in soils; (b) pores that are accessible only through smaller ones (constricted porosity) are not detected until the smaller pores are penetrated; (c) the apparatus may not have the capacity to enter the smallest pores of the sample (non-intruded porosity); and (d) the minimum practical pressure of the apparatus limits the maximum pore size to be detected (non-detected porosity). In this way, when the clay sample is intruded by mercury, the intruded void ratio estimated under the maximum applied pressure does not coincide with the estimated void ratio of the sample. Differences mainly arise due to the non-intruded porosity, for entrance pore sizes smaller than 10 nm, and the non-detectable porosity for pore sizes larger than 400 μm. In addition, the intrusion (pressure increase) and extrusion (pressure decrease) cycle do not close when the initial pressure is restored, indicating that some mercury has been permanently entrapped in the constricted porosity.

Experiments are performed in the AutoPore IV 9500, a mercury porosimeter that provides two stages in the application of pressure. The first, which corresponds to the low-pressure stage in which pressure is applied in the range between 0.0025 and 0.2 MPa, and the second high-pressure stage in which pressure is applied in the range between 0.2 and 220MPa. In the low-pressure stage, the computer uses dry nitrogen (dry air) to apply fluid pressure mercury; the high-pressure stage uses oil. The device and its ports are shown in Figure 3.39.

Figure 3.39 Mercury porosimeter (AutoPore IV 9500): (a) low pressure ports and (b) high pressure port

The porosimetry measures the total volume of mercury injected into the pores of the sample and the pressure applied to achieve this. Thus, when the pressure is increased, the pore size for each pressure increment is calculated while the volume of mercury required to fill these pores is measured. The pressure applied to the mercury at each increment gives information on the size of the pores and the total volume of mercury injected provides information on the porosity of the sample.

3.6.1.2 Sample preparation

Cubic samples of 10 mm^3 in the volume are trimmed from intact core samples or from oedometer samples after being tested. These samples require a pre-treatment before being installed in the porosimeter. Instantaneous freezing is carried out by plunging the samples into liquid nitrogen (-196 °C) and then applying vacuum to remove the pore water from the microstructure before the MIP test. In such conditions, water freezing occurs with very small ice crystals, and the 9% volume expansion that occurs under normal freezing conditions does not take place, optimising the preservation of the microstructure during dehydration (Delage

et al., 2006; Gonzalez-Blanco, 2017). Desbois et al. (2014) also show that no significant changes in the quantification of pore sizes and pore morphologies are produced due to this sublimation process and therefore good microstructure preservation is ensured.

3.6.1.3 Test procedure

The sample size is determined by the size of the sample holder or volume penetrometer, which is a cubic shape with an approximate size of 10 mm. Following the ASTM D4404-10 test procedure, once the sample is cut and dried by a process of "freeze drying", it is weighed and initially placed in the low-pressure port for the application of a vacuum (support sample is filled with mercury). Mercury pressure then increases from 0.0025 MPa to 0.2 MPa when the larger pores are filled. After this stage, the penetrometer is removed from the port, weighed again (including the sample and the mass of injected mercury) and placed inside the high-pressure port to fill the smaller pores up to a maximum pressure of 220 MPa (input pore sizes are about 7 nm). After completing this last filling stage, extrusion path starts releasing the pressure of the mercury. Some mercury particles that are being extruded are not permanently trapped in the porosity, which is not connected after pressure release (Romero and Simms, 2008). The lyophilisation process seems appropriate since the effects of the surface tension induced decline in the air-water interfaces are eliminated (Romero and Simms, 2008).

3.6.2 Field Emission Scanning Electron Microscopy (FESEM)

3.6.2.1 Description of FESEM

A scanning electron microscope (SEM) is a type of electron microscope that produces images of a sample by scanning the surface with a focused beam of electrons. The electrons interact with atoms in the sample, producing various signals that contain information about the sample’s surface topography. The electron beam is scanned in a raster scan pattern, and the beam’s position is combined with the detected signal to produce an image.

Field emission scanning electron microscopy (FESEM) provides topographical and elemental information at magnifications of 10x to 100,000x, with a virtually unlimited depth of field. Compared with the conventional SEM, the FESEM produces clearer, less electrostatically distorted images with spatial resolution down to 0.5 nm—three to six times better quality. Other advantages of FESEM include: (1) the ability to examine smaller-area contamination spots at electron accelerating voltages compatible with energy dispersive spectroscopy; (2) reduced penetration of low-kinetic-energy electrons probes closer to the immediate material surface; (3) high-quality, low-voltage images with negligible electrical charging of samples (accelerating voltages ranging from 0.5 to 30 kilovolts); and (4) essentially no need for placing conducting coatings on insulating materials. The FESEM equipment is shown in Figure 3.40.

Image-Pro Plus, an image processing software, is used to convert the images into binary figures containing only voids and solid particles. The voids and particles are represented by 0 and 1. A threshold (T) is set to distinguish them. When the pixel (P) is smaller than T, it is set to be 0; when P is larger than T, it is set to 1. The expression can be expressed as follows:

$$P = \begin{cases} 0, & P \le T \\ 1, & P > T \end{cases} \tag{3.22}$$

where T is the threshold and P is the pixel.

Parameters, representing the microstructural characteristics of the soil, can be obtained from the binary figures. They include porosity, fractal dimension, shape factor and degree of anisotropy, with porosity and fractal dimension identified as the two most crucial parameters.

The void ratio in soil is the ratio of void volume to particle volume, while the apparent void ratio obtained by FESEM tests is the ratio of void area to particle area.

$$e = \frac{S_l}{S_0} \times 100\% \tag{3.23}$$

where e is the apparent void ratio of the soil, %, and S_l and S_0 are the areas of voids and particles, respectively.

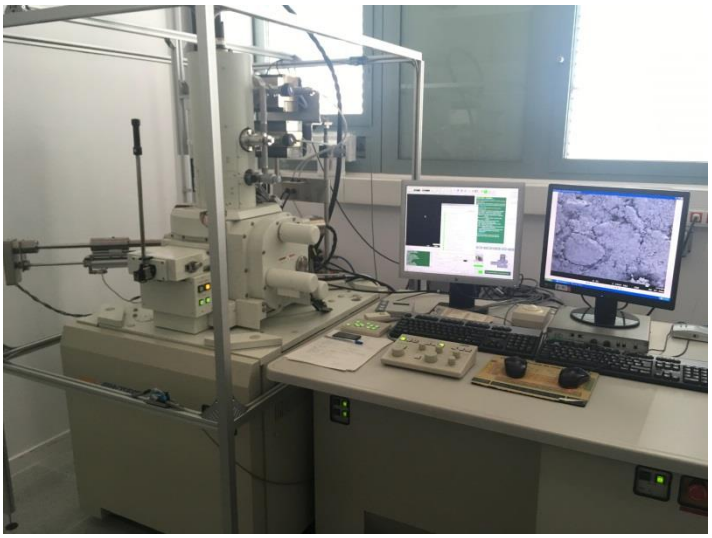

Figure 3.40 FESEM equipment

Some graphs can be divided into self-similarity and similar graphs with the number of N(r) according to some scale with r, and the fractal dimension can be obtained from the following relationship (Vallejo, 1996; You et al., 2017). Soil, composed of minerals of different sizes and morphology, is a fractal structure with self-similarity character. The degree of orientation can be reflected by the fractal dimension. The smaller the value, the worse the orientation and the bigger the degree of disorganisation and vice versa.

$$D = -\frac{\log N(r)}{\log r} \tag{3.24}$$

where D is the fractal dimension, r is the scale and $N(r)$ is the number of the similar graphs.

3.6.2.2 Sample preparation

Small cubical samples 10 mm in length were manually trimmed and freeze-dried following the same procedure as for MIP (section 3.6.1). Afterwards, in order to be observed with FESEM, samples were made conductive. This was done by coating them with an extremely thin layer of silver.

3.6.2.3 Test procedure

In most SEM microscopy applications, data is collected over a selected area on the surface of the sample and a two-dimensional image is generated that displays spatial variations in properties, such as chemical characterisation, texture, and orientation of materials. The selected area of the surface can be magnified to different target sizes (up to 6000× in this thesis) to acquire the images required for the experiments.

3.6.3 Particles (Pores) and Cracks Analysis System (PCAS)

3.6.3.1 Description of PCAS

Particle (Pores) and Cracks Analysis System (PCAS) is professional software used to quantify pores and cracks in soil using images. It was developed by Professor Chun Liu from Nanjing University. The software can be used to identify various pores and cracks automatically. Compared to traditional manual methods, image processing has the advantages of simplicity and high efficiency. A detailed description of the software and its applications can be found in Liu et al. (2011 and 2013). Some interesting results are indicated in Figure 3.41.

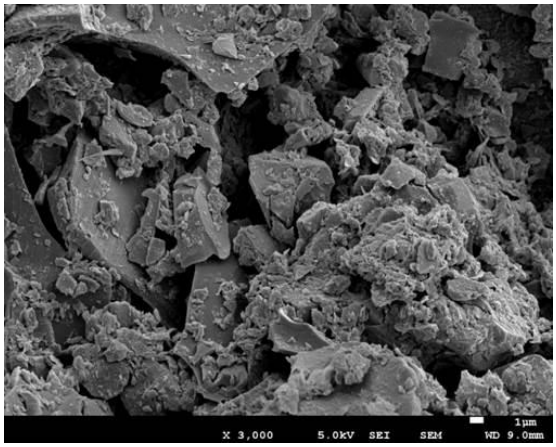

(a)

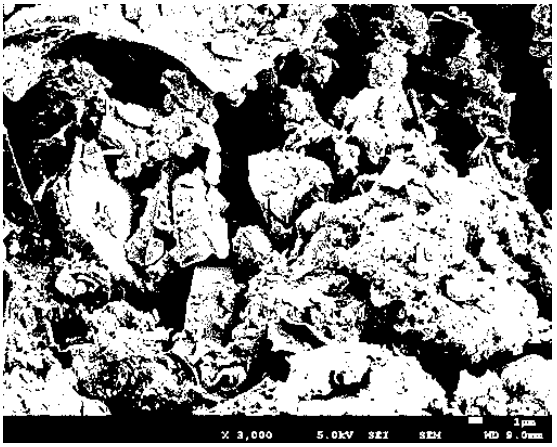

(b)

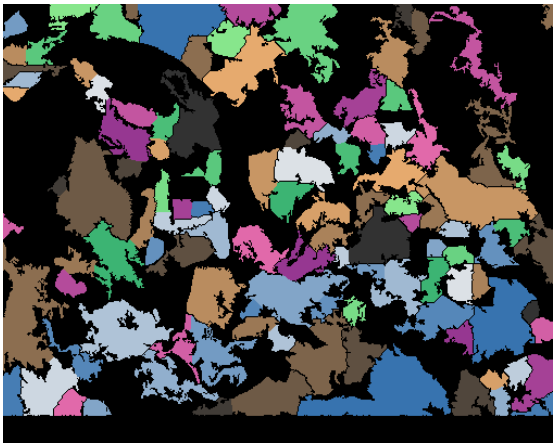

(c)

Figure 3.41 Analysis of sandstone by PCAS: (a) SEM image; (b) segmentation and(c) result

3.6.3.2 Image processing

Once the FESEM images are obtained, the process mainly involves two steps: (1) set thresholds, such as the grey level threshold (T) and the minimum pore area (S_0); and (2) click "Auto Analysis". The image is then processed in the software automatically and all the geometric parameters of the pores and the statistical parameters of the pore system are returned (Liu et al., 2011).

The image segmentation threshold is specified by the human-computer interaction operations. First, an initial large grey-level threshold is used to segment the image. In this case, many soil units are converted to black and regarded as pores. Then, the threshold value is gradually reduced until the soil units in the dark areas, such as those within the pores, are justly transformed to white. Lastly, the threshold around this value is adjusted to distinguish the pores from the soil units. The threshold value is determined using the user's judgement about the interface between the pores and the soil units. The user interface of the PCAS software is presented in Figure 3.42.

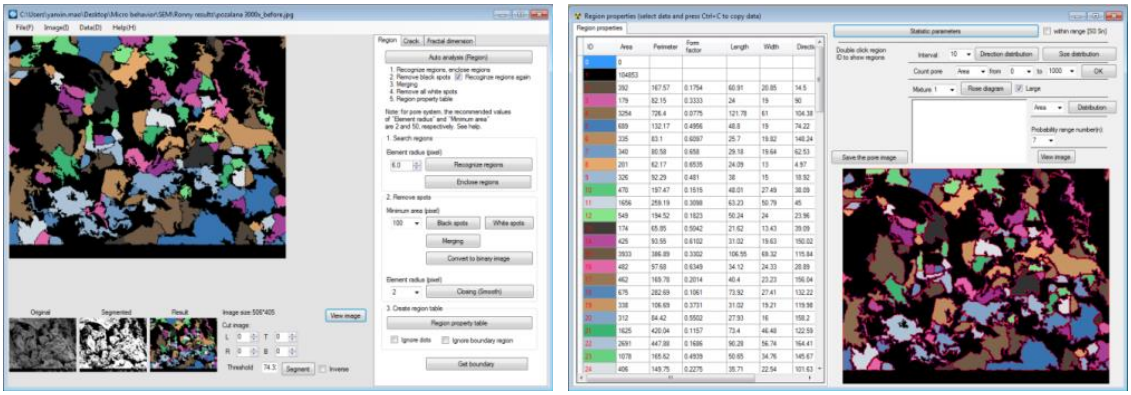

(a) (b)

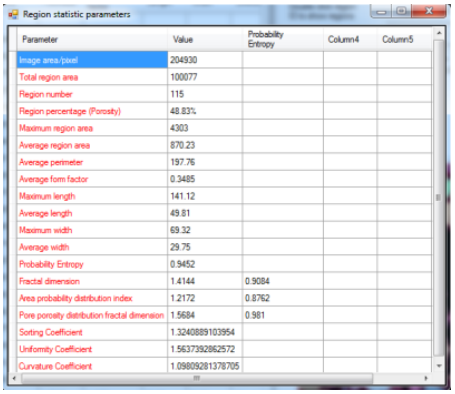

(c)

Figure 3.42 UI of PCAS: (a) image segmentation process, (b) data analysis and (c) statistical parameters of the processed image

3.6.4 Experimental program

In this thesis, the samples of Barcelona clayey silt with different stress and temperature paths will be investigated using the three different techniques mentioned above. As shown in Figure 3.38, the samples in the initial stage, after stress path and after stress-temperature path will be studied by MIP and SEM. The SEM results will be analysed automatically by PCAS. The techniques used and details of oedometer tests were introduced in Chapter 3.5.

3.7 Summary

All the equipment, experimental set-ups, and programs performed in this thesis are presented in this chapter. This included the measurement of ice content using EC, dielectric permittivity

and thermal conductivity, ERT monitoring of soil freezing process and its simulation and investigation of soil macro- and microstructure changes during different stress and temperatures paths using oedometer tests, MIP and FESEM tests.

Main highlights of the equipment modification and programs include:

- Building a configuration of cooling bath system, including a cooling machine with antifreeze liquid, a thermostat and a thermally isolated chamber to control the temperature varies from 20 ºC to -15 ºC;
- Developing a new data acquisition program with enough channels that each channel can be used to collect data on both displacement and temperature with different frequency at different time intervals automatically according to preset before the test;
- Modifying data acquisition software/hardware to increase channels for collecting data on thermocouples from previous three to five in order to satisfy the requirement for performing thermal conductivity tests;
- Modifying a set-up for measuring the thermal conductivity of soil to increase the thermal isolation of specimen during the test, to keep sand specimen non-deformed and to adapt both unfrozen and frozen soil conditions;
- Developing a new cylindrical ERT cell with 16 electrodes in the inner lateral wall, a freezing tube in the center of the specimen and thermally isolated polyethylene surrounding the whole cell to perform the freezing ERT tests;
- Modifying a set-up for performing temperature controlled oedometer tests including drying air by LiCl chamber when applying compressed air to oedometer cell, covering the connection point between LVDT and upper piston by PVC with polyethylene in case that the condensed vapor affects the accuracy of displacement measurement, building an independent supporting system for LVDT in case that expansion and contraction of immersed steel bar in antifreeze liquid induced by freezing and thawing affect the accuracy of displacement measurement.

Chapter 4 Exploring ice formation and migration in partially frozen soils

4.1 Preface

Ice content and its migration process have not been extensively studied in partially saturated soils (Liu and Si, 2011; Zhou et al., 2014), despite having important practical applications for the geocomposite capillary barriers used to reduce frost heaving in soils, for AGF in partially saturated soils and for engineered barriers that are subjected to the freezing and thawing process.

When dealing with the modelling of THM coupled processes induced by the freezing of saturated and unsaturated soils, an important issue is the definition of the freezing retention model, which links the saturation degree of the liquid phase (unfrozen water) to the temperature of the soil. The Clausius-Clapeyron-Poynting equation, which governs the condition for equilibrium between the coexisting liquid water and ice phases, together with a modified form of the van Genuchten equation to consider the liquid-ice surface tension is usually adopted to represent this freezing retention model (see for instance, Nishimura et al., 2009; Gens, 2010; Casini et al., 2013 and Casini et al., 2014).

To experimentally validate coupled THM models for frozen soils, cryogenic suction, together with ice content, are important stress variables to determine. Nevertheless, as cryogenic suction is usually difficult to measure directly, experimental efforts have been mainly concentrated on estimating ice content (or inversely, unfrozen water content) and the soil freezing retention curve SFRC.

4.1 Preface

For the direct measurement of ice content in frozen soil, several procedures have been proposed. They include the calorimeter technique (Williams, 1964), gas dilatometry (Koopmans and Miller, 1966; Spaans and Baker, 1995), dielectric spectroscopy (Bittelli et al., 2004), time domain reflectometry (TDR; Patterson and Smith, 1981; Watanabe and Wake, 2009; Mao et al., 2016), nuclear magnetic resonance (Smith and Tice, 1988), heat pulse probe (Liu and Si, 2011) and combined gamma ray attenuation and TDR (Zhou et al., 2014). However, it is still difficult to accurately measure the ice content of frozen soil both directly and indirectly.

At the same time, empirical and theoretical models have been developed to interpret these indirect experimental results and thus better assess the unfrozen water content of a given state of initial water content (volumetric / gravimetric) and temperature (Dillon and Anderson, 1966; Anderson and Tice, 1972; Liu and Yu, 2013; Mu, 2017). However, in most of the previously cited models, the information on porosity and initial degree of water saturation had not been usually considered. Konrad (1990) measured the SFRC of clayey silt at different void ratios, which highlighted the important effects of porosity on the retention properties of unfrozen water.

In this chapter, the ice contents (or unfrozen water content) of fine sand and clayey silt are determined using different measurements, including EC, dielectric permittivity, and thermal conductivity. For the preliminary study, a commercial FDR sensor is used to measure the bulk EC and relative dielectric permittivity of the soil during freezing; a modified Archie's law and a mixing α-model are proposed to interpret and predict the experimental results. To consider the effects of temperature on the measurement of EC, a new electrical setup, which is more accurated, is used instead of the commercial FDR sensor. A setup for measuring thermal conductivity is also used to explore the ice content and a corresponding empirical model is proposed to interpret and predict the measurements. To validate the above three approaches, the SFRCs estimated by combing the Clausius-Clapeyron equation with water retention data on the drying path are compared with using MIP results and experiments.

4.2 A preliminary study with commercial FDR sensor

4.2.1 Introduction

Four phases coexist in unsaturated frozen soils: soil solids, air, unfrozen water, and ice. Due to the several orders of magnitudes larger resistance of soil solids and air compared to unfrozen water, it is assumed that EC is mainly generated in unfrozen water. Therefore, exploring the changes of bulk EC can be used to infer the amount of unfrozen water. The ice content can be also determined using relative dielectric permittivity based on the similarity between soil dry-wetting and the freezing-thawing transition because the dielectric permittivity of ice coincides with those of soil matrices and is close to that of air (Baker et al., 1982; Flerchinger et al., 2006).

A commercial FDR sensor is used to obtain the bulk EC, relative dielectric permittivity, and temperature at this time. Two soils (fine sand and clayey silt) are prepared at different degrees of saturation and dry densities at room temperature. Different target temperatures, which are reached varying freezing rates and controlled with a thermal bath, are used. The equipment is described in Chapter 3 (section 3.3). The temperature at the soil freezing point is regarded as the full water state (no ice generated), while the minimum temperature (-20 °C) is regarded as the maximum ice state (even at this low temperature, some liquid water may be present that contributes to EC). The EC and dielectric permittivity values at the freezing point and at the minimum temperature are used to obtain the parameters of the proposed models. The extension of these models allows estimating ice content in partially saturated soils at different temperatures with known initial porosities and degree of saturations.

4.2.2 Theoretical models

4.2.2.1 Electrical conductivity (EC) model

The relationship between water content and soil bulk EC (or inversely, electrical resistivity) have been investigated by several authors (Kalinski and Kelly, 1993; Fukue et al., 1999; Chen et al., 2007; Muñoz-Castelblanco, 2012), who assumed that three phases existed in

unsaturated soil (solid, air and water) like parallel resistors. Due to the very high electrical resistivity of soil solid and air, the EC of soil takes place through ionic transport in the pore liquid phase (Fukue et al., 1999; Muñoz-Castelblanco, 2012). Archie (1942) proposed a simple empirical model to describe the relationship between EC and porosity of saturated soils, in cases where there is unknown information about the pore configuration. When it is extended to unsaturated soils, it can be written as (Hauck, 2002; Mao et al., 2016):

$$\sigma^{(l)} = a_l^{-1}\sigma_l n^{m_l} S_l^{p_l} \tag{4.1}$$

$$\sigma^{(i)} = a_i^{-1}\sigma_i n^{m_i} S_r^{p_i} \tag{4.2}$$

Equation (4.1) denotes the electrical conduction of soil in the unfrozen state, where $\sigma^{(l)}$ is the total EC of the soil, σ_l represents the EC of interstitial water, n is the porosity, S_r (and S_l) is the initial degree of water saturation, m_l is an exponent that can be related to soil structure, p_l is a saturation exponent and a_l is a tortuosity factor. Equation (4.2) indicates the situation of maximum frozen state (close to full frozen state with some unfrozen liquid contributing to EC); the volume change of water to ice is ignored and porosity is assumed to be constant during the freezing process. The values of parameters a_i , m_i and p_i in Equation (4.2) are expected to be different compared to Equation (4.1) because of phase change and the different tortuosity paths expected when ice and water are present.

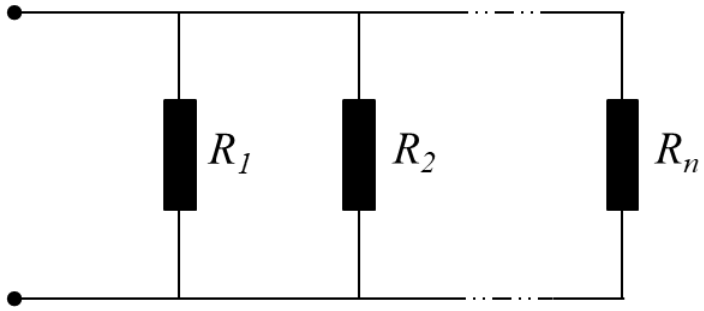

Figure 4.1 Schematic of parallel resistance

In accordance with a parallel configuration presented in Figure 4.1, the total current is the sum of the currents throughout the individual components. The equation can be described as:

$$\frac{1}{R_t} = \frac{1}{R_1} + \frac{1}{R_2} + \cdots + \frac{1}{R_n} \tag{4.3}$$

In unsaturated frozen soils, both the unfrozen water and the ice (with some unfrozen liquid) are regarded as conductive mediums; thus, the total soil EC can be expressed in an additive way as:

$$\sigma = \sigma^{(l)} + \sigma^{(i)} = a_l^{-1}\sigma_l n^{m_l} S_l^{p_l} + a_i^{-1}\sigma_i n^{m_i} S_r^{p_i} \tag{4.4}$$

where the degree of unfrozen water saturation S_l ranges from the initial degree of water saturation S_r to nearly zero during freezing.

In Equation (4.4), the parameters σ_l and σ_i can be measured in pure water at a temperature close to the freezing point and -20 °C, respectively. The other unknown parameters can be estimated by fitting the measurements of soil EC tests at the unfrozen state (close to freezing point) and at the maximum frozen state (-20 °C) under known initial porosity *n* and initial degree of water saturation S_r. When nearly all the interstitial water changes from the liquid state to the ice state during the freezing process, the EC of soil will not become zero because of salinity (and some remaining unfrozen liquid) and the minimum value equals to Equation (4.2). The extended Equation (4.4) can be used to describe the total EC of general coexisting four-phase frozen soil.

It could be argued that there might be some problem with the parallel resistor approach. If only one phase is present, either liquid water or ice (with some unfrozen water), this will be predominantly stacked onto the solid phase. Nevertheless, when both phases are coexisting, the ice could be ‘external’ to the liquid, which is also ‘external’ to the solid. Thus, the tortuosity path of the ice will change, and Archie’s exponent of the contribution to electrical conductivity will change as well during the freezing process. Despite this issue, the parallel configuration was considered valid for the interpretation of the results with the coexistence of unfrozen liquid and ice.

4.2.2.2 Dielectric permittivity model

There are two approaches that allow for calculating the soil water content from dielectric permittivity measurements: empirical and theoretical. The most popular empirical calibration curve was given by Topp et al. (1980) and the dielectric mixing model is a theoretical model proposed by de Loor (1964) and used by Dobson et al. (1985), Dirksen and Dasberg (1993) and Wilczek et al. (2011). The theoretical dielectric mixing model is adopted in this work, which is generally presented as follows (Wilczek et al., 2011):

$$\varepsilon^{\alpha} = \sum_{i} V_i \varepsilon_i^{\alpha} \tag{4.5}$$

where V_i is the volume fraction of i-th phase, ε_i is the dielectric permittivity of this phase and α is a model parameter.

If the bound water is considered, the four-phase dielectric mixing α-model (Dobson et al., 1985; Wilczek et al., 2011) has the following form:

$$\varepsilon^{\alpha} = (1-n)\varepsilon_s^{\alpha} + n(1-S_r)\varepsilon_a^{\alpha} + (1-b)nS_r\varepsilon_w^{\alpha} + bnS_r\varepsilon_{bw}^{\alpha} \tag{4.6}$$

where n is porosity, S_r is the degree of water saturation, b represents the fraction of bound water, subscripts "s", "a", "w", and "bw" denote the phases of soil solid, air, free water and bound water, respectively.

For simplicity, a constant model parameter β_l can be introduced to account for the bound water effect, where $\beta_l = \left[1 + b\left(\varepsilon_{bw}^{\alpha} / \varepsilon_w^{\alpha} - 1\right)\right]$. Therefore, the dielectric permittivity of soil at the unfrozen state can be described as:

$$\varepsilon^{(l)} = \left[(1-n)\varepsilon_s^{\alpha} + n(1-S_r)\varepsilon_a^{\alpha} + \beta_l nS_r\varepsilon_w^{\alpha}\right]^{1/\alpha} \tag{4.7}$$

A similar equation that can also be applied to present the dielectric permittivity of maximum frozen soil is

$$\varepsilon^{(i)} = \left[(1-n)\varepsilon_s^{\alpha} + n(1-S_r)\varepsilon_a^{\alpha} + nS_r\varepsilon_i^{\alpha} \right]^{1/\alpha} \tag{4.8}$$

For the condition of water and ice coexisting state in general unsaturated frozen soil, the equation can be extended as:

$$\varepsilon = \left[(1-n)\varepsilon_s^{\alpha} + n(1-S_l-S_i)\varepsilon_a^{\alpha} + nS_i\varepsilon_i^{\alpha} + \beta_l nS_l\varepsilon_w^{\alpha} \right]^{1/\alpha} \tag{4.9}$$

where S_l and S_i are the degree of unfrozen water and ice saturation, respectively. For simplicity, the volume change due to the phase transition during freezing is ignored, so that $S_r = S_l + S_i$.

In Equations (4.7) and (4.8), the dielectric permittivity of soil solid, water, ice and air can be measured in pure materials. The model parameters α and β can be obtained by fitting the measurements of soil permittivity tests at the unfrozen state (close to freezing point) and at the maximum frozen state (-20 °C) under known initial porosity *n* and initial degree of water saturation S_r.

Equations (4.4) and (4.9) can be applied to all of the above to estimate the ice amount (or unfrozen water content), using EC and permittivity measurements, in partially saturated soils at different temperature with known void ratio and initial water saturation degree, with $S_l < 1$ and $S_i < 1$.

4.2.3 Test results and analyses

4.2.3.1 Measurements of bulk EC and dielectric permittivity

The evolutions of bulk EC and permittivity of a sand sample during freezing and thawing are shown in Figure 4.2 (a) and 4.2 (b). It can be seen that the readings for bulk EC and (relative) dielectric permittivity in soil unfrozen state are tightly temperature-dependent. A temperature increased in the soil will cause an increase in ion mobility and a decrease in solution viscosity (Hayashi, 2003; Barron and Ashton, 2005). In the frozen state, the solution has been partially frozen; thus, the decrease of bulk EC and permittivity are mainly related to the phase change from water to ice. The freezing point of soil is -3.2 °C due to pore water salinity effects. For

simplicity, the temperature effect and the volume change during freezing have not been considered.

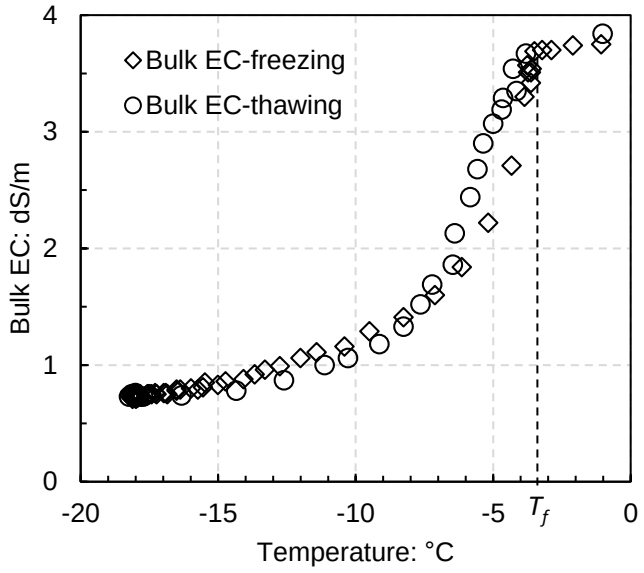

(a)

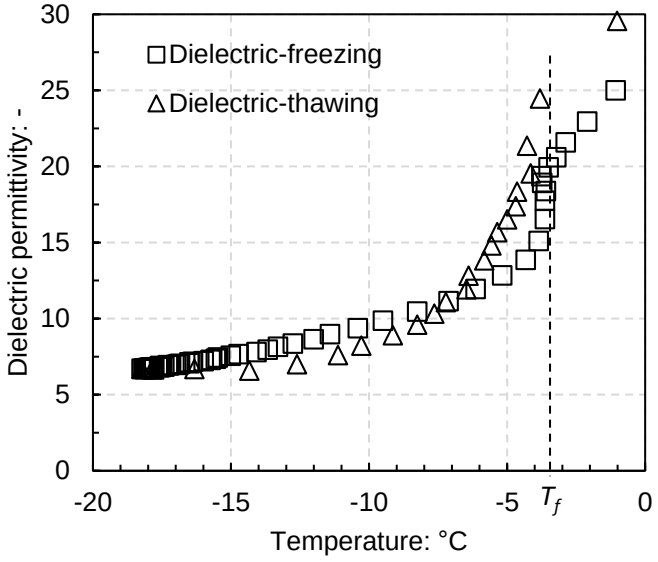

(b)

Figure 4.2 Evolution of (a) bulk EC and (b) permittivity during a freezing-thawing cycle of a sand sample (n = 0.49, S_l = 32.86%).

The two soils with different initial saturation degrees and dry densities are tested during a freezing-thawing cycle to log the readings for both bulk EC and permittivity at the unfrozen state S_i = 0, close to freezing point (-3.2 °C) and at maximum frozen state $S_l \approx 0$ (-20 °C) with still some unfrozen liquid, as shown in Figure 4.3. As only the beginning and ending measurements of the freezing process are needed, a quick-freezing rate was performed; it was approximately -0.12 °C/min. In order to understand easily and clearly, only freezing processes are presented. In total, 15 fine sand and 12 clayey silt samples have been tested. Some selected physical characteristics are listed in Table 4.1. It can be observed that the porosity of sand is around n=0.46, with major variations in the degree of water saturation. This is not the case with the clayey silt samples, in which the amount of water added affects the fabric and porosities (the porosities change from 0.31 to 0.51).

Table 4.1 Selected physical characteristics of tested samples

Sample	Dry density ρ_d / Mg/m^3	Porosity n / -	Initial degree of saturation S_r / %	Void ratio e
Castelldefels sand				
1	1.37	0.48	23.2	0.93
2	1.38	0.48	23.9	0.93
3	1.36	0.49	32.9	0.94
4	1.41	0.47	34.2	0.88
5	1.47	0.45	34.9	0.81
6	1.40	0.47	36.9	0.89
7	1.46	0.45	41.7	0.81
8	1.44	0.46	41.7	0.84
9	1.40	0.47	42.9	0.89
10	1.45	0.45	48.9	0.83
11	1.44	0.46	51.7	0.84
12	1.47	0.45	57.6	0.80
13	1.47	0.45	64.6	0.80
14	1.48	0.44	76.0	0.79
BCN clayey silt				
15	1.29	0.51	25.6	1.05
16	1.41	0.47	35.7	0.89
17	1.53	0.42	45.8	0.73
18	1.61	0.39	47.1	0.65

19	1.53	0.42	47.9	0.73
20	1.56	0.41	50.7	0.70
21	1.63	0.38	52.0	0.62
22	1.70	0.36	56.3	0.56
23	1.82	0.31	70.3	0.46
24	1.81	0.32	70.3	0.46
25	1.79	0.32	79.2	0.48
26	1.83	0.31	89.3	0.45

4.2.3.2 Analysis and curve fitting

Archie's second law has been used to fit the bulk EC readings for the two unsaturated soils and thereby to obtain the model parameters. The bulk EC values of the pure 5% NaCl solution at the maximum ice (-20 °C with some unfrozen liquid) and unfrozen liquid (-3.2 °C) states have been measured; those are σ_i = 8.44 dS/m and σ_l = 37.88 dS/m, respectively. As shown in Figure 4.3 (a) and 4.3 (b), Archie's second law can fit the experimental results quite well. The 1:1 scatters plot of the calculated values and measured values of bulk EC and permittivity are presented in Figure 4.4 (a) and 4.4 (b). The equation used to estimate the ice content of the partially saturated fine sand from the bulk EC readings is:

$$\sigma_{sand} = 119.12 n^{1.54} S_l^{2.0} + 20.39 n^{1.56} S_i^{1.7} \tag{4.10}$$

The equivalent expression for estimating ice content from the bulk EC readings for the clayey silt is:

$$\sigma_{silt} = 45.00 n^{0.90} S_l^{2.4} + 5.59 n^{0.86} S_i^{2.0} \tag{4.11}$$

As observed, the respective constants in these expressions affecting the unfrozen liquid are higher than σ_l=37.88 dS/m, whereas the constants linked to ice are higher (sand) and lower (clayey silt) compared to σ_i=37.88 dS/m. This seems to indicate a parameter a (linked to tortuosity) higher than 1 for the electrolyte close to the freezing point. In addition, an exponent m affecting the porosity lower than 1 has been obtained for the silty material

(exponent *m* is usually between 1.8 and 1.9). Despite these inconsistencies, which deviate from a clear physical meaning, it was preferred to keep the original fitted values.

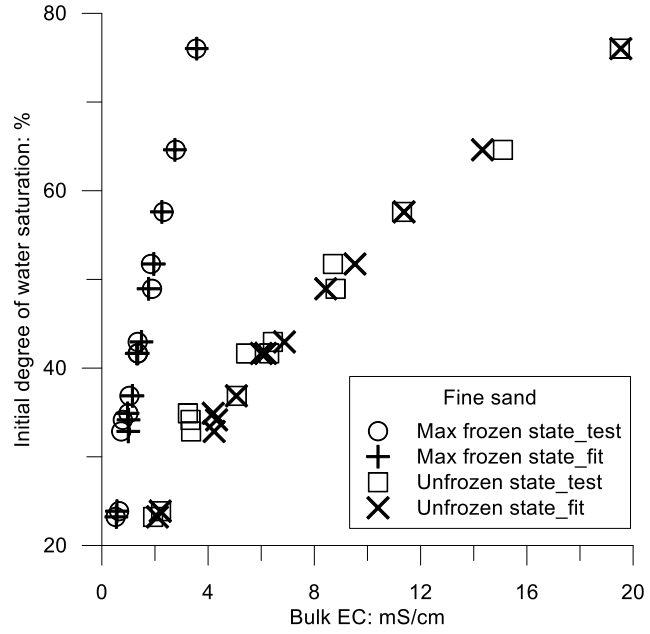

(a)

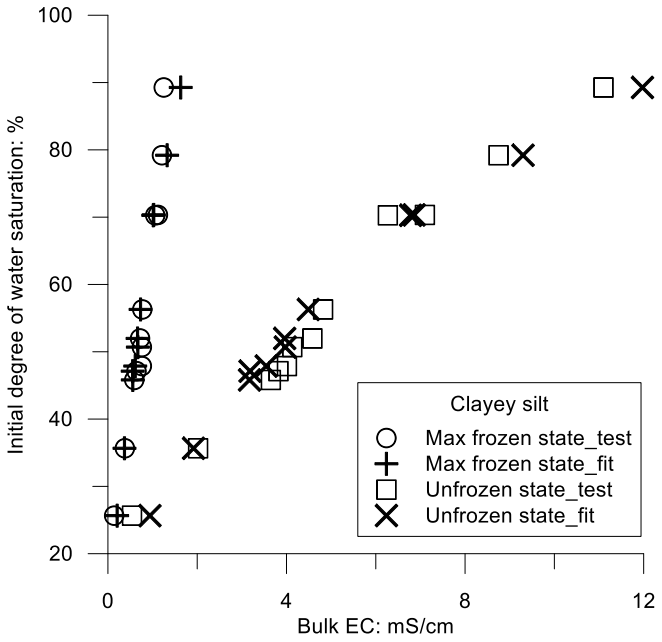

(b)

Figure 4.3 Bulk EC results for soils with different initial saturation degrees at both unfrozen state and maximum frozen state: (a) sand and (b) clayey silt

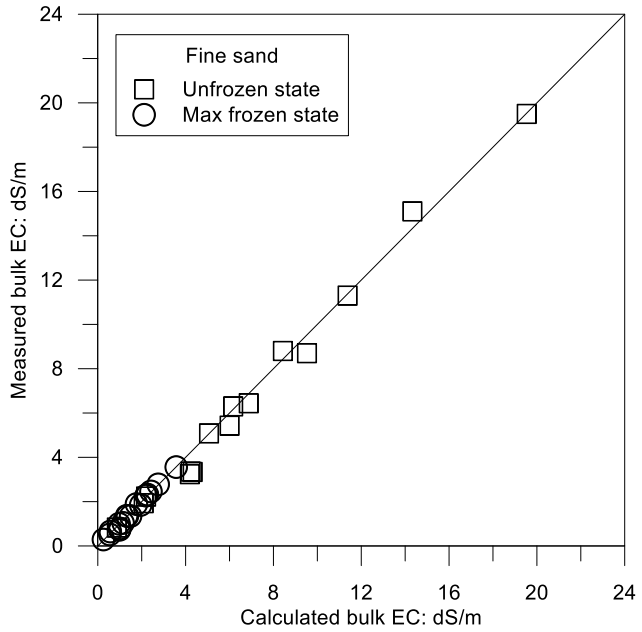

(a)

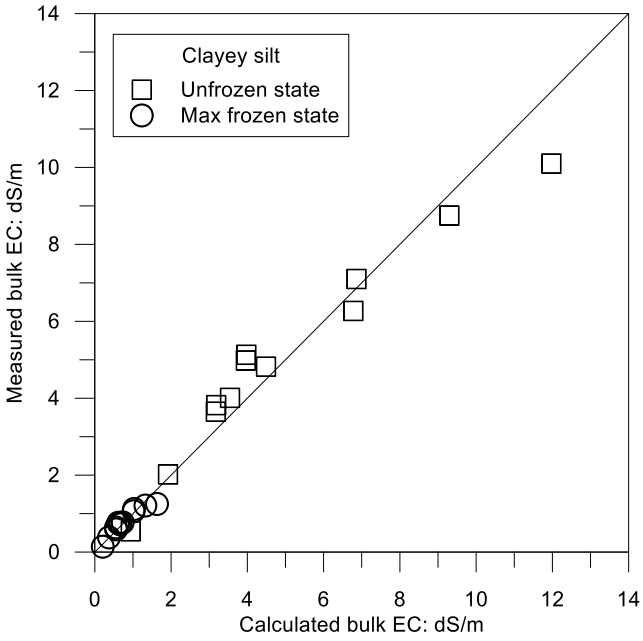

(b)

Figure 4.4 The 1:1 scatter plot of calculated vs measured bulk EC (a) fine sand and (b) clayey silt

The dielectric mixing α-model has been used to fit the permittivity measurements for the two unsaturated soils and thus to estimate the model parameters. The permittivity values of the

pure 5% NaCl solution at the maximum ice (-20 °C) and full unfrozen liquid (-3.2 °C) states are ε_i = 66.0 and ε_l = 195.0, respectively. High relative permittivity values have been measured due to important effects of frequency and EC (see Figures 2.2 and 2.3). The details of the interpretation can be found in Maeno et al. (1992), Thompson et al. (2007), Skierucha and Wilczek (2010), and Gong et al. (2013). As shown in Figure 4.5 (a) and 4.5 (b), the dielectric mixing α-model can fit the experimental results appropriately. The 1:1 scatter plots of calculated and measured relative dielectric permittivity are shown in Figure 4.6 (a) and 4.6 (b).

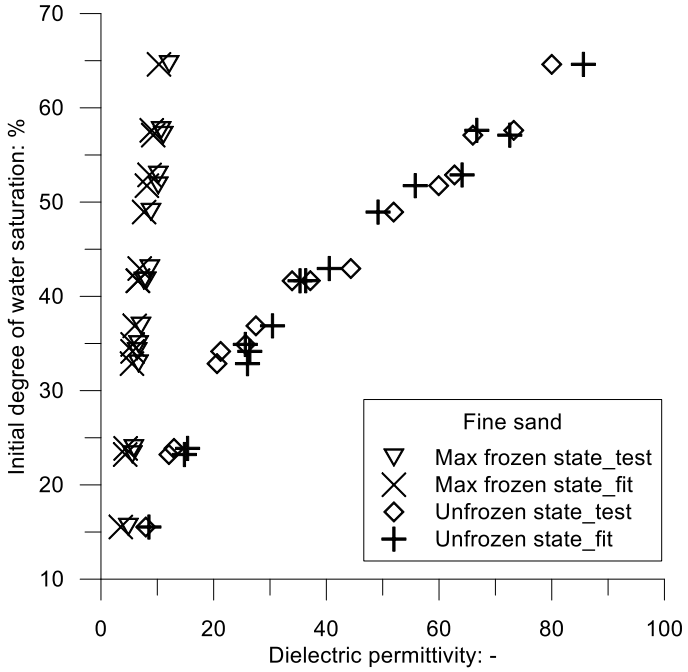

(a)

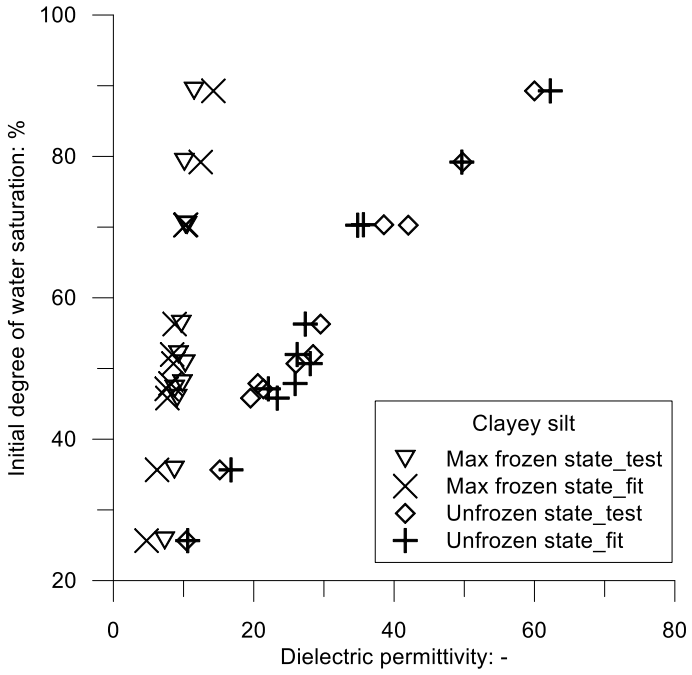

(b)

Figure 4.5 Permittivity results for soils with different initial saturation degrees at both unfrozen state and maximum frozen state: (a) fine sand and (b) clayey silt.

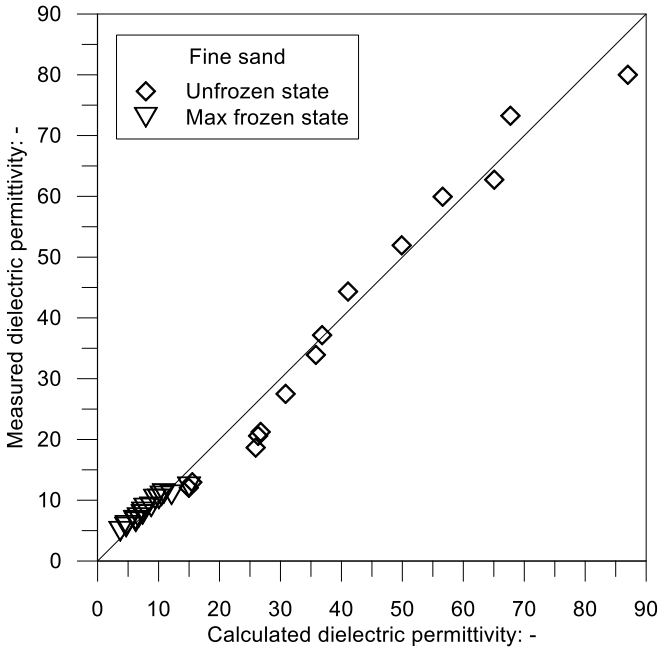

(a)

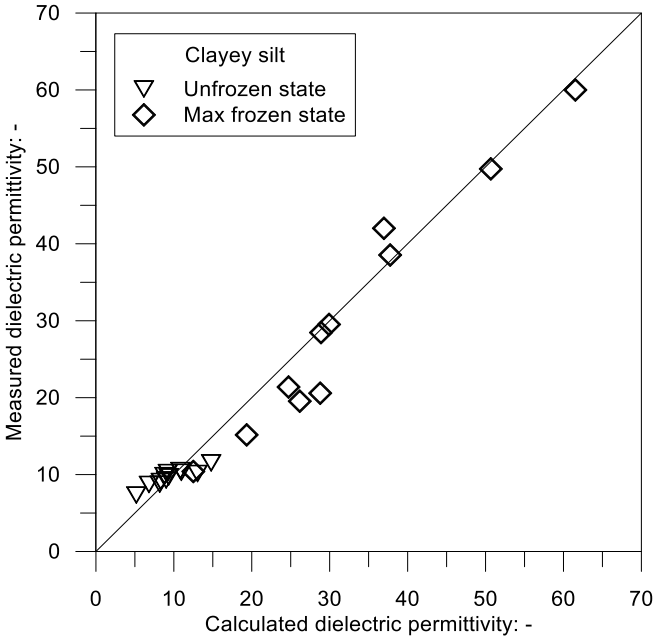

(b)

Figure 4.6 The 1:1 scatter plot of calculated vs measured (relative) dielectric permittivity: (a) fine sand and (b) clayey silt

The expression for estimating ice content in partially saturated sand samples from permittivity measurements is:

$$\varepsilon_{sand} = \left(8.73nS_l + 2.51nS_i - 0.52n + 1.52\right)^{3.33} \tag{4.12}$$

The corresponding expression for clayey silt is:

$$\varepsilon_{silt} = \left(1.47nS_l + 0.73nS_i - 0.15n + 1.15\right)^{10} \tag{4.13}$$

4.2.3.3 Verification of proposed models

To verify the proposed models, two experiments have been performed on the sand and clayey silt samples. Bulk EC and permittivity are measured at the same time in one sample during the slow freezing process (about -0.03 °C/min; see Figure 4.7 (a) and (b)). The ice amount at different temperatures is calculated by using the equations proposed above separately; see Figure 4.8, (a) and (b).

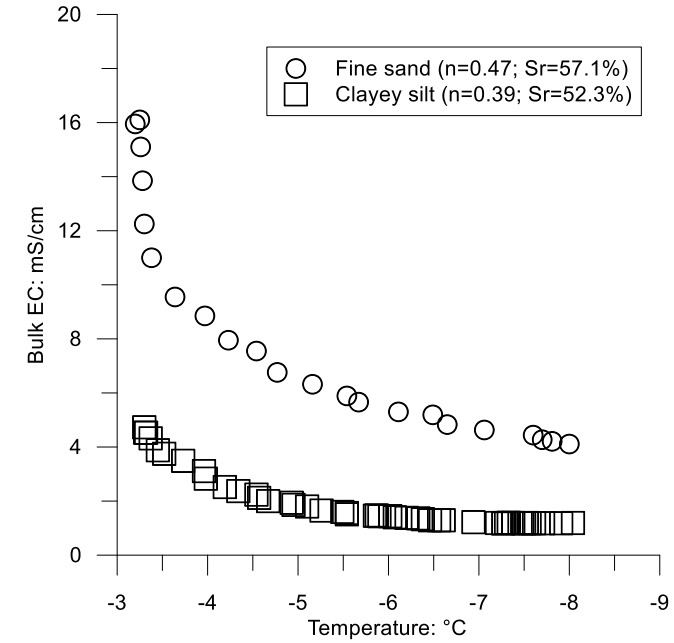

(a)

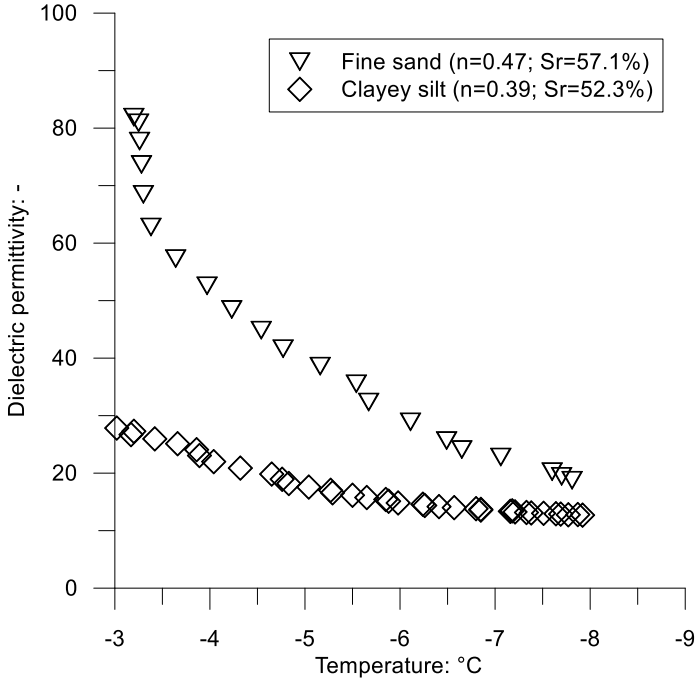

(b)

Figure 4.7 Measurements of bulk EC and permittivity in both fine sand and clayey silt samples at the same time during freezing: (a) bulk EC and (b) permittivity

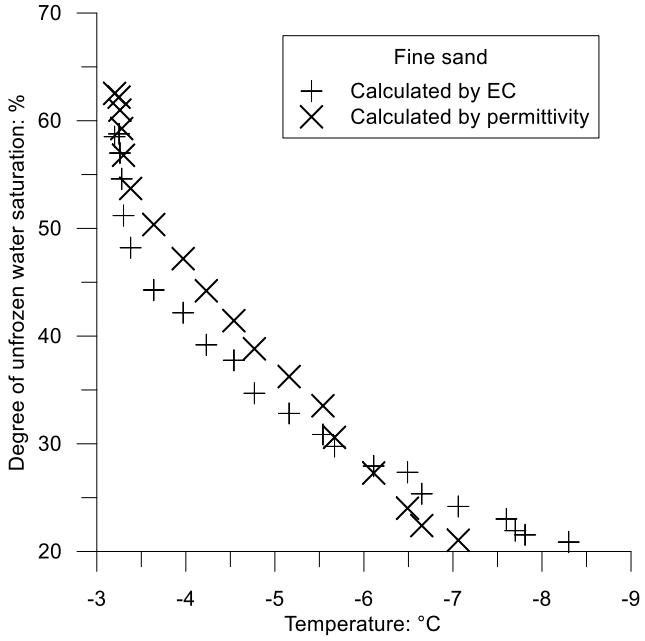

(a)

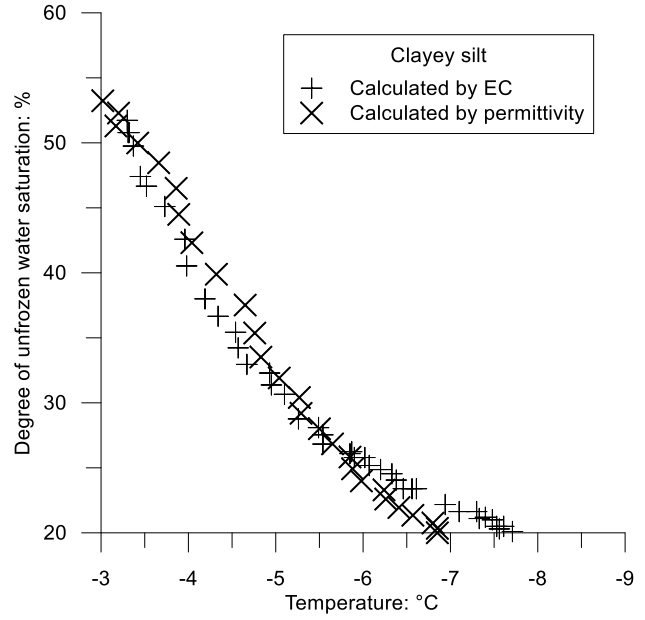

(b)

Figure 4.8 Validation of proposed models: (a) fine sand and (b) clayey silt.

It can be seen that the calculations between bulk EC and permittivity have a good consistency (despite the issues commented above) for degrees of unfrozen water saturation greater than 20%, in both the fine sand and clayey silt samples. Therefore, the proposed methods can be used with a commercial FDR to infer the ice amount (or unfrozen water content) of partially

saturated soils (for relatively high saturation samples) at known porosity and initial degrees of water saturation. The estimated results from bulk EC and permittivity at the lower saturation part (less than 20%) are more difficult to estimate.

4.2.3.4 Variations of unfrozen water saturation during freezing

The variations of unfrozen water saturation during the freezing process (with a slow rate of freezing), estimated using the permittivity measurements, for both fine sand and clayey silt are shown in Figure 4.9, which includes different samples with different porosities and initial degrees of water saturation. For easier comparison with measured results performed in natural soils by other authors (Fortier et al., 1996; Zhu and Carbee, 1987), the freezing point changes have been considered.

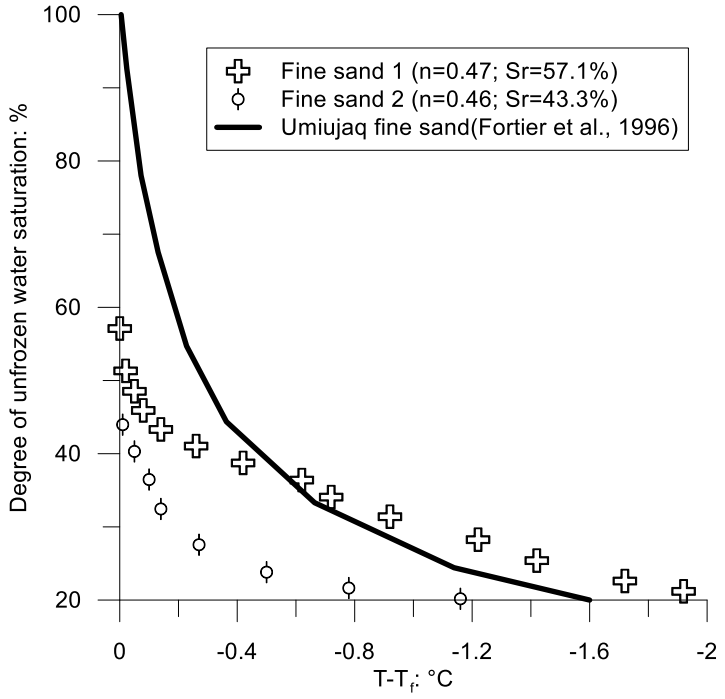

(a)

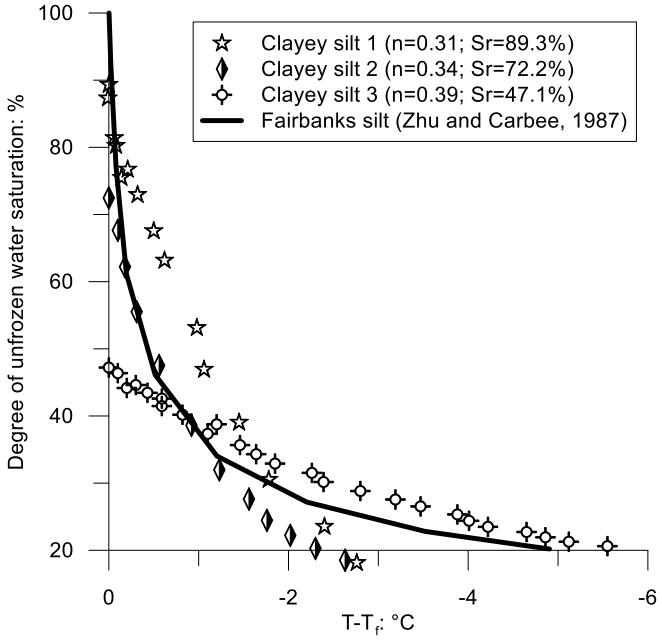

(b)

Figure 4.9 Variations of unfrozen water saturation during freezing process (estimated from permittivity measurements): (a) fine sand and (b) clayey silt

For the sand samples, the estimated results are similar to the results measured in Umiujaq fine sand by Fortier et al. (1996) using the field calorimetric method. For the clayey silt samples, it is interesting to note that even the estimated results are similar to measured results in Fairbanks silt by Zhu and Carbee (1987), but clayey silt sample 1, with lower water saturation and larger porosity, has a slower freezing efficiency, which may be due to some microstructural effects of silt. In addition, the general temperature gradient and salinity changes have an important influence on the growth of pore ice in the soil. (Arenson and Sego, 2006).

4.3 New interpretation proposal with new EC sensor

4.3.1 Introduction

In this section, the temperature dependence of EC is studied both at the phase change stage (liquid and ice: -3.2 °C~-15 °C) and the non-phase change stage with liquid (20 °C~-3.2 °C). The maximum value of EC that can be measured by the commercial FDR is 23.1 dS/m, which

is not enough for the soil samples with higher water saturation or for pure solutions. A new setup shown in Section 3.4 (see Figure 3.26 (a)) is used to perform EC tests on partially saturated frozen fine sand and clayey silt samples.

A modified Archie's second law that takes into consideration temperature dependence properties has been used to describe the relationship between the soil bulk EC and the temperature, porosity, and degree of unfrozen water saturation. Fine sand and clayey silt have been prepared at different target void ratios and degrees of saturation and are immersed in a cooling bath up to -15 °C. Measurements of bulk EC along the freezing paths have been used to calibrate parameters associated with the model described below. These calibrated models thus allow for determining the amount of ice content for a given state of the partially saturated soil (porosity, initial degree of water saturation and temperature).

4.3.2 Theoretical model

A 5% NaCl solution (mass basis) is used as interstitial water instead of pure water to better differentiate the EC values of ice and unfrozen water. Figure 4.10 shows EC values of the solution along the temperature decrease and freezing paths. A clear dependence on temperature is observed because of changes in ionic mobility and solution viscosity. It is interesting to note that the relationship between EC and temperature in the unfrozen state (without phase change) is linear but changes to nonlinear when below freezing point because of ice generation. The freezing point of 5% NaCl solution is around -3.2 °C, calculated from Blagden's law for dilute solutions.

A different assumption is considered in the model. It is assumed that only the liquid phase is contributing to EC in a parallel conductance concept since the EC value in pure ice is approximately three orders of magnitude lower than in liquid water (ionic mobility is restricted by ice lattice). The electrical conductivity of the solid phase is considered negligible in soils with the moderate specific surface, as in the previous model.

For the linear part above the freezing point, a simple equation can be used to fit the EC data of the solution with temperature:

$$\sigma_T(T) = aT + b \tag{4.14}$$

where σ_T is the EC of the solution along the temperature evolution (dS/m) and T is the temperature (°C). The fitted values of a and b are 1.32 and 42.45, respectively.

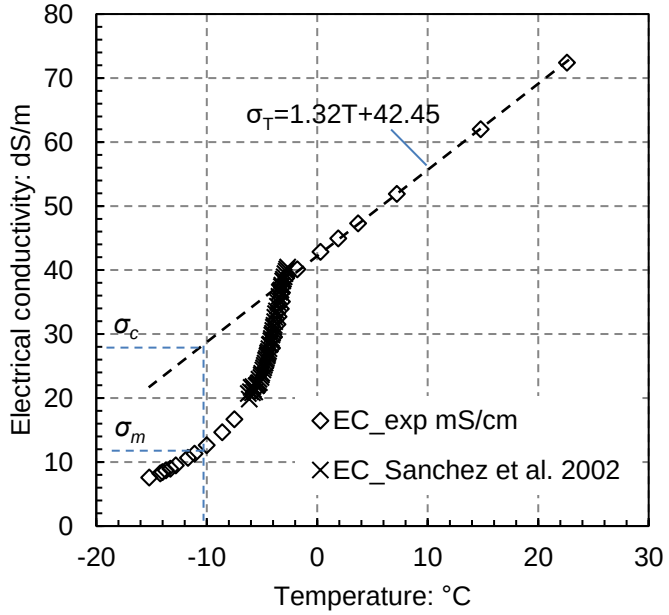

Figure 4.10 EC values of pure 5% NaCl solution along with temperature path (including results from Sanchez et al., 2002)

In the frozen branch of the curve, the difference in EC between extrapolated (linear extrapolation) and measured values is associated with ice formation. At the freezing point, the unfrozen water saturation S_l is still equal to 1. At nearly full ice (S_l closed to 0), the measured EC will tend towards zero. Therefore, the following expression can be proposed for S_l:

$$S_l = \frac{\sigma_m}{\sigma_T(T)} \tag{4.15}$$

where σ_m is the measured EC of the ice/liquid solution (dS/m) and σ_T is the extrapolated EC value in the negative temperature range from Equation (4.14).

These values are indicated in Figure 4.10. Results from Sánchez et al. (2002) have been also included in Figure 4.10, in which a good agreement with data from this study can be observed in relation to the evolution of EC with temperature in the freezing zone. The proposed

Equation (4.15) has been partially validated by comparison with the reported results from Sánchez et al. (2002) for ice concentration in 5% NaCl solution (see Figure 4.11). Sánchez et al. (2002) only presented the results on temperature from −3 °C to −6 °C, which has a good agreement with the extrapolated curve. From −6 °C on, only extrapolated results are plotted.

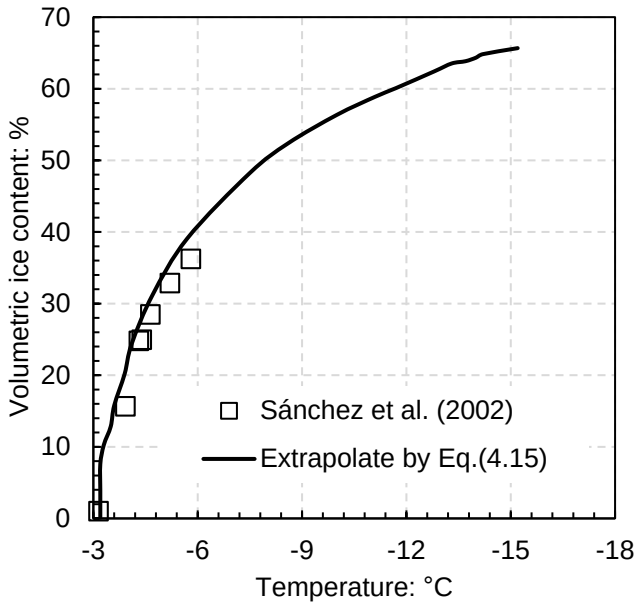

Figure 4.11 Comparison of measured and extrapolated volumetric ice content during freezing

Archie (1942) proposed a simple empirical model to link the bulk EC, σ, of sand and sandstone samples to porosity under saturated conditions. When extended to unsaturated soils, the expression can be written as (Hauck, 2002):

$$\sigma = \sigma_w n^p S_r^q \tag{4.16}$$

where σ_w is the EC of interstitial water, n is the porosity, and S_r is the initial degree of water saturation. p is an exponent that can be related to soil structure (usually between 1.8 and 1.9) and q is a saturation exponent, typically around 2.0.

By considering the temperature dependence of the interstitial water (Equation (4.14)), the bulk EC of the soil (Equation (4.16)) at different temperatures without phase change σ_T^* can be described by:

$$\sigma_T^* = \sigma_T\left(T\right) n^p S_r^q = \left(aT + b\right) n^p S_r^q \tag{4.17}$$

It is assumed that the porosity and the total mass of water (associated with S_r) do not change along the soil freezing and thawing paths. The unfrozen water saturation S_l in partially saturated soils would be similar to Equation (4.15), but using the extended Archie's law and corrected by the initial water saturation S_r, the equation can be rearranged as follows:

$$S_l = S_r \frac{\sigma_m}{\sigma_T^*} = \frac{\sigma_m}{\sigma_T\left(T\right)} n^{-p} S_r^{1-q} \tag{4.18}$$

4.3.3 Test results and analysis

The fine sand samples have been prepared at similar porosities but different water saturations. The clayey silt samples have been statically compacted at different initial degrees of saturation S_r and at different dry densities. Some selected physical properties of fine sand and clayey silt are summarised in Table 4.2.

Table 4.2 Selected physical characteristics of tested soil samples

Sample	Dry density ρ_d / Mg/m^3	Porosity n / -	Initial degree of saturation S_r / -
Fine sand			
1	1.621	0.393	0.531
2	1.621	0.393	0.620
3	1.626	0.391	0.790
4	1.647	0.383	0.772
5	1.615	0.395	0.867
Clayey silt			
1	1.903	0.282	0.730
2	1.921	0.275	1.000
3	1.874	0.293	0.859
4	1.683	0.365	0.500
5	1.503	0.433	0.239

The bulk EC of the fine sand and clayey silt samples has been measured along a temperature decrease and freezing path (from 20 °C to −15 °C). Figure 4.12 (a) shows the evolution of the bulk EC of the five fine sand samples along the temperature decrease path without phase change. Linear variations of the bulk EC with temperature are obtained, which are consistent with previous results for the interstitial water. It is a consequence of the very low EC of the mineral particles (primarily based on electron movement) relative to the EC of the electrolyte

(based on ionic movement). Figure 4.12 (b) presents the bulk EC drop of the different samples associated with the freezing stage.

Equation (4.17) is used to fit test results without phase change in Figure 4.12 (a). The 1:1 scatter plot of measured bulk EC values vs calculated EC values is presented in Figure 4.13, which displays an adequate agreement. The fitted model parameters are p = 1.65 and q = 1.86, which agree relatively well with the usual values adopted for Archie's law.

A detailed derivation and validation of Equation (4.18) are explained in Appendix A. Thus, the unfrozen water saturation in the partially saturated fine sand can be obtained with:

$$S_l = \frac{\sigma_m n^{-1.65} S_r^{-0.86}}{aT + b} \tag{4.19}$$

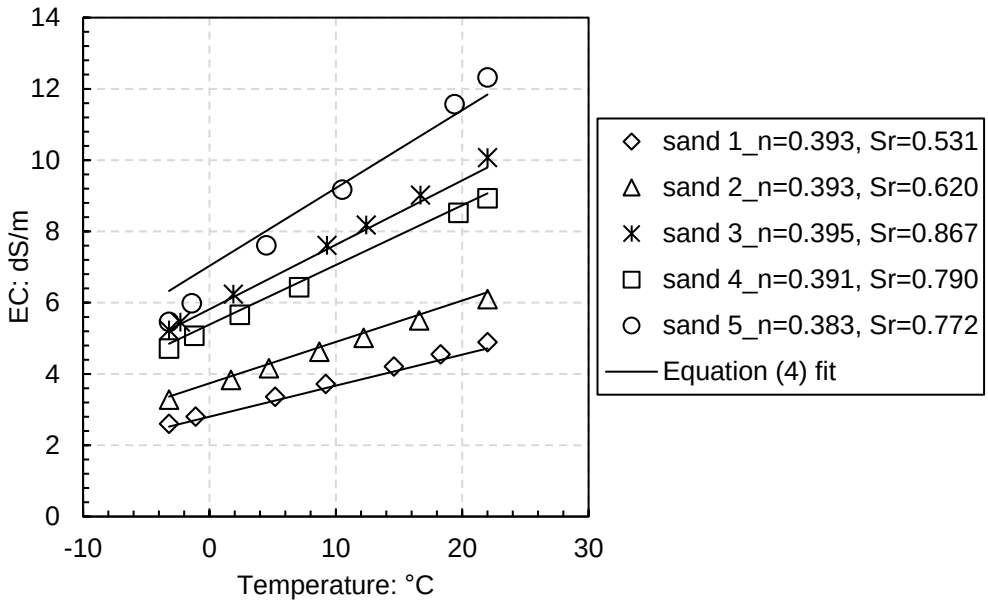

(a)

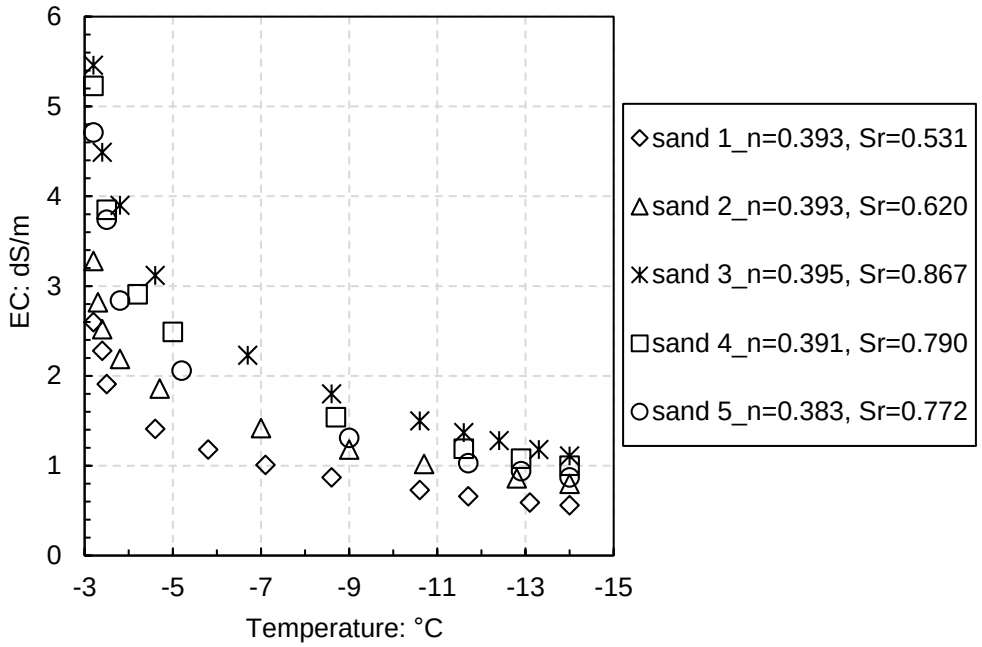

(b)

Figure 4.12 Bulk EC changes of fine sand along the temperature decrease and freezing paths: (a) above freezing point and (b) below the freezing point

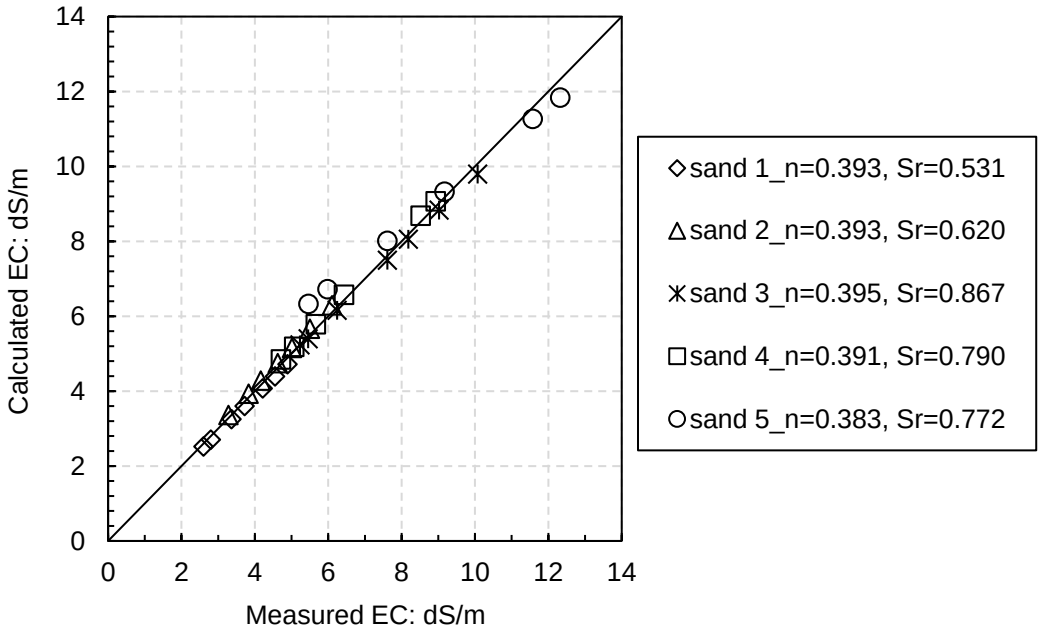

Figure 4.13 The 1:1 scatter plot of measured EC vs calculated EC of fine sand along the temperature decrease path without phase change

Equation (4.17) is also used to fit test results of clayey silt without phase change in Figure 4.14 (a). The 1:1 scatter plot of measured bulk EC values and calculated EC values is presented in Figure 4.15, which displays an adequate agreement. The fitted model parameters are p = 1.85 and q = 2.08, which agree well with the usual values adopted for Archie's law.

Thus, the unfrozen water saturation in the partially saturated clayey silt can be obtained with:

$$S_l = \frac{\sigma_m n^{-1.85} S_r^{-1.08}}{aT + b} \tag{4.20}$$

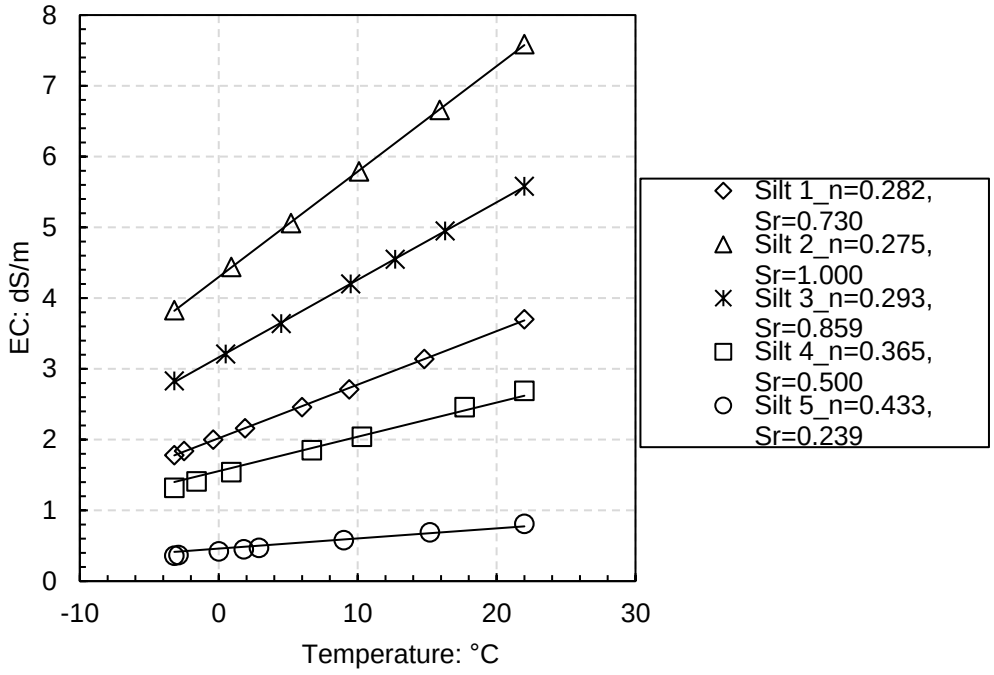

(a)

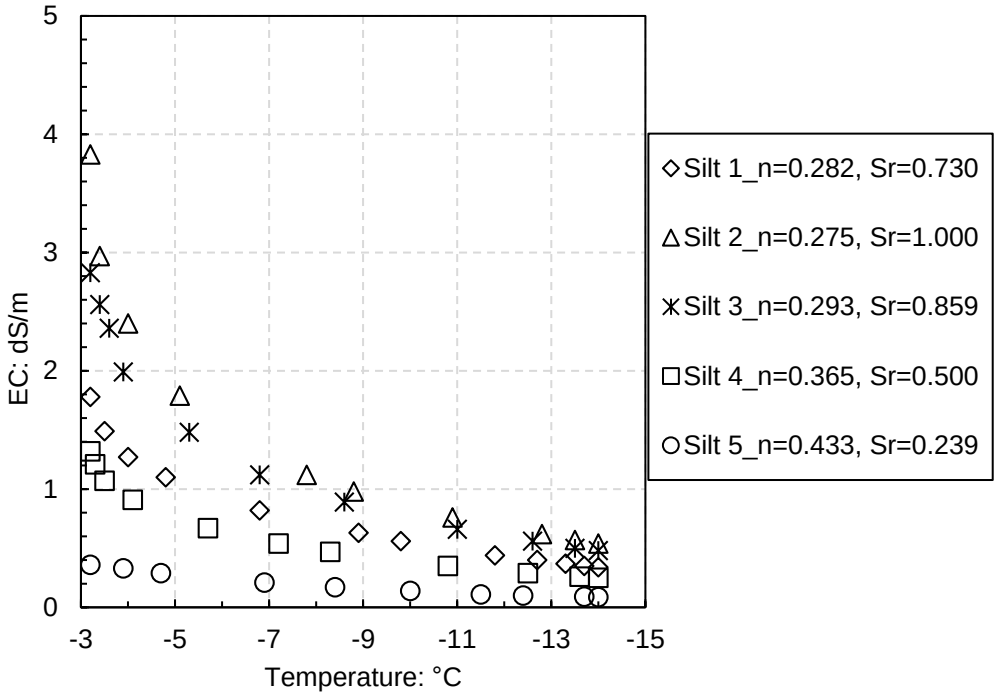

(b)

Figure 4.14 Bulk EC changes of clayey silt along the temperature decrease and freezing paths: (a) above freezing point and (b) below the freezing point

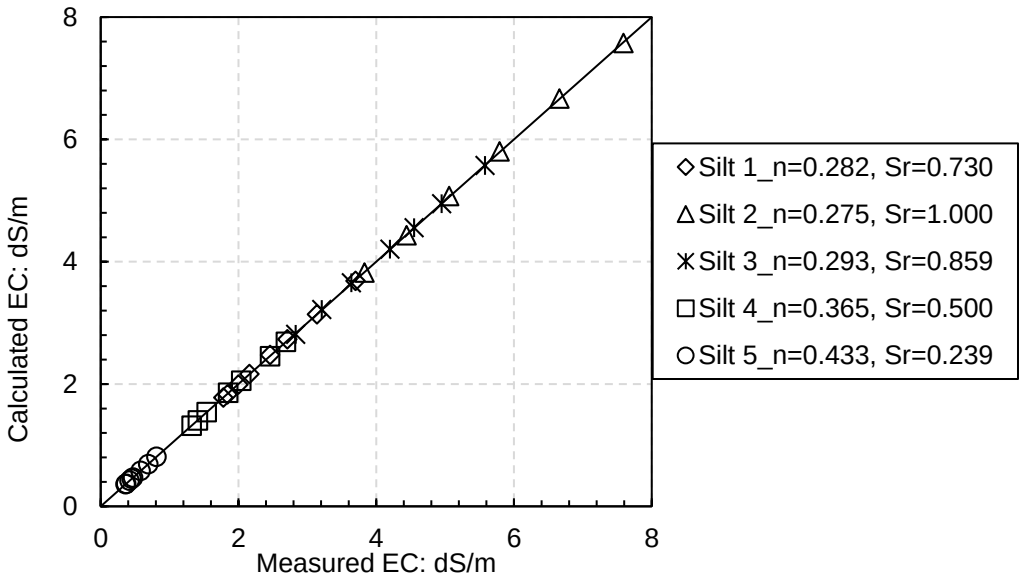

Figure 4.15 The 1:1 scatter plot of measured EC vs calculated EC of clayey silt along the temperature decrease path without phase change

The evolution of the unfrozen water saturation with the temperature of the five fine sand and five clayey silt samples are plotted in Figure 4.16 (a) and (b), respectively. Ice formation starts at around −3.2 °C due to salinity effects. In the beginning, ice generates quite fast with small temperature drops. And that the fine sand has a faster freezing rate than clayey silt due to the lower suction of fine sand than clayey silt. Nevertheless, at temperatures below −7 ºC, the evolutions of the unfrozen water saturation of the soil samples tend to converge to a residual value despite starting from different initial degrees of saturation. When compared to published results on natural frozen clayey silts with a lower salinity of the interstitial water, the current results tend to display higher unfrozen water saturations at the specified temperatures. Salinity not only affects the freezing point but also the residual unfrozen water content (Watanabe and Mizoguchi, 2002; Xiao et al., 2018). This observation justifies the first model used with the commercial FDR since some remaining bulk EC was considered under maximum ice content (some unfrozen liquid is still expected at this state).

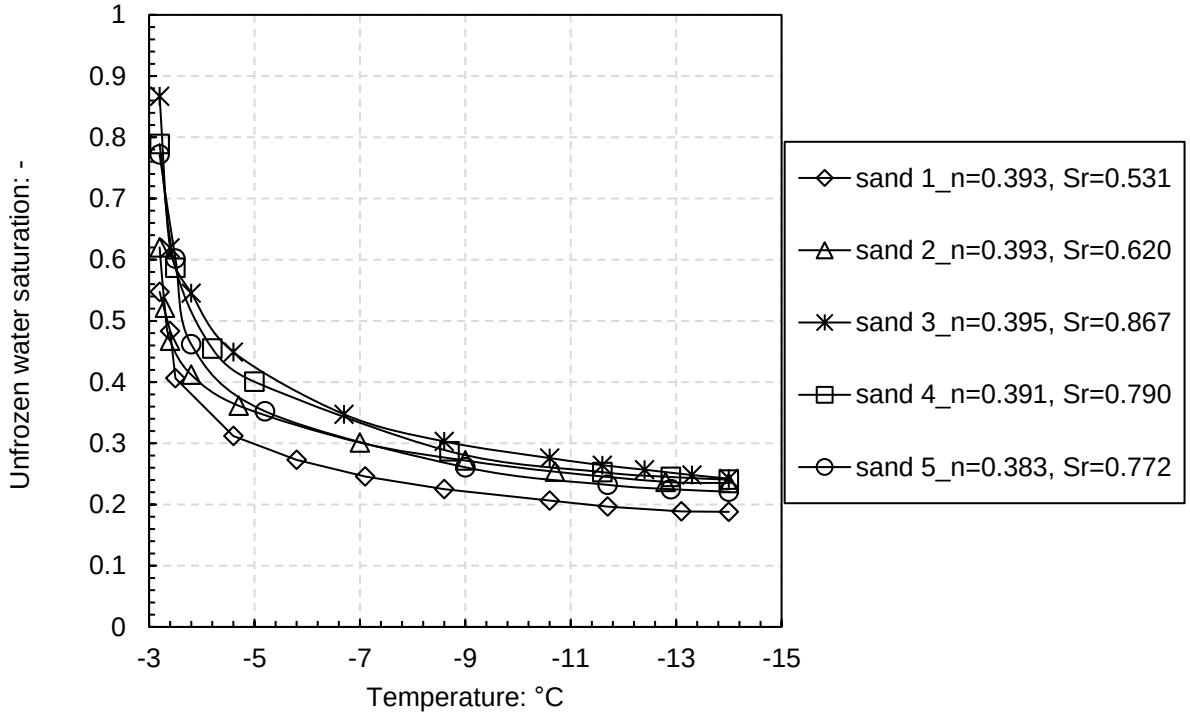

(a)

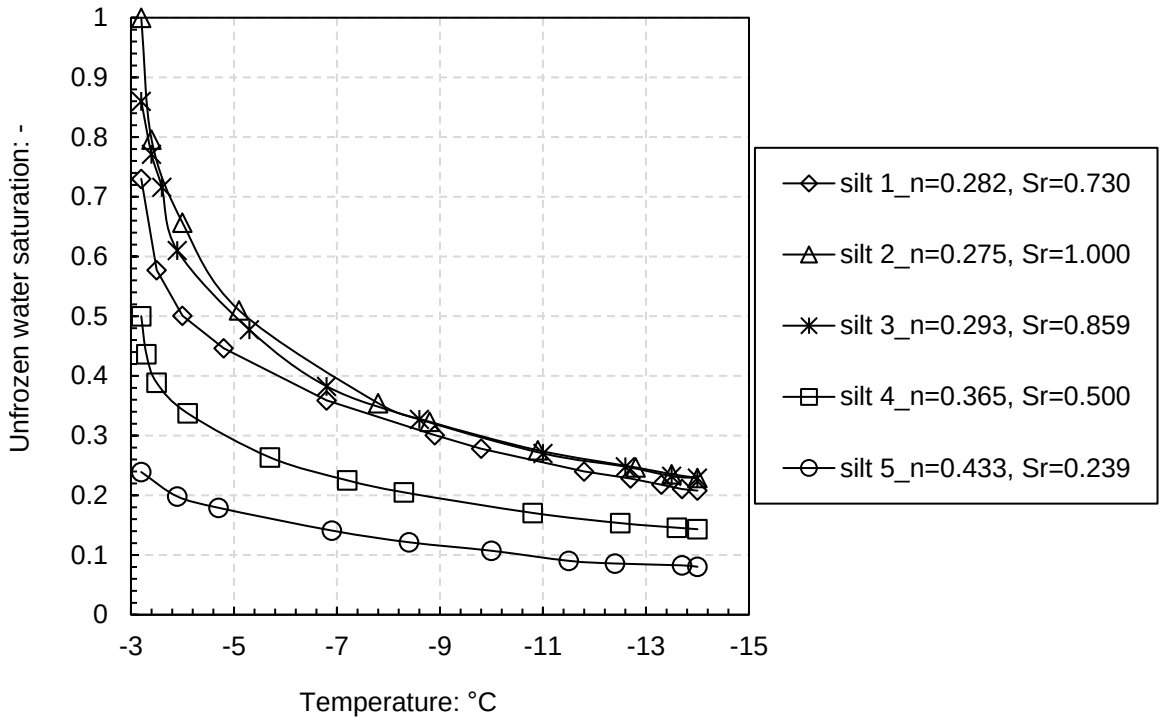

(b)

Figure 4.16 Estimated unfrozen water saturations with temperature for (a) fine sand and (b) clayey silt samples starting at different initial degrees of saturation

4.4 Thermal conductivity method

4.4.1 Introduction

The soil is a material with multiple phases, including solid soil, gas, water and/or ice (in the case of frozen soil). The thermal conductivity of soil is not only determined by the intrinsic physical properties of each phase but also affected by variations of each phase. The thermal conductivity of water, air, and ice are 0.6 W/m K, 0.024 W/m K and 2.2 W/m K, respectively. Many experimental results (Brandon and Mitchell, 1989; Farouki, 1981; Smits et al., 2010; Dong et al., 2015) indicate that varying water and ice saturation in soil systems play an important role in the thermal conductivity of soils.

In this section, the heat transfer mechanism of soil and the main governing factors of soil thermal properties are analysed and summarised. To study the water and/or ice saturation dependence of soil thermal conductivity, a complete theoretical model is proposed based on the geometric mean concept and a modified Chen's model (Cote and Konrad, 2005; Chen, 2008). A series of thermal tests have been performed using a new steady-state experimental setup (Romero et al., 2016) on fine sand and clayey silt with varying porosities, degrees of saturation and temperature (room temperature of 20 °C and low temperature of −15 °C). The experimental results are interpreted by the proposed model and model parameters are then estimated. The obtained model can be used to predict the thermal behaviour of the two tested soils.

4.4.2 Heat transfer mechanism and governing factors

There are three heat transfer mechanisms in a material medium: conduction through solids and liquids, convection in fluids and radiation, which does not need a material medium. The most effective means of transferring heat in dry particulate materials is through the solid contacts, while conduction through the gas phase and radiation has less relevant effects (Carslaw and Jaeger, 1959; Murashov and White, 2000). Heat transfer by convection plays an important role if the particle size D_{50} is larger than ~6 mm, allowing fluid flow through the porous network (Yun, 2005).

In this section, the scope of assessment of thermal conductivity models considers only heat transfer by conduction. It is assumed that soils are under room temperature (20 °C) or low temperature (−15 °C) and under a small temperature gradient. Thus, the liquid/ice phase change or water vapour enhancement induced by high temperature and the heat flux of fluid convection due to temperature gradient are minimised. Under these assumptions, the apparent or effective thermal conductivity of soil is often used to describe the heat transfer capability of multi-phase materials.

The heat flux q (W/m^2) at steady state is proportional to the thermal gradient by the coefficient of thermal conductivity λ (W/m·K), according to the constitutive equation of Fourier's law in one dimension:

$$q = -\lambda \frac{dT}{dx} \tag{4.21}$$

The rate of heat transfer in transient conditions is equal to the heat stored within the medium and the rate of internal heat generation, given by the continuity equation:

$$\frac{dq}{dx} = q_{store} - q_{generated} \tag{4.22}$$

where the heat stored in the material is $q_{stored} = \rho \cdot c \cdot \left(\partial T / \partial t\right)$, ρ (kg/cm^3) is the material mass density and c (J/kg·K) is the heat capacity. If there is no heat generation within the material, the $q_{generated}$ term equals to zero. Combining the above two equations leads to Fick's second law:

$$\frac{\partial^2 T}{\partial x^2} = -D \frac{\partial T}{\partial t} \tag{4.23}$$

where $D = \lambda / \left(\rho \cdot c\right)$ (m^2/s) is the thermal diffusivity, which reflects how fast heat will be transferred through a material. The negative sign indicates that heat transfer occurs in the direction opposite to the temperature gradient.

The thermal properties of soils under isothermal conditions are governed by several particle-level and macro-scale factors: mineralogy, particle size, particle shape, packing geometry, stress level, water content (degree of saturation), porosity, gradation, and cementation.

Mineralogy. Solid minerals are the most conducive constituents in the air-water-(ice)-solid soil system. Thus, they define the upper limit of the thermal conductivity. Soil comprising different mineral substances has different thermal conductivity (e.g., quartz > mica) (Gangadhara Rao and Singh, 1999; Tarnawski et al., 2002). Soils with a higher quartz content display larger thermal conductivity values (Tarnawski et al., 2009).

Particle size. and gradation Heat flux between particles is proportional to the radius of the particles. Larger particles and fewer contacts in a given volume result in higher thermal conductivity (Aduda, 1996; Gangadhara Rao and Singh, 1999). Well-graded soil exhibits higher heat transfer as small particles fill the interstitial pore space and increase the inter-particle coordination (Esch, 2004).

Packing geometry. Higher inter-particle coordination increases the thermal conductivity for a given particle size (Lambert and Fletcher, 1997b; Tarnawski et al., 2002). The contact conductance is more important than the radiational conductance (Lambert and Fletcher, 1997a). The thermal conduction at contacts results in a percolation-type conduction process (Sahimi and Tsotsis, 1997).

Stress level. Higher stresses result in higher contact radii leading to an increase in thermal conductivity. Granular chains under higher stress also give rise to more developed heat transfer paths (Vargas and McCarthy, 2001).

Water content. The fluid volume fraction is a dominant factor to the thermal conductivity in partially saturated soils. At the residual water content region, adding a small amount of water dramatically improves the thermal conduction. The increase of thermal conductivity with the increase of water content in unsaturated soils suggests the important role of pore fluid conduction (Singh and Devid, 2000).

Porosity. The lower the void ratio, the higher the thermal conductivity (Brandon and Mitchell, 1989; Yun and Santamarina, 2008).

Cementation. Cement and colloidal precipitation at particle contacts increase the contact area and thus the thermal conductivity (Tarnawski et al., 2002).

Through the analyses of the factors affecting the effective thermal conductivity of soils found in the literature, they can be generalised into few essential elements: thermal conductivity of each constituent (i.e., minerals, liquid, and air), water content (degree of saturation), soil type (e.g., particle size / shape) and particle contacts (e.g., coordination numbers), which can be

affected by a number of macro-level manifestation such as porosity, stress level, and gradation. The key governing factors are summarised in Table 4.3.

Table 4.3 Controlling factors in thermal conductivity variation of unsaturated soils (Dong et al., 2015)

Key governing factors	Features
Constituent	The thermal conductivity of solid minerals dominates the bulk property
Soil type	Different types of soil have different soil minerals, particle sizes, and shapes
Water content	The volume fraction of the water phase determines the thermal conductivity of partially saturated soils
Particle contact	The coordination number affected by stress level, packing density, gradation, et al. defines the thermal conduction skeleton

4.4.3 Theoretical model

As discussed in Chapter 2, the predictions of parallel/series models are much higher/lower than the real thermal conductivity of soil measured thought the saturation range. However, they set theoretical upper and lower limits of the possible estimation. The geometric mean model averages the thermal conductivity of each phase in the unsaturated soil mixture but overestimates the contribution of pore water at a low degree of water saturation and underestimates it at a high degree of water saturation (Dong et al., 2015).

The empirical models (Johansen, 1975; Cote and Konard, 2005; Lu et al., 2007) use certain mathematical functions to fit the experimental results and then determine the parameters in these functions to match with the certain type of soil. The empirical models work better than the parallel/series models and the geometric mean model through the whole range of saturation. Moreover, they integrate the key factors of the constituent in terms of the thermal conductivity at a dry state λ_{dry} and at a fully saturated state λ_{sat} and consider the degree of water saturation. They all normalise the equation of thermal conductivity based on λ values at the dry and saturated states, and the Kersten number K_e can be described as a function of water saturation.

To better understand the relationship of thermal conductivity with soil porosity and water saturation, a modified Chen's model (2008) is used to interpret the experimental results for the two soils in this section.

4.4.3.1 Estimation of thermal conductivity for saturated soils

Although many theoretical models have been used to calculate the thermal conductivity of saturated soils when the thermal conductivity of constituents do no differ by more than one order of magnitude, the geometric mean model is as successful as any other, and it is clearly the simplest (Sass et al., 1971). Thus, the geometric mean method is applied in this section for calculating the saturated thermal conductivity of unfrozen soils using the following expression:

$$\lambda_{sat\_u} = \lambda_s^{1-n} \lambda_w^n \tag{4.24}$$

Where λ_{sat_u} is the thermal conductivity of the saturated unfrozen soil; λ_s and λ_w are the thermal conductivity of solid particles and water (W/m·K), respectively; and n is the porosity of the soil, which can be described as:

$$n = 1 - \rho_d / \rho_s \tag{4.25}$$

where ρ_s and ρ_d are the density of solid particles and the dry density of soils (kg/m^3), respectively.

The thermal conductivity of saturated frozen soils can be calculated with

$$\lambda_{sat\_f} = \lambda_s^{1-n_f} \lambda_i^{n_f} \tag{4.26}$$

where λ_{sat_f} is the thermal conductivity of saturated frozen soil; λ_i is the thermal conductivity of ice, and n_f is the porosity of frozen saturated soils.

Due to the difference between the density of water and ice, the volume of voids will increase theoretically by 9% for saturated soil completely freezing in a closed system. However, the

research results in section 4.3 indicate the unfrozen water still exists in frozen fine-grained soil at very low temperature, which means the porosity changes will be less than 9%. For simplicity, it is assumed that the porosity does not change during freezing, so $n \approx n_f$.

The thermal conductivity of the saturated frozen fine-grained soils can be presented as

$$\lambda_{sat\_f} = \lambda_s^{1-n_f} \lambda_i^{n_f-\theta_u} \lambda_w^{\theta_u} \tag{4.27}$$

where $\theta_u = n_f S_{uw}$ is the volume fraction of unfrozen water in frozen fine-grained soils. When $\theta_u = 0$, Equation (4.27) reduces to Equation (4.26).

4.4.3.2 Determination of thermal conductivity for dry soils

Very few models have been developed to determine the λ_{dry} values, and their narrow applicability range (soil type and porosity) only offers few possibilities for development. However, Smith (1942) and Johansen (1975) demonstrated that the thermal conductivity of dry soils is very sensitive to porosity and to a lesser extent, to the particle shape of natural mineral soils and crushed rocks. In this test, the dry fine sand and clayey silt can be measured directly instead of estimating using an empirical approach.

4.4.3.3 Predicting the bulk thermal conductivity of soils

Instead of the normalised thermal conductivity concept proposed by Johansen (1975), a new modified Chen's model (2008) is used in this thesis. It allows the modelling of the thermal conductivity as a function of porosity and degree of water saturation, in an unfrozen state, which is written as

$$\lambda\left(n, S_r\right) = \lambda_s^{1-n} \lambda_w^{n} \left[\left(1-b\right) S_r + b\right]^{c} \tag{4.28}$$

Similarly, in the fully frozen state, it is written as

$$\lambda\left(n, S_r\right) = \lambda_s^{1-n} \lambda_i^{n} \left[\left(1-b\right) S_r + b\right]^{c} \tag{4.29}$$

The parameters in the equation can be obtained by the methodology mentioned above; hence, the expression can be used to predict the unknown bulk thermal conductivity of a wide range of soils in both the unfrozen and frozen states.

4.4.4 Test results and analysis

4.4.4.1 Experimental results

Several thermal conductivity tests are performed to increase knowledge of the setup and to study the response of fine sand and clayey silt samples at different degrees of water saturation and in the unfrozen and frozen states. The selected physical properties of the tested samples are listed in Tables 4.4 through 4.7. There are 15 fine sand samples tested at the unfrozen state (20 °C) and 10 samples tested at the frozen state (−15 °C). There are also 11 clayey silt samples tested at the same unfrozen state and 7 samples tested at the same frozen state.

Table 4.4 Selected physical properties of tested sand samples (unfrozen state)

Sample	Dry density ρ_d / Mg/m^3	Porosity n / -	Initial degree of saturation S_r / -	Measured thermal conductivity λ / W/m^{-1}K^{-1}
1	1.592	0.399	0.000	0.371
2	1.655	0.375	0.000	0.352
3	1.552	0.414	0.134	1.201
4	1.560	0.411	0.136	1.200
5	1.578	0.405	0.172	1.359
6	1.576	0.405	0.302	1.476
7	1.585	0.402	0.320	1.541
8	1.593	0.399	0.325	1.561
9	1.556	0.413	0.410	1.562
10	1.585	0.402	0.429	1.580
11	1.579	0.404	0.435	1.682

12	1.592	0.399	0.444	1.701
13	1.586	0.402	0.530	1.722
14	1.595	0.398	0.616	1.733
15	1.573	0.406	0.680	1.808

Table 4.5 Selected physical properties of tested sand samples (frozen state)

Sample	Dry density ρ_d / Mg/m^3	Porosity n / -	Initial degree of saturation S_r / -	Measured thermal conductivity λ / W/m^{-1}K^{-1}
1	1.552	0.414	0.000	0.343
2	1.516	0.428	0.087	1.366
3	1.479	0.442	0.162	1.676
4	1.482	0.441	0.162	1.520
5	1.515	0.428	0.249	1.975
6	1.545	0.417	0.344	1.985
7	1.541	0.418	0.437	2.372
8	1.473	0.444	0.519	2.739
9	1.514	0.429	0.569	2.663
10	1.538	0.420	0.735	3.092

Table 4.6 Selected physical properties of tested clayey silt samples (unfrozen state)

Sample	Dry density ρ_d / Mg/m^3	Porosity n / -	Initial degree of saturation S_r / -	Measured thermal conductivity λ / W/m$_{-1}$K$_{-1}$
1	1.442	0.460	0.000	0.120
2	1.523	0.429	0.139	0.410
3	1.535	0.425	0.141	0.353
4	1.568	0.413	0.293	0.661

5	1.683	0.370	0.431	0.951
6	1.736	0.350	0.470	0.959
7	1.717	0.357	0.510	1.159
8	1.802	0.325	0.637	1.300
9	1.768	0.338	0.936	1.641
10	1.721	0.355	0.964	1.595
11	1.826	0.316	0.998	1.638

Table 4.7 Selected physical properties of tested clayey silt samples (frozen state)

Sample	Dry density ρ_d / Mg/m^3	Porosity n / -	Initial degree of saturation S_r / -	Measured thermal conductivity λ / W/m^{-1}K^{-1}
1	1.532	0.426	0.142	0.646
2	1.591	0.404	0.221	1.039
3	1.709	0.360	0.333	1.122
4	1.698	0.364	0.345	1.338
5	1.728	0.353	0.414	1.408
6	1.786	0.331	0.542	1.586
7	1.895	0.290	0.867	2.305

The methods for calculating the thermal conductivity of soils are presented in section 4.4.4.1. For simplicity and continuity of the thesis, only two clayey silt samples are analysed here; the rest of the tests only present the measured final thermal conductivity values. Figure 4.17 (a) and (b) display the time evolutions of temperature (four thermocouples) during the thermal tests on unfrozen clayey silt and frozen clayey silt sample, respectively. In Figure 4.17 (a), the sample is prepared at room temperature and the temperature of T1 and T2 increases rapidly due to the upper heater being applied. After a certain time (500 seconds), the heat transfer

arrives at the bottom heater piston, which is why the temperature of T3 and T4 increased as well.

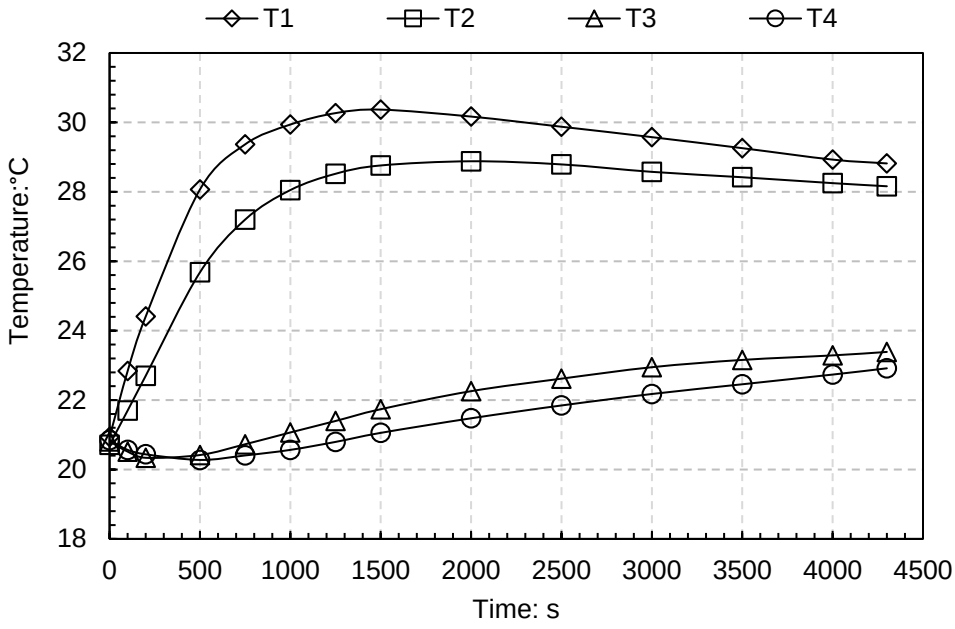

(a)

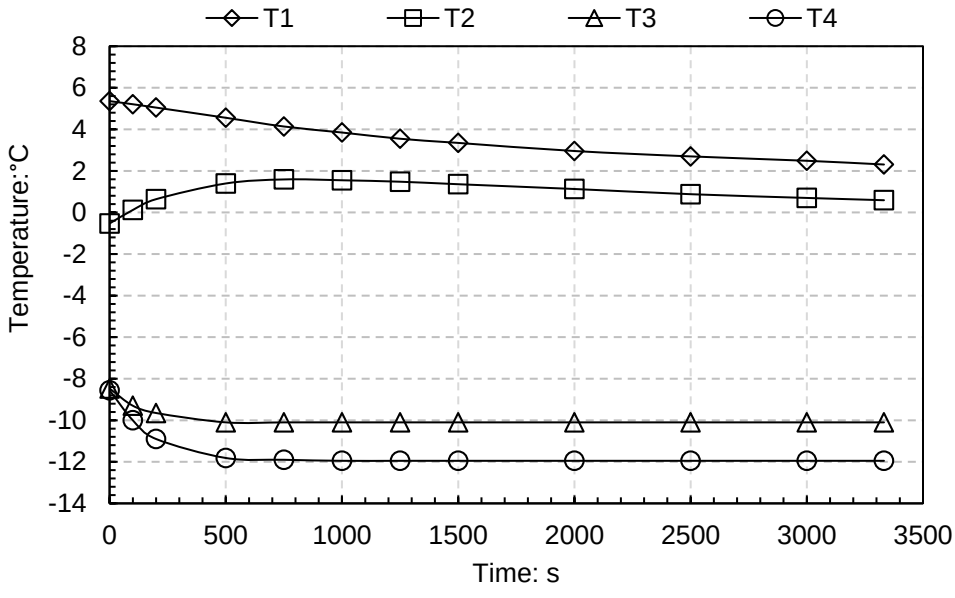

(b)

Figure 4.17 Time evolution of temperatures: (a) unfrozen clayey silt sample and (b) frozen clayey silt sample

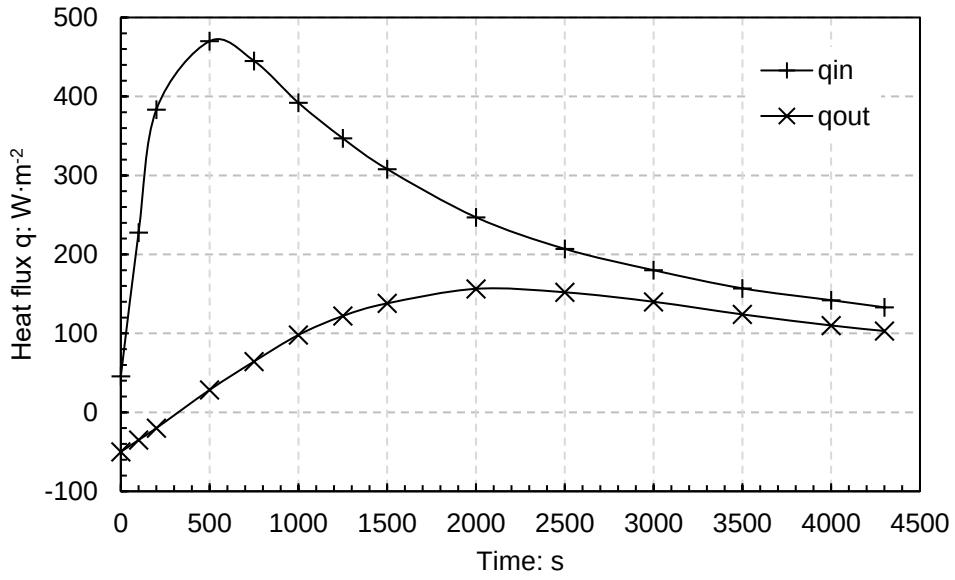

(a)

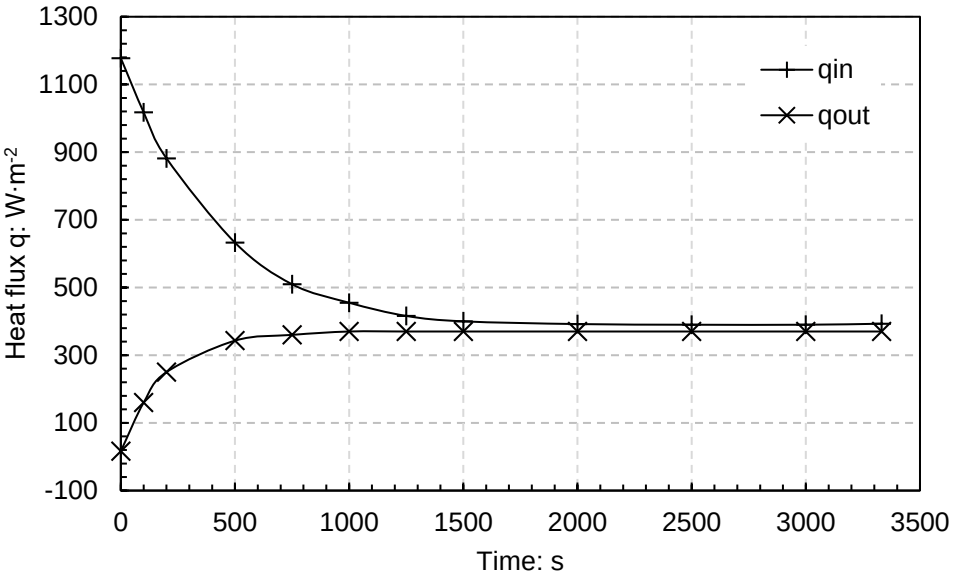

(b)

Figure 4.18 Time evolution of heat flux (inflow and outflow): (a) unfrozen clayey silt sample and (b) frozen clayey silt sample

The time evolutions of inflow and outflow heat fluxes are plotted in Figure 4.18 (a) and (b) for these two samples. The difference between inflow and outflow indicates the heat lost during the test. The evolution of $q_{ave} \cdot L/\Delta T$ for the different tests performed is plotted in Figure

4.19. q_{ave} represents the average inflow and outflow heat fluxes and ΔT has been estimated using T2 and T3 (L is the sample height). Under steady-state conditions, these plotted values represent the global (average) thermal conductivity of the heat flow. All the thermal conductivity results are summarised in Tables 4.4 through 4.7, including the initial porosity and initial degree of water saturation before the tests. It is assumed that the porosity and water content do not change during the thermal experiments.

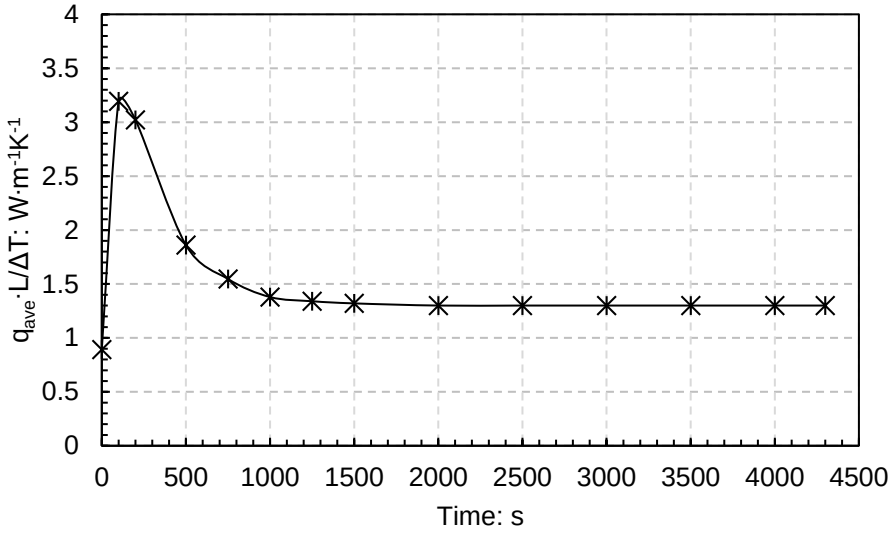

(a)

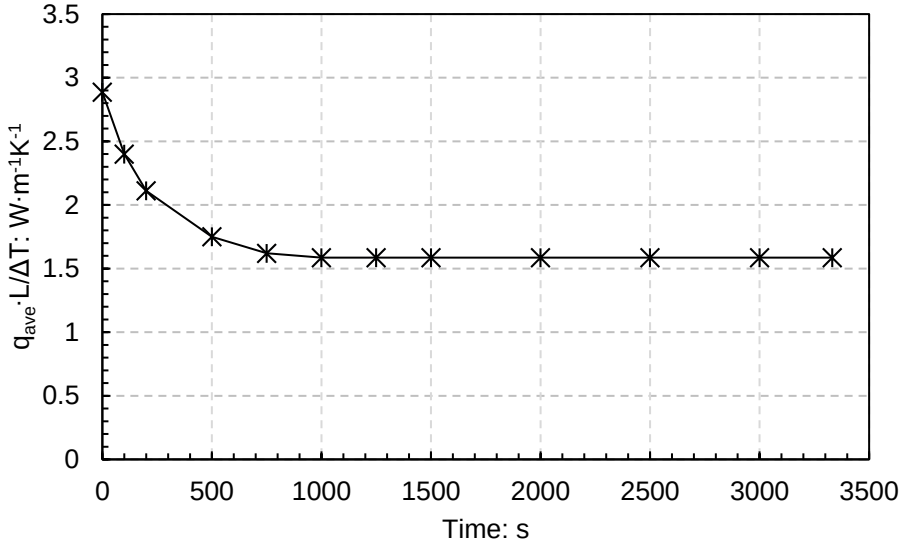

(b)

Figure 4.19 Time evolution of q_{ave}·$L/\Delta T$. Thermal conductivity at steady-state condition: (a) unfrozen clayey silt sample and (b) frozen clayey silt sample.

4.4.4.2 Data analyses

The thermal conductivity values at the range of saturation of sand samples are plotted in Figure 4.20 (a) and 4.21 (a). The porosities of tested fine sand samples are consistently around 0.4. The measured thermal conductivity of the dry sample λ_{dry} is 0.34 W/m·K at both the unfrozen and frozen states. The thermal conductivity of the sand solid λ_s is 4.65 W/m·K, which is fitted from the thermal conductivity of the saturated unfrozen sand and the saturated frozen sand samples using the geometric mean expression. Compared with the thermal conductivity measured by others, this result is lower. After performing the Bernard test, the percentage of carbonates has been confirmed by measuring the volume of CO_2 that reacted with HCl during the test; the mass fraction of CO_3^{2-} is around 30%. The primary materials of carbonates are calcite ($CaCO_3$) and dolomite ($MgCO_3$); therefore, the percentage of carbonates is between 42% and 50%. The carbonates have lower thermal conductivity than quartz. The details of Bernard tests are presented in Appendix B.

After fitting the results in Figure 4.20, the model parameters *b* and *c* have been obtained; they are 0.001 and 0.255, respectively. Figure 4.20 (b) is the 1:1 scatter plot of the measured and calculated thermal conductivity of the unfrozen fine sand samples with different degrees of saturation. Thus, the equation used to estimate the thermal conductivity of unfrozen fine sand is described as:

$$\lambda\left(n, S_r\right) = 4.65^{1-n} 0.6^{n} \left[\left(1-0.001\right) S_r + 0.001\right]^{0.255} \tag{4.30}$$

Similarly, the parameters *b* and *c* are 0.004 and 0.411; they are fitted from the experimental results shown in Figure 4.21. Figure 4.21 (b) is the 1:1 scatter plot of the measured and calculated thermal conductivity of the unfrozen fine sand samples with different degrees of saturation. Therefore, the equation for determining the thermal conductivity of frozen fine sand is presented as:

$$\lambda\left(n, S_r\right) = 4.65^{1-n} 2.2^{n} \left[\left(1-0.004\right) S_r + 0.004\right]^{0.411} \tag{4.31}$$

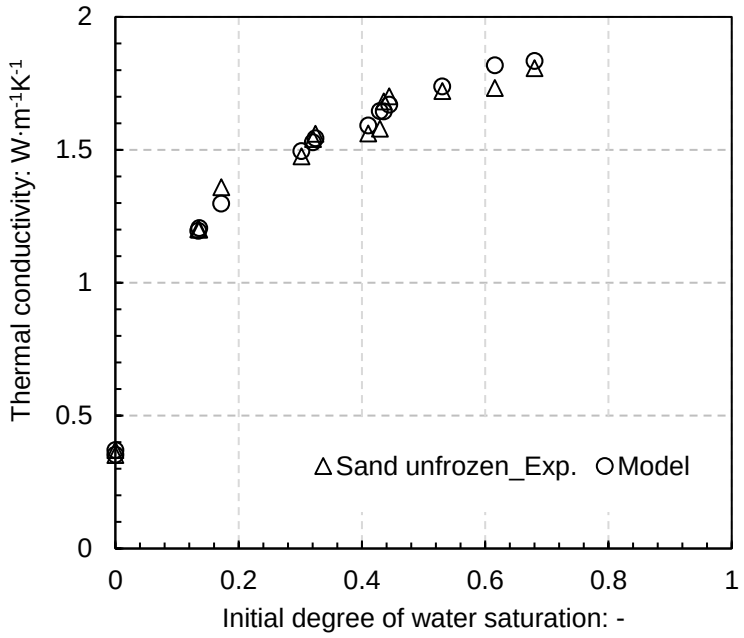

(a)

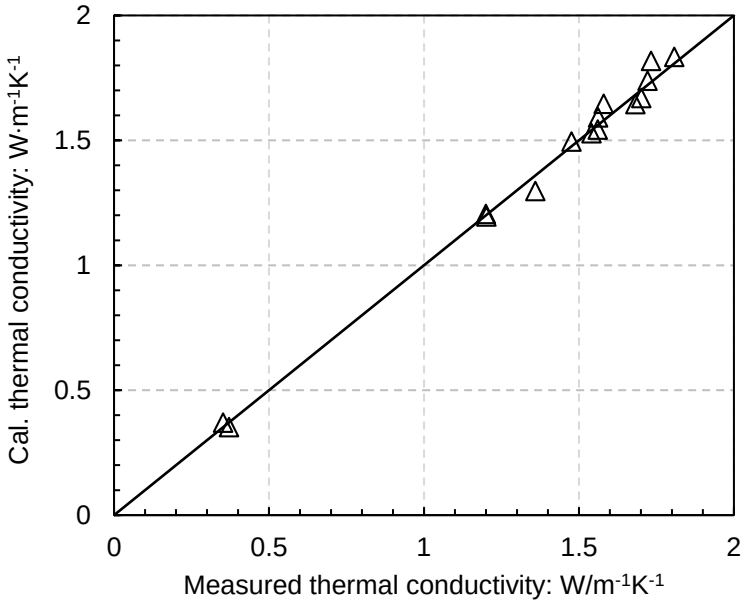

(b)

Figure 4.20 Comparison of measured and estimated results of unfrozen sand samples: (a) saturation range plot and (b) 1:1 scatter plot.

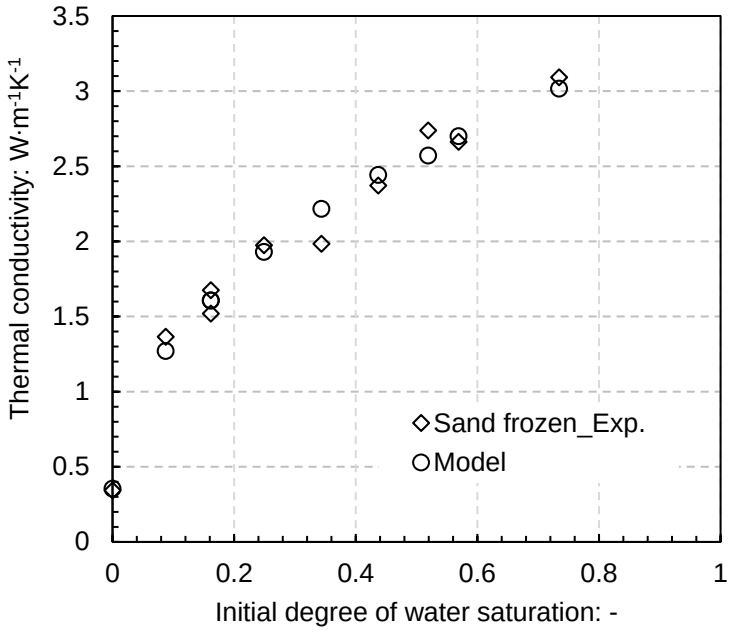

(a)

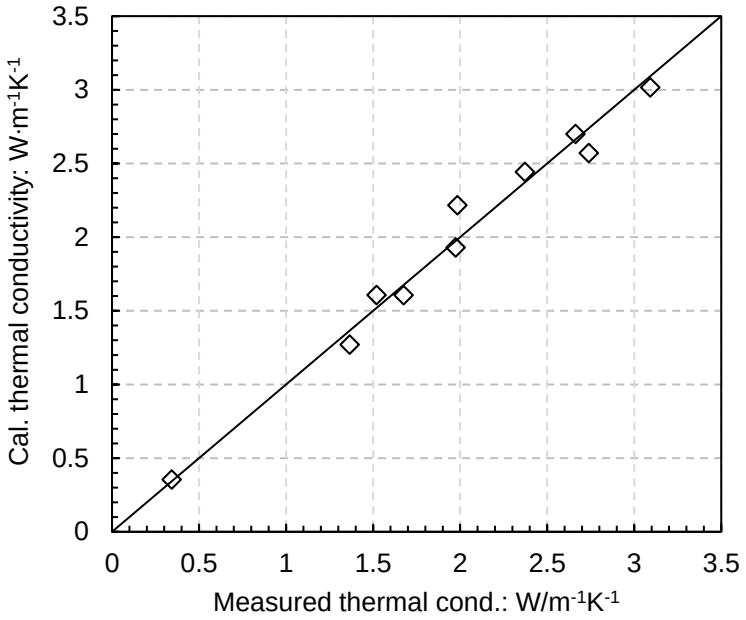

(b)

Figure 4.21 Comparison of measured and estimated results of frozen sand samples: (a) saturation range plot and (b) 1:1 scatter plot

For the clayey silt samples, the porosity of the prepared samples have some deviations in the different water content conditions. The higher the water content, the lower the porosity of the sample. The tested unfrozen results are illustrated in Figure 4.22 (a). The thermal conductivity of the dried clayey silt sample is 0.12 W/mK. The thermal conductivity of the clayey silt solid is fitted from the saturated unfrozen and frozen clayey silt result, which is 2.64 W/m·K. The modified Chen's model is used to fit the experimental results; the comparison of the measured and calculated results is shown in Figure 4.22 (b) in a 1:1 scatter plot. The parameters *b* and *c*, which has been obtained are 0.013 and 0.609, respectively. Thus, the equation used for predicting the unfrozen clayey silt sample with known porosity and initial degree of water saturation is plotted as:

$$\lambda\left(n,S_r\right)=2.64^{1-n}0.6^{n}\left[\left(1-0.013\right)S_r+0.013\right]^{0.609} \tag{4.32}$$

Similarly, the parameters *b* and *c* are 0.002 and 0.676, which are fitted from the experimental results of the frozen clayey silt sample, shown in Figure 4.23. Figure 4.23 (b) is the 1:1 scatter plot of the measured and calculated thermal conductivity of unfrozen clayey silt samples with different degrees of saturation. Therefore, the equation for determining the thermal conductivity of frozen fine sand is presented as:

$$\lambda\left(n,S_r\right)=2.64^{1-n}2.2^{n}\left[\left(1-0.002\right)S_r+0.002\right]^{0.676} \tag{4.33}$$

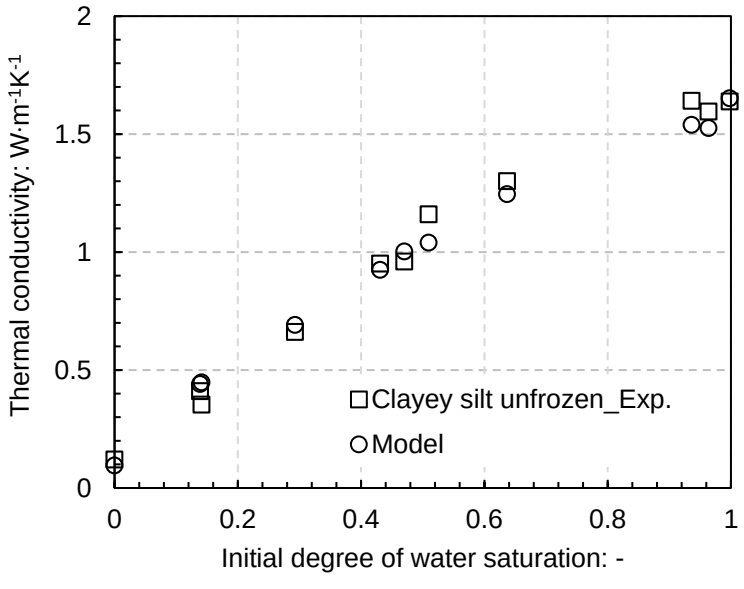

(a)

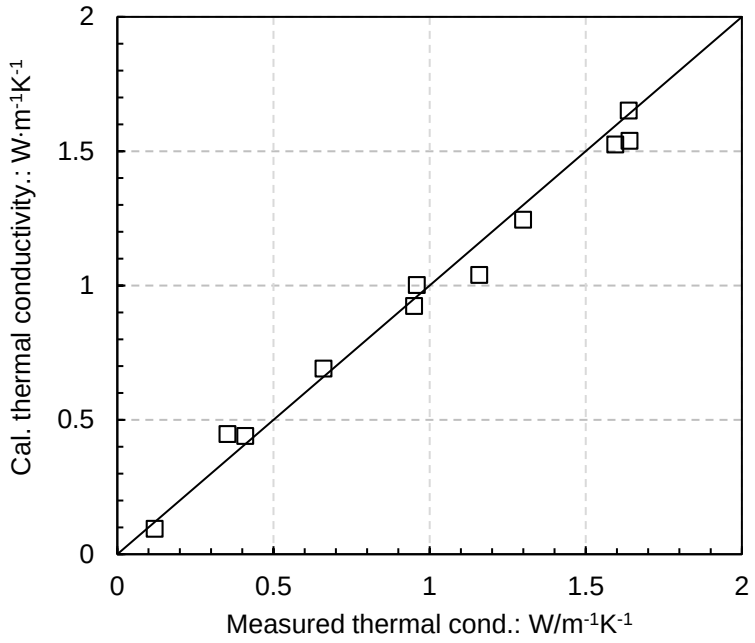

(b)

Figure 4.22 Comparison of measured and estimated results of unfrozen clayey silt samples: (a) saturation range plot and (b) 1:1 scatter plot

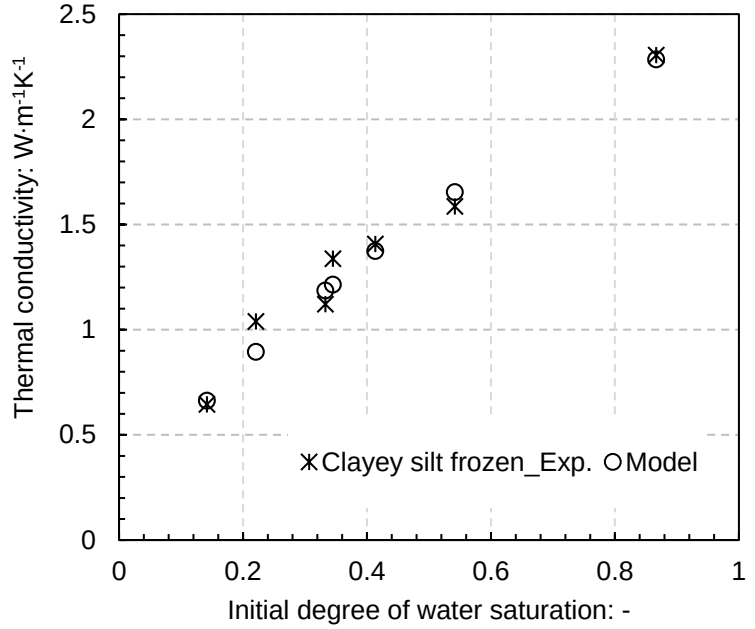

(a)

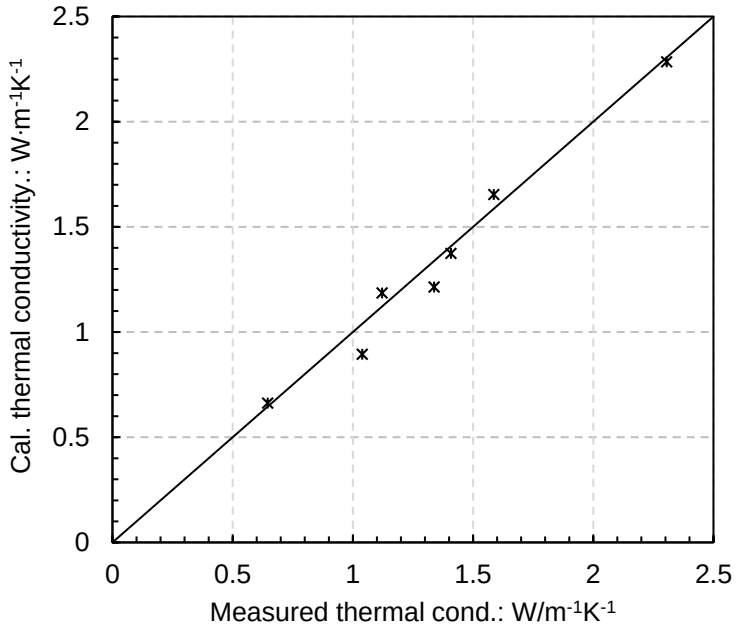

(b)

Figure 4.23 Comparison of measured and estimated results of frozen clayey silt samples: (a) saturation range plot and (b) 1:1 scatter plot

All fitted parameters *b* and *c* are listed in Table 4.8. As shown in Figures 4.20 (b) through 4.23 (b), the modified Chen's model fit the experimental results very well. The fitted equations are appropriate for estimating the thermal conductivity of fine sand and clayey silt samples at the unfrozen and full frozen states with known initial porosity and degree of saturation.

Table 4.8 Fitted parameters of Chen's model for different types of soil

Parameter	Sand_unfrozen	Sand_frozen	Clayey silt_unfrozen	Clayey silt_frozen
b	0.001	0.004	0.013	0.002
c	0.255	0.411	0.609	0.676

The change in thermal conductivity of soils with increasing degrees of saturation differs remarkably for different soil types. For sandy soil, the thermal conductivity increases immediately once the soil experiences a small increase in the degree of saturation. However, for clayey silt, it can be observed that the thermal conductivity evolution with changing the

degree of saturation is much smoother than sand. In the initial short stage of saturation range, only hydration water forms with the interaction of clay minerals; the water molecules are absorbed into mineral complex, which does not change the soil particle network or connectivity. This is the physical reason why rich fine-content soil like clayey silt is at the low degree of saturation, while the thermal conductivity of bulk soil barely changes. Dong et al. (2015) proposed a unified conceptual model to explain the thermal conductivity of different types of soil.

4.5 Soil freezing retention curve (SFRC) model

4.5.1 Introduction

Soil freezing retention curve (SFRC) is an expression depicting the relationship between unfrozen water content and the temperature of the soils during freezing. Unfrozen water can be transferred during the freezing and thawing process. The water flow is triggered by temperature gradients and the associated cryoscopic suction included. The amount of unfrozen water content affects the physical and mechanical properties of frozen soils, such as strength (compression and shear strengths), stiffness, thermal conductivity, specific heat, etc. (Dong et al., 2015; Bai et al., 2018). It may also influence the seepage characteristic of frozen soils (Watanabe and Wake, 2008; Watanabe and Flury, 2008), causing engineering problems such as frost heaving, thaw settlement, cumulative settlement during cyclic freezing/thawing, etc. (Peláez et al., 2014).

The SFRC of several soils has been measured using different direct and indirect techniques as reviewed in Chapter 2. In this chapter, a simple and precise setup is used to measure the unfrozen water content of fine sand and clayey silt during freezing (see section 4.3) and the modified Archie's law is applied to interpret the experimental results. To validate the estimated SFRC in section 4.3, different theoretical SFRC models are used here, including the method that combines the Clausius-Clapeyron equation with the van Genuchten model and the capillary bundle model with pore size distribution data from MIP tests.

Figure 4.24 is a typical case of the freezing retention curve of soil. The unfrozen water saturation of soil is kept as a constant (S_l) when the temperature is higher than the initial freezing point (T_f). The freezing point of soil is determined mainly by the concentration of solute in interstitial water (in this case, T_f = -3.2 °C). Then, the unfrozen water saturation reduces with the decrease in temperature. When the temperature is lower than a certain value, the unfrozen water saturation remains constant as the temperature continues to decrease. The unfrozen water saturation at this temperature is called the residual unfrozen water saturation (S_r), which is also affected by the salinity of the pore liquid. The decreased rate of unfrozen water saturation and final residual unfrozen water saturation vary in different types of soil. In these tests, the clayey silt has higher residual unfrozen water saturation compared to fine sand.

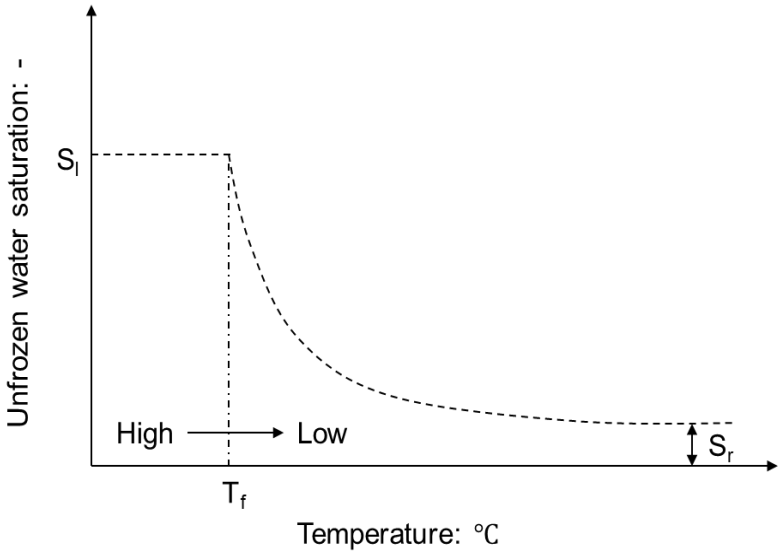

Figure 4.24 Freezing retention curve of soil

4.5.2 SFRC from combined CC-vG model

In order to express the data in terms of pressure, a number of researchers have considered freezing soil as a thermodynamic system in which the soil phase does not react with water in its various states (Nishimura et al., 2009; Lebeau et al., 2012). In such a system, the equilibrium between changes in chemical potential for each of the components, unfrozen water (w) and ice (i) is given by the Gibbs-Duhem equation, which is

$$d\mu_l = -s_w dT_l + \upsilon_l dP_l \tag{4.34}$$

$$d\mu_i = -s_i dT_i + \upsilon_i dP_i \tag{4.35}$$

where μ is the chemical potential, $\upsilon = 1/\rho$ is the specific volume, ρ is the density, P is the absolute pressure, s is the specific entropy and T is the absolute temperature. At equilibrium, the chemical potential and temperature of both components are equal, and the result is the well-known Clapeyron relation (Black, 1995):

$$\upsilon_l dP_l - \upsilon_i dP_i = \left(s_l - s_i\right) dT = \frac{l_l}{T} dT \tag{4.36}$$

which can be rearranged and integrated to give:

$$P_i - P_l + \left(1 - \frac{\upsilon_l}{\upsilon_i}\right)\left(P_l - P_0\right) = -\frac{1}{\upsilon_i} \int_{T=T_f}^{T} \frac{l_l}{T} dT \tag{4.37}$$

where l_l (=333.5 kJ/kg) is the specific latent heat from the fusion of water, T_f is the reference absolute temperature at the freezing point and P_0 is the reference absolute pressure (often taken as equal to atmospheric pressure). This relationship has often been used to describe the temperature-pressure behaviour in frozen porous media. Due to the ratio of υ_l and υ_i being close to 1, the influence of water pressure P_l is relatively minor. The equation reduces to:

$$P_i - P_l = -\rho_i l_l \ln\left(\frac{T}{T_f}\right) \tag{4.38}$$

The non-wetting ice invasion at P_i-P_l can be assumed to be equivalent to air intrusion at matrix suction s during a drying path for the same diameter pf pores x:

$$s = \frac{4\sigma_l \cos\theta_l}{x};\ P_i - P_l = -\frac{4\sigma_i \cos\theta_i}{x};\ P_i - P_l = -\frac{\sigma_i \cos\theta_i}{\sigma_l \cos\theta_l} s \approx 0.45s \tag{4.39}$$

where σ_l =0.073 N/m is the surface tension of liquid water at 20 °C and $\cos\theta_l$ =1 is the wetting coefficient for the air-water interface. σ_i =0.033 N/m is the surface tension of ice $\cos\theta_i$ is the wetting coefficient for the ice-water interface (θ_i ≈108°; see for instance Knight, 1971) and x is the entrance pore diameter for a cylindrical model.

The degree of saturation at certain suction, assuming non-deformable soil, is used to evaluate the unfrozen water saturation corresponding to the equivalent $P_i - P_l$ determined using Equation (4.39).

The van Genuchten (1980) model is widely employed to link the degree of water saturation with soil suction to describe the soil water retention curve, which is:

$$S_r = \left[1 + \left(\frac{s}{P}\right)^{\frac{1}{1-\lambda}}\right]^{-\lambda} \tag{4.40}$$

where P and λ are material constants.

By substituting Equation (4.38) and (4.39) into (4.40), the freezing retention curve can be presented as:

$$S_l = \left[1 + \left(\frac{-2.22\rho_i l_w \ln\left(T/T_f\right)}{P}\right)^{\frac{1}{1-\lambda}}\right]^{-\lambda} \tag{4.41}$$

4.5.3 SFRC from MIP results

For soils, a porous medium with different pore sizes, it is impossible to describe the pore structure with a uniform function. One possible solution is the up-scaling method from microstructure to macrostructure. MIP is one of the effective methods for obtaining the pore size distribution of soils. Capillary bundle models were proposed by some authors when dealing with the seepage of soils. This model is applied to the study of SFRC with two hypotheses:

(a) The pore of soil is simplified as a capillary (capillary bundle model);

(b) The freezing of pore water starts from macro-pores, and the freezing temperature of pore water reduces with the decrease in pore diameter.

The real structure of the soil is simplified in Figure 4.25.

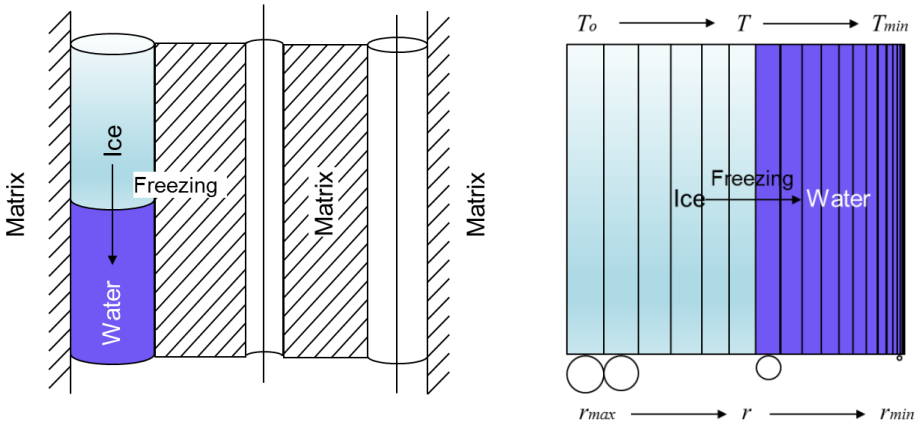

(a) (b)

Figure 4.25 Schematic diagrams of the model

The unfrozen water content in the process of freezing and thawing, based on hypothesis, is:

$$S_u(r) = \int_{r_{min}}^{r} f(r)V(r)dr \tag{4.42}$$

where $f(r)$ is the probability density related to pore radius r, $V(r)$ is the pore volume of pore radius r and $S_u(r_{\max}) = 1$.

The specific forms of $f(r)$ and $V(r)$ can be determined using MIP based on a capillary bundle model. Figure 4.26 is the curve of pore distribution through MIP. Figure 4.26 (a) is the relationship between pore volume and diameter, while Figure 4.26 (b) is the cumulative curve of the pore volume. The specific forms of $f(r)$ and $V(r)$ can be determined in Figure 4.26.

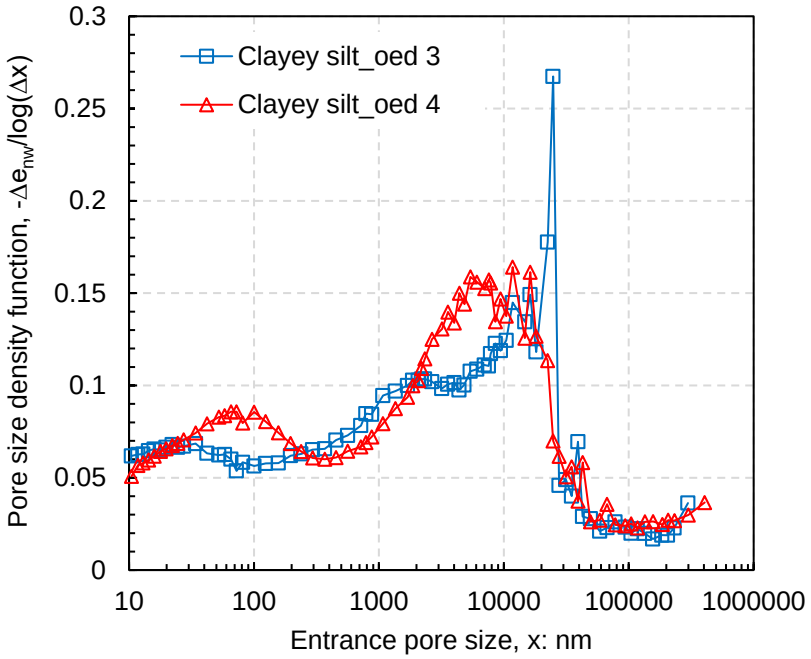

(a)

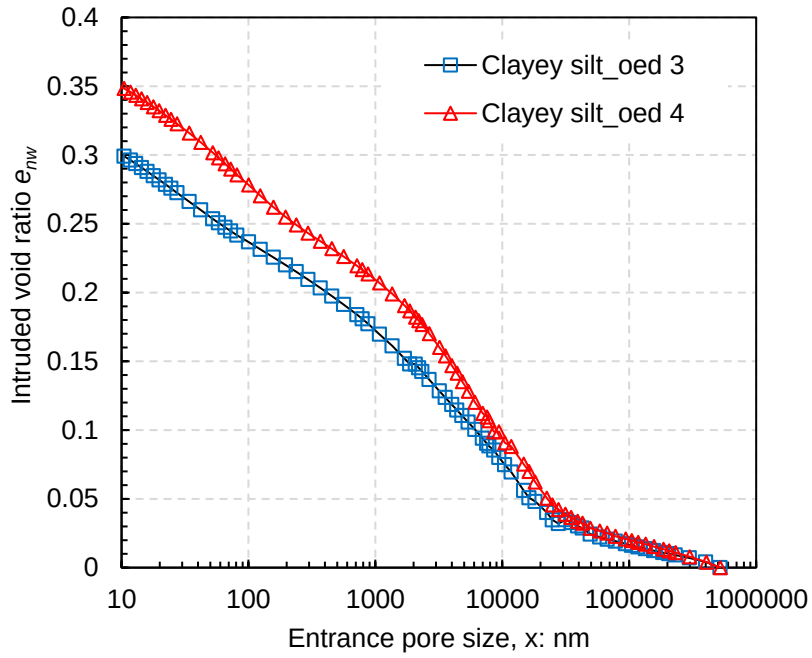

(b)

Figure 4.26 Pore size distribution of clayey silt: (a) Log-differential volume vs pore diameter; (b) Intruded void ratio vs pore diameter.

The freezing point of pore water is related to pore radius. In other words, the freezing temperature of the pore water with different pore radii is different. The relationship between the freezing temperature of pore water and the pore radius can be expressed as an implicit function:

$$r = g(T) \tag{4.43}$$

where T is the freezing temperature of pore water and r is the pore radius.

The specific form of $g(T)$ can is obtained by testing or theoretical derivation. The change at the freezing point due to the variation of the chemical potential of water with the capillary radius of r can be described with the following simplified formula (Ershov et al., 1979):

$$T_0 - T = \frac{T_0 \cdot 2\sigma}{Lr\rho_w}\cos\varphi \tag{4.44}$$

where T_0 is the freezing temperature of pure water under free conditions, which can be measured by the Kelvin scale; σ is the surface tension of water; φ is the contact angle of the solid-water interface; ρ_w is the density of water; L is the latent heat of fusion; and r is the radius of capillary.

Watanabe and Mizoguchi (2002) also proposed a similar formula. The freezing temperature of ice column with radius r is:

$$T_0 - T = \frac{T_0 \cdot \gamma}{Lr\rho_i} \tag{4.45}$$

where γ is the ice-liquid water interfacial free energy and ρ_i is the density of ice.

Substituting Equation (4.44) into Equation (4.45) results in:

$$S_u\left(g(T)\right) = \int_{T_{\min}}^{T} f\left(g(T)\right)V\left(g(T)\right)g'(T)\,dT \tag{4.46}$$

where $g'(T)$ is the derivative of $g(T)$; $T_{\min}$ is the freezing temperature of an ice column with radius $r_{\min}$, and T is the freezing temperature of an ice column with radius r.

As shown in Equation (4.46), S_u, f, g and g' are functions of temperature, so Equation (4.46) can be rewritten as:

$$S_u(T) = \int_{T_{\min}}^{T} f(T)V(T)g'(T)dT \tag{4.47}$$

The distribution function $F(T)$ is given by:

$$F(T) = f(T)V(T)g'(T) \tag{4.48}$$

Then, Equation (4.47) can be rewritten as:

$$S_u(T) = \int_{T_{\min}}^{T} f(T)dT \tag{4.49}$$

As shown in Equation 4.49, the soil freezing characteristic curve could be obtained if the specific formation of the distribution function $F(T)$ is determined.

4.5.4 Comparison and discussion

Figure 4.27 shows the estimated SFRC from Equation (4.41), which combines the van Genuchten model with the Clausius-Clapeyron equation. The material parameter λ=0.26 is obtained from SWRC and assumed constant in SFRC. The ice entry value P=0.46 MPa can be obtained from the estimated air entry value in SWRC using the relationship mentioned above. When comparing the estimated SFRC from SWCC with the previously measured result of saturated clayey silt sample by bulk EC, a very good agreement has been observed between both results, which gives confidence to the approach followed to estimate the unfrozen degree of saturation by bulk readings.

The figure 4.27 also includes the SFRCs estimated from proposed capillary bundle model with MIP results on two freeze-dried samples at n=0.293 and n=0.310 which are taken from

oedometer tests (OED 3 and OED 4) presented in Chapter 6. A similar procedure has been followed, in which the non-wetting mercury intrusion has been assumed to be equivalent to ice invasion and the degree of saturation of non-wetting mercury has been used to evaluate the unfrozen water saturation. The SFRCs based on MIP results also displays a consistent trend with previous results, although ice generates faster with small temperature drops close to the freezing point.

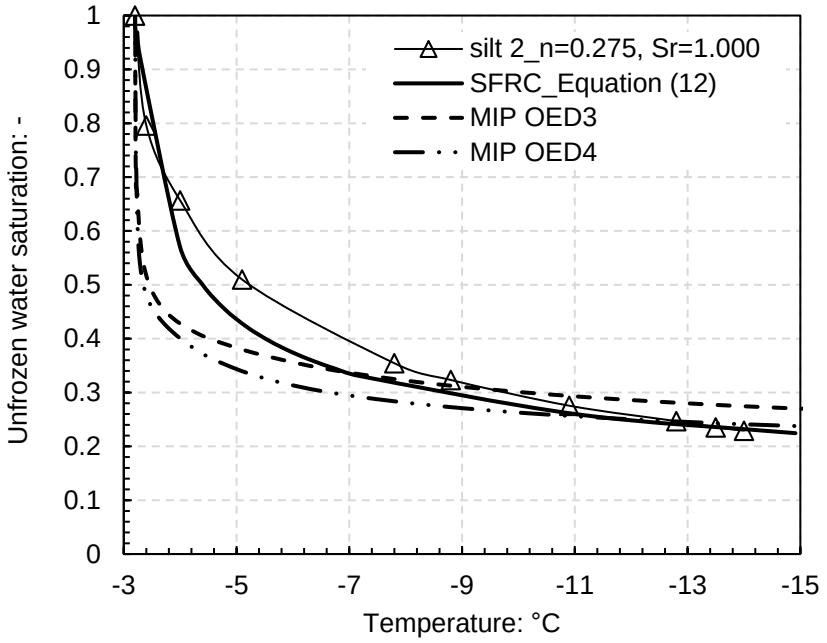

Figure 4.27 Comparisons of measured and estimated SFRCs by two proposed models

4.6 Summary

In this chapter, the main works include:

- Fine sand and clayey silt samples with varied porosities and degrees of water saturation are tested to register the bulk EC and relative dielectric permittivity readings at target temperatures during the freezing process using a commercial FDR sensor with a cooling bath system. Archie's second law and the theoretical dielectric mixing α-model are applied to fit the measurements of bulk EC and permittivity in

two partially saturated soils, respectively. The model parameters are obtained from both the full unfrozen state S_i=0 and the maximum frozen state S_f≈0 (some unfrozen liquid is still assumed to be at this maximum ice content). The extended models can be used to estimate the amount of ice content (or unfrozen water content) in the intermediate state with the coexisting of ice and liquid water. The inaccuracy of prediction in fine sand and clayey silt at lower degrees of saturation (less than 20%) is attributed to ignoring the temperature dependence properties of bulk EC and permittivity.

- The bulk electrical conductivity of fine sand and clayey silt specimens at five different initial degrees of water saturation have been measured along temperature decrease and freezing paths (from 20°C to -15°C). A 5% NaCl solution has been used as interstitial water to better discriminate electrical conductivity values between ice and unfrozen water. Archie's law together with a temperature dependent expression for the electrical conductivity of the interstitial water in the freezing zone has been used to interpret the experimental results and estimate the unfrozen water content at different temperatures. The proposed approach considers the porosity effects and the initial degree of saturation. The salinity of the interstitial water affects the freezing point, as well as the residual unfrozen water saturation below -7ºC.
- The thermal conductivity of fine sand and clayey silt samples is tested using a steady-state method. The soil samples are prepared at different initial porosities and different initial degrees of water saturation. Based on the analyses of the soil heat transfer mechanism and the governing factors of thermal conductivity, a modified Chen's empirical model is proposed to interpret and estimate the experimental results. The obtained equations can be used to estimate the thermal conductivity of fine sand and clayey silt with known porosity and degree of saturation, at both the unfrozen and frozen states.
- The unfrozen water results from the bulk EC measurements have been compared with the SFRC obtained by combining the Clausius-Clapeyron equation with the water retention data on drying, as well as with the MIP results. The very good agreement has been found between the proposed approach using bulk EC data and the experimental data from the water retention curve.

Chapter 5 ERT monitoring of soil freezing

5.1 Preface

In view of AGF applied in the construction of underground metro stations, the need for a continuous monitoring of the freezing evolution in frozen areas has been considered in recent years (Viggiani and de Sanctis, 2009; Casini et al., 2014). Surface geophysical measurements, such as EC, have been widely used both in situ and under laboratory conditions because of its low cost and non-destructive testing (Comina et al., 2008; Hauck, 2016). In this regard, mono-dimensional experiments had been performed to estimate the evolution of the degree of water saturation of pollutant infiltration in column tests (Kamon et al., 2003), to track consolidation and sedimentation processes (McCarter and Desmazes, 1997; Blewett et al., 2001); and to investigate soil liquefaction (Jinguuji et al., 2007).

Additionally, to evaluate the variability of the electrical field across the specimens, the tomographic reconstruction of the resistivity field had been applied in geophysical prospecting (Reynolds, 1997; Hauck, 2002). ERT is a tool that allows monitoring of the spatial distribution of EC (or its inverse, resistivity) within an object from impedance measurements at its surface (Comina et al., 2008). Geotechnical laboratory cells with ERT capabilities in two or three dimensions have been described by Borsic et al. (2005), Comnia et al. (2008), Damasceno et al. (2009) and Cosentini et al. (2012). ERT images have been used to detect the location of heterogeneities (Borsic et al., 2005; Comina et al., 2008), to image the salt transport (Damasceno et al., 2009; Comina et al., 2010; 2011), to estimate the hydraulic parameters of unsaturated soil samples (Consentini et al., 2012). In the above-cited works, the ERT experiments were all performed at room temperature, and consequently, the effects of temperature have never been considered.

This paper presents a 2-Dimensional laboratory cell with ERT capabilities for monitoring the heterogeneities and ice formation during soil freezing process. A modification of cell allows freezing the sample from the centre and conducting thermal isolation from outside. The temperature at two points in the sample is measured using inserted thermocouples. Four partially saturated soil samples have been tested, i.e. homogeneous fine sand, homogeneous clayey silt, fine sand with an opening and clayey silt with sand inclusion. A small cell is used to measure the EC of soils with different porosity and degree of water saturation at different temperatures (from 20 °C to -15 °C), thereby the relationship between soils sample with known initial conditions and EC are obtained. The pre-existing more conductive and less conductive heterogeneities and ice content induced from freezing can totally be distinguished distinctly. The tomography images at different times are then reconstructed in temperature using the proposed equations and compared with the measured ones. The consistency between reconstructed and measured temperature demonstrates the correctness of the proposed equation. Then the tomography images are reconstructed to plot the ice content (or inversely, unfrozen water content) during freezing. This work serves as a pilot study to monitor ice formation in unsaturated frozen soils using geophysical techniques.

5.2 ERT results of homogeneous saturated samples

5.2.1 EC images of fine sand and clayey silt samples during freezing

A homogeneous saturated specimen of fine sand (see in Figure 3.29 a) is performed in the ERT setup during the freezing process. The sample is prepared at porosity around n=0.37, the degree of water saturation at around S_r=0.91. Due to the low retention capacity of sand, it is difficult to keep the exact degree of saturation throughout the sample. The size of the sample is 80 mm in diameter and 50 mm in height. The initial porosity and initial degree of water saturation are assumed constant along the sample and during the freezing process. Therefore, the measured variations of the local bulk EC of sand can be directly extrapolated to local variations of water freezing (or ice content) through the proposed modified second Archie's law described in Chapter 4.

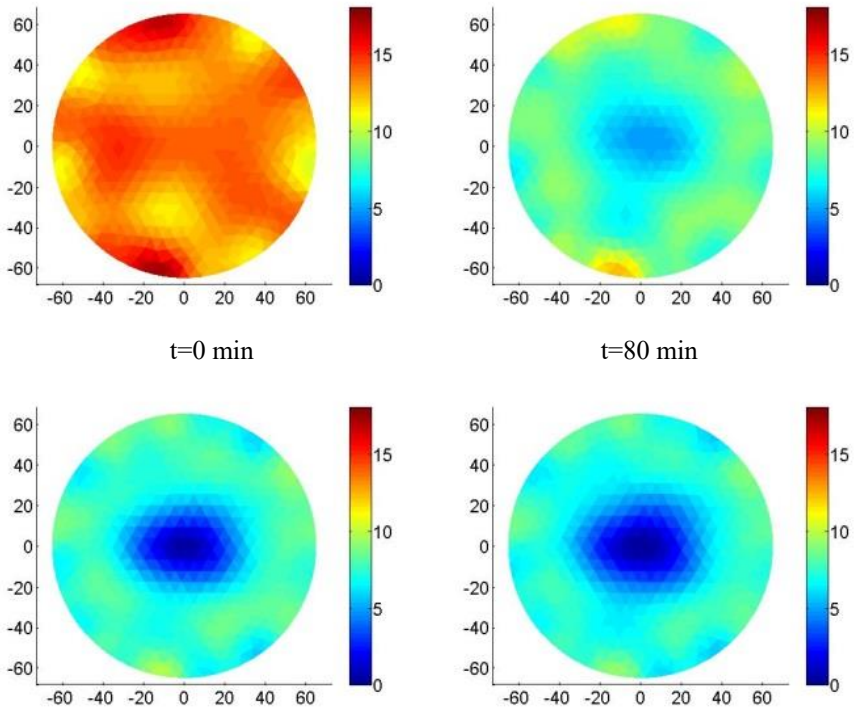

Figure 5.1 Two-dimensional freezing on homogeneous saturated sand sample 1 (n=0.38; S_r=0.91): images of the EC values at different times

In Figure 5.1, the reconstructed images of the EC of fine sand during freezing are presented. To shorten the number of plots, only images at the initial (0 min), 80 mins, 160 mins and 240 mins are shown, which give general variations of EC along time. It can be observed that at the initial state (0 min), the EC image is generally homogenous with values around 15 dS/m. Some small irregular contour of the image is probably due to the slight inhomogeneity of the sample preparation. The surface area and flatness of electrodes are not the same for all 16 electrodes, which also may induce some variability in the measurements. When the elasped time arrives at 80 mins, it is obviously the lower area that appears in the centre of the sample, around 5 dS/m, which indicates ice generation in this area. The EC of the remaining surface decreases to 10 dS/m because the EC of water has a strong temperature dependent response even though there is not phase change (details can be seen in Chapter 4). With elapsed time going on (from 80 mins to 240 mins), the EC of the lower zone becomes lower (close to 0

dS/m) and the area enlarges, which illustrates that the frozen area becomes larger and the ice content in this area becomes higher.

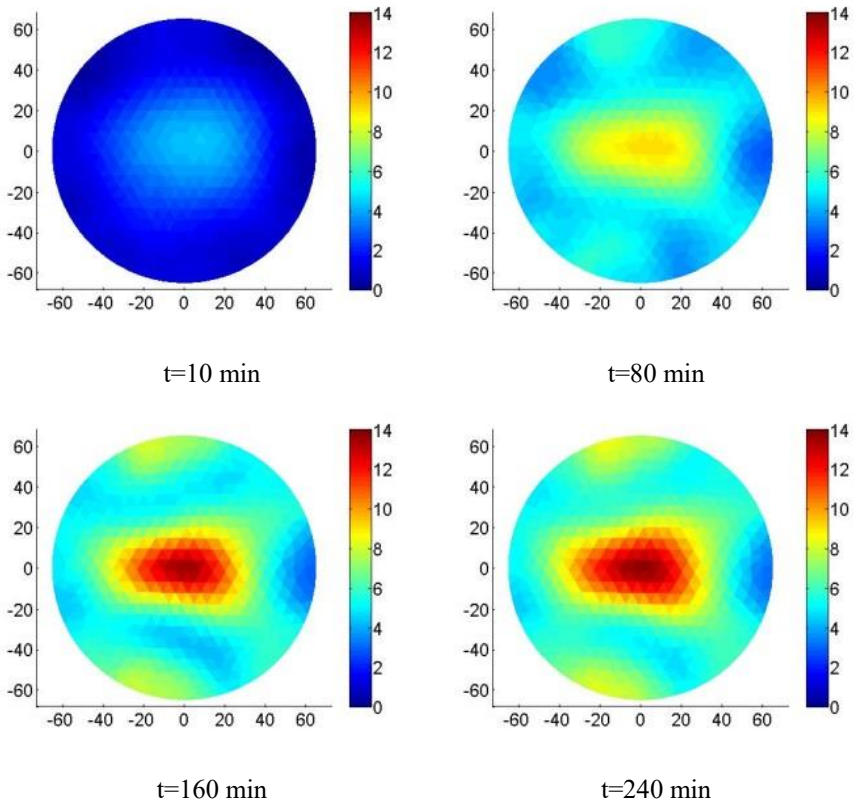

Figure 5.2 Two-dimensional freezing on homogeneous saturated sand sample 1 (n=0.38; S_r=0.91): images of the EC difference at different times compared with initial values

The differences of EC images at certain elapsed times compared with the initial state are plotted in Figure 5.2. The EC image at 10 mins has almost no change compared to the initial state except for a little drop at the centre. This means that the EC of the saturated fine sand is very sensitive to temperature. This temperature dependent behaviour of EC should be always considered when accurately detecting some properties of soils. The freezing rate at different area has inverse proportion with the distance from the centre, the closer the distance the higher freezing rate, and vice versa. Because the sample is frozen at the centre, the freezing rate is also affected by the thermal conductivity of the soil. The investigation in Chapter 4 has illustrated the thermal conductivity of soils is related to phase change between ice and water because the thermal conductivities of ice and water are 2.2 W/m·K and 0.6 W/m·K, respectively. It seems that the contours of EC difference (in Figure 5.2) are not exactly

circular compared with the ones of EC values (in Figure 5.1). These are mainly attributed to some inhomogeneity at the initial state (see Figure 5.1, t=0 min).

Two thermocouples are inserted into the samples at the position of 1/3 radius and 2/3 radius to explore the temperature evolutions of samples at different points during temperature decrease and freezing path. The temperature evolutions of these two points in the saturated fine sand along time are plotted in Figure 5.3. The fine sand sample is prepared at 18 °C, lower than room temperature. The temperatures of these two points decrease rapidly along the initial 50 minutes. Then the decrease of temperature goes slowly than at the beginning. When time goes to 150 minutes, the temperature at point A is lower than the freezing point (-3.2 °C), which means ice starts to be generated. At time 260 mins, the highest temperature is around -2 °C, which indicates this point can never be frozen with this system.

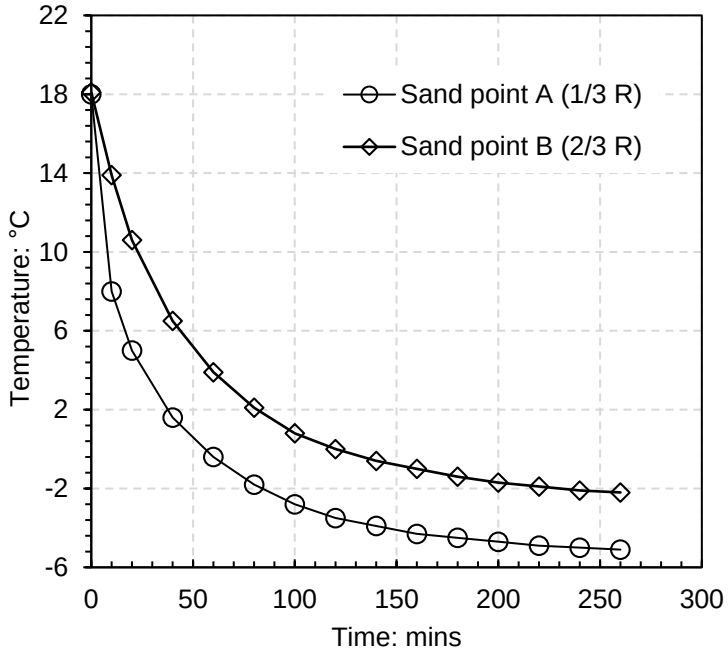

Figure 5.3 Temperature evolutions of selected points in the saturated fine sand during freezing path

A saturated clayey silt specimen has been also installed in the ERT setup and EC images at different times are measured during freezing. The sample is prepared at porosity n=0.26, the degree of water saturation S_r=100%. The size of the sample is 80 mm in diameter and 50 mm

in height. The initial porosity and initial degree of water saturation are assumed constant during the freezing process and along the sample, and therefore the measured variations of the local EC can be directly transferred to local variations of temperature or ice content.

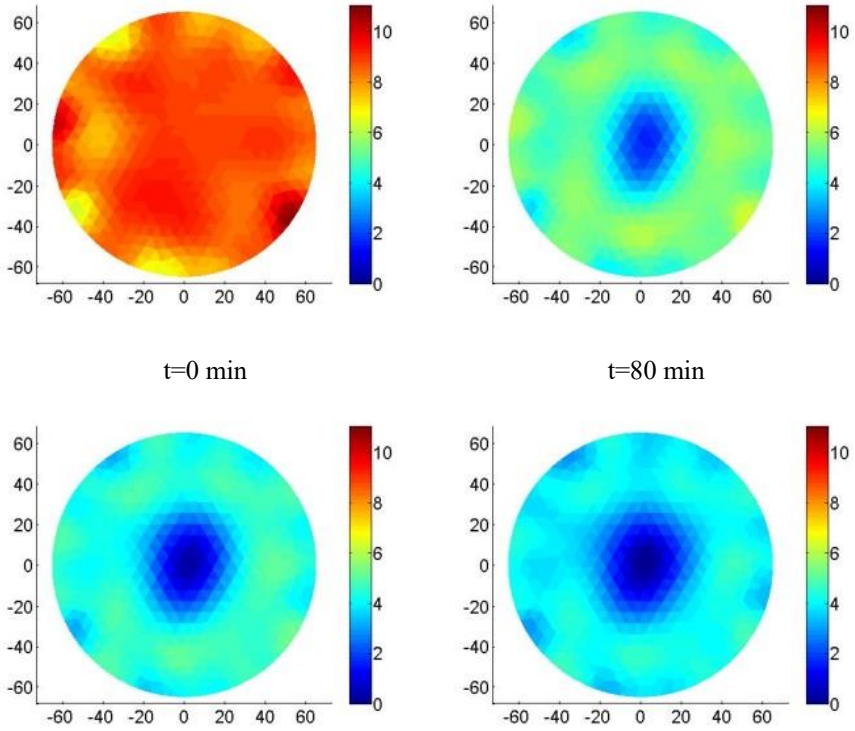

t=0 min t=80 min

t=160 min t=240 min

Figure 5.4 Two-dimensional freezing on homogeneous saturated clayey silt sample (n=0.26; S_r=1.00): images of the EC values at different times

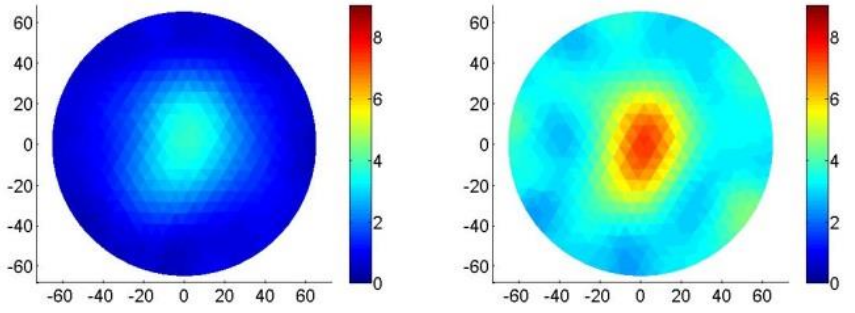

t=10 min t=80 min

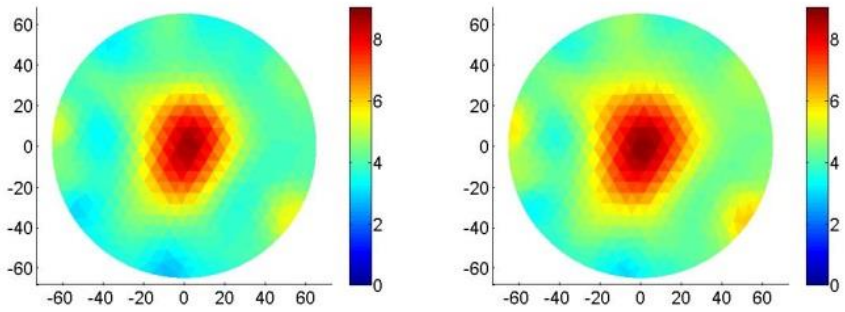

t=160 min t=240 min

Figure 5.5 Two-dimensional freezing on homogeneous saturated clayey silt sample (n=0.26; S_r=1.00): images of the EC difference at different times compared with initial values

The reconstructed images of measured EC of clayey silt at different times during freezing are plotted in Figure 5.4. There are only four images (at elapsed times 0 min, 80 mins, 160 mins and 240 mins) that are shown to give an idea of EC dropping during soil freezing. At the initial state (0 min), the EC image is homogeneous reaching values of 11 dS/m. Some small variations in the proximity of electrodes are probably caused by variations of the surface area and flatness of electrodes (silver foil). At 80 minutes, the EC at the centre of the soil sample drops to around 2 dS/m, which indicates ice is generated at this time. When time goes to 160 and 240 minutes, the frozen area becomes larger and the lowest value drops close to 0 dS/m, which means the maximum ice is formed. Except for the central area, the EC of the rest of the area also decreases during freezing. The reduction of EC is due to the EC of soil having a strong response to temperature without changing phase. The detailed interpretation can be found in Chapter 4, section 4.3.

In Figure 5.5, the differences of EC images of clayey silt at certain times compared with the initial state are plotted. The difference image at 10 mins shows the time-dependent properties of EC of clayey silt. The difference images of clayey silt at certain times also show axi-symmetric properties, which indicates that the prepared clayey silt sample is homogeneous and unified. It can be seen that the sample is only partially frozen after 240 minutes. The frozen area is around 1/3 of the whole area. In the frozen area, there are also some variations

due to the deviation of ice content, which relates to temperature and time. Other interpretations of the images are similar to fine sand samples in section 5.2.1.

As a similar measurement to that performed with fine sand, the temperature evolutions of selected points in saturated clayey silt during freezing path are shown in Figure 5.6. The clayey silt sample is prepared at 22 °C. At the initial stage, the temperature sharply drops to a freezing point due to the sensitive temperature-dependent properties of EC. When it reaches the freezing point, the phase change will take place, which increases the total thermal conductivity of soils. The increase of thermal conductivity will slow down the freezing rate at this central zone. The freezing process of clayey silt starts at around 200 minutes, which indicates a slower freezing process compared to the fine sand sample. Point B is not frozen until 260 minutes.

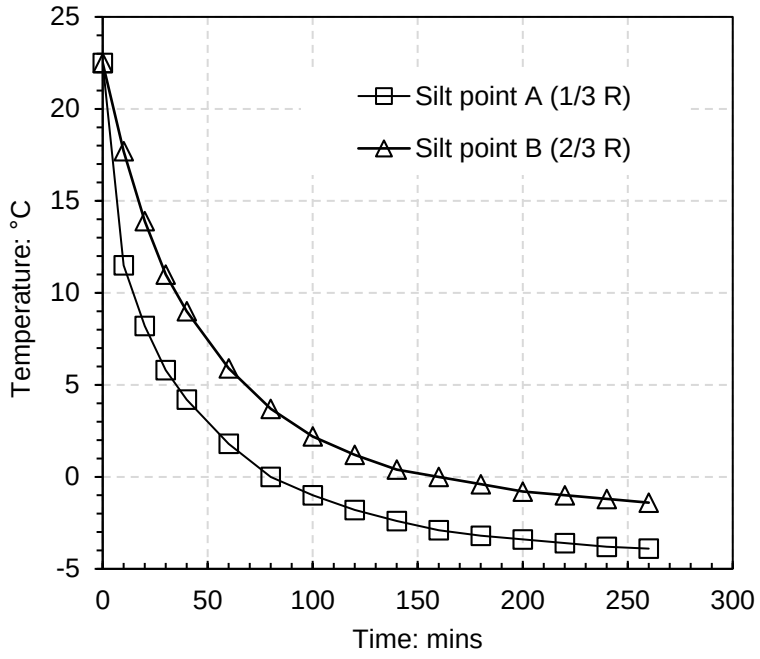

Figure 5.6 Temperature evolutions of selected points in saturated clayey silt during freezing path

5.2.2 Reconstructed images of temperature

As described in Section 4.3, the bulk EC of soils (fine sand and clayey silt) can be linked with soil initial porosity, initial degree of water saturation and temperature, which is deduced from Archie's second law above the freezing point T_0, as shown below:

$$\sigma_T^* = \sigma_T(T) n^p S_r^q = (aT + b) n^p S_r^q \quad (T \geq T_0) \tag{5.1}$$

In which, parameters *a* and *b* can be estimated from pure 5% NaCl solution (interstitial water in the experiments) measurements during temperature decrease from 20 °C to 0 °C where the phase change does not occur. The relationship between EC and temperature is linear in this range. The fitted parameters *a* and *b* are 1.32 and 42.45, respectively. Meanwhile, the parameters *p* and *q* are quite dependent on soil properties, which are determined by several experiments on fine sand and clayey silt with various initial porosities and saturation degrees. The detailed information can be found in Section 4.3. After determining all model parameters, the equation for describing the relationship between bulk EC and temperature above freezing point can be presented as:

Fine sand:

$$\sigma_T^* = (1.32T + 42.45) n^{1.65} S_r^{1.86} \quad (T \geq T_0) \tag{5.2}$$

Clayey silt:

$$\sigma_T^* = (1.32T + 42.45) n^{1.85} S_r^{2.08} \quad (T \geq T_0) \tag{5.3}$$

Below the freezing point (-3.2 °C), the measurements of bulk EC are no longer linear due to phase change from water to ice. In order to find a simple method to describe the relationship between bulk EC and temperature in the range of the frozen range, the following inverse function is applied to fit the results:

$$\sigma_T^* = -\frac{k}{T} \quad (T < T_0) \tag{5.4}$$

where *k* has a response to the initial volumetric water content of the soil, $k = \beta n S_r$, T< -3.2 °C is temperature, β=118 is constant that can be obtained from pure 5% NaCl solution (see Figure 5.7). Substituting $k = \beta n S_r$ into Equation (5.4), the expression of describing the total EC of soil along the temperature below freezing point can be presented as

$$\sigma_T^* = -\frac{\beta n S_r}{T}\left(T < T_0\right) \tag{5.5}$$

The expressions describing the bulk EC of fine sand and clayey silt along the temperature range (from 20 °C to -15 °C) can be plotted as follows:

Fine sand:

$$\sigma_T^* = \begin{cases} \left(1.32T + 42.45\right) n^{1.65} S_r^{1.86} & \left(T \geq T_0\right) \\ -118 n^{1.65} S_r^{1.86} / T & \left(T < T_0\right) \end{cases} \tag{5.6}$$

Clayey silt:

$$\sigma_T^* = \begin{cases} \left(1.32T + 42.45\right) n^{1.85} S_r^{2.08} & \left(T \geq T_0\right) \\ -118 n^{1.85} S_r^{2.08} / T & \left(T < T_0\right) \end{cases} \tag{5.7}$$

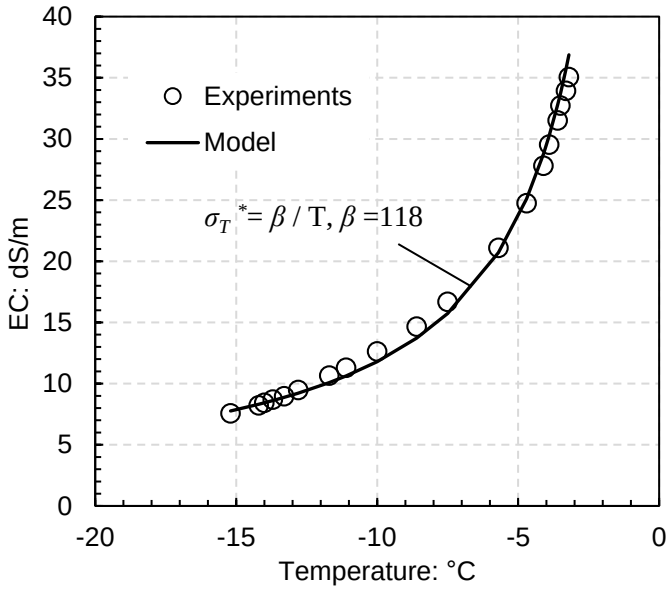

Figure 5.7 Measured and fitting results of EC of pure 5% NaCl solution at low temperature

As described in Section 4.3, the bulk EC of fine sand and clayey silt samples with various initial porosities and saturation degrees are plotted in Figure 5.8 and 5.10, respectively. The equations proposed above are then used to fit the experimental results. The fitting results give a good agreement with the measurements of both soils. The 1:1 scatter plot of calculated vs measured results of fine sand and clayey silt are plotted in Figure 5.9 and 5.11, respectively.

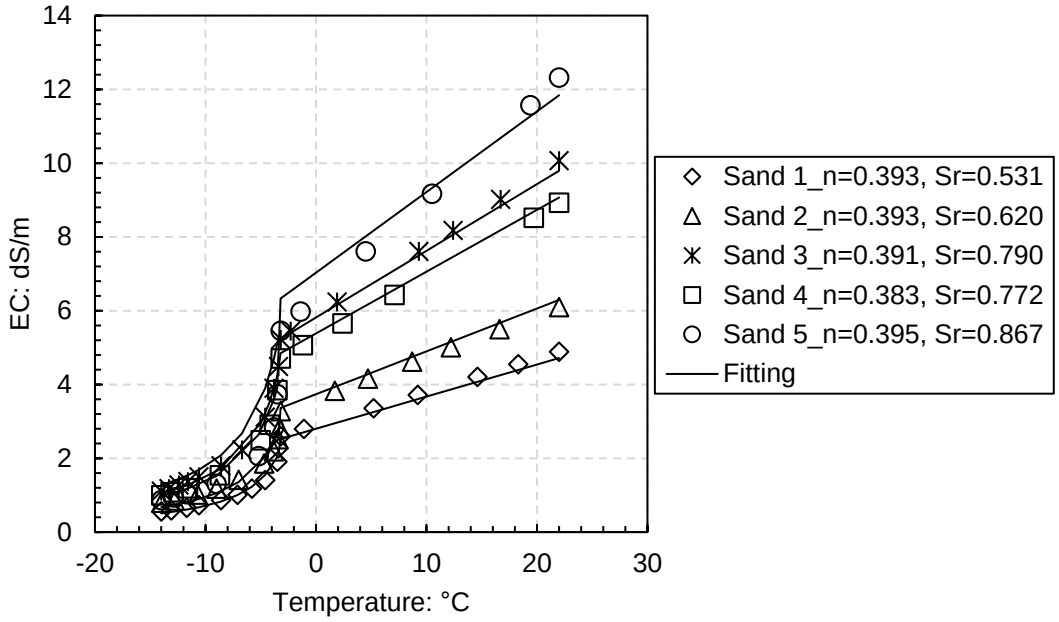

Figure 5.8 Comparison of measured and calculated bulk EC of fine sand samples along the temperature decrease and freezing path

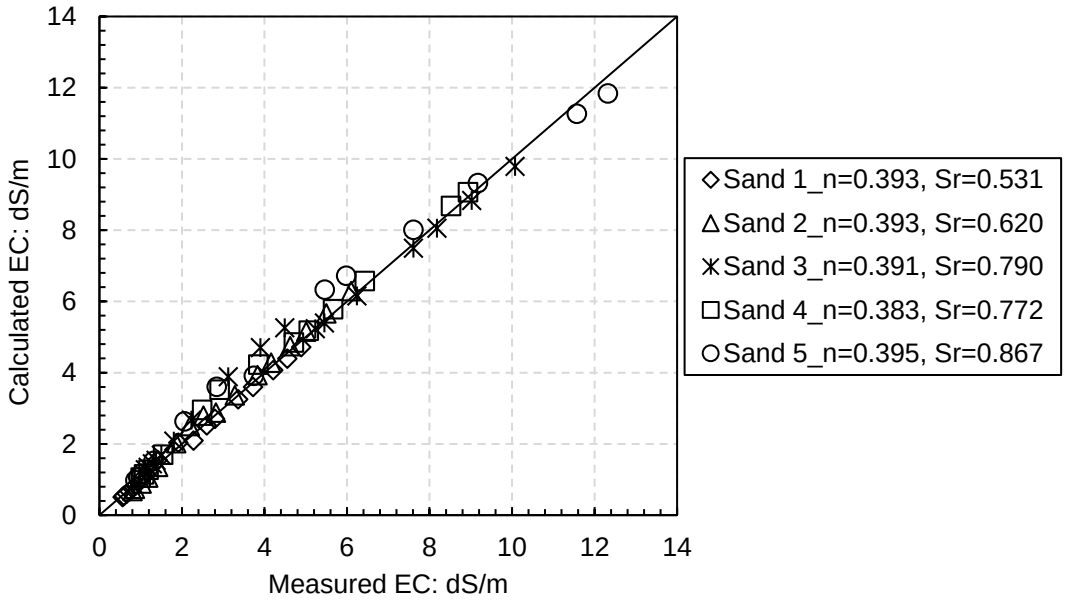

Figure 5.9 The 1:1 scatter plot of measured and calculated bulk EC of fine sand along the temperature decrease and freezing path

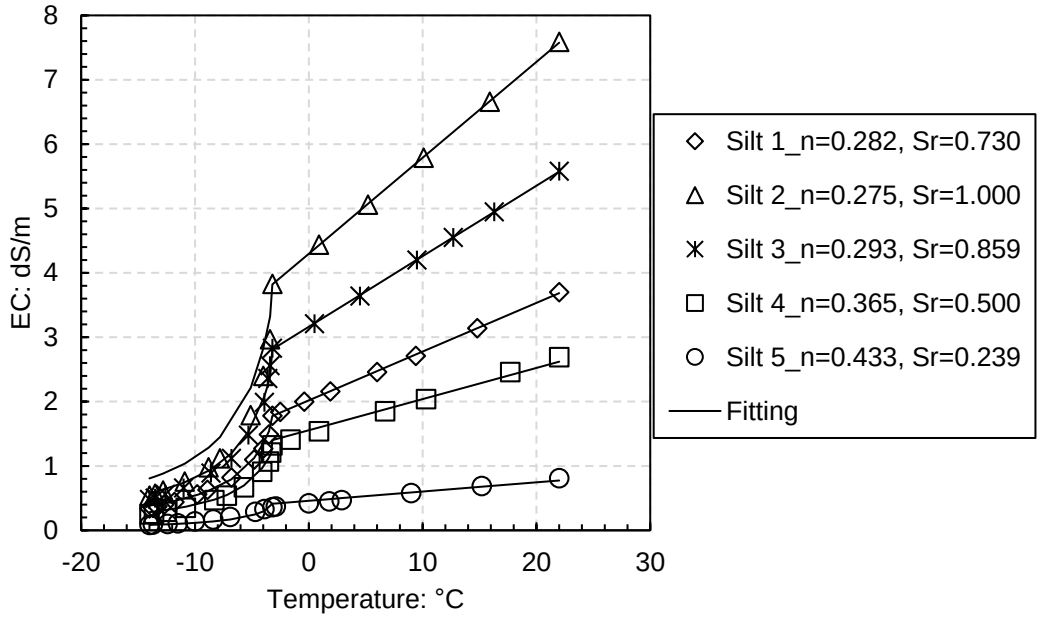

Figure 5.10 Comparison of measured and calculated bulk EC of clayey silt samples along the temperature decrease and freezing path

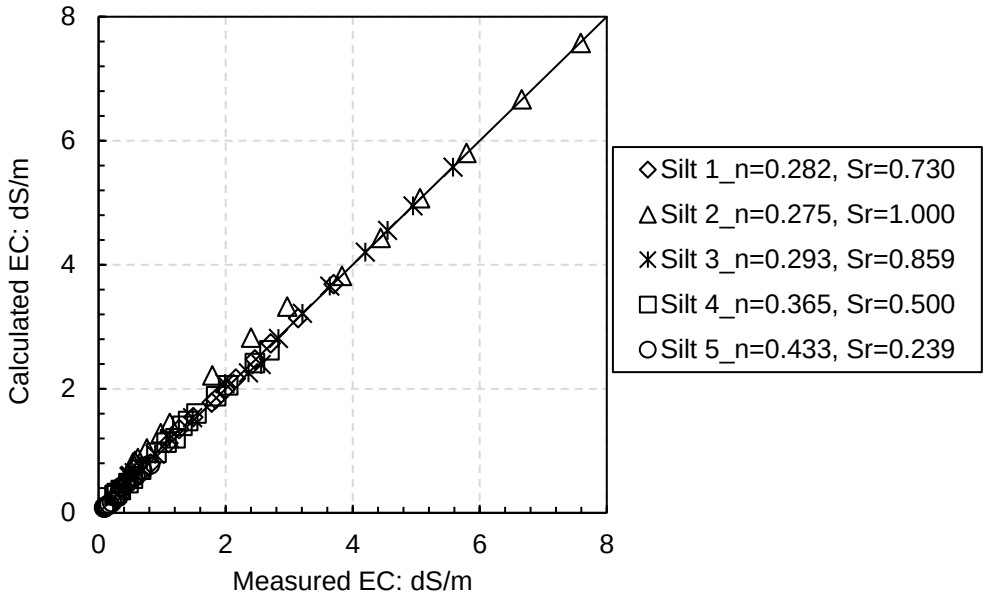

Figure 5.11 The 1:1 scatter plot of measured and calculated bulk EC of clayey silt along temperature decrease and freezing path

Based on the obtained Equations (5.6) and (5.7), the images of EC can be transferred to temperature images. It is meaningful to understand the temperature evolution during soil freezing. The reverted Equations can be rewritten as:

$$T=\begin{cases}\dfrac{\sigma_T^*}{an^pS_r{}^q}-\dfrac{b}{a} & \left(\sigma_T^*\geq\left(aT_0+b\right)n^pS_r{}^q\right)\\ -118n^pS_r{}^q\Big/\sigma_T^* & \left(\sigma_T^*<\left(aT_0+b\right)n^pS_r{}^q\right)\end{cases} \tag{5.8}$$

Introducing the different values of each parameter for fine sand and clayey silt, the equation can be plotted as:

Fine sand:

$$T=\begin{cases}\dfrac{\sigma_T^*}{1.32n^{1.65}S_r^{1.86}}-32.16 & \left(\sigma_T^*\geq 38.23n^{1.65}S_r^{1.86}\right)\\ -118n^{1.65}S_r^{1.86}\Big/\sigma_T^* & \left(\sigma_T^*<38.23n^{1.65}S_r^{1.86}\right)\end{cases} \tag{5.9}$$

Clayey silt:

$$T=\begin{cases}\dfrac{\sigma_T^*}{1.32n^{1.85}S_r^{2.08}}-32.16 & \left(\sigma_T^*\geq 38.23n^{1.85}S_r^{2.08}\right)\\ -118n^{1.85}S_r^{2.08}\Big/\sigma_T^* & \left(\sigma_T^*<38.23n^{1.85}S_r^{2.08}\right)\end{cases} \tag{5.10}$$

When transferring to images of temperature from EC for saturated fine sand and clayey silt samples (see Figure 5.1 and 5.4), their initial porosity and degree of water saturation are introduced into Equation (5.9) and (5.10). Then, the equations become:

Fine sand:

$$T=\begin{cases}\dfrac{\sigma_T^*}{0.22}-32.16 & \left(\sigma_T^*\geq 6.50\ dS/m\right)\\ -18.36\Big/\sigma_T^* & \left(\sigma_T^*<6.50\ dS/m\right)\end{cases} \tag{5.11}$$

Clayey silt:

$$T=\begin{cases}\dfrac{\sigma_T^*}{0.14}-32.16 & \left(\sigma_T^*\geq 4.08\ dS/m\right)\\ -11.52\Big/\sigma_T^* & \left(\sigma_T^*<4.08\ dS/m\right)\end{cases} \tag{5.12}$$

After using MATLAB program, the calculated temperature images of fine sand and clayey silt are shown in Figures 5.12 and 5.13. The images show that the variations in temperature are axi-symmetric, which means the prepared samples of fine sand and clayey silt are homogeneous. The small deviations in the proximity of the electrodes are probably due to contact problems between soil and electrodes.

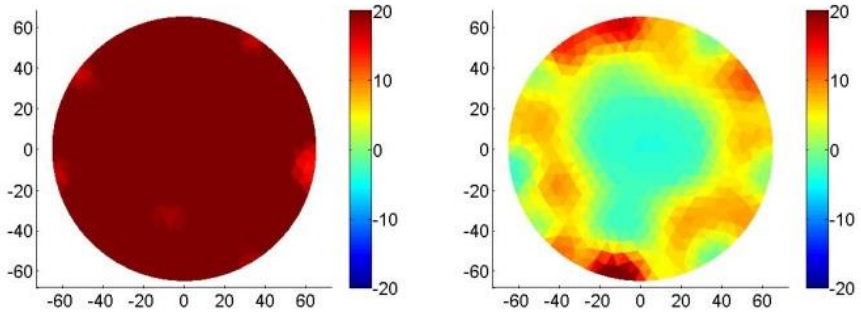

t=0 min t=80 min

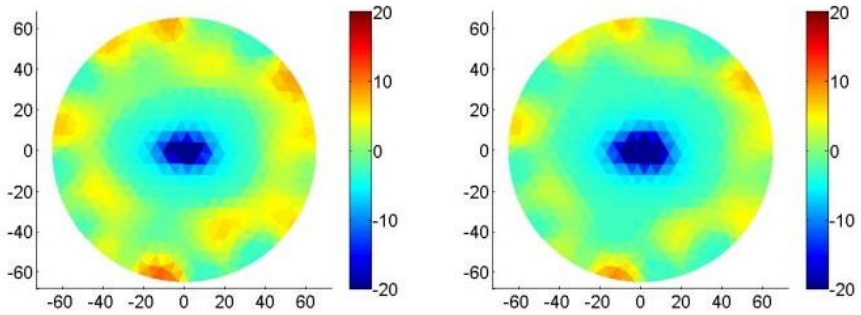

t=160 min t=240 min

Figure 5.12 Two-dimensional freezing on the homogeneous saturated sand sample (n=0.38; S_r=0.91): images of the temperature values at different times

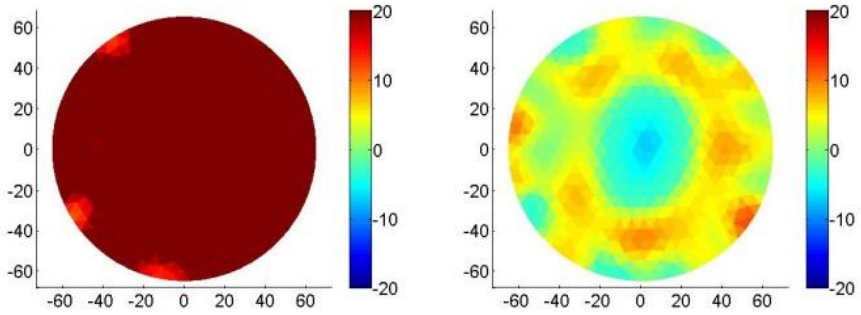

t=0 min t=80 min

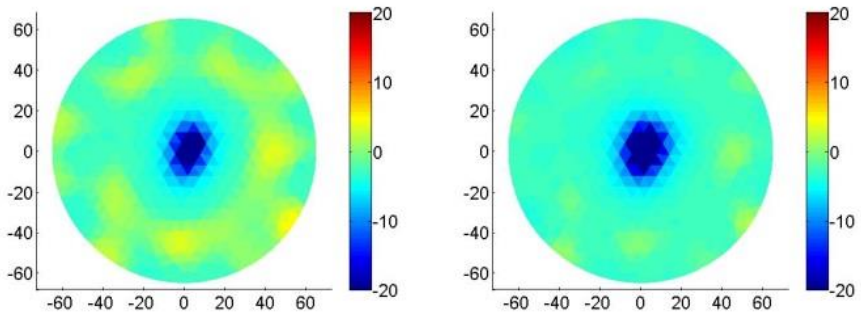

t=160 min t=240 min

Figure 5.13 Two-dimensional freezing on homogeneous saturated clayey silt sample (n=0.26; S_r=1.00): images of the temperature values at different times

To validate the proposed expressions for the two soils, which are used to extrapolate temperature from EC values, the reconstructed temperature results are compared with measured ones. The temperature values of mesh points at the positions of 1/3 radius and 2/3 radius are selected. The comparisons of measured and reconstructed temperatures of point A and B for fine sand and clayey silt are plotted in Figure 5.14 (a) and 5.14 (b), respectively. The reconstructed results have a quite good agreement with measured ones. Their consistency demonstrates the reliability of the proposed equations. Thereby, the proposed Equation (5.9) and (5.10) can be used to describe the temperature evolutions from EC measurements with known sample initial porosity and degree of water saturation.

5.2.3 Reconstructed images of ice content

As interpreted in section 4.3 of Chapter 4, the unfrozen water content (inversely, ice content) in partially saturated frozen soils at different temperature can be described by Equation 5.13. The detailed derivation of this equation can be found in Appendix A.

$$S_l = S_r \frac{\sigma_m}{\sigma_T^*} = \frac{\sigma_m}{\sigma_T(T)} n^{-p} S_r^{1-q} \tag{5.13}$$

By introducing the values of each parameter for different soils, the expressions for describing fine sand can be presented as:

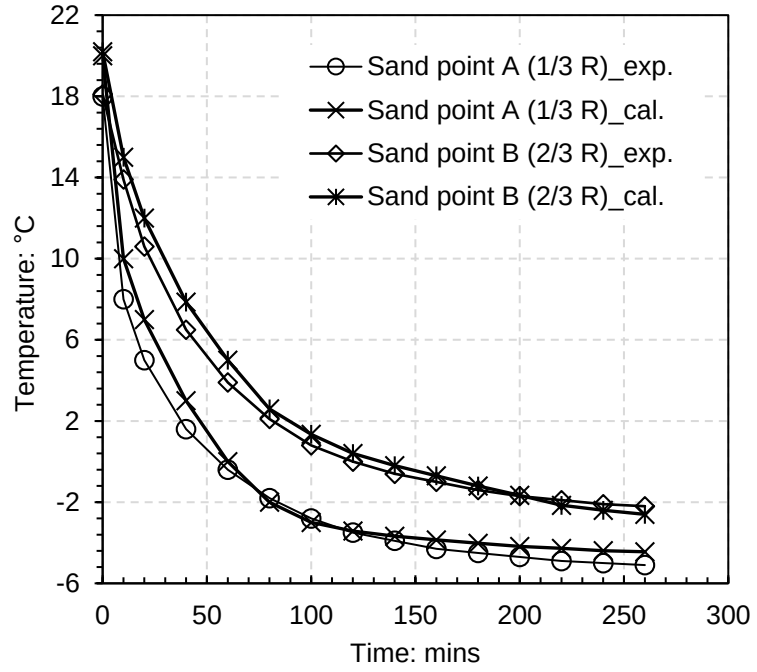

(a)

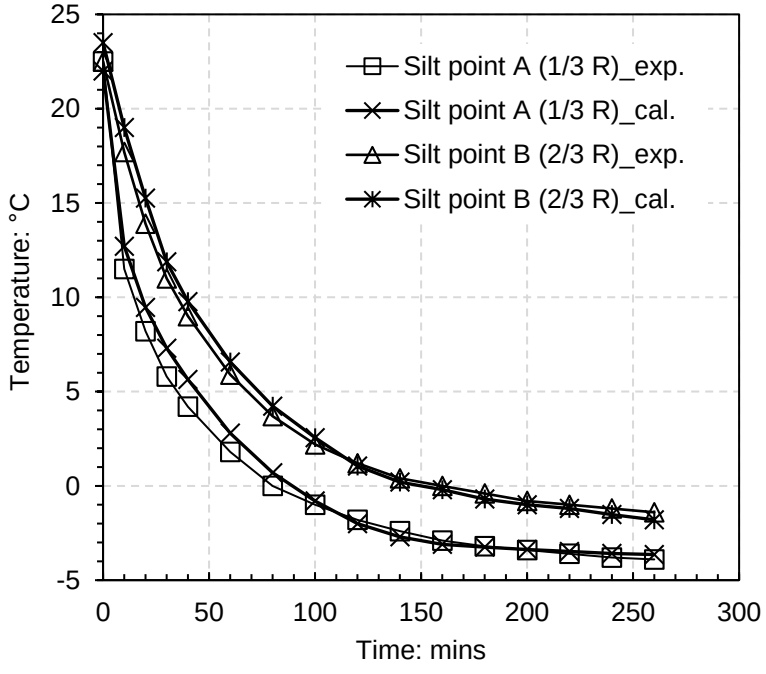

(b)

Figure 5.14 Comparison of reconstructed and measured temperature in ERT test: (a) saturated fine sand and (2) saturated clayey silt

$$S_l = \frac{\sigma_m n^{-1.65} S_r^{-0.86}}{1.32T + 42.45} \tag{5.14}$$

In a similar way, for clayey silt, it has

$$S_l = \frac{\sigma_m n^{-1.85} S_r^{-1.08}}{1.32T + 42.45} \tag{5.15}$$

When reconstructing the images of the unfrozen water content of the saturated fine sand sample, the initial porosity n=0.38 and initial degree of water saturation S_r=0.91 are introduced into Equation (5.14). It has:

$$S_l = \frac{5.35\sigma_m}{1.32T + 42.45} \tag{5.16}$$

The reconstructed images of unfrozen water content (inversely, ice content) of saturated fine sand at different temperatures (0 min, 80 mins, 160 mins and 240 mins) are presented in Figure 5.15. At the initial state, the whole sample is in the unfrozen state with an initial water saturation of 0.91. At 80 minutes, the frozen area generates but with lower ice content. The unfrozen water content is around 0.7–0.8. When elapsed time reaches to 160 minutes, the frozen area becomes larger than before. The unfrozen water content currently drops down to 0.1–0.2 in the centre. The frozen area is axi-symmetric. The unfrozen water content has an inverse proportion with radius, closer to centre the lower the unfrozen water content is, and vice versa. At the time of 240 minutes, the frozen area is more lager than that of 160 minutes. It is important to point out that the soil sample is not fully frozen even in the central area due to the difficulty of freezing interstitial water in small pores. The detailed interpretation can be found in Chapter 4. The inhomogeneity around the boundary is due to the contact problem of electrodes and soils, which does not mean the ice generates in that area.

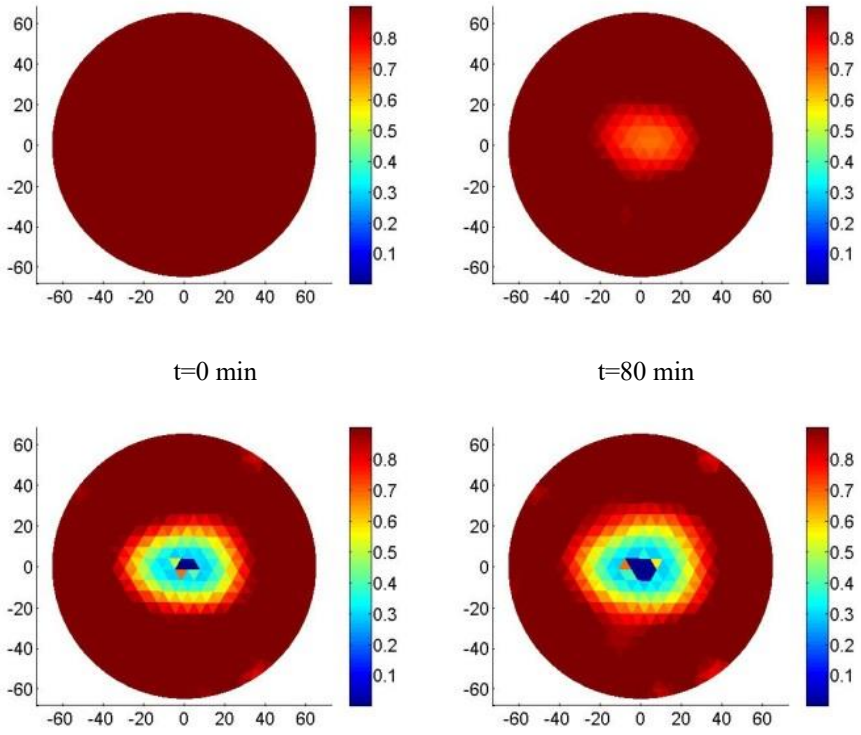

Figure 5.15 Two-dimensional freezing on the homogeneous saturated fine sand sample (n=0.38; S_r=0.91): images of the unfrozen water content at different times

When reconstructing the images of unfrozen water of saturated clayey silt sample, the initial porosity n=0.26, initial degree of water saturation S_r=1.00 are introduced into Equation 5.15. It simplifies to:

$$S_l = \frac{12.09\sigma_m}{1.32T + 42.45} \tag{5.17}$$

When using Equation (5.14) to link the images of EC and temperature, the unfrozen water content of saturated clayey silt sample at different times are presented in Figure 5.16. Similar behaviour with the fine sand sample can be found in these images. Compared with fine sand, the clayey silt has a slower freezing rate due to the lower porosity of sample that makes freezing more difficult to develop. A good performance of ERT setup can be observed in both soils, which demonstrates its ease to use in detecting ice content in frozen soils.

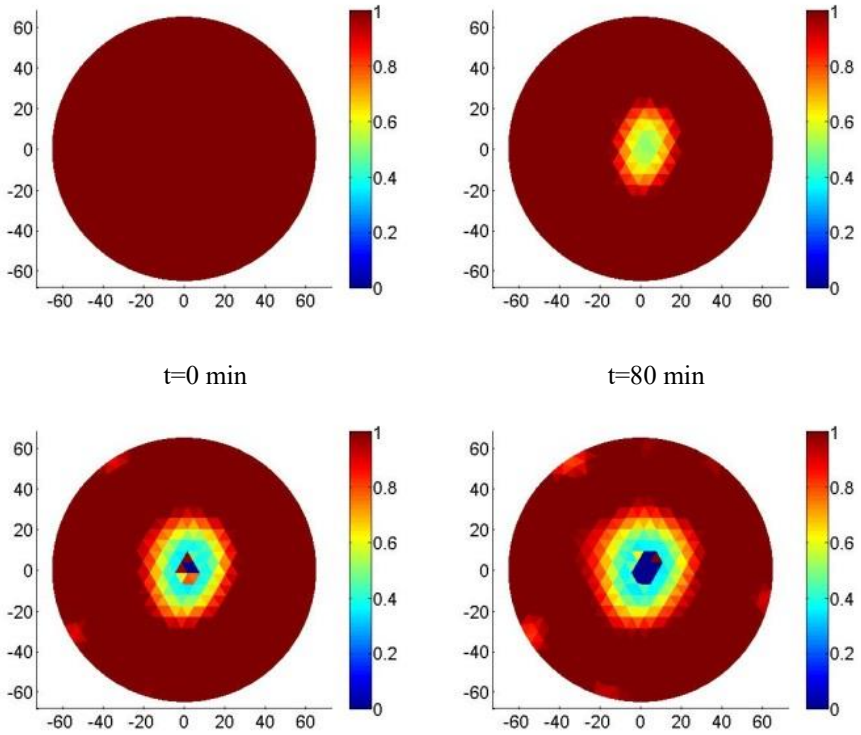

Figure 5.16 Two-dimensional freezing on homogeneous saturated clayey silt sample (n=0.26; S_r=1.00): images of the unfrozen water content at different times

5.3 ERT results of homogeneous unsaturated samples

Compared with homogeneous saturated soil samples, the homogeneous partially saturated ones have some special behaviour due to existing suction associated with partial saturation and the induced cryogenic suction on freezing. These suction in soils may cause the water migration to occur during freezing from unfrozen area to frozen area. In this section, two unsaturated fine sand samples and two unsaturated clayey silt samples with different initial water saturation are presented and analysed. In order to understand water migration in frozen soils, unsaturated fine sand with three freezing-thawing cycles is also discussed.

5.3.1 EC images of fine sand and clayey silt samples during freezing

A homogeneous fine sand 2 with the initial porosity n = 0.38 and saturation degree S_r = 0.55 is performed in ERT setup and its images of EC at different freezing times are presented in Figure 5.17. Similar results of fine sand 3 with initial porosity n = 0.37 and water saturation S_r = 0.70 are presented in Figure 5.18. In the initial stage of freezing, the EC images of both samples are generally uniform but with different average values. The EC of fine sand 2 is around 8 dS/m, lower than that of fine sand 3, which is approximately 12 dS/m. The EC difference for both samples at the initial state is mainly due to the difference in the initial degree of water saturation. The higher the initial saturation of sample, the higher the EC values will be obtained.

After freezing process is performed on samples, the axi-symmetric decrease of EC can be observed in the images of both samples along time. It is interesting to find that, different from the phenomenon of the saturated sample, the contours in the unfrozen area are not homogeneous. An annular contour in the image during freezing occurs with EC values at the centre and the boundary that are similar, the area of higher values is in the middle between the centre and the boundary. A similar phenomenon of sand sample 2 and sand sample 3 can be observed but with different EC values.

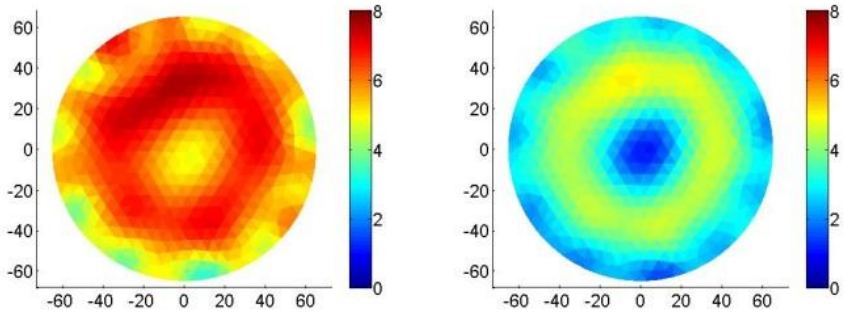

t=10 min t=80 min

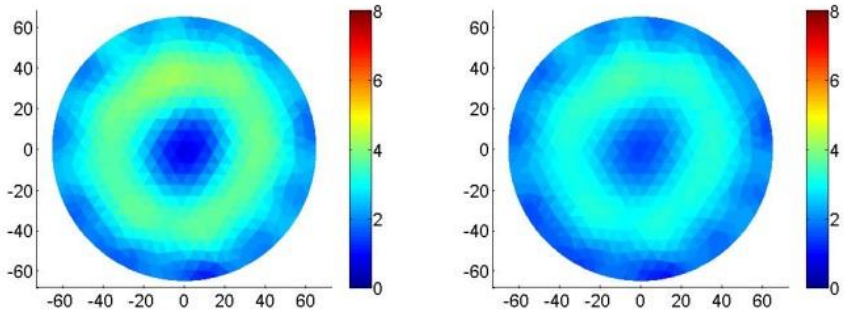

t=160 min t=240 min

Figure 5.17 Two-dimensional freezing on homogeneous unsaturated sand sample 2 (n=0.38; S_r=0.55): images of the EC values at different times

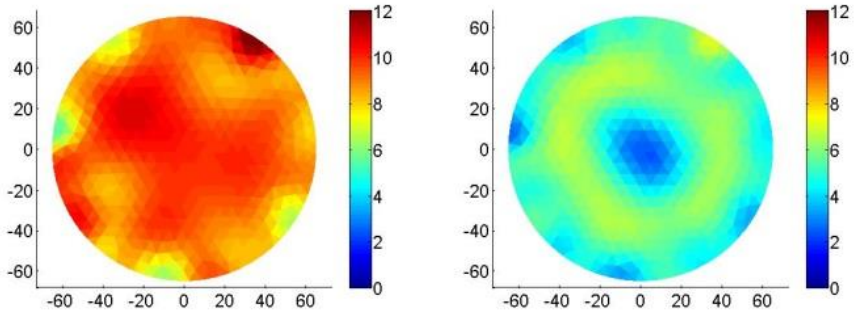

t=0 min t=80 min

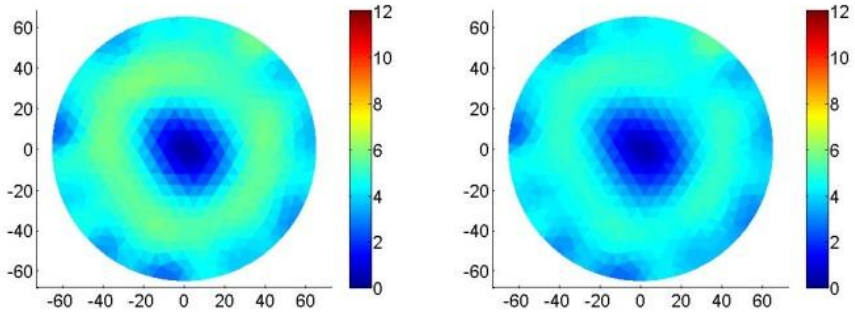

t=160 min t=240 min

Figure 5.18. Two-dimensional freezing on homogeneous unsaturated sand sample 3 (n=0.37; S_r=0.70): images of the EC values at different times

To clearly investigate the behaviour of sand freezing, the EC difference images compared with the initial state of two sand samples are presented in Figures 5.19 and 5.20, respectively. The maximum EC drop in sand 2 is around 5 dS/m, lower than that of sand 3, due to the lower initial degree of water saturation in sand 2. As shown in Figure 5.19, the EC difference images of t=10 minutes and t=80 minutes have axi-symmetric variations of EC. This means the prepared sand sample is homogeneous and the variations of EC are caused by the temperature decrease without phase change or with a little phase change from water to ice. At time t=160 minutes, the ice generates obviously at the centre of the sample, which induces high cryogenic suction in the frozen area. The cryogenic suction would absorb the interstitial water from unfrozen area to frozen area. That is why the EC difference contours of t=160 minutes and t=240 minutes are a little chaotic and non-axi-symmetric. In contrast, the EC difference contours of sand 3 have a more regular behaviour than that of sand 2 because the higher initial water saturation of sand 3 that induces lower suction.

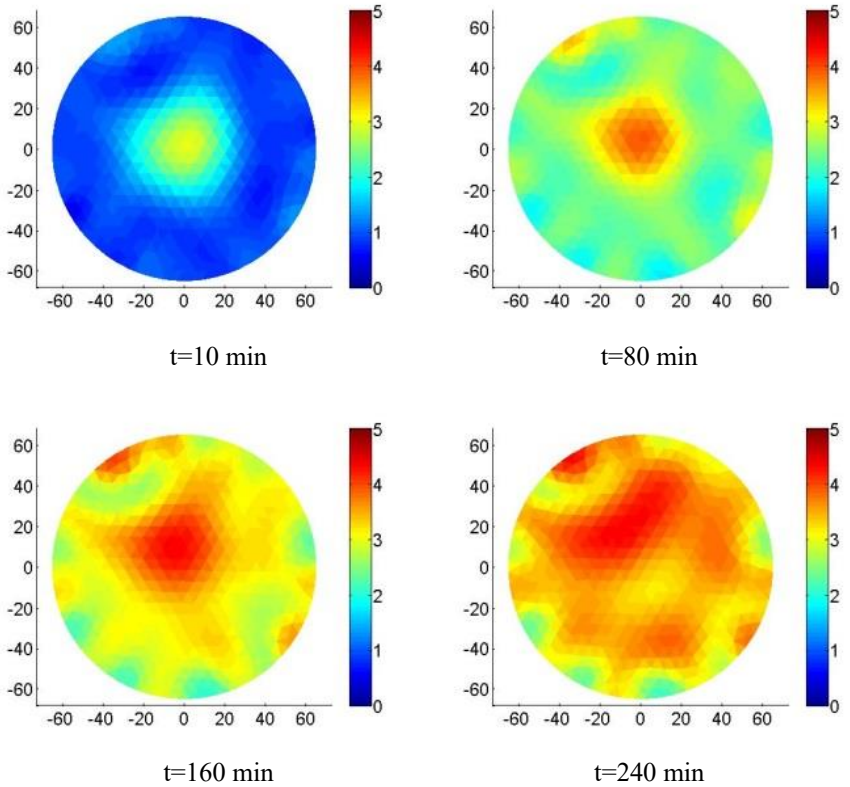

Figure 5.19 Two-dimensional freezing on homogeneous unsaturated sand sample 2 (n=0.38; S_r=0.55): images of the EC difference at different times compared with initial values

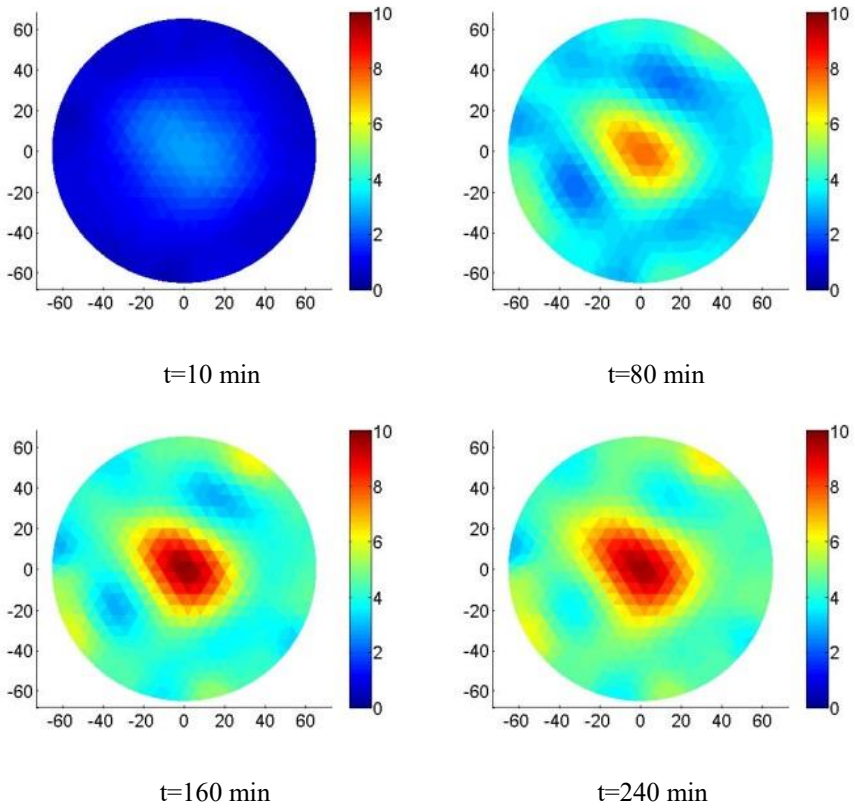

Figure 5.20 Two-dimensional freezing on homogeneous unsaturated sand sample 3 (n=0.37; S_r=0.70): images of the EC difference at different times compared with initial values

For similarity, a homogeneous clayey silt sample 2 with the initial porosity n=0.36 and saturation S_r=0.52 is tested using the ERT setup along the freezing path and its images of measured EC at different times are plotted in Figure 5.21. Meanwhile, homogeneous clayey silt sample 3, with initial porosity n=0.30 and initial water saturation S_r=0.84, is also tested using the same procedure as sample 2. EC images of sample 2 at different times are shown in Figure 5.22. The images of EC for two clayey silt samples at the beginning of the test show the homogeneous properties of the samples. The average EC value of clayey silt 2 is lower than that of clayey silt 3; they are 5 dS/m and 8 dS/m, respectively. It is due to the differences in the initial degree of water saturation between the two soils since clayey silt 2 has a lower saturation than clayey silt 3.

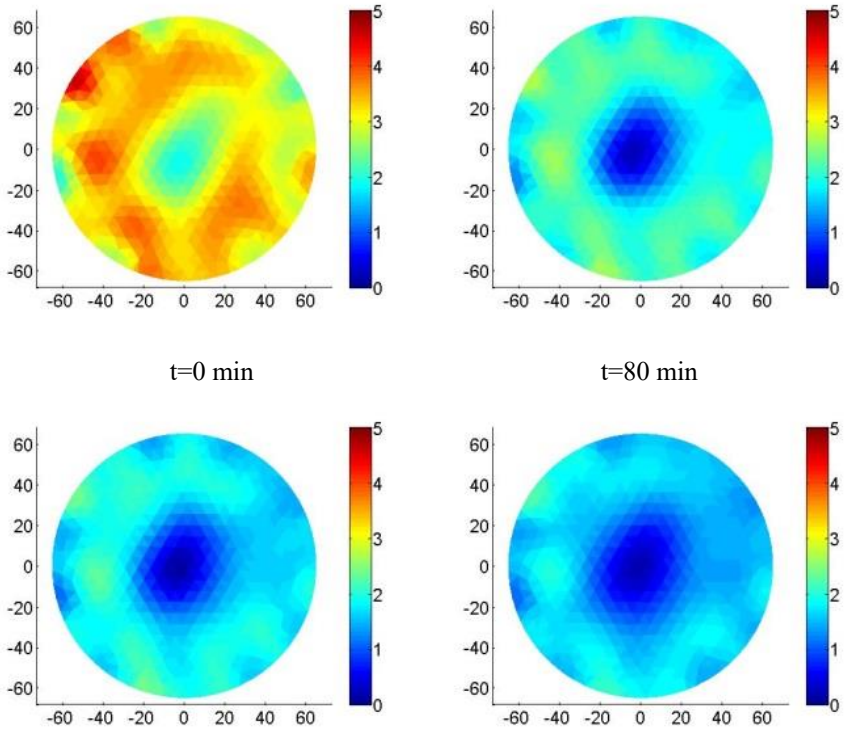

Figure 5.21 Two-dimensional freezing on homogeneous unsaturated clayey silt sample 2 (n=0.36; S_r=0.52): images of the EC values at different times

Compared with the experimental results of clayey silt sample 3, the clayey silt sample 2 has more chaotic EC contours at different times during the freezing process, which is due to existing higher suction and induced cryogenic suction. An annular contour can also be found in unsaturated clayey silt samples 2 and 3, the lower EC area occurs not only at the centre but also at the boundary of the samples. As discussed above, the lower electrical conductivities in the central area is due to the phase change in the frozen state. However, the lower electrical conductivities near boundary do not mean the ice generates but the interstitial water in the soils is migrated from boundary area to the middle area due to the suction difference between these two zones.

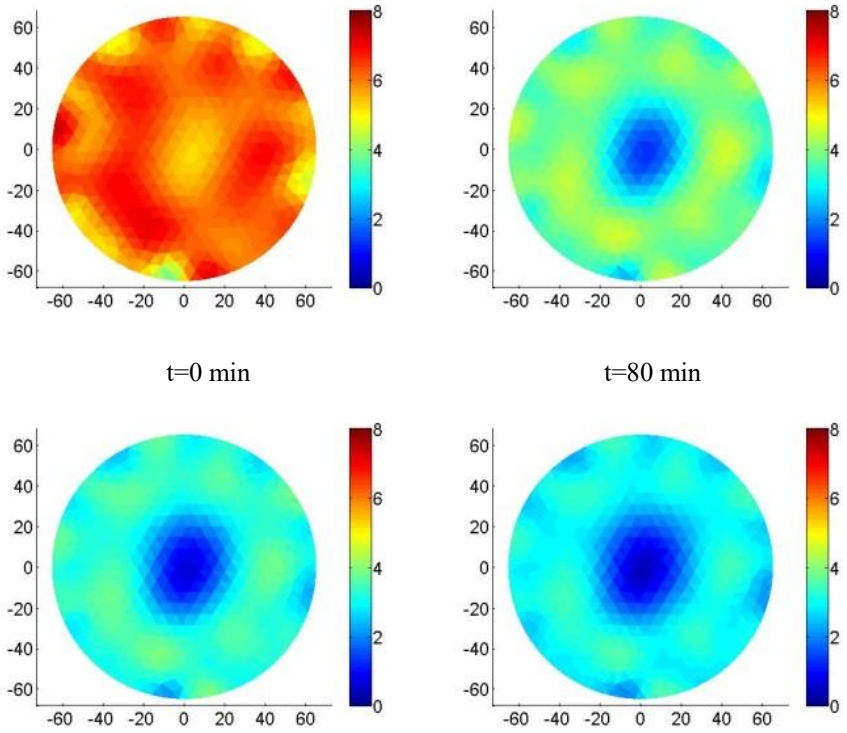

t=0 min t=80 min

t=160 min t=240 min

Figure 5.22 Two-dimensional freezing on homogeneous unsaturated clayey silt sample 3 (n=0.30; S_r=0.84): images of the EC values at different times

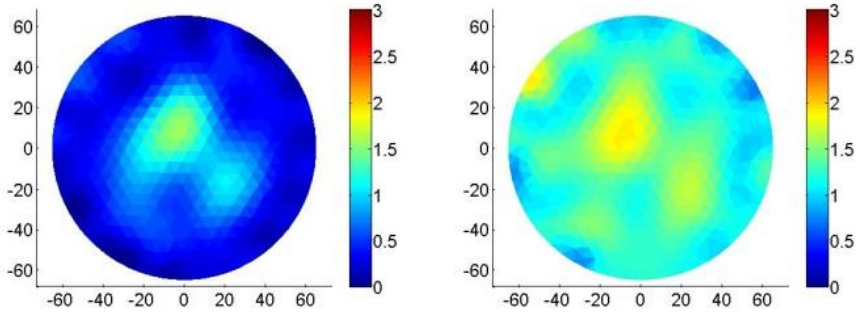

t=10 min t=80 min

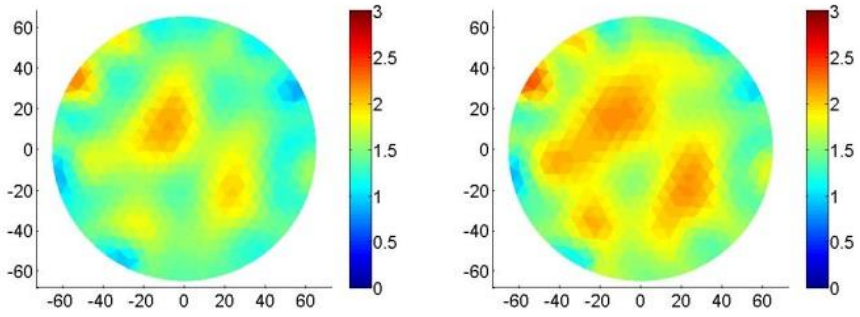

t=140 min t=240 min

Figure 5.23 Two-dimensional freezing on homogeneous unsaturated clayey silt sample 2 (n=0.36; S_r=0.52): images of the EC difference at different times compared with initial values

For clearly interpreting the behaviour of unsaturated clayey silt soils freezing, the EC difference images between certain freezing times and initial state are also indicated here (see Figure 5.23 and 5.24). As interpreted in unsaturated fine sand samples, the chaotic contours are caused by the induced cryogenic suction. It is interesting to find that, the clayey silt sample with an initial degree of water saturation S_r=0.84 has more chaotic EC contours compared with the fine sand sample 3 (S_r=0.70). This is mainly due to the clayey silt sample has higher suction than fine sand, the detailed measurements of suction in two soils can be found in Chapter 3, section 3.2 (soil properties).

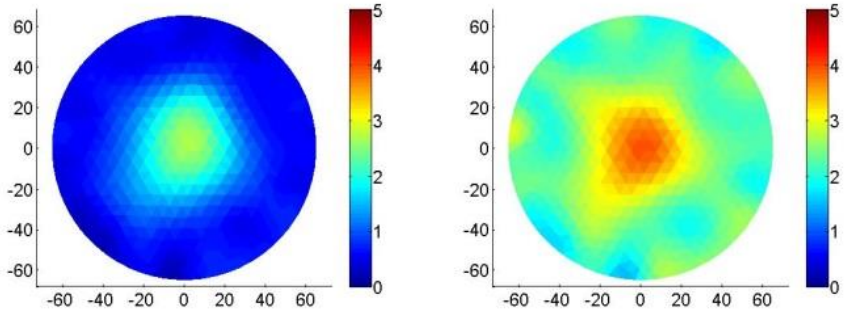

t=10 min t=80 min

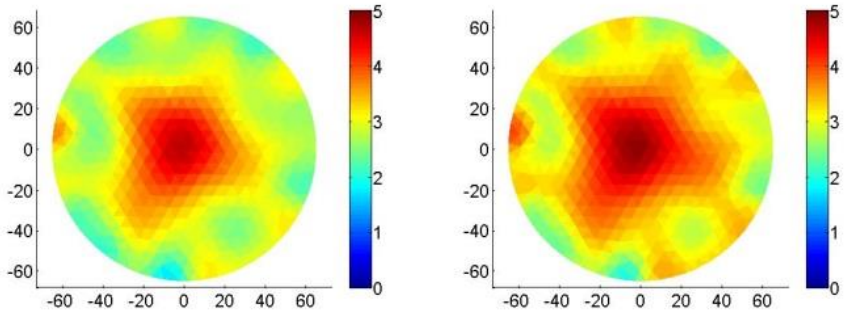

t=160 min t=240 min

Figure 5.24 Two-dimensional freezing on homogeneous unsaturated clayey silt sample 3 (n=0.30; S_r=0.84): images of the EC difference at different times compared with initial values

5.3.2 EC images of fine sand with three freezing-thawing cycles

In the above sections, all the issues we discussed are related to soil samples along a single freezing process. However, what is the behaviour of the soil after several freezing-thawing cycles? In this section, an unsaturated fine sand sample with initial porosity n=0.42 and initial water saturation S_r=0.78 is tested using the ERT setup during three freezing-thawing cycles. The EC images of the sand sample after the first, second and third freezing cycles are presented in Figure 5.25, 5.26 and 5.27, respectively. The EC images of fine sand sample 4 are similar to that of fine sand sample 1 (n=0.38; S_r=0.91). The sample is frozen from the centre along time and the amount of ice has an inverse proportion with the radius. For the unfrozen area, the electrical conductivities of it decrease along time but keep almost homogeneous. The reason is that the initial saturation of fine sand sample 4 is relatively high, which means it has a lower suction. The induced cryogenic suction is also expected to be low, which cannot induce important interstitial water movements.

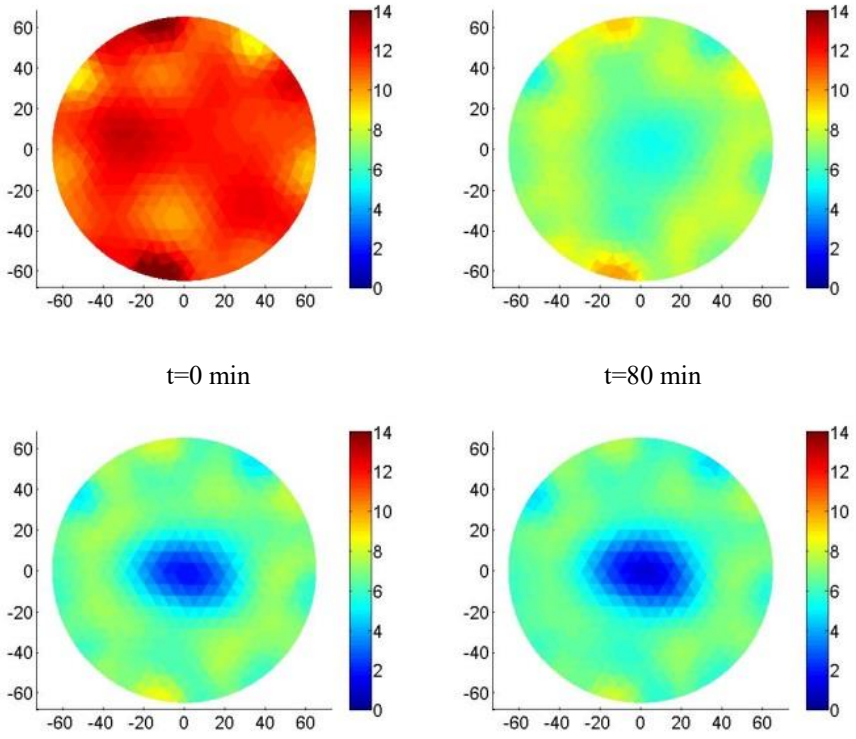

Figure 5.25 Two dimensional freezing on homogeneous unsaturated fine sand sample 4 (n=0.42; S_r=0.78) in the 1st freezing cycle: images of the EC values at different times

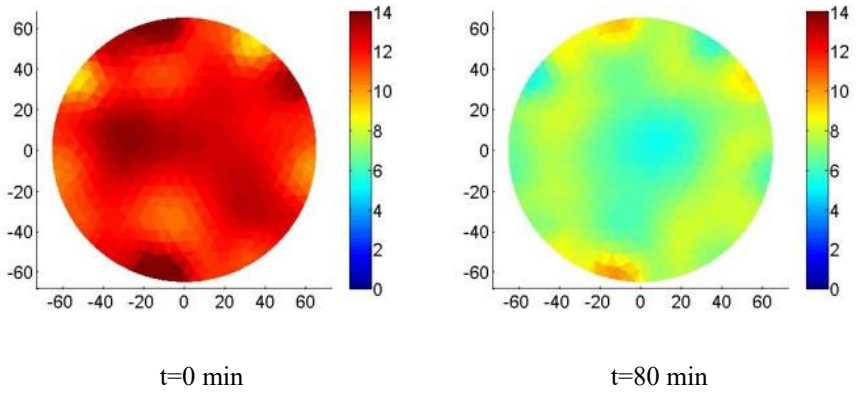

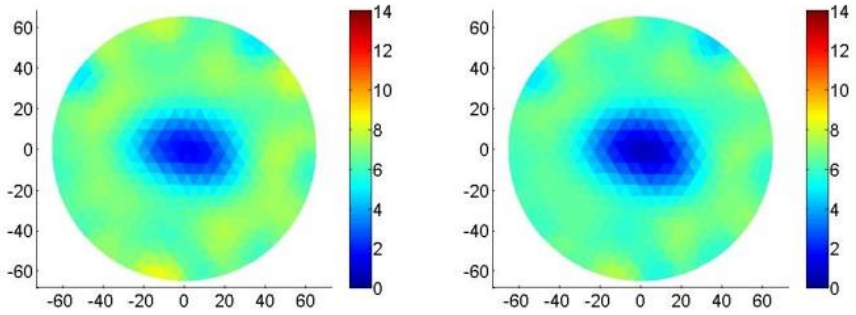

t=160 min t=240 min

Figure 5.26 Two-dimensional freezing on homogeneous unsaturated fine sand sample 4 (n=0.42; S_r=0.78) in the 2nd freezing cycle: images of the EC values at different times

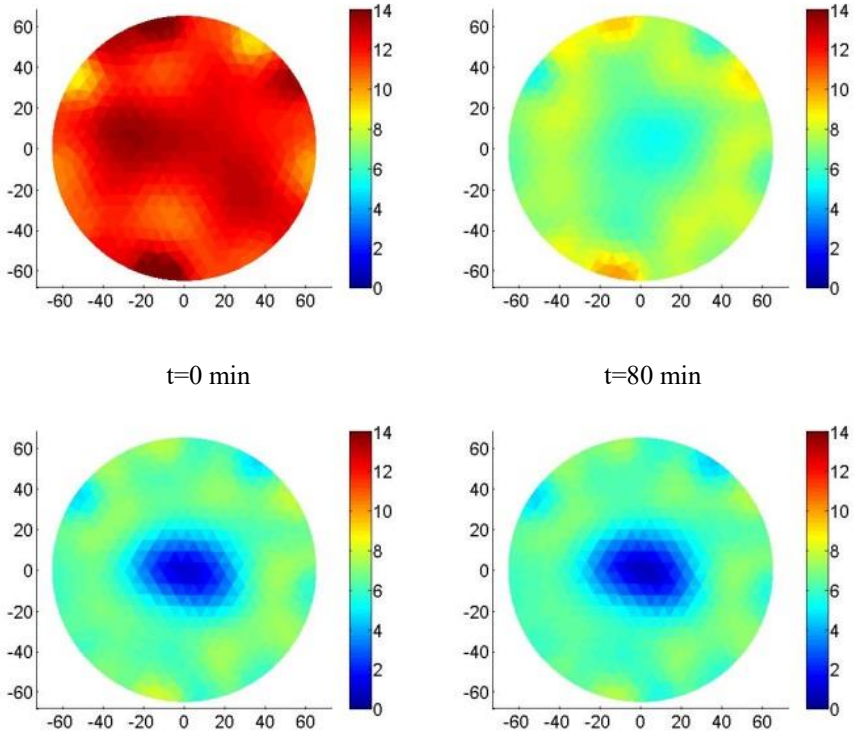

t=0 min t=80 min

t=190 min t=240 min

Figure 5.27 Two-dimensional freezing on homogeneous unsaturated fine sand sample 4 (n=0.42; S_r=0.78) in the 3rd freezing cycle: images of the EC values at different times

Due to fine sand sample 4 being prepared almost homogeneously, the freezing contours on the EC images (first freezing cycle) are regular. After the first freezing cycle, the antifreeze liquid is stopped flowing through the central tube and thawing process starts. After 12 hours, the sample is completely thawed, and temperature increases up to room temperature (20 °C). In the initial state of the second freezing cycle, the image of EC is homogeneous again. The images of EC in second and third cycles are almost the same.

Two points are selected to observe the EC evolutions of the sample, point A is located at the one-third radius and point B is located at the two-third radius. The EC evolutions of two selected points of the sample in three freezing cycles are presented in Figure 5.28. It can be observed that at the beginning, the evolution of EC for both points is nearly the same. After t=100 minutes, the curves of these two points start separating, point A has a faster decrease rate than point B. In figure 5.29, comparisons of EC evolution at selected point A and B are shown, which indicates the freezing-thawing process on unsaturated soils can make the distribution of interstitial water in the soil more homogeneous due to the increase and decrease of cryogenic suction.

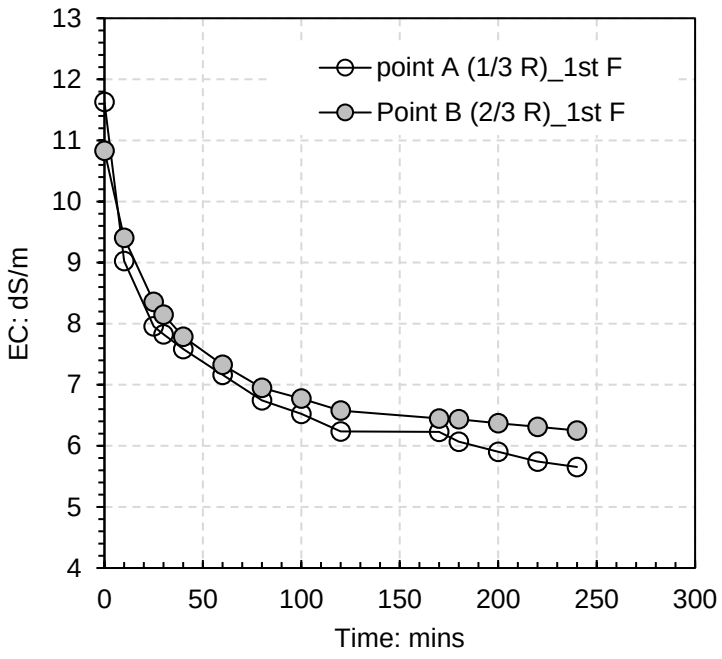

(a)

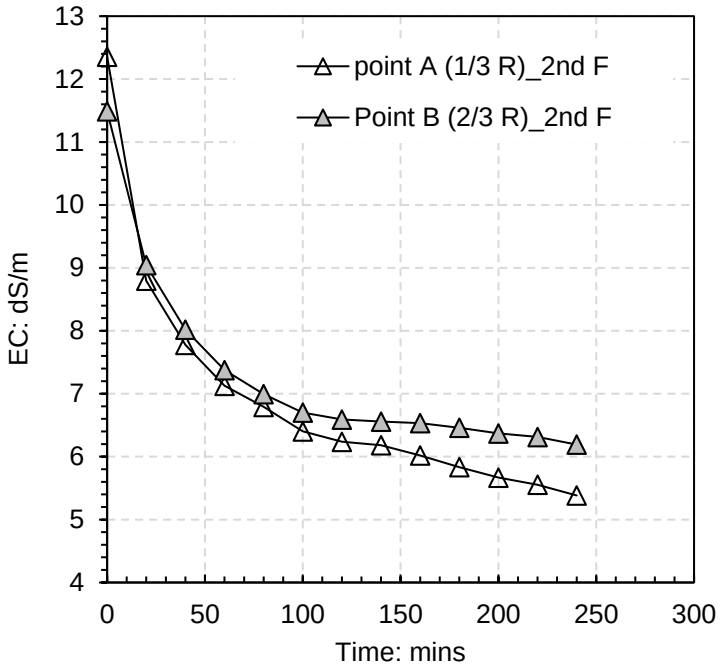

(b)

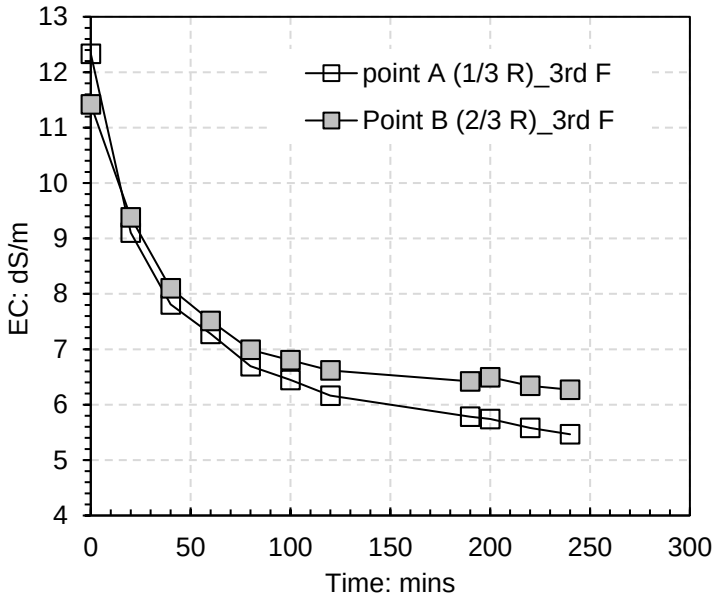

(c)

Figure 5.28 Evolutions of EC at selected points along time during freezing: (a) 1st freezing cycle; (b) 2nd freezing cycle and (c) 3rd freezing cycle

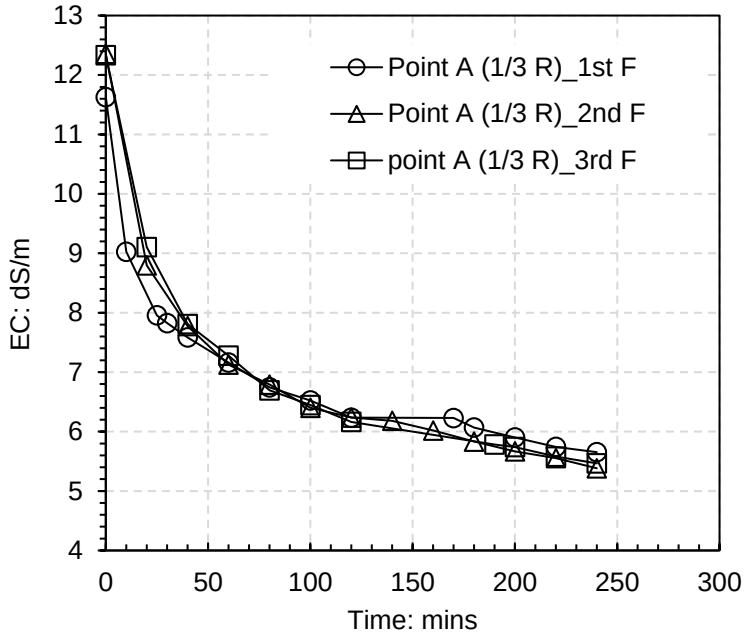

(a)

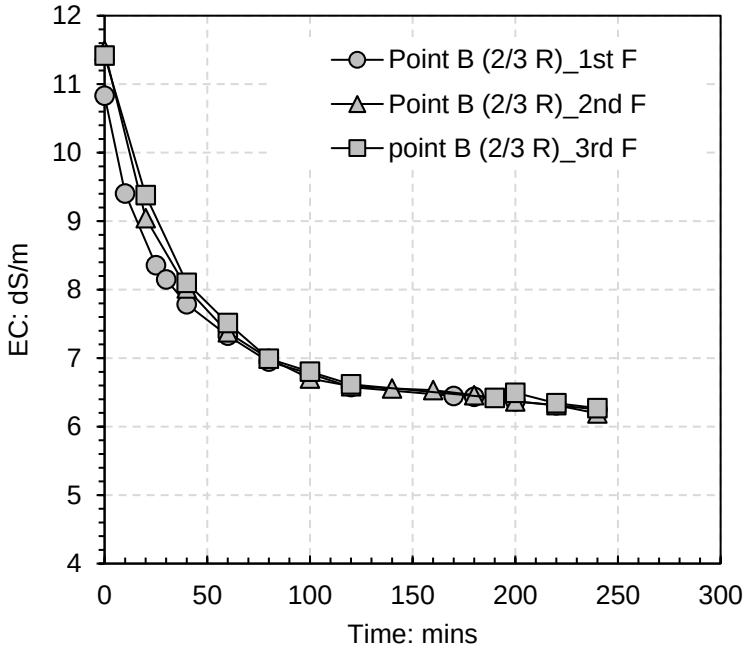

(b)

Figure 5.29 Comparison of EC evolutions at a selected point in different freezing cycles: (a) point A and (b) point B

The EC difference images of sand sample 4 during different freezing cycles are also plotted in Figure 5.30, 5.31 and 5.32, respectively. It can be also seen that the images of the first cycle have slight differences compared to the second and third ones. Some small interstitial water migration can be observed during the freezing process. However, the cryogenic suction would decrease and finally disappear during the thawing process.

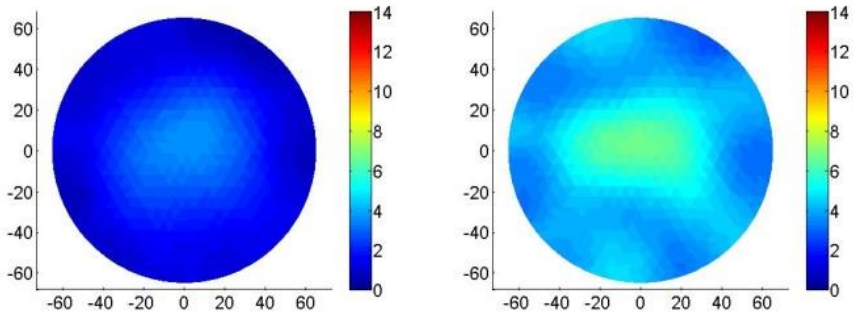

t=10 min t=80 min

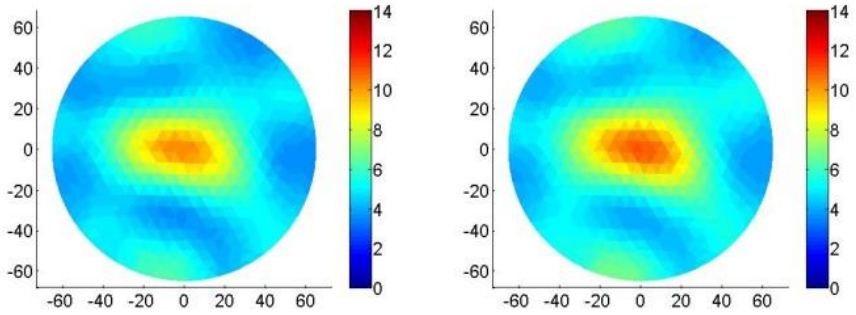

t=170 min t=240 min

Figure 5.30 Two-dimensional freezing on homogeneous unsaturated fine sand sample 4 (n=0.42; S_r=0.78) in the 1st freezing cycle: difference images of EC values at different times compared with the initial state

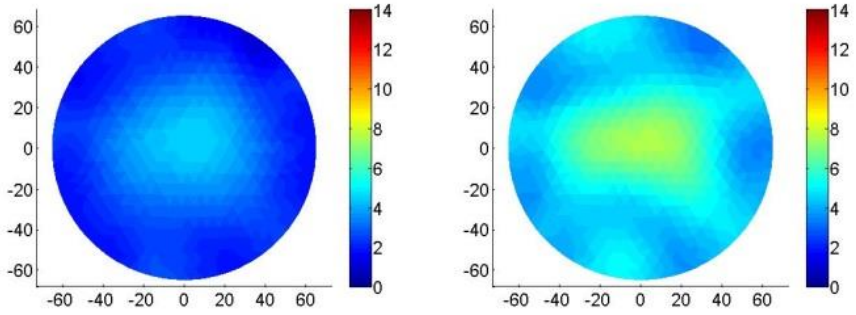

t=20 min t=80 min

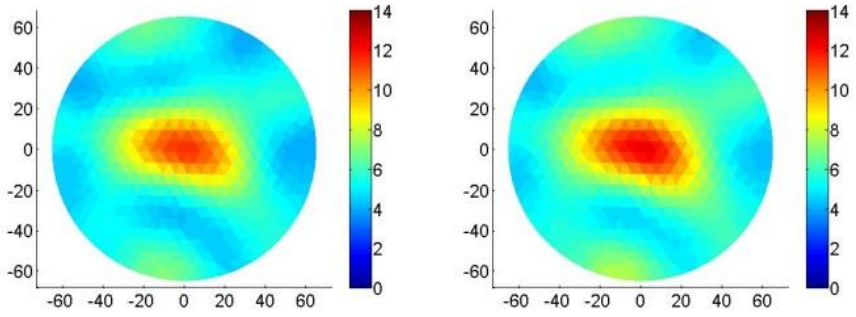

t=160 min t=240 min

Figure 5.31 Two-dimensional freezing on homogeneous unsaturated fine sand sample 4 (n=0.42; S_r=0.78) in the 2nd freezing cycle: difference images of EC values at different times compared with the initial state

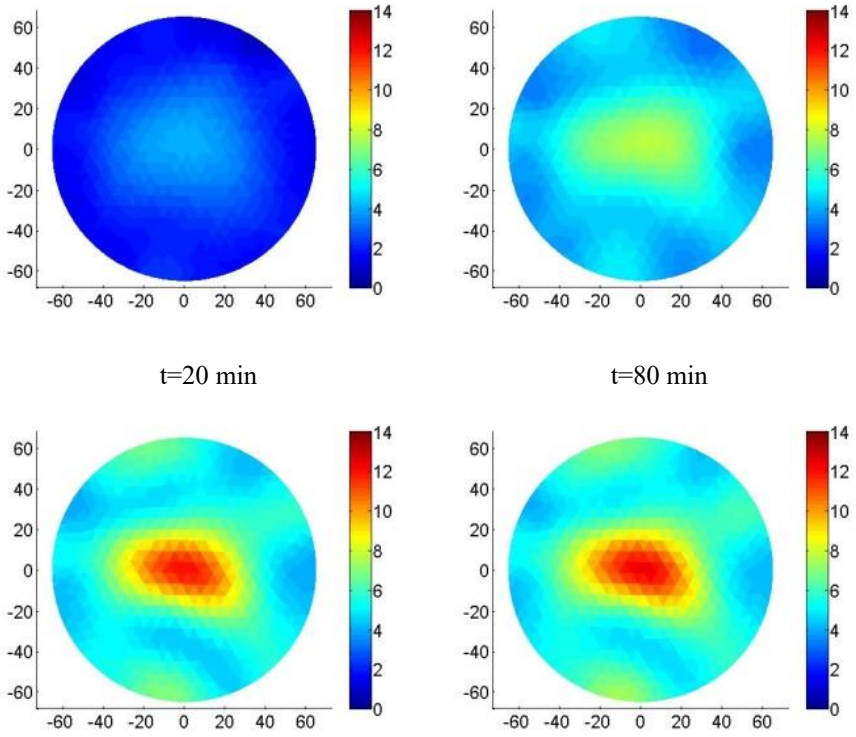

t=20 min t=80 min

t=190 min t=240 min

Figure 5.32 Two-dimensional freezing on homogeneous unsaturated fine sand sample 4 (n=0.42; S_r=0.78) in the 3rd freezing cycle: difference images of EC values at different times compared with the initial state

5.4 ERT results of heterogeneous frozen samples

5.4.1 Homogeneous unsaturated sand with an opening

To investigate the heterogeneity of soils using the ERT setup, a homogeneous unsaturated fine sand sample 5 (n=0.40; S_r=0.67) is prepared with a cylindrical opening, which is 17 mm in diameter. The picture of the prepared fine sand sample can be found in Chapter 3, Section 3.4. In Figure 5.33, the images of EC of fine sand sample 5 at different freezing times are presented. At the initial state at time t=0 minutes, it shows general homogeneous contours around 12 dS/m of the image except for an obvious circular area (the cylindrical opening), which is close to 0 dS/m. This means the ERT setup can immediately detect the opening hole existing in the sample because the EC of air is several orders of magnitudes lower than sand. It is worthwhile to recall that, because of the regularisation techniques adopted in the solution of the inverse problem, the final solution is a smooth representation, whereas the problem is characterised by sharp boundaries. Hence, it is not possible to quantify exactly the difference between the actual size of the inclusions and their size in the reconstructed image. Nevertheless, if a given threshold of conductivity is chosen in the reconstructed image, the position of the inclusion can be better estimated.

Figure 5.34 represents the EC difference images of fine sand sample 5 at certain freezing times compared with the initial state. The behaviour of EC evolution is similar to other unsaturated fine sand samples. However, the EC contours are not perfectly circular especially in the part close to the opening hole.

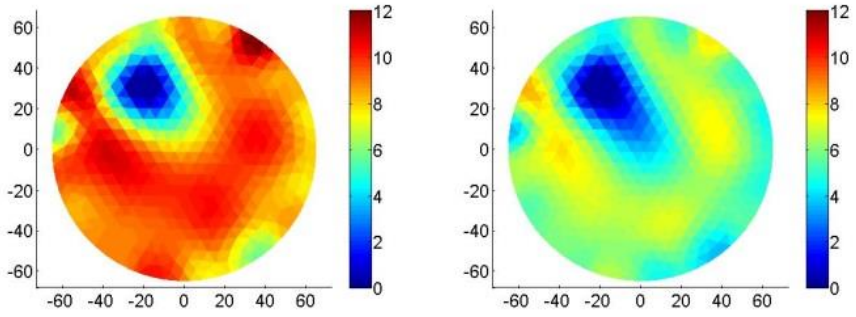

t=0 min t=60 min

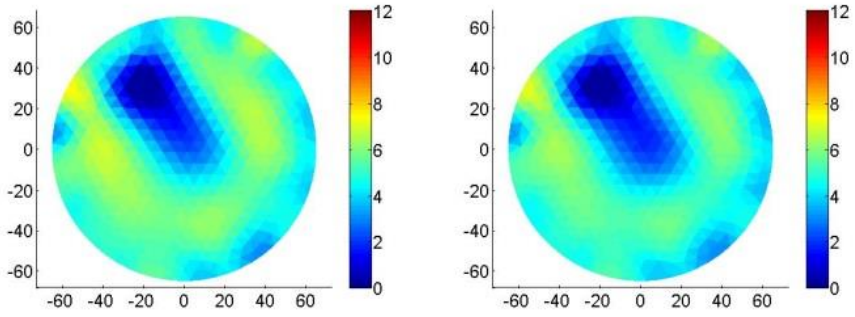

t=120 min t=170 min

Figure 5.33 Two-dimensional freezing on homogeneous unsaturated sand sample 5 (n=0.40; S_r=0.67) with an opening: images of the EC values at different times

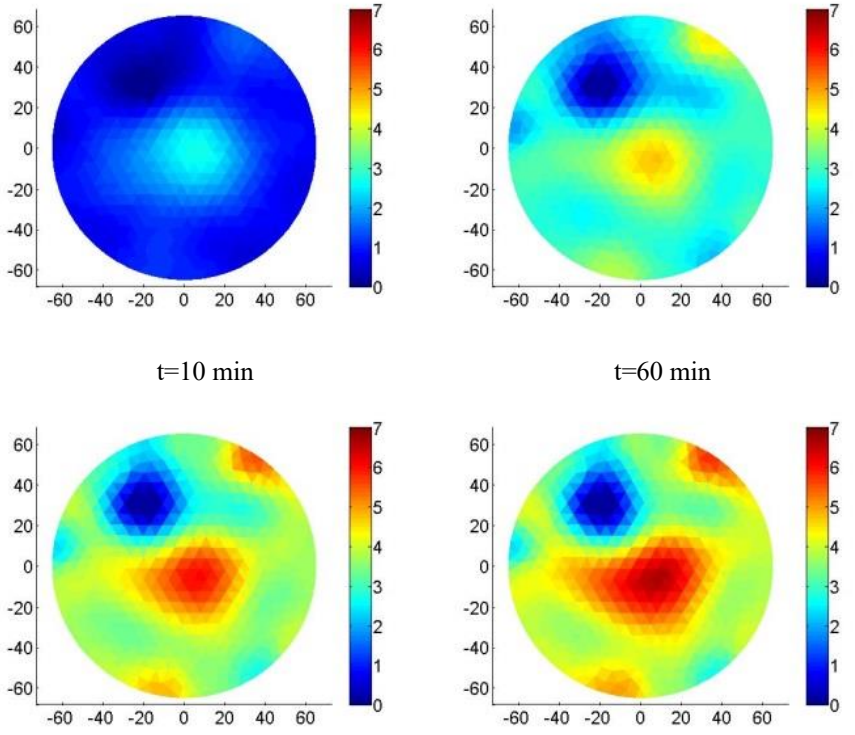

t=10 min t=60 min

t=120 min t=170 min

Figure 5.34 Two-dimensional freezing on homogeneous unsaturated sand sample 5 (n=0.40; S_r=0.67) with an opening: images of the EC difference at different times compared with initial values

5.4.2 Homogeneous unsaturated clayey silt with the sand inclusion

It is proven that ERT setup has a good performance on detecting heterogeneity of soils, which has some less conductive inclusions. Furthermore, to investigate the capability of the ERT setup for detecting more conductive inclusions in the soils, a homogeneous unsaturated clayey silt sample with fine sand inclusion (cylindrical column with a diameter of 17 mm) is prepared. The picture of prepared sample is presented in Section 3.4. The reconstructed images of EC are shown in Figure 5.35.

At the initial condition (room temperature), the sand inclusion cannot be explicitly detected, since EC values are very similar. As the freezing process proceeds, the heterogeneity gradually appears, and the EC reduction occurs at a faster rate in the direction of the sand inclusion. There are two possible causes. One possibility is that the clayey silt has a lower thermal conductivity than fine sand, which has been measured and illustrated in Chapter 4. This means fine sand would be frozen faster than the clayey silt. The other possibility is that clayey silt has a higher suction than fine sand, which is also indicated in Chapter 3. This means that the interstitial water in fine sand can easily migrate to the clayey silt when suction is not equilibrated between them. The EC difference images of clayey silt sample 4 at certain freezing times compared with the initial state are presented in Figure 5.36. The results demonstrate that the ERT setup can be used to monitor and locate the high conductive inclusions in the soils.

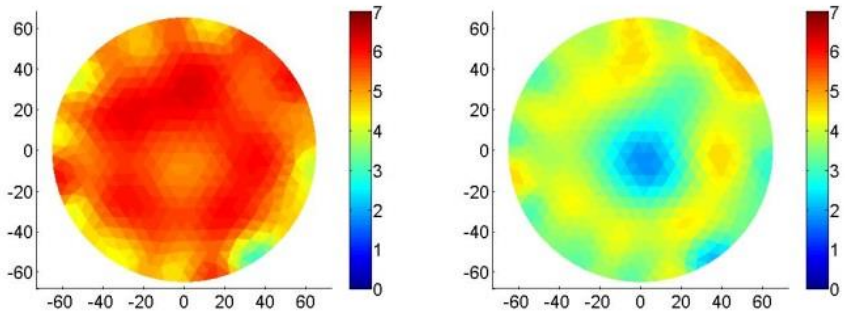

t=0 min t=60 min

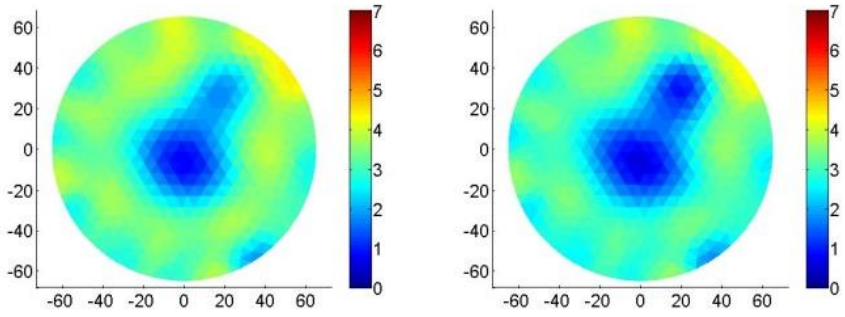

t=140 min t=220 min

Figure 5.35 Two-dimensional freezing on homogeneous unsaturated clayey silt sample 4 (n=0.30; S_r=0.81) with sand inclusion (n=0.40; S_r=0.67): images of the EC values at different times

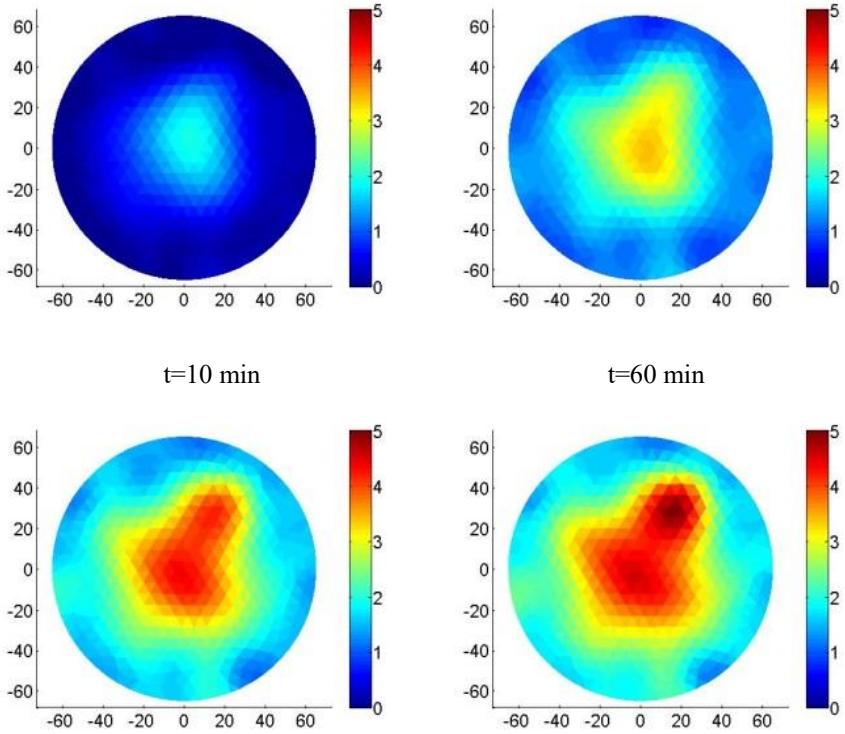

t=10 min t=60 min

t=140 min t=220 min

Figure 5.36 Two-dimensional freezing on homogeneous unsaturated clayey silt sample 4 (n=0.30; S_r=0.81) with sand inclusion (n=0.40; S_r=0.67): images of the EC difference at different times compared with initial values

5.5 Summary

This chapter aimed to evaluate the use of ERT for the detection and characterisation of ice content and pre-existing heterogeneities in frozen soil samples.

- A saturated fine sand sample and a saturated clayey silt sample are tested in a modified ERT setup to explore the behaviour of soil freezing. Good images of the EC of soils at different times are obtained, which demonstrate the good performance of the ERT setup. A proposed expression is used to reconstruct the images of temperature evolution along time and is verified using measured results for both soils. The images of soil bulk EC are then translated to images of unfrozen water content (ice content) along the freezing path. It is clear the ERT setup and proposed models can image the temperature and ice content evolution of soils during the freezing path.
- Unsaturated homogeneous fine sand and clayey silt samples with different initial water saturation are tested using the ERT setup in one or more freezing cycles. The unsaturated soil freezing process would induce interstitial water migration from the unfrozen area to the frozen area because of cryogenic suction. The freezing-thawing process on unsaturated soils can make the distribution of interstitial water in the soil more homogeneous due to the increase and decrease of cryogenic suction. The ERT setup can be used to monitor the induced inhomogeneity of soils.
- A homogeneous fine sand sample with an opening hole and a homogeneous clayey silt sample with a sand inclusion are tested using the ERT setup. The experimental results illustrate that both low conductive and high conductive inclusions can be monitored using the ERT techniques. This provides a new possibility for detecting the internal heterogeneity of geomaterials in some important engineering applications.
- Further ongoing exploration includes the study of a process related to the couple THM behaviour of frozen soils and the freezing-thawing cycles using the improved ERT setup. The numerical modelling of the thermo-hydraulic behaviour of the aforementioned tests will also be conducted to estimate the hydraulic parameters and thermal of frozen soils.

Chapter 6 Volume change behaviour and micro-structural changes on a freezing/thawing cycle

6.1 Introduction

As introduced in Chapter 1, frost action in soils involves the processes of freezing and thawing. The resulting phenomenon of frost heave and thaw settlement are commonly observed in seasonally frozen soils, which could damage engineering infrastructures. Controlling of frost heave and thaw settlement is also one of the most important factors for successfully applying the AGF technique in geotechnical engineering applications. Furthermore, the global warming would change the active layer of permafrost (upper crust layer where active freezing-thawing cycles occur), which leads to extensive settlement of the ground surface. Therefore, it is very important to understand soil behaviour during the freezing and thawing process.

In this chapter, the total volume change behaviour of three soils (two pyroclastic soils, Pozzolana and Yellow Tuff, and Barcelona clayey silt) are firstly investigated using temperature-controlled oedometer tests. The two pyroclastic soil samples are prepared as intact as-retrieved samples and clayey silt is prepared at a reconstituted state. The oedometer tests include two types: one is only after stress path (loading-unloading path); the other one is after stress and thermal path (loading-freezing-thawing-unloading path). The loading vertical stress steps are 200, 500, 600 and 800 kPa. The thermal path is from room temperature (20 °C) to -15 °C by certain target steps and then returns to room temperature again.

Secondly, to explore the microstructure changes of soils, the samples after oedometer tests are freeze-dried to conduct MIP and FESEM tests. The FESEM results are analysed using the

PCAS program to study the changes in multiple factors, such as average porosity, average pore diameter, pore area, fractal dimension, abundance and anisotropic rate of pores and particles. Combined MIP and FESEM results can give important information about soils after different stress and thermal paths.

6.2 Volume change behaviour of soils after stress and thermal path

6.2.1 Introduction

In this section, eight soil samples are presented, which include two Pozzolana samples, two Yellow Tuff samples, and four clayey silt samples. For clayey silt samples, two samples are tested on the loading-unloading path and two other samples are performed on the loading-freezing-thawing-unloading path. The experimental program of clayey silt oedometer tests is described in Chapter 3. Two Pozzolana samples are performed on the loading-freezing-thawing-unloading path and the final vertical stresses are up to 200 and 500 kPa, respectively. Two Yellow Tuff samples are performed on the similar path with Pozzolana but with different final stresses of 500 and 800 kPa, respectively. The temperature of the thermal path on Pozzolana and Yellow Tuff ranges from 22 °C to -20 °C, a little different from the clayey silt. The experimental results of Pozzolana and Yellow Tuff are described in Peláez et al. (2014).

6.2.2 Stress path at room temperature

The oedometer test results of two reconstituted saturated clayey silt samples at different initial void ratios are presented in Figure 6.1, using a log scale. One loading and unloading cycle is part of the test. In Figure 6.1 (a), the virgin consolidation line is nearly linear, and the unloading path also approximates to linear. Because the sample clayey silt A is prepared in very loose condition, the initial void ratio of it is around 1.110. In contrast, the sample clayey silt B as shown in Figure 6.1 (b), is prepared at denser state than clayey silt A; its void ratio is 0.472. The pre-consolidation path is applied to compress the soil. It is clearly seen in Figure

6.1 (b) that the curve becomes linear after the vertical stress is more than 200 kPa. We can deduce that the pre-consolidation pressure is around 200 kPa.

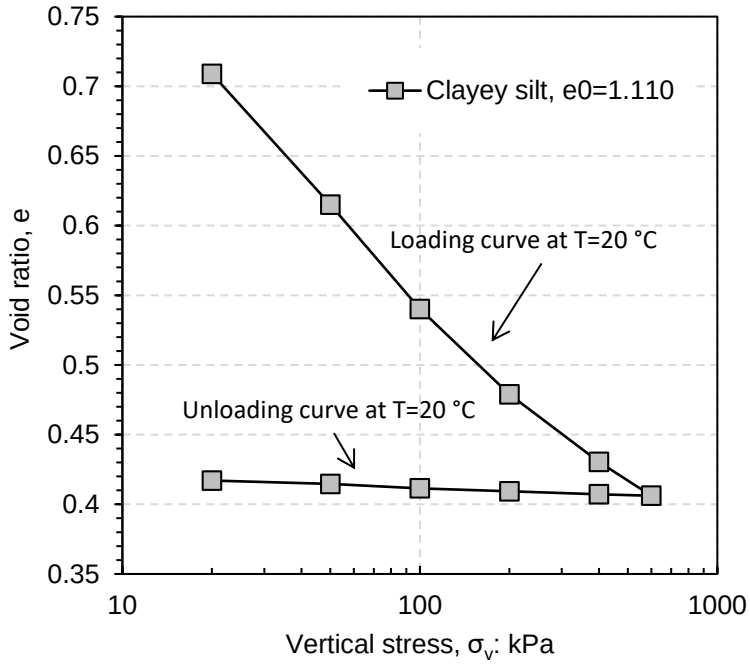

(a)

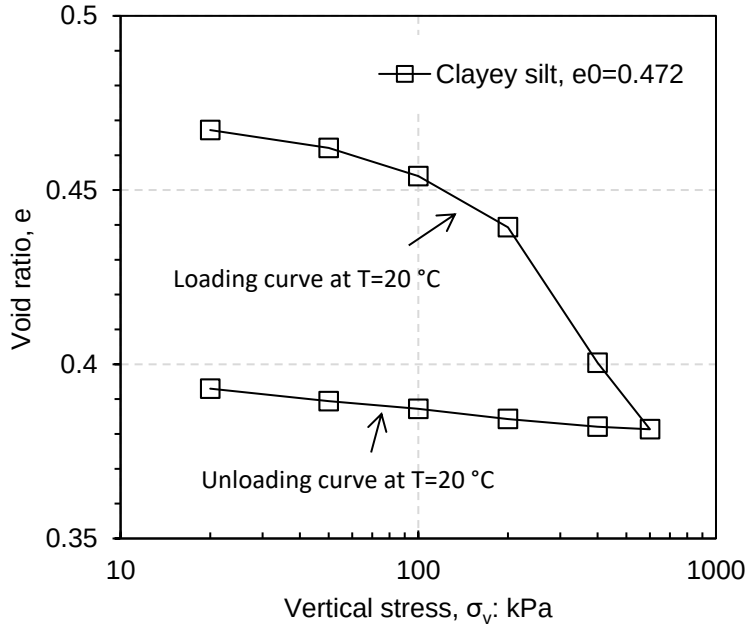

(b)

Figure 6.1 Oedometer tests on clayey silt in the log σ_v-e plane: (a) e_0=1.110 and (b) e_0=0.472

To compare the variations of void ratios of clayey silt A and clayey silt B, they are plotted together in Figure 6.2, using a log scale. It is interesting to find that for the loading curve, the linear part of both samples at the stress range between 200 kPa and 600 kPa have the same inclination. It normally defined the variation of void ratio e as a function of the change of effective stress σ_v plotted in a log scale (water pressure is under atmospheric conditions). Therefore, the deformation characteristic of over-consolidated soil can be presented as

$$C_c = -\frac{\Delta e}{\Delta \log \sigma_v} \tag{6.1}$$

where C_c is the compression index, Δe is the variation of the void ratio and $\Delta \log \sigma_v$ is the variation of vertical effective stress.

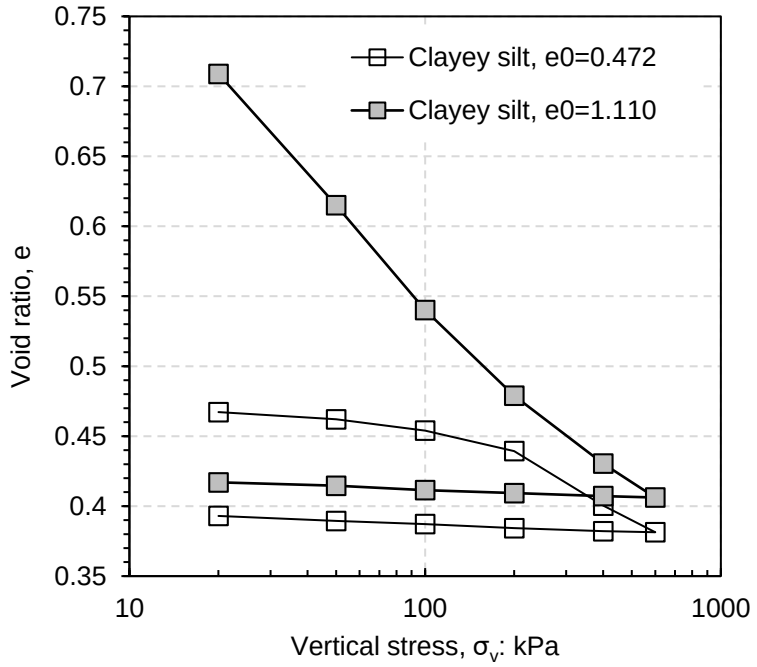

Figure 6.2 Comparison of two oedometer tests on clayey silt samples with a different initial void ratio

After calculating, the compression index C_c for clayey silt A and clayey silt B are equal to 0.2. The swelling index C_s, using a similar definition to that of the compression index C_c, is used to describe the elastic deformation characteristics during soil unloading path. After being measured in Figure 6.2, the swelling index C_s for both clayey silt A and clayey silt B are the

same and equal to 0.004. It indicates that the swelling index C_s is not affected by soil initial void ratios. The elastic deformation can be observed on the loading-unloading path for clayey silt samples. It is necessary to indicate that the permanent deformation of soil is the total deformation minus the elastic deformation.

6.2.3 Stress and thermal path

From above section, we know the behaviour of soil after stress path of loading and unloading. But what will be the behaviour of soil after stress and thermal paths? In this section, three soils are investigated including two pyroclastic soils (Pozzolana and Yellow tuff) and clayey silt. Different stress and thermal path are applied to the samples. The experimental results are presented below.

6.2.3.1 Clayey silt

The experimental results of two oedometer tests for clayey silt samples are reported in this section. These two oedometer tests for clayey silt samples follow the same stress and thermal path, but the samples are prepared at different initial void ratios (e=0.85 and 0.46 separately). The vertical stress path for loading is 20→50→100→200→400→600 kPa, and unloading path is the same, but in descending order, that is 600→400→200→ 100→50 kPa. Due to some limitation in controlling temperature in the cooling bath, the thermal path is simplified as 20→-3→-16→-4→20 °C, and same steps are followed but with the inverse order.

The log σ_v-e plane of clayey silt C in the oedometer test is presented in Figure 6.3 (a), and its volume change during the temperature cycle is presented in Figure 6.3 (b). The inclination of the curve at the stress range between 400 and 600 kPa can be used to define the compression index C_c =0.22.

The variation of void ratio along with the freezing and thawing path is shown in Figure 6.3 (b). On the freezing path, at the temperature around -3 °C, the total void ratio slightly increases up to 0.461, which means the ice forms (ice has a lower density than water, which means ice has a larger volume). It is necessary to the point that tap water is used in the oedometer tests and that soil freezing point is approximately at 0 °C. At the temperature -16

°C, the void ratio increases up to 0.464. The total void ratio change induced by freezing is Δe=0.004. This phenomenon is consistent with the research conclusions obtained in Chapter 4 that the ice forms when the temperature is lower than a freezing point but cannot be fully frozen at a very low temperature (-16 °C in this test) because of the existing suction and micro-pores.

During thawing path, the points of the void ratio are always below than the corresponding points on the freezing path. The total variation of void ratio induced by the whole freezing and thawing cycle in clayey silt C is Δe=-0.004. It is important to highlight that the freezing-thawing cycle induces soil settlement, as shown in Chapter 1, Figure 1.3. It also indicates that the freezing and thawing process would probably induce some microstructure changes in the clayey silt. These microstructural changes appear also to change the swelling index during unloading (C_s is approximately zero and elastic deformation disappear after freezing and thawing process).

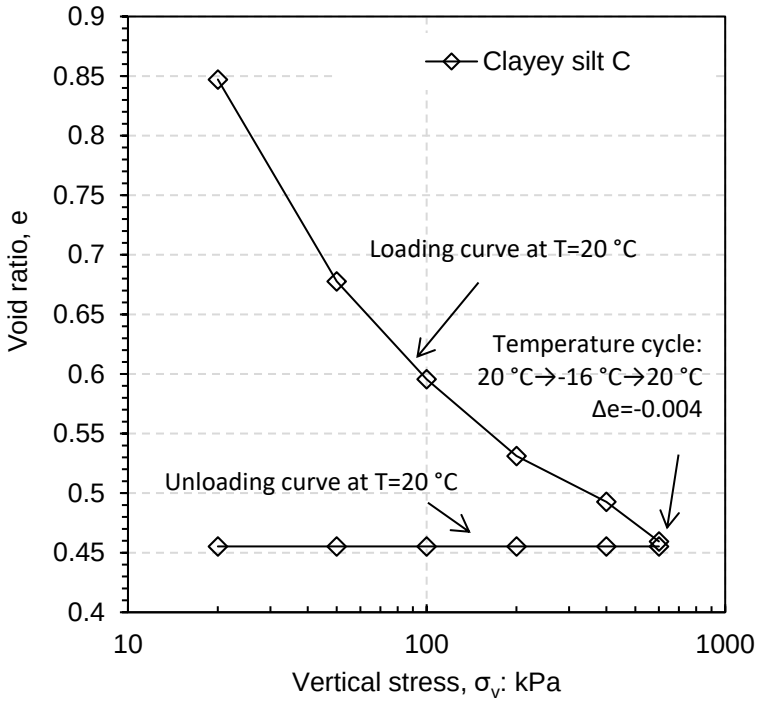

(a)

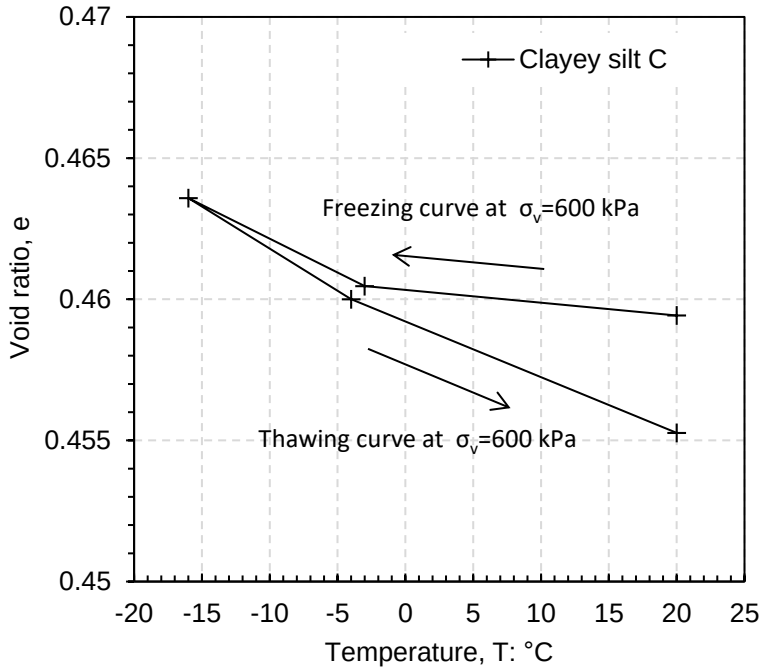

(b)

Figure 6.3 Oedometer tests of clayey silt e_0=1.110 (a) stress path and (b) thermal path.

The log σ_v-e plane of clayey silt D in the oedometer test is shown in Figure 6.4 (a) and its volume change behaviour with temperature are additionally presented in Figure 6.4 (b). The loading curve in logarithm scale is not linear due to pre-consolidation is applied in preparing soil specimen. The inclination of the curve at the stress range between 400 and 600 kPa can be taken as the compression index C_c because this slope is higher and the same as that of clayey silt C (see Figure 6.5 (a)), which is C_c=0.22.

As shown in Figure 6.4 (b), the volume change behaviour of clayey silt D during freezing and thawing process is similar to that of clayey silt C. The variation of void ratio induced by a cycle of freezing and thawing is Δe=-0.004. It is important to indicate that the volume change after freezing and thawing path is resulted from both phase changes (water to ice and then to water) and flow of excess water out of the saturated soil. Drainage during thawing leads to additional soil volume change, and the amount depends on the soil structural changes that occur during the previous freezing cycle (freezing is assumed to occur under water undrained conditions).

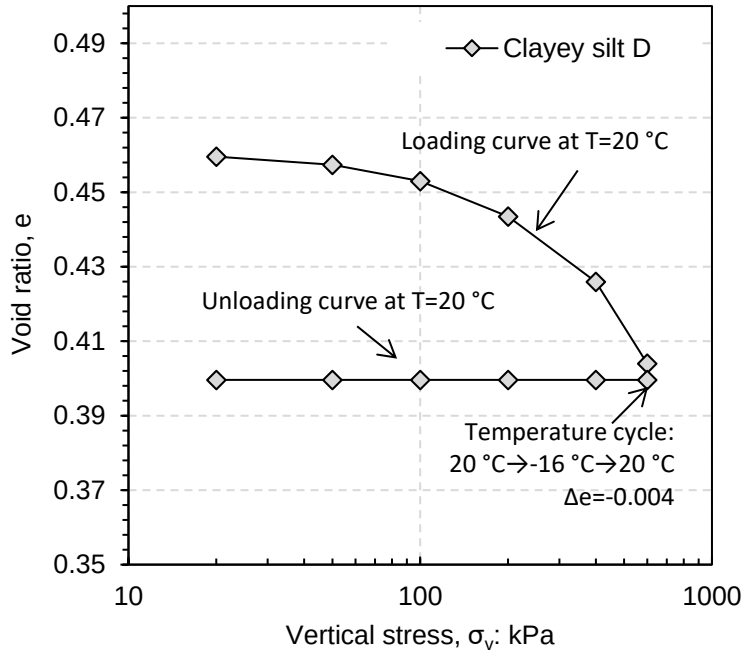

(a)

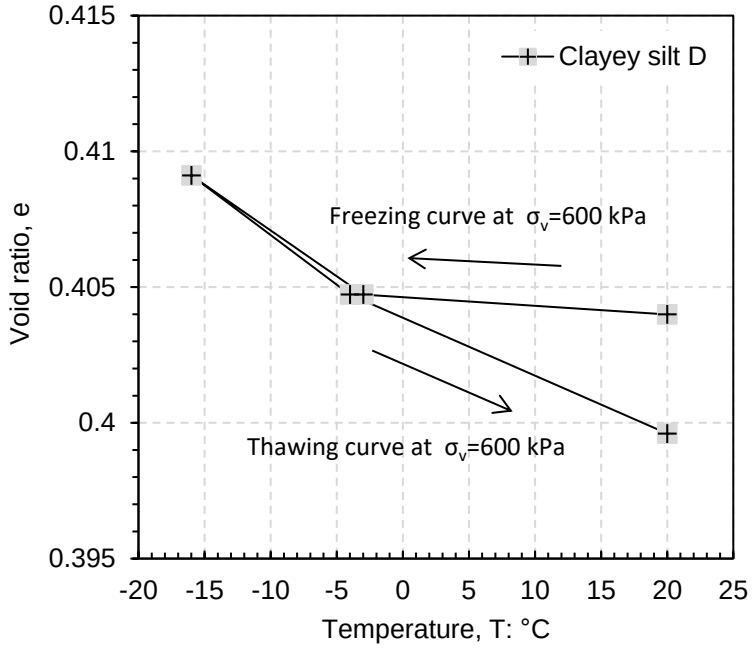

(b)

Figure 6.4 Oedometer tests of clayey silt e_0=0.462 (a) stress path and (b) thermal path

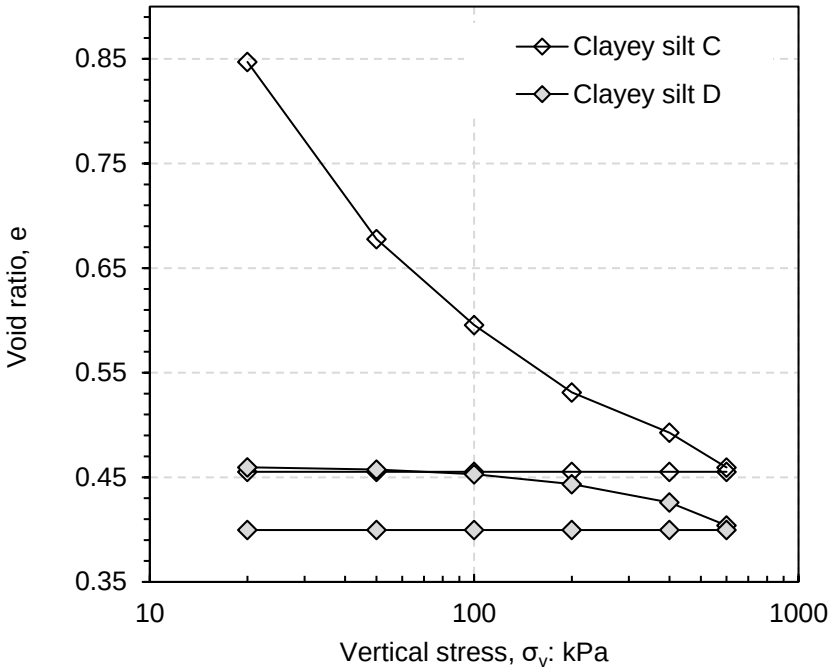

(a)

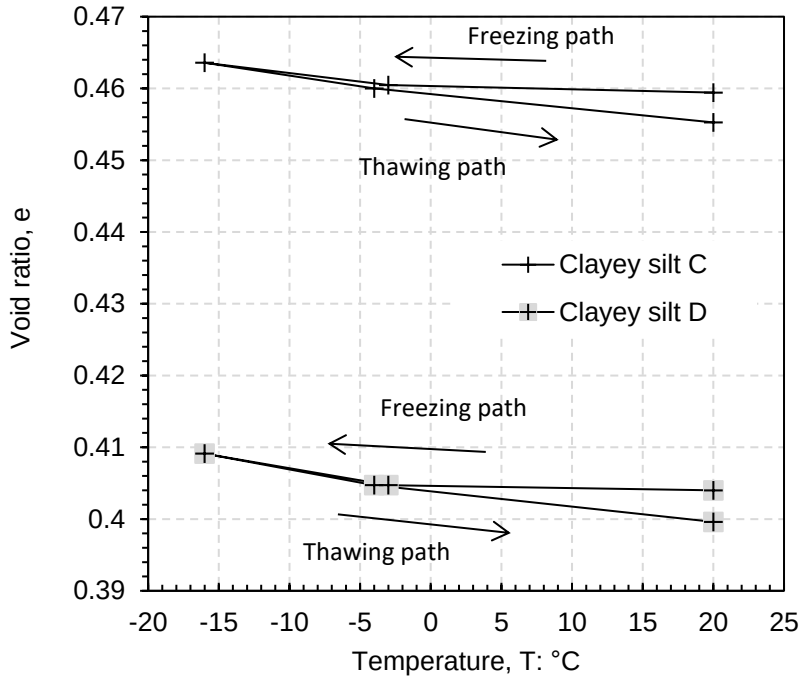

(b)

Figure 6.5 Comparison of two oedometer tests on clayey silt samples: (a) stress path and (b) thermal path

To compare both results, the variations of the void ratio for clayey silt C and clayey silt D after stress and thermal paths are plotted together in Figure 6.5 (a) and (b), respectively. It is interesting to find that the inclinations of two curves at the stress range between 400 and 600 kPa are the same. The unloading curves also have the same slope with swelling index $C_s \approx 0$ after a cycle of freezing and thawing. The thermally induced variations of the void ratio for both samples are the same, which are Δe=-0.004.

6.2.3.2 Pozzolana

Two oedometer tests under saturated conditions are presented in this section: one oedometer test for Pozzolana with maximum vertical stress 200 kPa and another one for Pozzolana with maximum vertical stress 500 kPa (Peláez et al., 2014). The experimental results of these two oedometer tests are plotted in Figure 6.6 (a) and (b), respectively. The void ratio decrease on loading up to 200 kPa is similar in both samples with a $\Delta e \approx$-0.02. For Pozzolana B, a yielding behaviour can be observed in the last step up to 500 kPa that demonstrates the pre-consolidation stress of natural Pozzolana should be between 200 and 500 kPa. The thermal path of freezing-thawing shows an accumulated plastic deformation of Δe =-0.03 for Pozzolana A (σ_{vmax}=200 kPa) and Δe=-0.02 for Pozzolana B (σ_{vmax}=500 kPa). In the unloading step, the elastic deformation of Pozzolana can be observed that curves of both samples are nearly linear. The swelling index C_s for both Pozzolana A and Pozzolana B are 0.001 and 0.004, respectively. The combined plot of experimental results of Pozzolana A and B are presented in Figure 6.7.

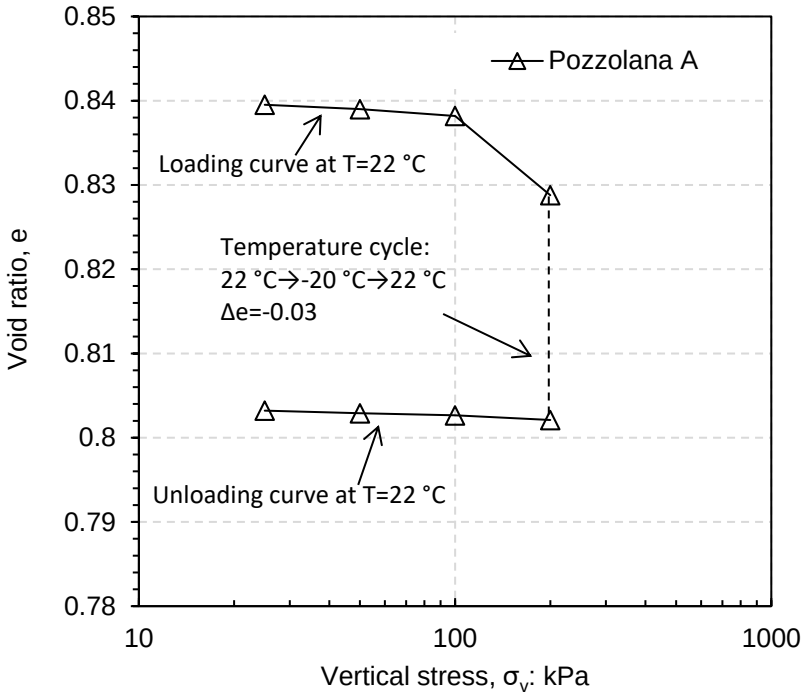

(a)

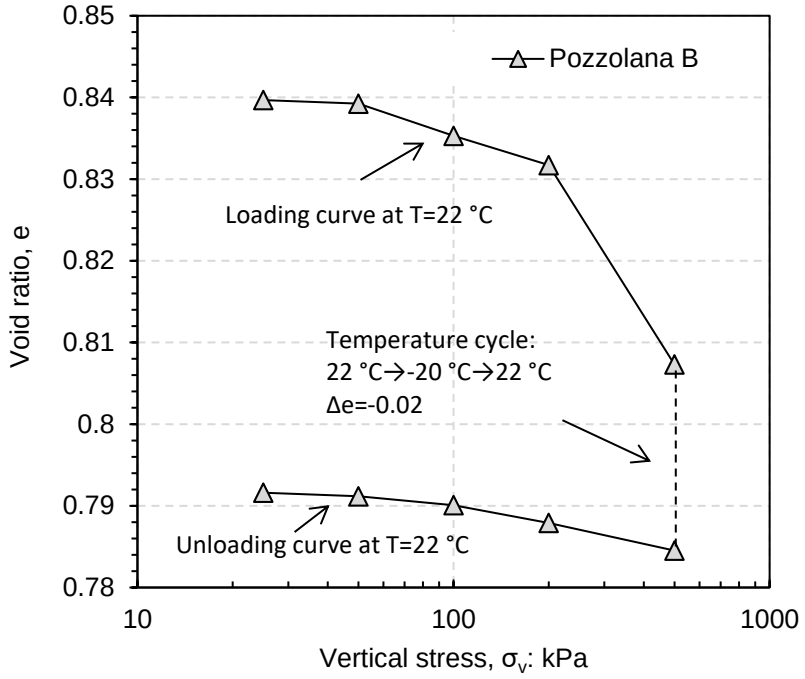

(b)

Figure 6.6 Oedometer tests on Pozzolana in the log σ_v-e plane: (a) σ_{vmax}=200 kPa and (b) σ_{vmax}=500 kPa.

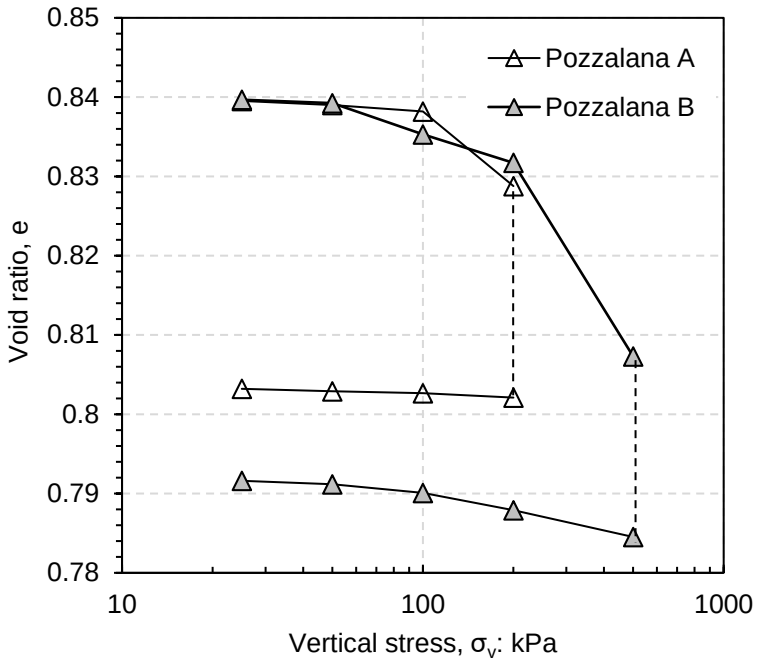

Figure 6.7 Comparison of two oedometer tests on Pozzalana samples with different maximum loading pressure

6.2.3.3 Yellow Tuff

The experimental results of two saturated oedometer tests for Yellow Tuff are reported in this section, one is with maximum vertical stress σ_{vmax}=500 kPa, and the other is with maximum vertical stress =800 kPa (Peláez et al., 2014). The variations of the void ratio along with log σ_{vmax} for these two samples are presented in Figure 6.8 (a) and (b), respectively. The combined plot of Yellow Tuff A and B can be seen in Figure 6.9.

During the vertical stress loading stage, similar behaviour can be observed for both samples in the stress range from 0 to 500 kPa. The small deviation of two curves is probably due to the initial inhomogeneity of prepared specimens. The only slight increase of inclination is observed in the figure at stress range from 500 to 800 kPa (e-log σ_v plane). This information suggests that the proper yielding has not been reached until the vertical stress of 800 kPa and it would be higher.

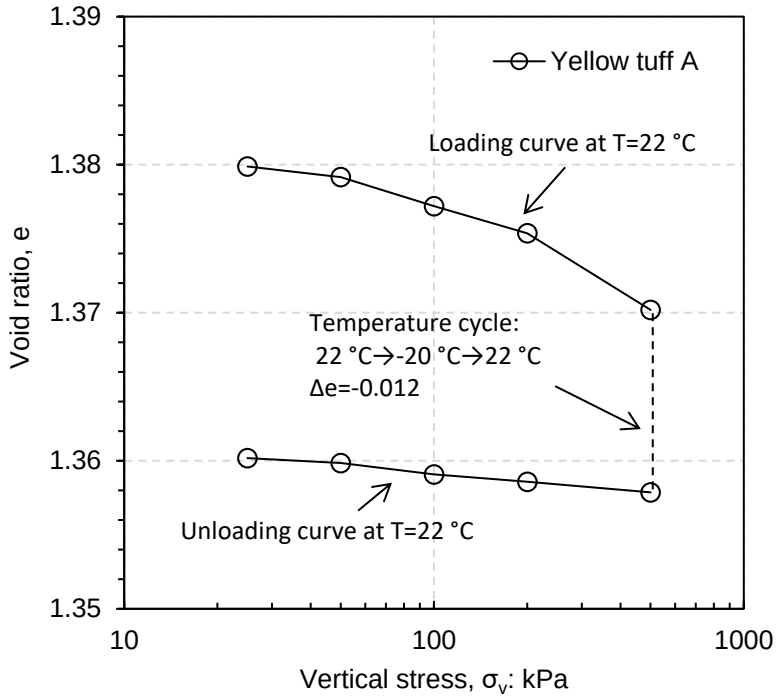

(a)

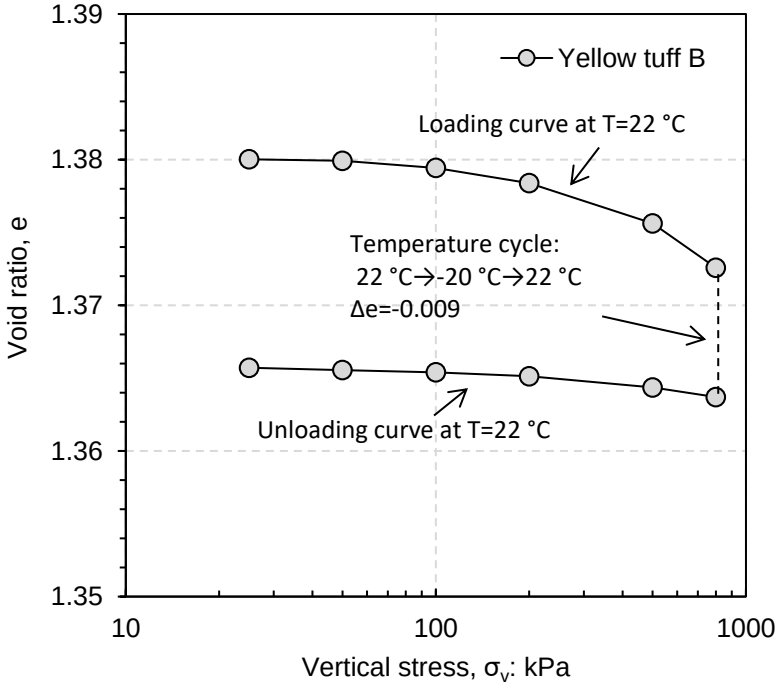

(b)

Figure 6.8 Oedometer tests on Yellow Tuff in the log σ_v-e plane: (a) σ_{vmax}=500 kPa and (b) σ_{vmax}=800 kPa.

The thermal stress path of freezing and thawing on two samples exhibited irreversible permanent deformation under the certain constant vertical stress. The deformation of Yellow Tuff A at vertical stress σ_{vmax}=500 kPa is Δe (T)=-0.012 and that of Yellow Tuff B at vertical stress σ_{vmax}=800 kPa is Δe (T)=-0.009. The elastic deformation behaviour is observed at unloading path, that swelling index of Yellow Tuff A is C_s=0.0017, and that of Yellow Tuff B is C_s=0.0012.

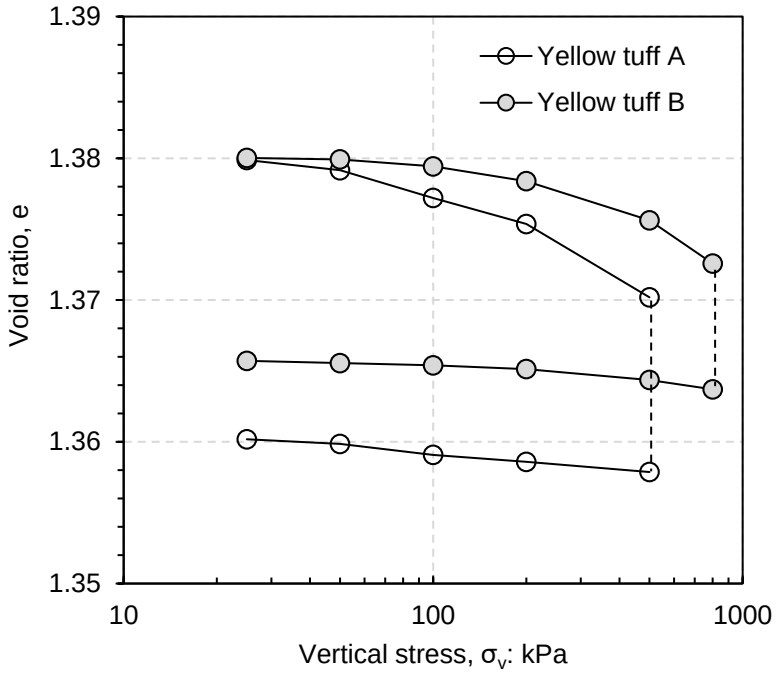

Figure 6.9 Comparison of two oedometer tests on Yellow Tuff samples with different maximum loading pressure

6.2.4 Discussion

The total deformation of soil in oedometer test includes two parts, irreversible (permanent) deformation and elastic (reversible) deformation. The total deformation is the sum of irreversible and elastic deformations. When comparing one-dimensional oedometer tests for clayey silt samples after loading and unloading path with those after loading-freezing-thawing-unloading path, the freezing-thawing cycle induces an additional settlement and

reduces the elastic deformation from C_s=0.004 to C_s≈0 for clayey silt. It is a pity there are not oedometer tests on Pozzolana and Yellow Tuff following loading-unloading paths that can be used to compare with the oedometer tests of these two soils following the loading-freezing-thawing-unloading path. It is supposed that the freezing-thawing process would probably reduce the soil elastic deformation, i.e. swelling index of soil at unloading path.

When comparing the oedometer test results of all above soils at different initial conditions, different loading stresses, it is interesting to find that for clayey silt samples, the initial void ratios of prepared samples do not affect the final freezing-thawing settlement. The freezing-thawing settlement for clayey silt C and D are both Δe=0.004 even though their initial void ratios are 1.110 and 0.462, respectively. This is due that both attend approximately the same void ratio before the freezing-thawing paths.

The effect of loading pressure on soil freezing-thawing settlement can be observed on both Pozzolana and Yellow Tuff samples. That freezing-thawing settlement of Pozzolana at 200 kPa has a higher settlement (Δe=-0.03) than Pozzolana at 500 kPa (Δe=-0.02). Similarly, the freezing-thawing settlement of Yellow Tuff at 500 kPa is Δe=-0.012, higher than Δe=0.009 from that of Yellow Tuff at 800 kPa. It is supposed that the loading stress constrains the freezing-thawing settlement of soils, the higher loading stress, the smaller the settlement. To explicitly understand the freezing-thawing settlement of different soils at different loading pressures, the normalised freezing-thawing settlement versus void ratio for different soils are presented in Figure 6.10. The $\Delta\varepsilon_v$ is calculated from equation

$$\Delta\varepsilon_v = -\frac{\Delta e}{1+e_i} \tag{6.2}$$

where Δe is the freeze-thawed settlement of void ratio, e_i is the void ratio before the freeze-thaw process.

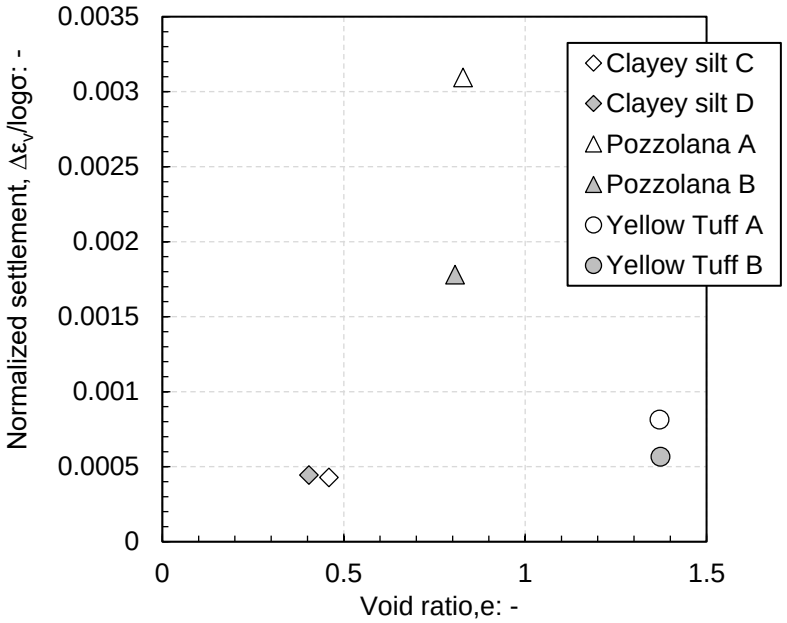

Figure 6.10 Normalised freezing-thawing settlements versus void ratio before the freezing-thawing cycle for different types of soils

6.3 Microstructural changes of soils

6.3.1 Introduction

Volume change behaviour of soils after oedometer tests with loading and thermal paths would cause the microstructure changes of soils. In this section, MIP tests are performed on soil samples to explore the microstructure changes after different stress and thermal path. It can be observed from MIP results that the variations of pore size distribution of soil samples at different stress and thermal paths such as initial sample, sample after stress path and sample after stress and thermal paths. The cumulative intrusion volumes with the pressure and pore diameter of soil samples can also be detected using MIP results.

The FESEM test can provide topographical and elemental information at high magnifications. Compared with convention SEM, FESEM produces clearer, less electrostatically distorted images with spatial resolution down to 1.5 nm-three to six times better. The soil samples after

oedometer tests are also performed on FESEM tests. The PCAS program is used to analyse the FESEM results and obtain some physical factors including average porosity, average pore diameter, pore area and fractal dimension etc. The analysed FESEM results can be used to verify the MIP results each other.

6.3.2 MIP results

6.3.2.1 Clayey silt

Figure 6.11 describes the pore size distribution functions for four clayey silt samples regarding the intruded volume of mercury referred to the volume of solids (non-wetting void ratio e_{nw}) for different entrance pore sizes x. The four samples include initial clayey silt sample after being reconstituted, clayey silt sample after freezing-thawing, clayey silt sample B (after stress loading and unloading) and clayey silt D (after stress path and thermal path).

As indicated in the figure, the initial clayey silt sample is dominated by macropores, which a peak density of pore size at around 100 μm. The stress loading and unloading decreases the macropore entrance size from 100 μm to 15 μm. The sizes of pores at the range between 1 μm and 10 μm are a little bit enlarged after freezing and thawing path under the constant vertical stress of 600 kPa. Without the loading-unloading path, the pores enlargement can be also observed in the initial sample only after freezing-thawing path, at the pore sizes between 1 μm and 10 μm. The reason why the freezing-thawing process enlarges the soil pore sizes is due to the density difference between water and ice, which the volume of ice is 1.09 times of that of water. Freezing usually occurs under water undrained conditions. Meanwhile, it is very interesting to find that the micropores less than 1 μm are not affected by the stress and temperature paths. Comparing the initial sample with the sample after freezing-thawing path, it can be found that the peak of pore sizes reduces from 100 μm to 80 μm, which is probable associated with the soil settlement on thawing.

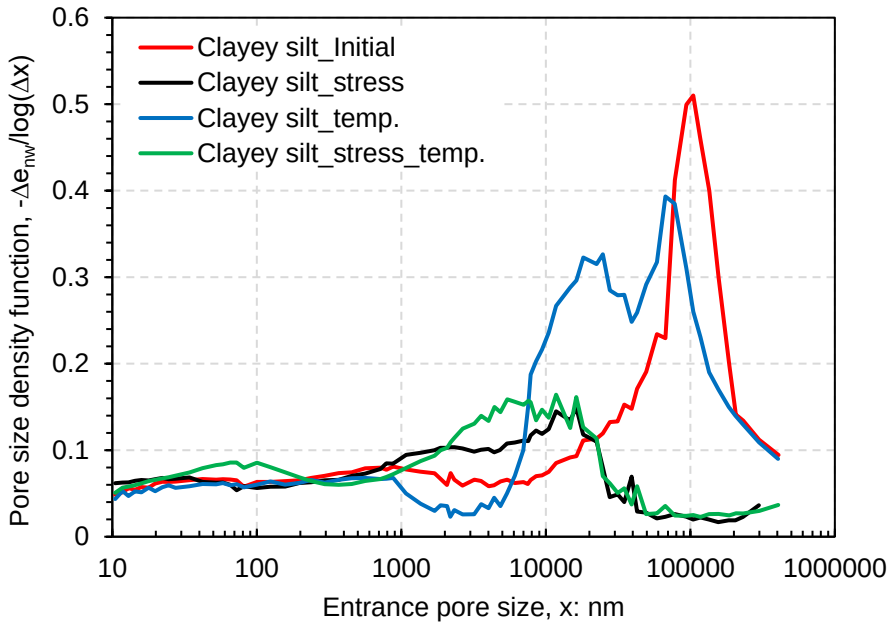

Figure 6.11 Pore size distribution curves from MIP on four clayey silt samples: initial sample, sample after thermal path, consolidated sample after stress path and conslidated sample after the stress-thermal path

6.3.2.2 Pozzolana

The pore size distributions of the intact Pozzolana sample and that after oedometer test of the loading-freezing-thawing-unloading path (Pozzolana B in above oedometer tests, Peláez et al., 2013) are presented in Figure 6.10, regarding the intruded volume of mercury referred to the volume of solids (non-wetting void ratio e_{nw}) for different pore size x. For Pozzolana samples, only one type of pores is observed from MIP results with sizes between 100 and 10000 nm. The peak density of pore sizes for intact Pozzolana sample is at around 1300 nm, and it shifts to 1000 nm after oedometer test along with stress and thermal paths. The curves in Figure 6.12 demonstrates that the oedometer test decreases the main pore sizes and induces some enlargement of macropores at sizes more than 10000 nm.

Normally the loading path decreases the pore size of soils (particular the macropores), and the freezing-thawing process could probably enlarge pores in soils. It is supposed that the decrease of pores is caused by both the loading-unloading path and freezing-thawing path. As there are not separate oedometer tests on Pozzolana sample along with the loading-unloading

path, it is difficult to know how much the deformation is induced by stress path and thermal path separately. The increase of pores is probably induced by the freezing-thawing process.

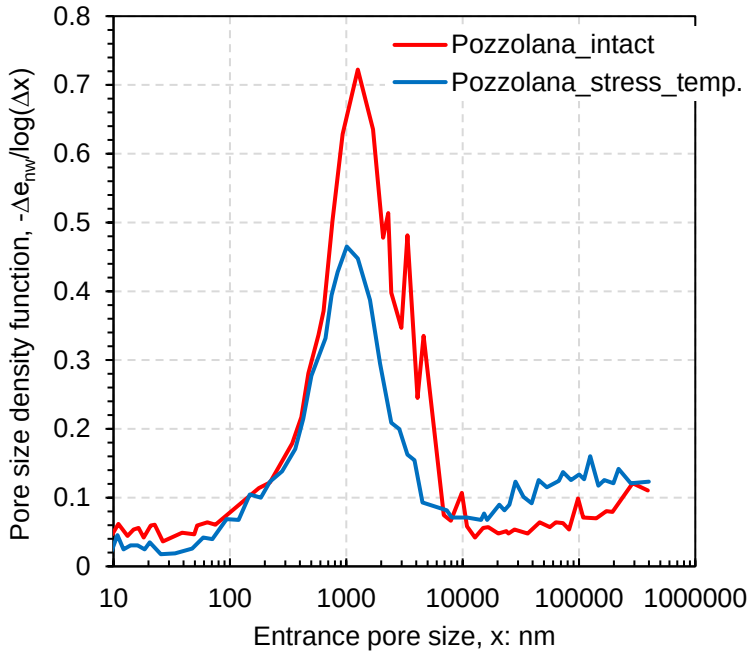

Figure 6.12 Pore size distribution curves from MIP on Pozzolana samples before and after the stress-thermal path

6.3.2.3 Yellow Tuff

The pore size distributions of the intact Yellow Tuff sample and that after oedometer test of loading-freezing-thawing-unloading (Yellow Tuff B in above oedometer tests, Peláez et al., 2013) are presented in Figure 6.13. Double structures in the intact Yellow Tuff sample are observed; the peak densities of the macro- and micro-pores are at 8 μm and 40 nm, respectively. The pore sizes of Yellow Tuff sample become homogeneous after stress and temperature loading and unloading, which are between 20 nm and 10 μm. It is supposed that the decrease of both macro and micropores are induced by stress path and the increase of pores at sizes of 100 -1000 nm is induced by the thermal path.

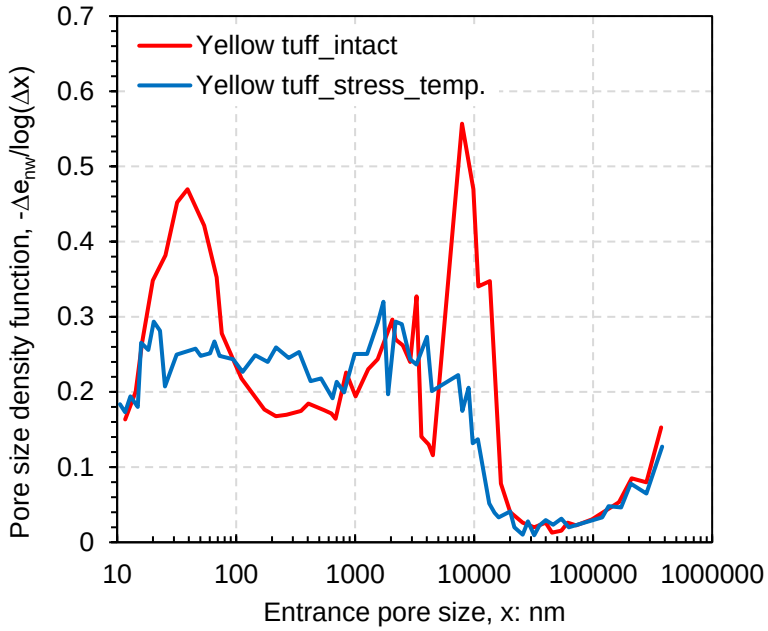

Figure 6.13. Pore size distribution curves from MIP on Yellow Tuff samples before and after the stress-thermal path

6.3.2.4 Discussion

After comparing with the MIP results of above three soils, the behaviour of pore size distributions of different type of soils is various. For clayey silt samples, due to separated stress controlled oedometer tests and stress-temperature controlled oedometer tests, it is clear to find that the loading-unloading path decreases the macropores and have no effects on micropores but the temperature freezing and thawing under certain stress would enlarge some pores. However, for Pozzolana sample, only one type of pores is observed in intact sample and after stress and temperature paths. Some enlargement of pores has been observed at sizes larger than 100000 nm that could be associated with the thermal path. For Yellow Tuff sample, it can be seen that path of stress and temperature would decrease both the micro and macro pores and make the pores focus on the sizes between 20 nm and 10 μm. To better understand the distribution evolutions of soils at their microstructure scale, the FESEM images of each soil with a different history of stress and thermal paths were obtained, as shown below.

6.3.3 FESEM results and PCAS analysis

6.3.3.1 Clayey silt

The reconstituted saturated clayey silt sample is prepared at only keep 20 kPa. The initial clayey silt sample, the initial sample after a cycle of freezing and thawing, the sample after a cycle of loading and unloading (Clayey silt A in section 6.2.2) and the sample after a cycle of the loading-freezing-thawing-unloading path are cut into one cubic centimetre and freeze-dried to perform the FESEM tests. For simplicity, they are called clayey silt (a), clayey silt (b), clayey silt (c) and clayey silt (d) hereinafter, respectively. The original FESEM images of these samples at different magnifications are presented in Appendix D. To analyse the variations of selected statistical parameters using the PCAS image processing program on these four samples, some of the original FESEM images are selected and processed to remove unnecessary information and leave only a plotting scale. As PCAS is an image processing program, it is also necessary to remove all boundary areas (black areas) that would be recognised as porosity area during PCAS processing. After processing the original FESEM images, the areas of interest of these four samples are selected and plotted in Figure 6.14.

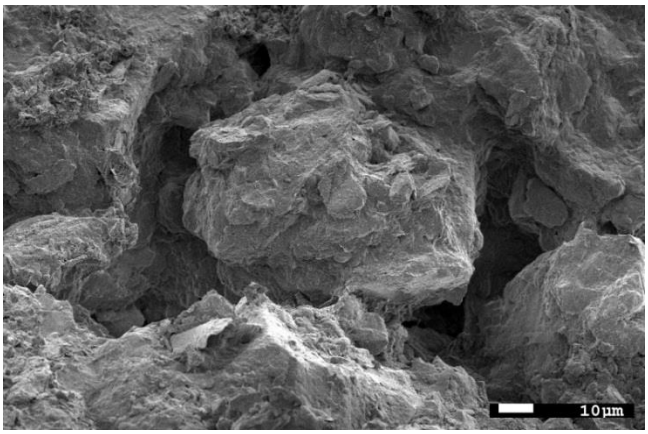

(a)

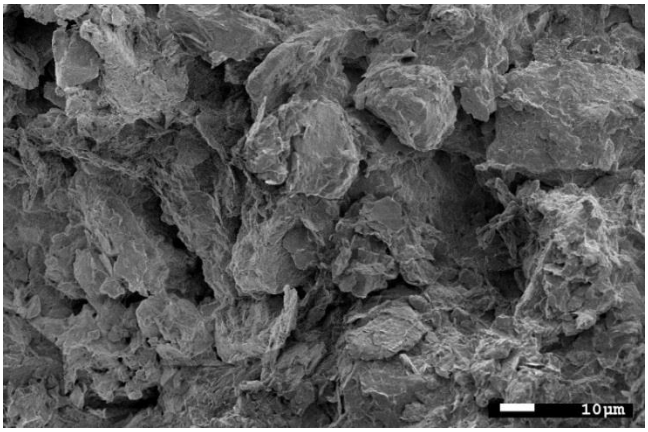

(b)

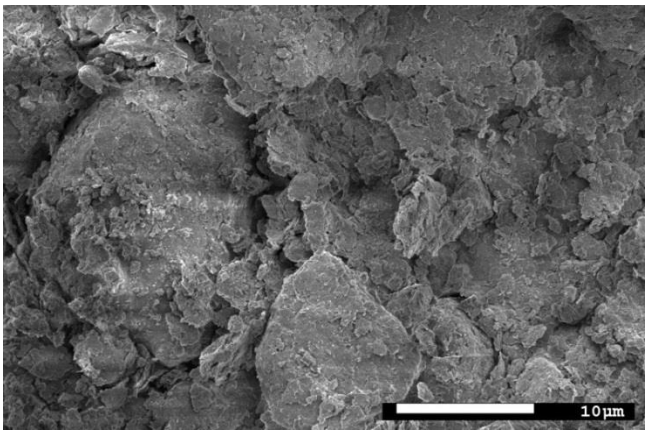

(c)

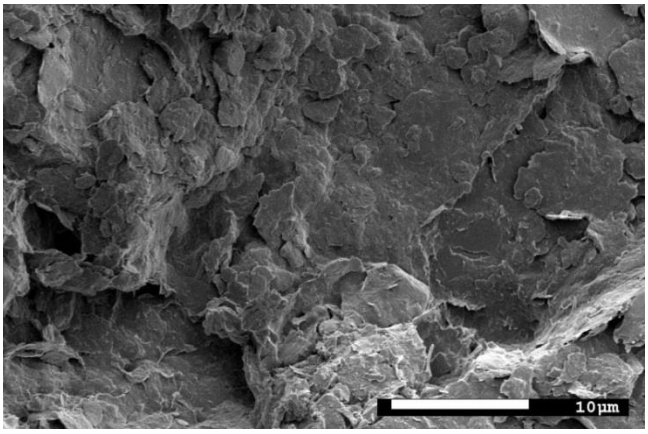

(d)

Figure 6.14 FESEM images of clayey silt sample: (a) initial sample; (b) after temperature path; (c) after stress path and (d) after stress temperature path

When applying the FESEM images in the PCAS program, they would first be segmented into series of white and black areas by a threshold value, in which white indicates soil particle and black indicates pores. The threshold value can be automatically used or adjusted by hand. To compare the changes of four images, it is important to keep the same threshold value. A threshold value of 70 is applied to these images of clayey silt samples, and their binary images with many dots are presented in Figure 6.15.

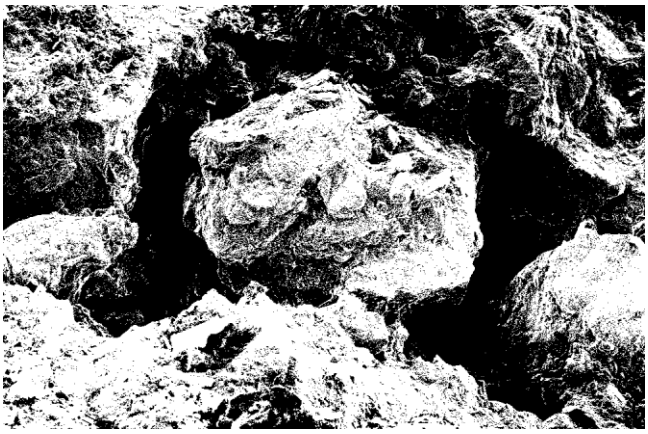

(a)

(b)

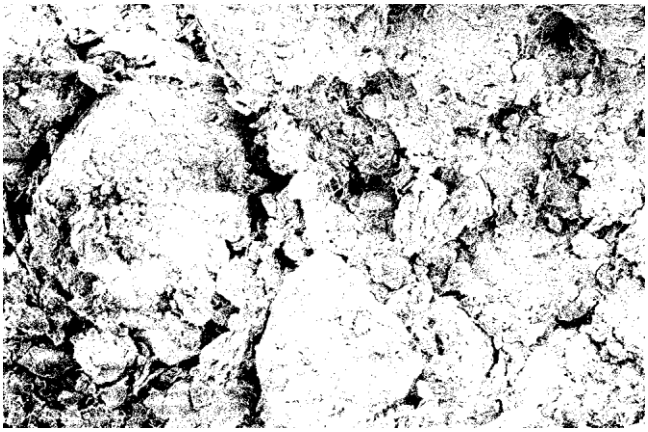

(c)

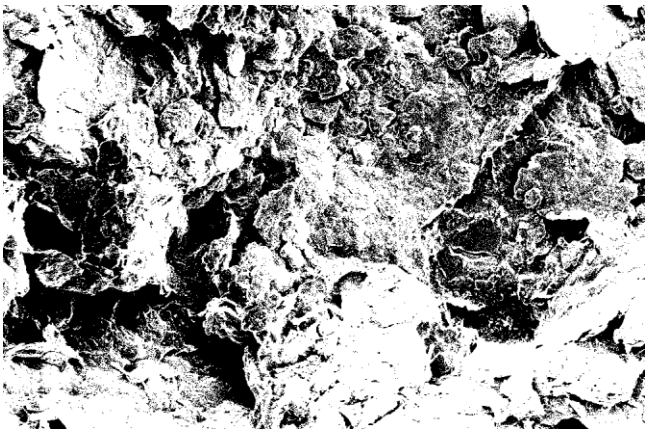

(d)

Figure 6.15 Binary images with many dots of clayey silt: (a) initial sample; (b) after temperature path; (c) after stress path and (d) after stress temperature path

The binary images are then used to recognise the pore regions by searching regions with more than a one element radius (pixel) and enclosing those regions. The white and black spots that are less than 20 pixels are removed to simplify the analysis. Then the binary images are recognised again, and the vector images of the four clayey silt samples are presented in Figure 6.16. The coloured regions with different areas stand for the soil particles and the black regions are pores.

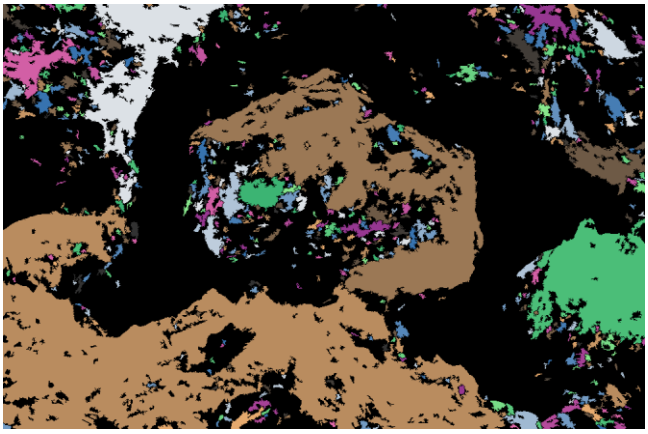

(a)

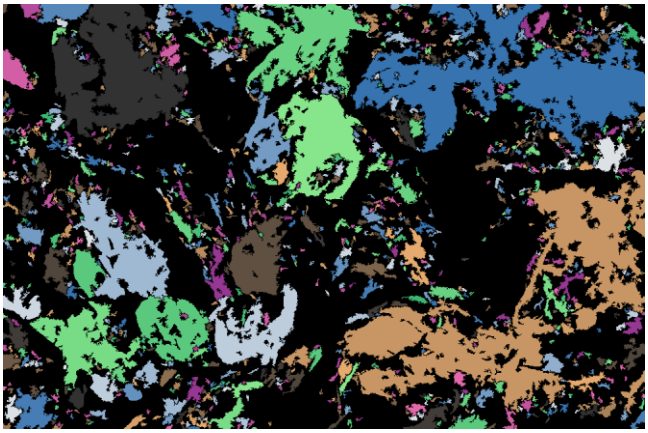

(b)

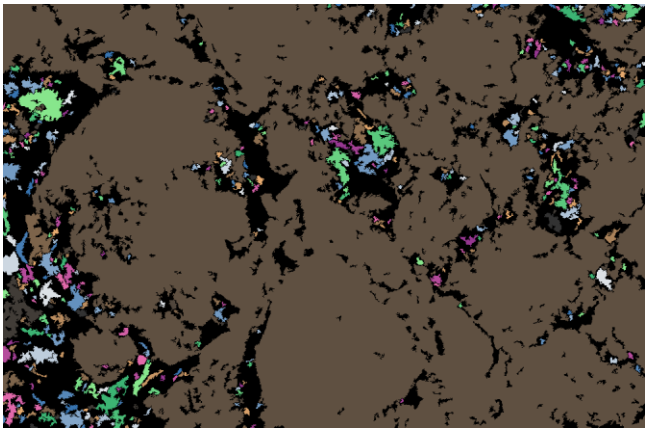

(c)

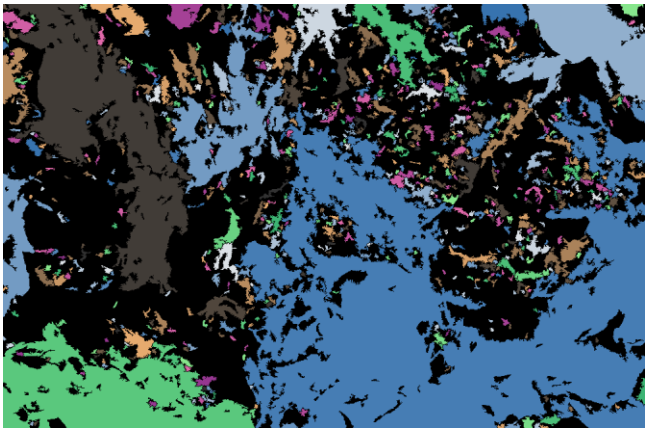

(d)

Figure 6.16 Vector images (pores are divided into rectangles) of clayey silt: (a) initial sample; (b) after temperature path; (c) after stress path and (d) after stress temperature path

After segmentation and recognition of pores in FESEM images, the specific statistical parameters of the pores, listed in Table 6.1, are automatically analysed by the program. To compare the variations of selected parameters of clayey silt samples after different stress and temperature path, two column charts are presented in Figure 6.17 (a) and (b) separately. The selected parameters include average region area, average perimeter, average form factor, fractal dimension and uniformity coefficient. The physical definition and expressions are explained in Appendix D. It is easy to understand the meaning of average area and perimeter of pores. The fractal dimension and average form factor give the complexity of pores, in which generally higher fractal dimensions or lower average form factor would increase the complexity of pores. The decrease of the uniformity coefficient indicates the soil particles have become more uniform.

Table 6.1 Region statistical parameters of Clayey silt samples

Parameter	Clayey silt (a)	Clayey silt (b)	Clayey silt (c)	Clayey silt (d)
Image area/pixel	660000	660000	660000	660000
Total region area	275263	283312	501654	361745
Region number	679	1051	504	798
Region percentage (Porosity)	41.71%	42.93%	76.01%	54.81%
Maximum region area	114950	46688	455583	160887

Average region area	405.39	269.56	995.35	453.31
Average perimeter	68.61	67.92	67.35	73.33
Average form factor	0.44	0.44	0.47	0.44
Maximum length	838.71	556.53	1197.75	752.83
Average length	18.07	17.67	17.14	18.51
Maximum width	348.00	281.84	660.00	520.00
Average width	10.01	10.15	10.01	10.25
Probability entropy	0.98	0.99	0.99	0.99
Fractal dimension	1.26	1.27	1.28	1.30
Area probability distribution index	2.08	1.96	2.06	2.00
Pore porosity distribution fractal dimension	2.07	1.81	2.06	1.94
Sorting coefficient	1.22	1.45	1.05	1.23
Uniformity coefficient	1.40	1.66	1.07	1.41
Curvature coefficient	1.09	0.99	1.00	1.09

In Figure 6.17 (a), the average area of pores and average perimeter of pores of clayey silt samples are presented. At a certain vertical stress, the freezing and thawing path could decrease the average area of pores; see clayey silt (a) and (b) and clayey silt (c) and (d). However, it is interesting to find that at higher vertical stress, the freezing-thawing path could increase the average perimeter of pores, which makes the shape of pores more complex. It is also indicated in Figure 6.17 (b) that the average form factor decreases, and fractal dimension increases after freezing and thawing. The uniformity coefficient increases after freezing and thawing. When compared the initial sample with sample after stress path, it can be observed that the average area and perimeter of pores would decrease after stress path as well as the uniformity coefficient. However, the average form factor and fractal dimension have no important changes after stress path.

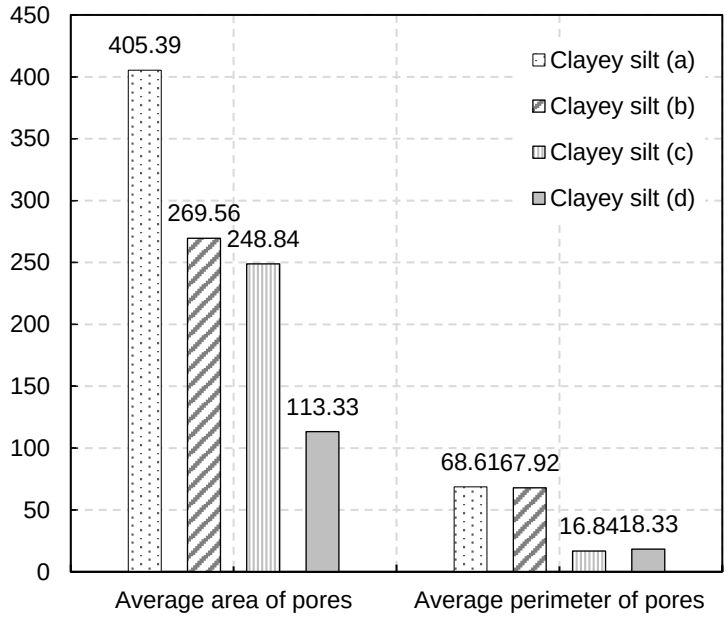

(a)

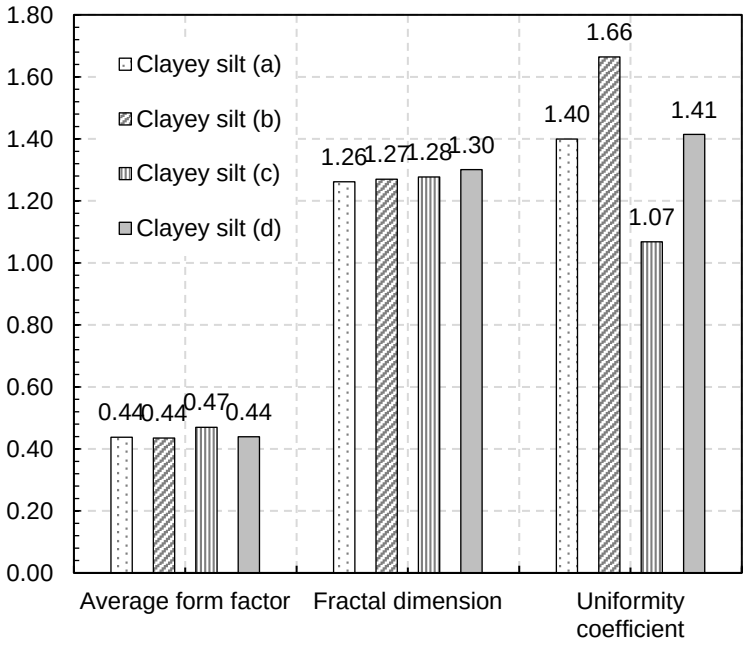

(b)

Figure 6.17 Selected statistical parameters of clayey silt samples from analysis of PCAS: (a) average area of pores and average perimeter of pores and (b) average form factor, fractal dimension and uniformity coefficient

6.3.3.2 Pozzolana

The intact Pozzolana sample and the sample after stress and temperature path of loading-unloading-freezing-thawing process (Pozzolana B as shown in section 6.2.3) are cut into one cubic centimetre and freeze-dried to perform the FESEM tests. The original FESEM images of intact Pozzolana sample and sample B are presented in Appendix E. To analyse the variations of the selected statistical parameters with the PCAS image processing program, in these two samples, original FESEM images at a magnification of 3000× are selected and processed to remove unnecessary information and leave only a plotting scale. As PCAS is an image processing program, it is also necessary to remove all boundary areas (black areas) that would be recognised as porosity area during PCAS processing. After processing the original FESEM images, the interesting areas of those two samples are plotted in Figure 6.18.

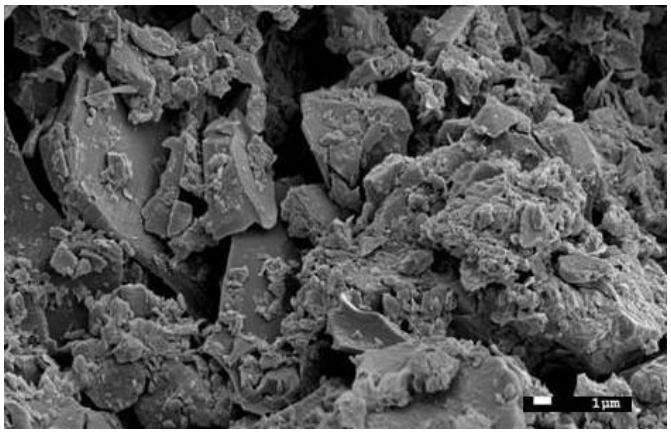

(a)

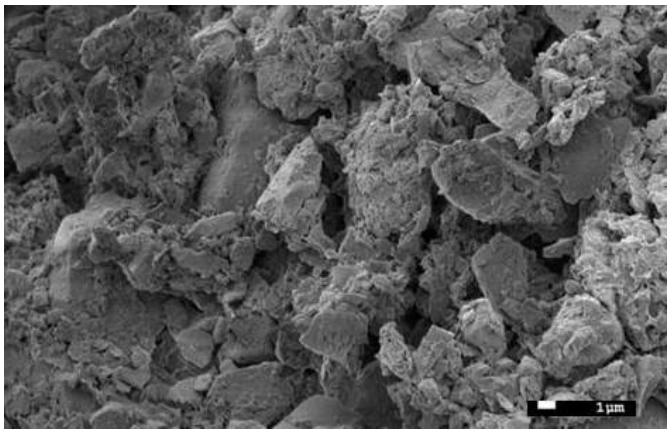

(b)

Figure 6.18 FESEM images of Pozzolana sample: (a) intact sample and (b) after the stress-thermal path

When applying the FESEM images in the PCAS program, they would first be segmented into series of white and black areas by a threshold value that white indicates soil particle and the black indicates pores. The threshold value can be automatically used or adjusted by hand. To compare the changes of two images, it is important to keep the same threshold value. A threshold value of 77 is applied to both images of Pozzolana samples, and their binary images with many dots are presented in Figure 6.19.

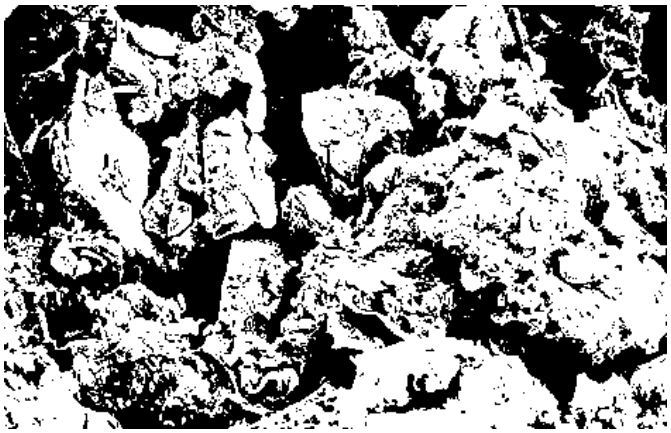

(a)

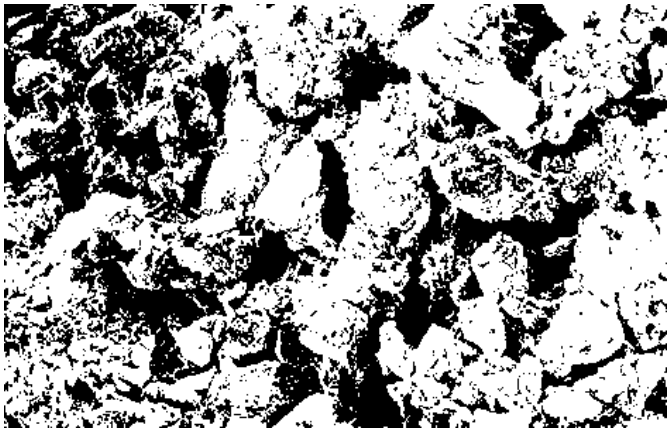

(b)

Figure 6.19 Binary images with many dots of Pozzolana: (a) intact sample and (b) after the stress-thermal path

The binary images are then used to recognise the pore regions by searching regions with more than a one element radius (pixel) and enclosing those regions. The white and black spots that are less than 20 pixels are removed to simplify the analysis. Then the binary images are recognised again, and the vector images of two Pozzolana samples are presented in Figure

6.20. The colour regions with different areas stand for the soil particles, and the black regions are pores.

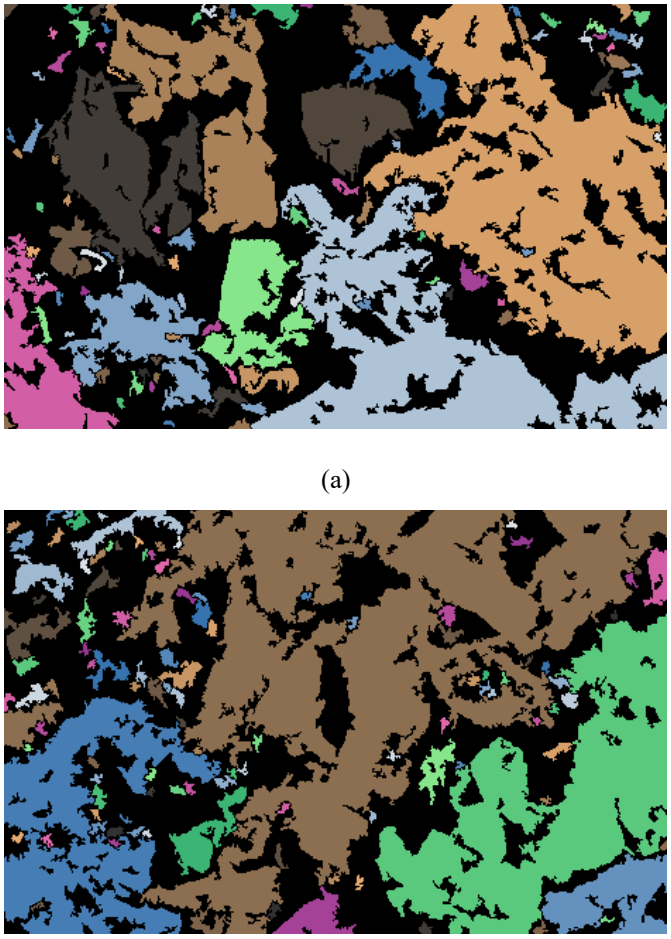

(a)

(b)

Figure 6.20 Vector images (pores are divided into rectangles) of Pozzolana: (a) intact sample and (b) after the stress-thermal path

After segmentation and recognition of pores in FESEM images, the specific statistical parameters of pores are listed in Table 6.2, which is automatically analysed by the program. To compare the variations of selected parameters of Pozzolana samples before and after the stress-temperature path of the loading-freezing-thawing-unloading path, two column charts are presented in Figure 6.21 (a) and (b) separately.

Table 6.2 Region statistical parameters of Pozzolana samples

Parameter	Pozzolana_before	Pozzolana_after
Image area/pixel	141000	141000
Total region area	80247	87475
Region number	97	114
Region percentage (Porosity)	56.91%	62.04%
Maximum region area	24639	42566
Average region area	827.29	767.32
Average perimeter	126.83	111.68
Average form factor	0.4712	0.465
Maximum length	317.42	465.59
Average length	28.71	24.68
Maximum width	174	274.66
Average width	16.62	14.43
Probability entropy	0.9215	0.97
Fractal dimension	1.3019	1.3142
Area probability distribution index	1.9999	1.8032
Pore porosity distribution fractal dimension	1.5223	1.7884
Sorting coefficient	1.3899	1.1892
Uniformity coefficient	1.6702	1.2226
Curvature coefficient	1.0867	0.9862

In Figure 6.21 (a), the average area of pores and average perimeter of pores are presented. Both the average area and the perimeter of pores decrease after the sample with stress loading and temperature freezing path. This phenomenon can also be observed in original FESEM images, in which large particles with large pores are observed in the image of Pozzolana_before and relatively smaller particles and smaller pores in the image of Pozzolan_after. Furthermore, the particles' surfaces of Pozzolana_before are much smoother than that of Pozzolana_after. As shown in Figure 6.21 (b), the average form factor and fractal dimension do not change a lot after stress and temperature path, which means the complexity of pores is more or less similar. The large drop in uniformity coefficient after stress and temperature path indicates the sample becomes more uniform.

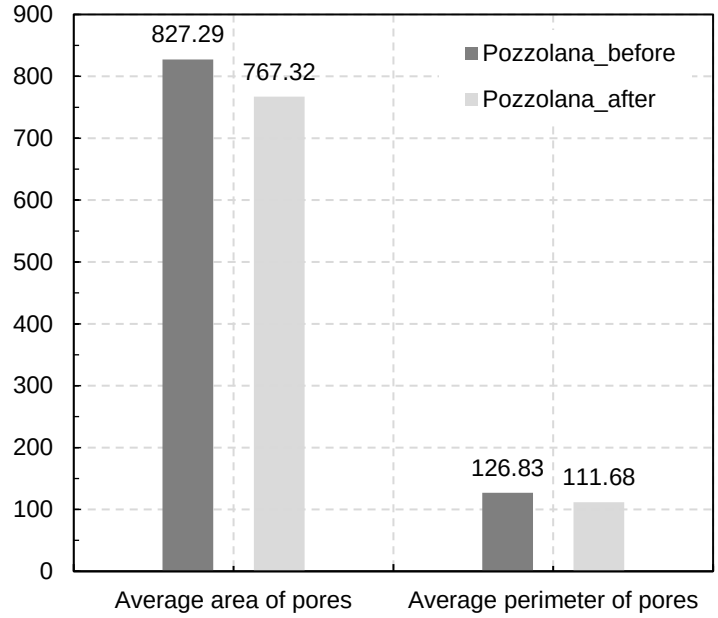

(a)

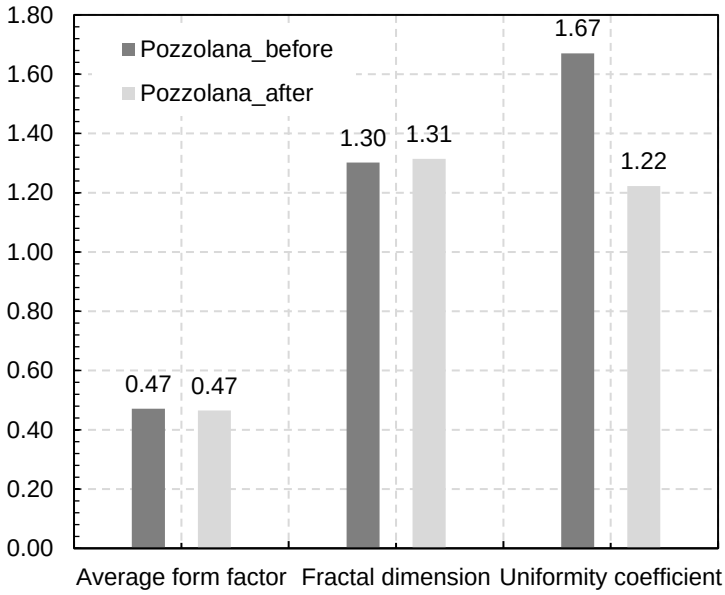

(b)

Figure 6.21 Selected statistical parameters of Pozzolana samples from analysis of PCAS: (a) average area of pores and average perimeter of pores and (b) average form factor, fractal dimension and uniformity coefficient

6.3.3.3 Yellow Tuff

The intact Yellow Tuff sample and the sample after stress and temperature path of loading-unloading-freezing-thawing process (Yellow Tuff B as shown in section 6.2.3) are cut into one cubic centimetre and freeze-dried to perform the FESEM tests. The original FESEM images of intact Yellow Tuff sample and sample B are presented in Appendix E. To analyse the variations of selected statistical parameters by the PCAS image processing program, in these two samples, original FESEM images at a magnification of 3000× are selected and processed to remove unnecessary information and leave only a plotting scale. As PCAS is an image processing program, it is also necessary to remove all boundary areas (black areas) that would be recognised as porosity area during PCAS processing. After processing the original FESEM images, the interesting areas of those two samples are selected in Figure 6.22.

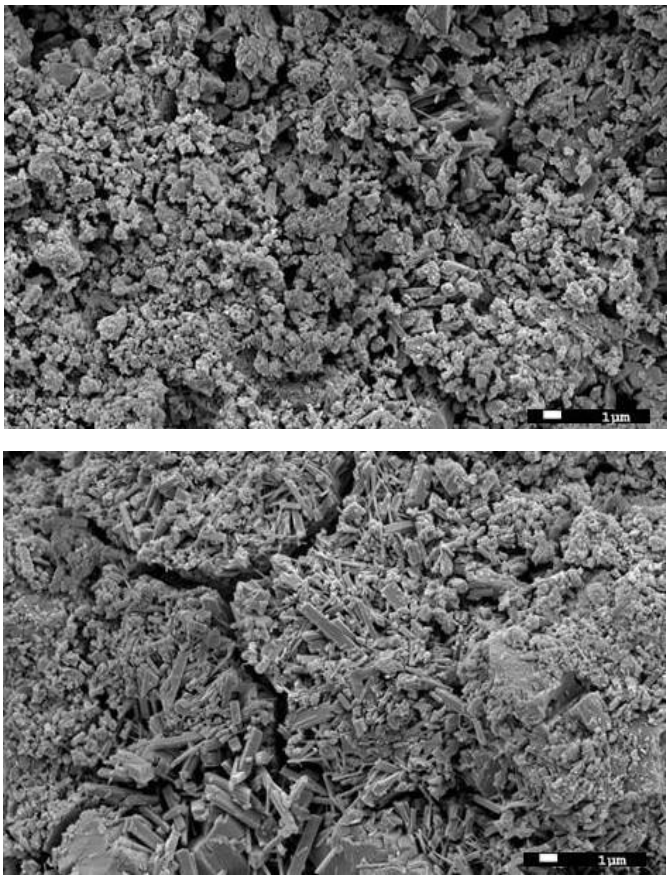

(a)

(b)

Figure 6.22 FESEM images of Yellow Tuff: (a) intact sample and (b) after the stress-thermal path

When applying the FESEM images in the PCAS program, they would first be segmented into series of white and black areas by a threshold value, in which white indicates soil particle and the black indicates pores. The threshold value can be automatically used or adjusted by hand. To compare the changes of two images, it is important to keep the same threshold value. A threshold value of 88 is applied to both images of Yellow Tuff samples, and their binary images with many dots are presented in Figure 6.23.

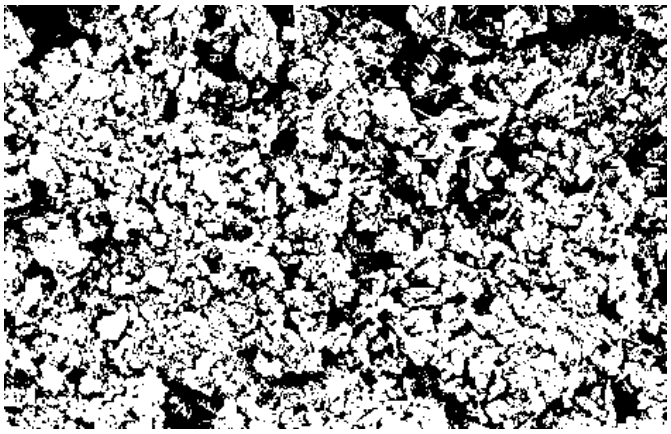

(a)

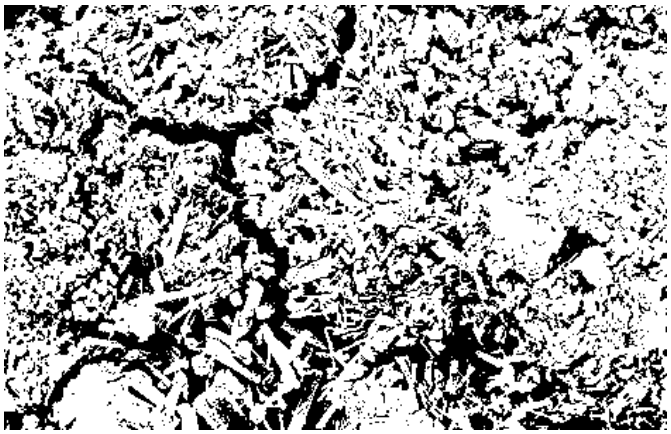

(b)

Figure 6.23 Binary images with many dots of Yellow Tuff: (a) intact sample (b) after stress and thermal path

The binary images are then used to recognise the pore regions by searching regions more than one element radius (pixel) and enclose the regions. The white and black spots less than 20 pixels are removed to simplify the analysis. Then the binary images are recognised again, and the vector images of two Yellow Tuff samples are presented in Figure 6.24. The colour

regions with different surface areas stand for the soil particles, and the black regions are pores.

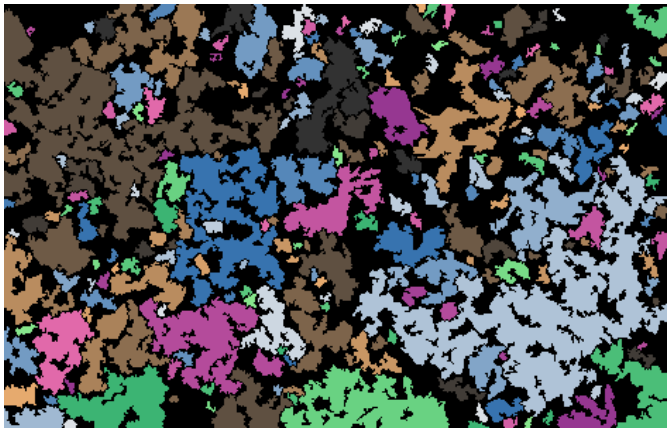

(a)

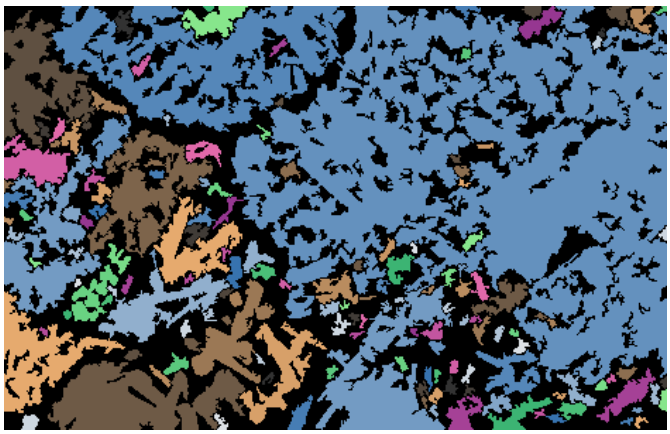

(b)

Figure 6.24. Vector images (pores are divided into rectangles) of Yellow Tuff: (a) intact sample and (b) after stress and thermal path

After segmentation and recognition of pores in FESEM images, the specific statistical parameters of pores are listed in Table 6.3, which is automatically analysed by the program. To compare the variations of selected parameters of Yellow Tuff samples before and after the stress-temperature path of the loading-freezing-thawing-unloading path, two column charts are presented in Figure 6.25 (a) and (b) separately.

Table 6.3 Region statistical parameters of Yellow Tuff samples

Parameter	Yellow Tuff_before	Yellow Tuff_after
Image area/pixel	141000	141000
Total region area	79191	91849
Region number	251	160
Region percentage (Porosity)	56.16%	65.14%
Maximum region area	10853	43111
Average region area	315.5	574.06
Average perimeter	95.02	103.34
Average form factor	0.4571	0.4471
Maximum length	238.36	346.49
Average length	23.23	24.63
Maximum width	147.41	264.79
Average width	14.06	14.51
Probability entropy	0.9823	0.9692
Fractal dimension	1.3427	1.3212
Area probability distribution index	1.5642	1.7472
Pore porosity distribution fractal dimension	1.2897	1.462
Sorting coefficient	1.5637	1.4389
Uniformity coefficient	1.8790	1.4897
Curvature coefficient	1.1096	0.9897

As shown in Figure 6.25 (a), both the average area of pores and the average perimeter of pores increased after the stress and temperature path, which is contrary to what expected. When returning to the original FESEM images, it can be observed that crack fissures occur on the sample with a stress and thermal cycle. Table 6.3, it indicates the statistical number of pores decreases from 251 to 160. Therefore, if taking no account of generated crack fissures, the average area of pores and average perimeter of pores of Yellow Tuff sample would decrease after a stress and thermal cycle. As plotted in Figure 6.25, the average form factor and fractal dimension of Yellow tuff do not change a lot after temperature controlled oedometer tests since the maximum vertical stress applied in the tests are lower than the yield stress of the soil. (see oedometer test in section 6.2.3). The decrease of uniformity coefficient states the sample becomes more uniform after a stress and thermal cycle.

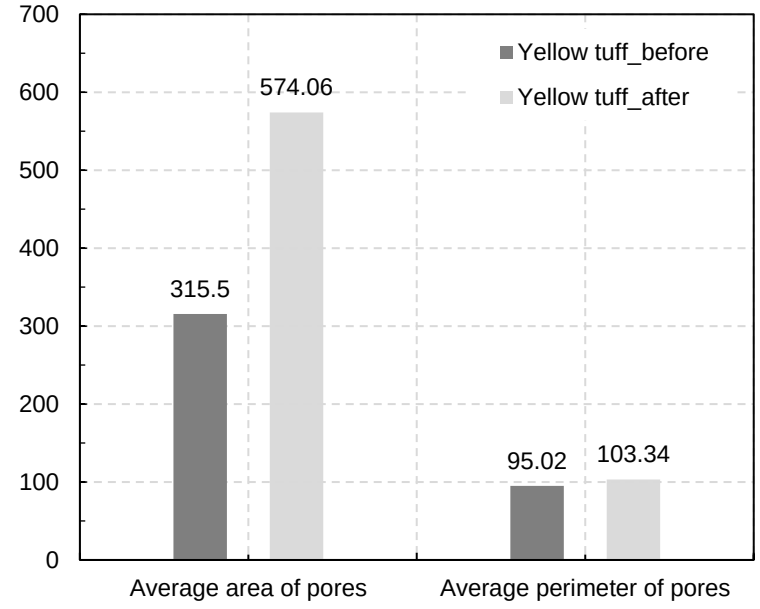

(a)

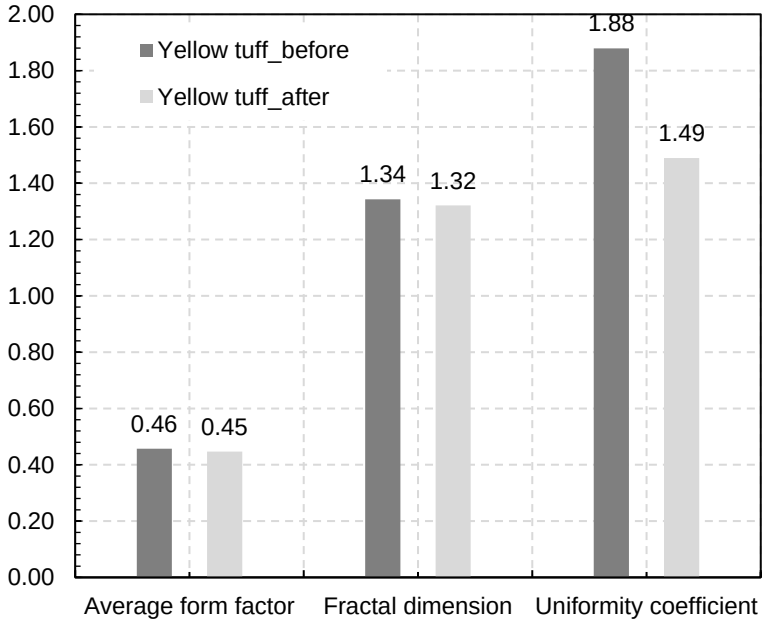

(b)

Figure 6.25 Statistical parameters of the Yellow Tuff sample before and after stress-thermal path: (a) average area of pores and average perimeter of pores and (b) average form factor, fractal dimension and uniformity coefficient

6.3.3.4 Discussion

Comparing the results of above three types of soils, it is important to say that the stress load and unload and temperature freeze and thaw path could decrease the average area and perimeter of pores that means the soil would be compressed. This conclusion has a good agreement with the oedometer test results and MIP results. In addition, the uniformity coefficient of soils would decrease after stress and temperature path, which means the samples are more homogeneous than before.

Even though the variations of average form factor and fractal dimension are not obvious in Pozzolana and Yellow Tuff samples. The reason is that the loading stresses on these two samples are not enough to make the soil yield. As it is observed on oedometer tests, the yielding stress of Pozzolana is between 200 and 500 kPa and that of Yellow Tuff is larger than 800 kPa. However, the trend shows that the stress and temperature path could decrease the average form factor and increase the fractal dimension, which means the complexity of the soils increased after the stress and thermal path.

6.4 Summary

In this chapter, the volume change behaviour of three soils after oedometer tests is investigated in this section, including two clayey silt samples under the loading-unloading path and two Pozzolana samples, two Yellow Tuff samples and two clayey silt samples under the loading-freezing-thawing-unloading path. Different void ratios of clayey silt samples are prepared. The final loading stresses for the Pozzolana samples are 200 and 500 kPa separately. Those for the Yellow Tuff samples are 500 and 800 kPa respectively. The experimental results demonstrate that: firstly, the soil freezing-thawing process would probably reduce the elastic deformation of a soil sample on subsequent unloading (swelling index close to 0). Secondly, the prepared initial void ratio of soil does not affect the final freezing-thawing settlement. However, the final loading stress constrains the freezing-thawing settlement of soils; the higher loading stress results in a smaller settlement.

Meanwhile, microstructure changes are also investigated using MIP and FESEM tests. The MIP results indicate the stress path decreases the macrostructure. The freezing-thawing cycle indicate some enlargement of pore volume. The FESEM results were analysed by the PCAS program automatically which also supported the MIP results.

Chapter 7 Conclusions and future research works

7.1 Summary and conclusions

The thesis has contributed to the understanding from a fundamental physical viewpoint of the coupled hydro-mechanical behavior of partially saturated and saturated soils during freezing and thawing. The emphasis on the fundamental study has been placed on the following aspects.

- Bulk electric conductivity EC, relative dielectric permittivity, and thermal conductivity measurements have been calibrated and used to exploring ice content (unfrozen liquid saturation) on partially saturated frozen soils (fine sand and clayey silt) at different temperatures. Different initial porosity and degrees of water saturation have been considered.
- A modification of Archie's law has been proposed to estimate the unfrozen liquid saturation. Model predictions have been compared to soil freezing retention curves obtained by combining the Clausius-Clapeyron equation with water retention data on drying, as well as with a capillary model with mercury intrusion porosimetry MIP results.
- The EC model has been used to monitor the temporal and spatial evolution of freezing processes performed in an updated electrical resistivity tomography ERT cell with data acquisition and reconstruction software. Homogeneous soils and with low and high conductive inclusions have been studied.
- The study of the volume change behaviour of different soils (clayey silt, Pozzolana, and Yellow Tuff) and the corresponding microstructural changes along different stress and temperature paths (loading/unloading paths at constant temperature and

freezing/thawing cycle at constant vertical stress). The microstructural changes after freezing/thawing paths have been studied using MIP and field emission scanning electron microscopy FESEM observations, which have been analysed using PCAS image processing software.

Before performing the experiments mentioned above, some required updates and modifications of the testing cells have been undertaken. The main improvements of the setups include the following aspects:

- Improving a cooling bath system, with antifreeze liquid, a thermostat and a thermally isolated chamber to control the temperature variation from 20 ºC to -15 ºC.
- Developing a new data acquisition software with enough channels to collect data on both displacements and temperatures at different time intervals.
- Modifying a set-up for measuring the thermal conductivity of soils to increase the thermal isolation of specimens during the test, and to adapt the set-up for both unfrozen and frozen soil conditions (partially for testing sand).
- Developing a new cylindrical ERT cell with 16 electrodes in the lateral Perspex wall, a freezing tube in the center of the specimen and thermally isolated polyethylene surrounding the whole cell to perform the freezing ERT tests.
- Modifying the set-up for performing temperature-controlled oedometer tests including drying the air with LiCl when applying compressed air for the vertical stress; measuring the soil temperature with thermocouple; covering the connection point between LVDT and the upper rod by PVC with polyethylene to avoid that the condensed vapor affects the measurement of the vertical displacements and building an independent support system for the LVDT to minimize thermal effects on the measurement of vertical displacements.

The main conclusions obtained during this investigation are presented and discussed below:

- The modified Archie's law and mixing alpha model have been initially used to fit the experimental results of bulk electrical conductivity and relative dielectric permittivity

results on two partially saturated soils with a commercial FDR probe. The model parameters have been determined under full unfrozen liquid $S_i = 0$ and maximum ice content $S_l \approx 0$ conditions. The models have been extended to cover intermediate states of unfrozen liquid saturation. The fitted equations have been proposed for estimating the ice content from bulk electrical conductivity and dielectric permittivity measurements at different porosities and partially saturation states for fine sand and clayey silt.

- The bulk electrical conductivity of fine sand and clayey silt specimens at five different initial degrees of water saturation has been measured along temperature decrease and freezing paths (from 20°C to -15°C) with an improved small cell with plate and needle electrodes and thermocouples. A 5% NaCl solution has been used as interstitial water to improve the contrast between ice and unfrozen water electrical conductivity values. Temperature reduction has induced a decrease of electrical conductivity, which can be associated with a reduction of the mobility of ions dissolved in the liquid phase (above the freezing point) and a decrease of available unfrozen liquid (that is the main carrier of electrical current) on freezing. Archie's law together with a temperature dependent expression for the electrical conductivity of the interstitial water in the freezing zone has been used to interpret the experimental results and estimate the unfrozen water content at different temperatures, since the electrical conductivity of the solid phase is, as a first approximation, negligible in soils with moderate specific surface. The proposed approach considers the porosity effects and the initial degree of saturation. The salinity of the interstitial water affects the freezing point, as well as the residual unfrozen liquid saturation below -7ºC.
- The thermal conductivity of fine sand and clayey silt specimens at several different initial degrees of saturation has been measured at room temperature (20 ºC, full unfrozen state) and low temperature (-15 ºC, maximum frozen state). Tap water has been used as interstitial water to decrease salinity effects on soil freezing. A modified Chen's empirical model has been successfully used to interpret the experimental results, which considers the thermal conductivity of each constituent in the soil, as well as the initial porosity and the initial degree of saturation.

- The unfrozen water fraction of soils at different temperatures from bulk electrical conductivity measurements have been compared with the soil freezing retention curves obtained by combining the Clausius-Clapeyron equation with water retention data on drying path, as well as with a bundle capillary model with mercury intrusion porosimetry data. Very good agreements have been found between the proposed approach using bulk electrical conductivity data and the two selected freezing retention curve models. The consistency between these indirect methods has validated the approach followed for the interpretation of bulk electrical conductivity measurements.
- Two-dimensional electrical resistivity tomography ERT tests on the saturated homogeneous fine sand and clayey silt soils have been performed and test results have been interpreted to evaluate the transient freezing of a cylindrical sample that was exposed to very low temperatures at its central axis and adiabatic conditions at the external boundaries. Reconstructed maps of EC were interpreted with the proposed model to determine the temporal and spatial evolutions of unfrozen liquid saturation and temperature. The reconstructed temperatures at selected points had a good agreement with measured ones by thermocouples, which demonstrated the validity of the proposed model. ERT test results showed water migration effects associated with the induced cryogenic suction on freezing. ERT results also allowed correctly detecting and evaluating the effects of low and high conductivity inclusions on a transient freezing process.
- The transient temporal and spatial evolutions along the freezing process are valuable data to be interpreted with the coupled FEM Code_Bright. In addition, the experience collected has shown that electrical methods can be a viable tool for the laboratory study of the physical processes related to freezing and thawing, and possibly also for in situ monitoring of engineering works.
- Regarding the volume change behaviour, a small irreversible compression has been systematically detected after a freezing/thawing cycle on different soils, which depended on the current stress state (at higher stresses a lower irreversible

compression has been detected). Mercury intrusion porosimetry MIP results have indicated that the freezing/thawing process might have decreased the macropore volume (between aggregates) and enlarge some micropore volume. The image analyses of the electron microscopy observations also allowed detecting some decrease of the porosity and the average macropore diameter after a freeze-drying cycle, which was consistent with the macroscopic phenomenological response (irreversible compression) and the MIP results.

7.2 Future research works

There are still some additional issues that can be proposed based on this thesis:

- To increase the bulk EC of the unfrozen liquid, a 5% NaCl solution was used as interstitial water in most of the experiments in the thesis. Nevertheless, some effect of salinity on relative dielectric permittivity was found when using the commercial FDR. The salinity also affected not only the freezing point but also the residual unfrozen liquid saturation. Therefore, it will be worth exploring the freezing behavior of soils with a lower salinity of the pore water.
- The thermal conductivity of soil samples with different initial porosity and degrees of saturation were measured at room temperature (20 °C) and at a low temperature (-15 °C). Furthermore, it would be interesting to design a new setup that can be used to measure the thermal conductivity of the soil along the freezing process. An expression should be proposed accordingly to also determine the ice content by thermal conductivity measurements. It is also possible to use heat capacity to distinguish the ice and water in frozen soils, the heat capacity of water and ice are 75.33 (at 25 °C) and 38.09 (at -10 °C) $J/mol^{-1}K^{-1}$, respectively.
- The 3D electric resistivity tomography oedometer cell developed jointly by Politecnico di Torino and UPC could be used to explore the temporal and spatial evolution of unfrozen liquid saturation on freezing, as well as the changes undergone on temperature and loading paths. A new setup should be designed to induce the freezing process along the central axis of the sample.

- Besides oedometer conditions, it will be also worth investigating the volume change behavior and the shear strength response using a triaxial cell prepared for freezing/thawing paths. The recently developed triaxial cell by Università degli Studi di Roma 'Tor Vergata' and UPC with the freezing system along the axis of the cylindrical sample would be an interesting apparatus to perform these tests.
- The cryogenic suction could be directly measured using a psychrometer, tensiometer or axis translation technique. To delay the freezing of the liquid, saline water could be used instead of pure water. Specific calibrations would be required.
- The newly proposed freezing retention and thermal conductivity models could be implemented in Code_Bright to simulate the soil THM behavior along a freezing path. The numerical modeling of the soil response during the aforementioned ERT tests could be also used to estimate thermal and freezing retention parameters of the frozen soils.

References

Abu-Hassanein, Z. S., Benson, C. H., & Blotz, L. R. (1996). Electrical resistivity of compacted clays. *Journal of geotechnical engineering*, 122(5), 397-406.

Aduda, B. O. (1996). Effective thermal conductivity of loose particulate systems. *Journal of materials science*, 31(24), 6441-6448.

Alonso, E. E., & Romero, E. (2003). Collapse behaviour of sand. *In Proc. Of the 2nd Asian Conference on Unsaturated Soils*. Osaka, Japan, 325-334.

Andersland, O. B., & Ladanyi, B. (2004). Frozen ground engineering. *John Wiley & Sons*.

Anderson, D. M., & Tice, A. R. (1972). Predicting unfrozen water contents in frozen soils from surface area measurements. *Highway research record*, 393, 12-18.

Archie G. E. (1942). The electrical resistivity log as an aid in determining some reservoir characteristics. *Transactions of the AIME*, 146(01), 54-62.

Arenson, L. U., & Sego, D. C. (2006). The effect of salinity on the freezing of coarse-grained sands. *Canadian Geotechnical Journal*, 43(3), 325-337.

Arulmoli, K., Arulanandan, K., & Seed, H. B. (1985). New method for evaluating liquefaction potential. *Journal of Geotechnical Engineering*, 111(1), 95-114.

Avellaneda, M., & Torquato, S. (1991). Rigorous link between fluid permeability, electrical conductivity, and relaxation times for transport in porous media. *Physics of Fluids A: Fluid Dynamics*, 3(11), 2529-2540.

Bai, R., Lai, Y., Zhang, M., & Yu, F. (2018). Theory and application of a novel soil freezing characteristic curve. *Applied Thermal Engineering*, *129*, 1106-1114.

Bai, W., Kong, L. and Guo, A. (2013). Effects of physical properties on electrical conductivity of compacted lateritic soil. *Journal of Rock Mechanics and Geotechnical Engineering*, 5(5), 406-411.

Baker, T. H. W., Davis, J. L., Hayhoe, H. N., & Topp, G. C. (1982). Locating the frozen-unfrozen interface in soils using time-domain reflectometry. *Canadian Geotechnical Journal*, 19(4), 511-517.

Barker, R., & Moore, J. (1998). The application of time-lapse electrical tomography in groundwater studies. *The Leading Edge*, 17(10), 1454-1458.

Barnett, T. P., Adam, J. C., & Lettenmaier, D. P. (2005). Potential impacts of a warming climate on water availability in snow-dominated regions. *Nature*, 438(7066), 303.

Barrera, M. (2002). Estudio experimental del comportamiento hidro-mecánico de suelos colapsables (in Spanish). *Ph.D. thesis*, Universitat Politècnica de Catalunya, Barcelona, Spain.

Barron, J. J., & Ashton, C. (2005). The effect of temperature on conductivity measurement. *TSP*, 7(3).

Barry-Macaulay, D., Bouazza, A., Singh, R. M., Wang, B., & Ranjith, P. G. (2013). Thermal conductivity of soils and rocks from the Melbourne (Australia) region. *Engineering Geology*, 164, 131-138.

Bena, E. (2003). Tomografia elettrica di impedenza per la stima della quantita` di solido in miscela bifase liquido-solido. *Master thesis*, Politecnico di Torino (in Italian).

Bittelli, M., Flury, M., & Roth, K. (2004). Use of dielectric spectroscopy to estimate ice content in frozen porous media. *Water resources research*, 40(4).

Black, P. B. (1995). Applications of the Clapeyron equation to water and ice in porous media (No. CRREL-95-6). *COLD REGIONS RESEARCH AND ENGINEERING LAB HANOVER NH*.

Blewett, J., McCarter, W. J., Chrisp, T. M., & Starrs, G. (2001). Monitoring sedimentation of a clay slurry. *Geotechnique*, 51(8), 723-728.

Boike, J., and K. Roth. (1997). Time domain reflectometry as a field method for measuring water content and soil water electrical conductivity at a continuous permafrost site, *Permafrost Periglac*, 8(4), 359–370.

Borsic, A., Comina, C., Foti, S., Lancellotta, R. & Musso, G. (2005). Imaging heterogeneities with electrical impedance tomography: laboratory results. *Géotechnique*, 55(7), 539-547.

Borsic, A. (2002). Regularization methods for imaging from electrical measurements. *PhD thesis*, School of Engineering, Oxford Brookes University.

Brandon, T. L., & Mitchell, J. K. (1989). Factors influencing thermal resistivity of sands. *Journal of Geotechnical Engineering*, 115(12), 1683-1698.

Breckon, W. R. (1990). Image reconstruction in electrical impedance tomography. *PhD thesis*, Oxford Brookes Polytechnic.

Buehler, M., Cobos, D., & Dunne, K. (2011). Dielectric constant and Osmotic Potential from Ion-Dipole Polarization Measurements of KCl and NaCl-doped Aqueous solutions. *ISEMA Proceeding*.

Buenfil, C., Romero, E., Lloret, A., & Gens, A. (2005). Experimental study on the hydro-mechanical behaviour of a silty clay. *Unsaturated Soils. Advances in Testing, Modelling and Engineering Applications*. London: Taylor & Francis Group, 15-28.

Calderón, A. P. (2006). On an inverse boundary value problem. *Computational & Applied Mathematics*, 25(2-3), 133-138.

Cárdenas, O. E., Weber, R. C., Romero, E., Lloret, A., & Suriol, J. (2015). Studying collapse behaviour of sandy silt under generalised stress conditions. *In Proceeding 6th International Symposium on Deformation Characteristics of Geomaterials*, IOS Press Amsterdam, 462-469.

Carslaw, H. S., & Jaeger, J. C. (1959). Conduction of heat in solids: *Oxford Science Publications* (p. 510). Oxford, England.

Casini F., Gens A., Olivella S. & Viggiani G. (2013). Coupled phenomena induced by freezing in a granular material. *In Proceedings of the International Symposium*, ISSMGE TC 215, 467-473.

Casini, F., Gens Solé, A., Olivella Pastallé, S., & Viggiani, G. (2016). Artificial ground freezing of a volcanic ash: laboratory tests and modelling. *Environmental Geotechnics*, 3(3), 1-14.

Casini, F., Gens Solé, A., Olivella Pastallé, S., & Viggiani, G. (2016). Artificial ground freezing of a volcanic ash: laboratory tests and modelling. *Environmental Geotechnics*, 3(3), 1-14.

Chang, D.K. and Lacy, H.S. (2008). Artificial Ground Freezing in Geotechnical Engineering. *International Conference on Case Histories in Geotechnical Engineering*, 5.

Chen, S. X. (2008). Thermal conductivity of sands. *Heat and Mass Transfer*, 44(10), 1241-1246.

Cheney, M., Isaacson, D., Newell, J. C., Simske, S., & Goble, J. (1990). NOSER: An algorithm for solving the inverse conductivity problem. *International Journal of Imaging Systems and Technology*, 2(2), 66-75.

Cheng, G., & Wu, T. (2007). Responses of permafrost to climate change and their environmental significance, Qinghai-Tibet Plateau. *Journal of Geophysical Research: Earth Surface*, 112(F2).

Cheng, G., & Zhao, L. (2000). The problems associated with permafrost in the development of the Qinghai-Xizang Plateau. *Quaternary Sciences*, 20(6), 521-531.

Colombo, G., Lunardi, P., Cavagna, B., Cassani, G., & Manassero, V. (2008, September). The artificial ground freezing technique application for the Naples underground. *In Proceedings of Word Tunnel Congress* (Vol. 910921).

Comina, C., Cosentini, R. M., Foti, S. & Musso, G. (2010). Electrical tomography as laboratory monitoring tool. *Rivista Italiana di Geotecnica*, 44, 15-26.

Comina, C., Cosentini, R. M., Della Vecchia, G., Foti, S., & Musso, G. (2011). 3D-electrical resistivity tomography monitoring of salt transport in homogeneous and layered soil samples. *Acta Geotechnica*, 6(4), 195-203.

Comina, C., Foti, S., Musso, G., & Romero, E. (2008). EIT Oedometer: an advanced cell to monitor spatial and time variability in soil with electrical and seismic measurements. *Geotechnical Testing Journal*, 31(5), 404-412.

Cosentini, R. M., Della Vecchia, G., Foti, S. & Musso, G. (2012). Estimation of the hydraulic parameters of unsaturated samples by electrical resistivity tomography. *Géotechnique*, 62(7), 583-594.

Côté, J., & Konrad, J. M. (2005). A generalized thermal conductivity model for soils and construction materials. *Canadian Geotechnical Journal*, 42(2), 443-458.

Damasceno, V. M., Fratta, D. & Bosscher, P. J. (2009). Development and validation of a low-cost electrical resistivity tomographer for soil process monitoring. *Canadian Geotechnical Journal*, 46(7), 842-854.

Dash, J. G., Leger, R., & Fu, H. Y. (1997). Frozen soil barriers for hazardous waste confinement (No. CONF-970208--PROC).

Decagon Devices, Inc, Em50/Em50R/Em50G Em50 Series Data Collection System: Operator's Manual. (2015). http://manuals.decagon.com / Manuals/13453_Em50_Web.pdf.

De Loor G. P. (1964). Dielectric properties of heterogeneous mixtures with a polar constituent. *Applied Scientific Research, Section B*, 11(3-4), 310-320.

Desbois, G., Urai, J. L., Hemes, S., Brassinnes, S., De Craen, M., & Sillen, X. (2014). Nanometer-scale pore fluid distribution and drying damage in preserved clay cores from Belgian clay formations inferred by BIB-cryo-SEM. *Engineering Geology*, 179, 117-131.

De Vries, D. A. (1963). Thermal properties of soils. Physics of plant environment. *Physics of plant environment. Wiley*, New York, 210–235.

Dillon, H. B., & Andersland, O. B. (1966). Predicting unfrozen water contents in frozen soils. *Canadian geotechnical journal*, 3(2), 53-60.

Dirksen C. & Dasberg, S. (1993). Improved calibration of time domain reflectometry soil water content measurements. *Soil Science Society of America Journal*, 57(3), 660-667.

Dobson M. C., Ulaby F. T., Hallikainen M. T. & El-Rayes M. A. (1985). Microwave dielectric behaviour of wet soil—Part II: Dielectric mixing models. IEEE Trans. *Geosci. Remote Sens*, 23(1), 35-46.

Donazzi, F., Occhini, E., & Seppi, A. (1979). Soil thermal and hydrological characteristics in designing underground cables. *In Proceedings of the Institution of Electrical Engineers*, 126(6), 506-516.

Dong, Y., McCartney, J. S., & Lu, N. (2015). Critical review of thermal conductivity models for unsaturated soils. *Geotechnical and Geological Engineering*, 33(2), 207-221.

Erchul, R. A., & Gularte, R. C. (1981). Electrical resistivity used to measure liquefaction of sand. *ASTM Geotechnical Testing Journal*, 108, 778–782.

Ershov, E. D. (1979). Fazoviy Sostav Vlagi v Myerzlih Porodah (The Phase Composition of Water in Frozen Soils). *Izd. Mosk. Univ*., Moskva.

Esch, D. C. (2004). Thermal analysis, construction, and monitoring methods for frozen ground. TCCRE Monographs. *American Society of Civil Engineers*, 498.

Farouki, O. T. (1981). The thermal properties of soils in cold regions. *Cold Regions Science and Technology*, 5(1), 67-75.

Flerchinger, G. N., Seyfried, M. S., & Hardegree, S. P. (2006). Using soil freezing characteristics to model multi-season soil water dynamics. *Vadose Zone Journal*, 5(4), 1143-1153.

Fortier, R., Allard, M., & Sheriff, F. (1996). Field estimation of water ice phase composition of permafrost samples using a calorimetric method. *Canadian geotechnical journal*, 33(2), 355-362.

Fukue M., Minato T., Horibe H. & Taya N. (1999). The microstructures of clay given by resistivity measurements. *Engineering Geology* 54, 43–53.

Gangadhara Rao, M. V. B. B., & Singh, D. N. (1999). A generalized relationship to estimate thermal resistivity of soils. *Canadian Geotechnical Journal*, 36(4), 767-773.

Glover, P. W., Hole, M. J., & Pous, J. (2000). A modified Archie's law for two conducting phases. *Earth and Planetary Science Letters*, 180(3-4), 369-383.

Gong H., Shao Y., Brisco B., Hu Q. & Tian W. (2013). Modelling the dielectric behaviour of saline soil at microwave frequencies. *Canadian Journal of Remote Sensing*, 39(1), 17-26.

Gonzalez-Blanco, L. (2017). Gas migration in deep argillaceous formations: Boom clay and indurated clays. *PhD thesis*. Universitat Politècnica de Catalunya, Barcelona.

Harris, J. S. (1995). Ground freezing in practice. *Thomas Telford*.

Hauck, C. (2002). Frozen ground monitoring using DC resistivity tomography. *Geophysical Research Letters* 29(21): 1-4.

Hayashi, M. (2004). Temperature-electrical conductivity relation of water for environmental monitoring and geophysical data inversion. *Environmental monitoring and assessment*, 96(1), 119-128.

Hayhoe, H. N., Topp, G. C., & Bailey, W. G. (1983). Measurement of soil water contents and frozen soil depth during a thaw using time-domain reflectometry. *Atmosphere-Ocean*, 21(3), 299-311.

He, H., & Dyck, M. (2013). Application of multiphase dielectric mixing models for understanding the effective dielectric permittivity of frozen soils. *Vadose Zone Journal*, 12(1), 1-22.

Holder, D. S. (2004). Electrical impedance tomography: Methods, history and applications. *London: Institute of Physics*.

Hua, P., Webster, J. G., & Tompkins, W. J. (1988). A regularised electrical impedance tomography reconstruction algorithm. *Clinical Physics and Physiological Measurement*, 9(4A), 137-141.

Ishizaki, T., Maruyama, M., Furukawa, Y., & Dash, J. G. (1996). Pre-melting of ice in porous silica glass. Journal of crystal growth, 163(4), 455-460.

Jinguuji, M., Toprak, S., & Kunimatsu, S. (2007). Visualization technique for liquefaction process in chamber experiments by using electrical resistivity monitoring. *Soil Dynamics and Earthquake Engineering*, 27(3), 191-199.

Johansen O (1975) Thermal conductivity of soils. N.H. CRREL Draft English Translation 637. *Ph.D. thesis*, University of Trondheim, Trondheim, Norway.

Jones, S. B., & Or, D. (2003). Modelled effects on permittivity measurements of water content in high surface area porous media. *Physica B: Condensed Matter*, 338(1-4), 284-290.

Kalinski, R. J., & Kelly, W. E. (1993). Estimating water content of soils from electrical resistivity. *Geotechnical Testing Journal*, 16(3), 323-329.

Kamon, M., Endo, K., & Katsumi, T. (2003). Measuring the k–S–p relations on DNAPLs migration. *Engineering Geology*, 70(3-4), 351-363.

Kelly, W. E. (1977). Electrical resistivity for estimating permeability. *Journal of the Geotechnical Engineering Division*, 103(10), 1165-1169.

Kersten, M. S. (1949). Laboratory research for the determination of the thermal properties of soils. *University of Minnesota*, Minneapolis engineering experiment station.

Knight, C. A. (1971). Experiments on the contact angle of water on ice. *Philosophical Magazine*, 23(181), 153-165.

Kolehmainen, V. (2001). Novel approaches to image reconstruction in diffusion tomography. *PhD thesis*, Department of Applied Physics, Kuopio University, Finland.

Konrad, J. M. (1990). Unfrozen water as a function of void ratio in a clayey silt. *Cold regions science and technology*, 18(1), 49-55.

Koopmans, R. W. R., & Miller, R. D. (1966). Soil Freezing and Soil Water Characteristic Curves1. *Soil Science Society of America Journal*, 30(6), 680-685.

Lambert, M. A., & Fletcher, L. S. (1997). Thermal contact conductance of spherical rough metals. *Journal of heat transfer*, 119(4), 684-690.

Lambert, M. A., & Fletcher, L. S. (1997). Review of models for thermal contact conductance of metals. *Journal of thermophysics and heat transfer*, 11(2), 129-140.

Lebeau, M., & Konrad, J. M. (2012). An extension of the capillary and thin film flow model for predicting the hydraulic conductivity of air-free frozen porous media. *Water Resources Research*, 48(7).

Liang, Z., Ioannidis, M. A., & Chatzis, I. (2000). Permeability and electrical conductivity of porous media from 3D stochastic replicas of the microstructure. *Chemical engineering science*, 55(22), 5247-5262.

Lionheart, W. R., Kaipio, J., & McLeod, C. N. (2001). Generalized optimal current patterns and electrical safety in EIT. *Physiological Measurement*, 22(1), 85-90.

Liu, C., Shi, B., Zhou, J., & Tang, C. (2011). Quantification and characterization of microporosity by image processing, geometric measurement and statistical methods: Application on SEM images of clay materials. *Applied Clay Science*, 54(1), 97-106.

Liu, C., Tang, C. S., Shi, B., & Suo, W. B. (2013). Automatic quantification of crack patterns by image processing. *Computers & Geosciences*, 57, 77-80.

Liu, G., & Si, B. C. (2011). Soil ice content measurement using a heat pulse probe method. *Canadian Journal of Soil Science*, 91(2), 235-246.

Liu, Z., & Yu, X. (2013). Physically based equation for phase composition curve of frozen soils. Transportation Research Record: *Journal of the Transportation Research Board*, (2349), 93-99.

Lovell, M. A. (1985). Thermal conductivity and permeability assessment by electrical resistivity measurements in marine sediments. *Marine Georesources & Geotechnology*, 6(2), 205-240.

Lu, S., Ren, T., Gong, Y., & Horton, R. (2007). An improved model for predicting soil thermal conductivity from water content at room temperature. *Soil Science Society of America Journal*, 71(1), 8-14.

Maeno, N., Araki, T., Moore, J., & Fukuda, M. (1992). Dielectric response of water and ice in frozen soils. *Physics and Chemistry of Ice*, 381-386.

Mao, Y., Romero E. & Gens A. (2016). Exploring ice content on partially saturated frozen soils using dielectric permittivity and bulk electrical conductivity measurements. *In E3S Web of Conferences*, 9, 07005.

Mao, Y., Romero E., & Gens A. (2018). Ice formation in unsaturated frozen soils. *The 7th international conference on unsaturated soils*, Hong Kong.

Mao, Y., Romero E. & Gens A. (2018). Evaluating the ice content in unsaturated frozen soils. *Géotechnique letters*, (submitted).

Maxwell, J. C. (1881). A treatise on electricity and magnetism (Vol. 1). *Clarendon press*.

McCarter, W. J. (1984). The electrical resistivity characteristics of compacted clays. *Geotechnique*, 34(2), 263-267.

McCarter, W. J., & Desmazes, P. (1997). Soil characterization using electrical measurements. *Geotechnique*, 47(1), 179–183.

McLachlan, D. S., Blaszkiewicz, M., & Newnham, R. E. (1990). Electrical resistivity of composites. *Journal of the American Ceramic Society*, 73(8), 2187-2203.

Mora, R.S. (2016). Efectos de la microestructura en el comportamiento hidromecánico de suelos compactados. *PhD thesis*, Universitat Politècnica de Catalunya, Spain.

Mu, Q. 2017. Hydro-mechanical behaviour of loess at elevated and sub-zero temperatures. *PhD thesis*, University of Science and Technology, Hong Kong.

Munoz-Castelblanco J., Pereira J. M., Delage P. & Cui Y. J. (2012). The influence of changes in water content on the electrical resistivity of a natural unsaturated loess. *ASTM Geotechnical Testing Journal*, 35(1), 11-17.

Murashov, V. V., & White, M. A. (2000). Thermal conductivity of crystalline particulate materials. *Journal of materials science*, 35(3), 649-653.

Nelson, F. E., Anisimov, O. A., & Shiklomanov, N. I. (2001). Subsidence risk from thawing permafrost. *Nature*, 410(6831), 889.

Nelson, F. E. (2003). (Un) frozen in time. *Science*, 299(5613), 1673-1675.

Nishimura, S., Gens, A., Olivella, S., & Jardine, R. J. (2008). THM-coupled finite element analysis of frozen soil: formulation and application. *Géotechnique*, 59(3), 159–171.

Orru, R., Licheri, R., Locci, A. M., Cincotti, A., & Cao, G. (2009). Consolidation/synthesis of materials by electric current activated/assisted sintering. *Materials Science and Engineering*: R: Reports, 63(4-6), 127-287.

Patterson, D. E., & Smith, M. W. (1981). The measurement of unfrozen water content by time domain reflectometry: Results from laboratory tests. *Canadian Geotechnical Journal*, 18(1), 131-144.

Paulson, K., Breckon, W., & Pidcock, M. (1992). Electrode modelling in electrical impedance tomography. *SIAM Journal on Applied Mathematics*, 52(4), 1012-1022.

Peláez, R.R. 2013. Congelación artificial de dos suelos naturales. Un enfoque experimental con desarrollo de equipo, *Master thesis*, Universitat Politècnica de Catalunya, 1-76.

Pelaez, R., Casini, F., Romero, E., Gens, A., & Viggiani, G. (2014). Freezing-thawing tests on natural pyroclastic samples. *In 6th International conference on Unsaturated Soils*, 1689-1694. Taylor & Francis Group.

Ping, Y., Cai-gao, S., Chaowen, D., Jie-ming, K., & Ting, Z. (2003). Application of artificial freezing method in Zhang Fuyuan station of Nanjing subway. *Rock and Soil Mechanics*, 24(S2), 388-391.

Polydorides, N., & Lionheart, W. R. (2002). A Matlab toolkit for three-dimensional electrical impedance tomography: a contribution to the Electrical Impedance and Diffuse Optical Reconstruction Software project. *Measurement science and technology*, 13(12), 1871-1883.

Porretta, R., & Bianchi, F. (2016). Profiles of relative permittivity and electrical conductivity from unsaturated soil water content models. *Annals of Geophysics*, 59(3), 0320.

Reynolds, J. M. (2011). An introduction to applied and environmental geophysics. *John Wiley & Sons*.

Rhoades, J. D., Raats, P. A. C., & Prather, R. J. (1976). Effects of Liquid-phase Electrical Conductivity, Water Content, and Surface Conductivity on Bulk Soil Electrical Conductivity 1. *Soil Science Society of America Journal*, 40(5), 651-655.

Rhoades, J. D., & van Schilfgaarde, J. (1976). An Electrical Conductivity Probe for Determining Soil Salinity 1. *Soil Science Society of America Journal*, 40(5), 647-651.

Rhoades, J. D., Waggoner, B. L., Shouse, P. J., & Alves, W. J. (1989). Determining soil salinity from soil and soil-paste electrical conductivities: Sensitivity analysis of models. *Soil Science Society of America Journal*, 53(5), 1368-1374.

Roberts, J. N., & Schwartz, L. M. (1985). Grain consolidation and electrical conductivity in porous media. *Physical Review B*, 31(9), 5990.

Romero, E., & Simms, P. H. (2008). Microstructure investigation in unsaturated soils: a review with special attention to contribution of mercury intrusion porosimetry and environmental scanning electron microscopy. *Geotechnical and Geological Engineering*, 26(6), 705-727.

Romero, E., Sau, N., Lima, A., Van Baelen, H., Sillen, X., & Li, X. (2016). Studying the thermal conductivity of a deep Eocene clay formation: Direct measurements vs back-analysis results. *Geomechanics for Energy and the Environment*, 8, 62-75.

Romero E. and Sau N. (2016) Thermal conductivity of Ypresian clays: experimental setup for thermal conductivity and pre-conditioning of samples: final report. *ONDRAF/NIRAS*.

Roth, K., Schulin, R., FluÈ hler, H. and Attinger,W. (1990). Calibration of time domain reflectometry for water content measurement using a composite dielectric approach. *Water Resources Research*, 26(10), 2267-2273.

Russo, G., Corbo, A., Cavuoto, F., & Autuori, S. (2015). Artificial Ground Freezing to excavate a tunnel in sandy soil. Measurements and back analysis. *Tunnelling and Underground Space Technology*, 50, 226-238.

Sahimi, M., & Tsotsis, T. T. (1997). Transient diffusion and conduction in heterogeneous media: Beyond the classical effective-medium approximation. *Industrial & engineering chemistry research*, 36(8), 3043-3052.

Sambuelli, L., Lollino, G., Morelli, G., Socco, L. V., & Bidone, L. (2002). First experiments on solid transport estimation in river-flow by fast impedance tomography. *In proceeding of 8th EEGS-ES Meeting*, Aveiro, CD-ROM.

Sego, D. C., Robertson, P. K., Sasitharan, S., Kllpatrick, B. L., & Pillai, V. S. (1994). Ground freezing and sampling of foundation soils at Duncan Dam. *Canadian Geotechnical Journal*, 31(6), 939-950.

Seyfried, M. S., & Murdock, M. D. (1996). Calibration of time domain reflectometry for measurement of liquid water in frozen soils. *Soil Science*, 161(2), 87-98.

Shang, J. Q., Lo, K. Y., & Inculet, I. I. (1995). Polarization and conduction of clay-water-electrolyte systems. *Journal of geotechnical engineering*, 121(3), 243-248.

Shastri, A., & Sanchez, M. (2012). Mechanical modelling of frozen soils incorporating the effect of cryogenic suction and temperature. *In Geo-Congress 2012*: State of the Art and Practice in Geotechnical Engineering, 2492-2501.

Singh, D. N., & Devid, K. (2000). Generalized relationships for estimating soil thermal resistivity. *Experimental Thermal and Fluid Science*, 22(3-4), 133-143.

Skierucha, W., & Wilczek, A. (2010). A FDR sensor for measuring complex soil dielectric permittivity in the 10–500 MHz frequency range. *Sensors*, 10(4), 3314-3329.

Smits, K. M., Sakaki, T., Limsuwat, A., & Illangasekare, T. H. (2009). Determination of the thermal conductivity of sands under varying moisture, drainage/wetting, and porosity conditions-applications in near-surface soil moisture distribution analysis. *AGU Hydrology Days*.

Smith, M. W. & Tice, A. R. (1988). Measurement of the unfrozen water content of soils: a comparison of NMR and TDR methods. *In Proceedings of the 5th International Conference on Permafrost*:473-477.

Somersalo, E., Cheney, M., & Isaacson, D. (1992). Existence and uniqueness for electrode models for electric current computed tomography. *SIAM Journal on Applied Mathematics*, 52(4), 1023-1040.

Spaans, E. J., & Baker, J. M. (1995). Examining the use of time domain reflectometry for measuring liquid water content in frozen soil. *Water Resources Research*, 31(12), 2917-2925.

Spaans, E. J., & Baker, J. M. (1996). The soil freezing characteristic: Its measurement and similarity to the soil moisture characteristic. *Soil Science Society of America Journal*, 60(1), 13-19.

Stähli, M., & Stadler, D. (1997). Measurement of water and solute dynamics in freezing soil columns with time domain reflectometry. *Journal of Hydrology*, 195(1-4), 352-369.

Sylvester, J., & Uhlmann, G. (1987). A global uniqueness theorem for an inverse boundary value problem. *Annals of mathematics*, 153-169.

Tarnawski, V. R., Leong, W. H., Gori, F., Buchan, G. D., & Sundberg, J. (2002). Inter-particle contact heat transfer in soil systems at moderate temperatures. *International journal of energy research*, 26(15), 1345-1358.

Tarnawski, V. R., Momose, T., & Leong, W. H. (2009). Assessing the impact of quartz content on the prediction of soil thermal conductivity. *Geotechnique*, 59(4), 331-338.

Thompson R. B., Gallardo M., Fernandez M. D., Valdez L. C. & Martinez-Gaitan, C. (2007). Salinity effects on soil moisture measurement made with a capacitance sensor. *Soil Science Society of America Journal*, 71(6), 1647-1657.

Tice, A. R. (1978). Determination of unfrozen water in frozen soil by pulsed nuclear magnetic resonance. *In Proc. of 3rd International Conference on Permafrost*, 149-155.

Tice, A. R., Oliphant, J. L., Nakano, Y., & Jenkins, T. F. (1982). Relationship between the ice and unfrozen water phases in frozen soil as determined by pulsed nuclear magnetic resonance and physical desorption data (No. CRREL-82-15). *COLD REGIONS RESEARCH AND ENGINEERING LAB HANOVER NH*.

Topp, G. C., Davis, J. L. and Annan, A. P. (1980). Electromagnetic determination of soil water content: measurements in coaxial transmission lines. *Water Resources Research*, 16(3), 574-582.

Topp, G. C., & Davis, J. L. (1981). Detecting infiltration of water through soil cracks by time-domain reflectometry. *Geoderma*, 26(1-2), 13-23.

Van Genuchten, M. T. (1980). A closed-form equation for predicting the hydraulic conductivity of unsaturated soils 1. *Soil science society of America journal*, 44(5), 892-898.

Vargas, W. L., & McCarthy, J. J. (2001). Heat conduction in granular materials. *AIChE Journal*, 47(5), 1052-1059.

Vauhkonen, M. (1997). Electrical impedance tomography and prior information. *PhD thesis*, Department of Applied Physics, Kuopio University, Finland.

Viggiani, G. M. B., & De Sanctis, L. (2009). Geotechnical aspects of underground railway construction in the urban environment: the examples of Rome and Naples. *Geological Society*, London, *Engineering Geology Special Publications*, 22(1), 215-240.

Watanabe, K., & Mizoguchi, M. (2002). Amount of unfrozen water in frozen porous media saturated with solution. *Cold Regions Science and Technology*, 34(2), 103-110.

Watanabe, K., & Mizoguchi, M. (2002). Amount of unfrozen water in frozen porous media saturated with solution. *Cold Regions Science and Technology*, 34(2), 103-110.

Watanabe, K., & Flury, M. (2008). Capillary bundle model of hydraulic conductivity for frozen soil. *Water Resources Research*, 44(12).

Watanabe, K., & Wake, T. (2008). Hydraulic conductivity in frozen unsaturated soil. *In Proceedings of the 9th International Conference on Permafrost*, 29, 1927-1932.

Watanabe, K., & Wake, T. (2009). Measurement of unfrozen water content and relative permittivity of frozen unsaturated soil using NMR and TDR. *Cold Regions Science and Technology*, 59(1), 34-41.

Weast, R. C. (1986). Handbook of physics and chemistry. *CRC Press*, Boca Raton, 1983–1984.

Webb, P. A. (2001). An introduction to the physical characterization of materials by mercury intrusion porosimetry with emphasis on reduction and presentation of experimental data. *Micromeritics Instrument Corp, Norcross, Georgia*.

Wilczek A., Skierucha W. & Szyplowska A. (2011). Influence of moisture and salinity of soil on its dielectric permittivity. *Acta Agrophysica*, 197, 5-87.

Williams P. J. (1964). Unfrozen water content of frozen soils and soil moisture suction. *Geotechnique*, 14(3), 231-246.

Xiao, Z., Lai, Y., & Zhang, M. (2018). Study on the freezing temperature of saline soil. *Acta Geotechnica* 13(1): 195-205.

Yoshikawa, K., & Overduin, P. P. (2005). Comparing unfrozen water content measurements of frozen soil using recently developed commercial sensors. *Cold Regions Science and Technology*, 42(3), 250-256.

Yun TS (2005) Mechanical and thermal study of hydrate-bearing sediments, *Ph.D.* Georgia Institute of Technology, Atlanta.

Yun, T. S., & Santamarina, J. C. (2008). Fundamental study of thermal conduction in dry soils. *Granular matter*, 10(3), 197.

Zhang, T., Frauenfeld, O.W., Serreze, M.C., Etringer, A., Oelke, C., McCreight, J., Barry, R.G., Gilichinsky, D., Yang, D., Ye, H. and Ling, F., 2005. Spatial and temporal variability in active layer thickness over the Russian Arctic drainage basin. *Journal of Geophysical Research: Atmospheres*, 110(D16).

Zhou, X., Zhou, J., Kinzelbach, W., & Stauffer, F. (2014). Simultaneous measurement of unfrozen water content and ice content in frozen soil using gamma-ray attenuation and TDR. *Water Resources Research*, 50(12), 9630-9655.

Zhu Y. & Carbee D. L. (1987). Creep and strength behaviour of frozen silt in uniaxial compression. *Cold Regions Research and Engineering Laboratory, CRREL* Report 87-10.

Zimov, S. A., Schuur, E. A., & Chapin, F. S. (2006). Permafrost and the global carbon budget. *Science*, 312(5780), 1612-1613.

Appendix A Derivation of ice content expression

The famous Archie's second law links the electrical conductivity of soil with the soil porosity and degree of water saturation, which can be presented as

$$\sigma = \sigma_w n^p S_r^q \tag{B.1}$$

where σ is the total electrical conductivity of soil, σ_w is the electrical conductivity of interstitial water, n is porosity, S_r is the degree of water saturation, p and q are the constant parameters.

As described in the main text of Chapter 4, the bulk electrical conductivity of soil is highly dependent on temperature. At the temperature more than freezing point (not phase change), the relationship between bulk electrical conductivity and temperature are linear which is obtained and shown as

$$\sigma_T = aT + b \tag{B.2}$$

Where T is temperature, a and b are fitted from pure 5% NaCl solution that a=1.32 dS·℃/m and b=42.45 dS/m.

Substituting (B.2) into (B.1), the bulk electrical conductivity of soil along with temperature can be described as

$$\sigma_T^* = \sigma_T n^p S_r^q \tag{B.3}$$

For saturated soils, when the temperature is lower than the freezing point, the ice would generate, and the unfrozen water saturation can be described as

$$S_l = \frac{\sigma_m}{\sigma_T^*} = \frac{\sigma_m}{\sigma_T} n^{-p} S_r^{-q} \tag{B.4}$$

In the condition of soil saturated state, the ratio of measured electrical conductivity and calculated electrical conductivity from Equation (B.3) is equal to the ratio of unfrozen water volume and initial water volume, that is

$$\frac{\sigma_m}{\sigma_T^*} = \frac{V_{uw}}{V_w} \tag{B.5}$$

where V_{uw} is the volume of unfrozen water, V_w is the initial volume of water.

For the condition of unsaturated soils, the degree of water saturation can be presented as

$$S_r = \frac{V_w}{V_p} \tag{B.6}$$

where V_p is the volume of pores in the soil. In the saturated condition, $V_w = V_p$.

The unfrozen water saturation can also be presented as the ratio of the volume of unfrozen water and the total volume of pores, that is

$$S_l = \frac{V_{uw}}{V_p} \tag{B.7}$$

In terms of electrical conductivity measurements, the unfrozen water saturation can also be presented as

$$S_l = S_r \frac{\sigma_m}{\sigma_T^*} \tag{B.8}$$

Substituting Equation (B.5) into (B.8), that is

$$S_l = S_r \frac{\sigma_m}{\sigma_T^*} = \frac{V_w}{V_p} \frac{V_{uw}}{V_w} = \frac{V_{uw}}{V_p} \tag{B.9}$$

Therefore, the correctness of Equation (B.8) is verified. The unfrozen water saturation in terms of electrical conductivity measurements can be presented as

$$S_l = S_r \frac{\sigma_m}{\sigma_T^*} = \frac{\sigma_m}{\sigma_T} n^{-p} S_r^{1-q} \tag{B.10}$$

Appendix B Measurement of carbonate content in sand

The fine sand used in these experiments is from Casteldefells, Barcelona. Depending on analysis of its geologic origin, the sand is formed from the decomposition of mountain Garraf. Another possibility of sand formation is from the coastal transport of fine fractions of sediments. Hence, the carbonates in sand include probably calcite ($CaCO_3$), dolomite ($CaCO_3 \cdot MgCO_3$) and etc. The percentage of carbonate is defined as the total carbonates which are contained in 100 g of dry sand. In this test, we assume that all the carbonate components are calcium carbonate ($CaCO_3$).

B.1 Principle

The determination of carbonates content (%) in the sand is based on the volumetric analysis of the carbon dioxide CO_2, which is liberated during the application of hydrochloric acid solution HCl in soil's carbonates and is described with the following reaction:

$$(CaCO_3 + MgCO_3 \text{ etc.}) + 2\ HCl \rightarrow (CaCl_2 + MgCl_2 \text{ etc.}) + H_2O + CO_2 \uparrow \qquad (C.\ 1)$$

During the application of the acid into the sand sample, a characteristically foaming is observed which is the evidence of carbon dioxide's liberation and the existence of carbonate salts consequently.

B.2 Instrument

The schematic picture of calcimeter setup is shown in Figure B.1.

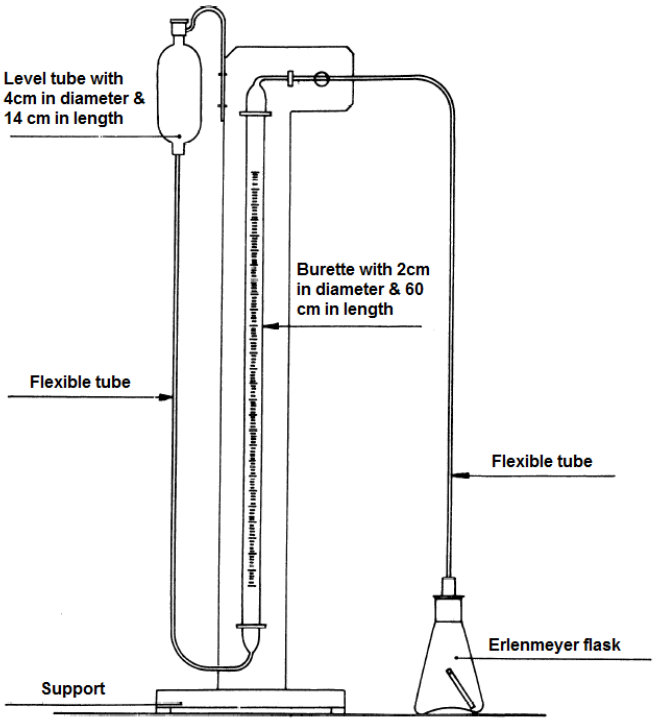

Figure B1. Schematic of the calcimeter setup

B.3 Procedure

The standard test procedures are shown as below:

- Weigh prepared soil sample and transfers it into the Bernard apparatus conical flask.
- Afterwards, fill the glass of the apparatus until the 3/4 of its height with HCl solution and place it into the conical flask attentively. Pay attention, that the tubule stays upright with the acid (Solution of HCl) inside.

- Cap the conical flask with its particular plug and then zeroizes the level of the filling solution. With the left hand bring the pear-shaped glass container next to the graduated column for the fluids both in the pear-shaped container and in the graduated tube stand in the same level (note L_0).
- With the right hand, shake gently the conical flask, so, the HCl solution comes in contact with the prepared soil sample.
- Then CO_2 liberates. The filling solution of graduated column descends due to the pressure of liberated CO_2.
- At the same time, we lower the pear-shaped container for its fluid level to remain at the same level as the fluid of the column. This way the hydrostatic pressure equalizes.
- When the liberation of the CO_2 is finished, stop the agitation and note the column's reading L_f.

In case the carbonate content is too high, and the liberated gas displaces all the fluid from the graduated column repeat the process, decreasing the quantity of the prepared soil sample into around 1.0000 g with an accuracy of 0.1 mg. For every series of measurements, we should execute one determination of 0.2 g $CaCO_3$ for calibration. The measurements should preferably be executed in a temperature-controlled room because temperature difference will influence the measurements significantly.

B.4 Calculation

Calculate the changes in the volume of the gas produced by the sample (V_1), the calcium carbonate standards (V_2) by subtracting the initial value in the calibrated tube from the final value. The carbonate content is calculated with the formula:

$$w(\mathrm{CaCO_3}) = \frac{m_1 V_2}{m_2 V_1} \cdot 100\% \qquad \text{(C. 2)}$$

where $w(CaCO_3)$ is the percentage of carbonate content of the oven-dried soil; m_1 is the mass of the calcium carbonate standards in grams; m_2 is the mass of the test portion in grams; V_1 (

$= L_f^{'} - L_0^{'}$) is the mean volume of carbon dioxide produced by reaction of the calcium carbonate standards, in millilitres; V_2 ($= L_f - L_0$) is the volume of carbon dioxide produced by reaction of the test portion, in millilitres.

B.5 Results

The experimental results and their calculation are obtained and shown in Table A.1. After calculating, the carbonate content is obtained at around 23.37% that is the reason why the thermal conductivity of fine sand in this thesis is lower than ones measured by others in quartz sand.

Table A.1 Experimental results of Bernard test

Number	m_1/g	m_2/g	$L_0^{'}$/mL	$L_f^{'}$/mL	L_0/mL	L_f/mL	w/%
1	0.2001	1.0134	5	61	11	78	22.57
2	0.2004	0.7571	8	66	8	60	23.73
3	0.1991	0.9070	8	67	7	71	23.81
Average							23.37

Appendix C Principles of PCAS image processing

Pore (Particle) and Cracks Analysis System (PCAS), the image processing soft, is used to convert the images into the binary images concluding only voids and particles. Pixels (P) are in the range of 0-255 in the binary images, while 0 and 1 are used to represent the voids and particles. Threshold (T) is set to distinguish them. When the pixel is smaller than T, is set to be 0, while it is 1 when the pixel is larger than T, which can be expressed as follows:

$$P = \begin{cases} 0, & P \le T \\ 1. & P > T \end{cases} \tag{D.1}$$

where T is the threshold and P is the pixel.

Parameters, representing the microstructural characteristics of the soil, can be obtained from the binary figures and vector figures, such as porosity, fractal dimension, abundance, shape factor and rate of anisotropic, while porosity and fractal dimension are identified as the two most key parameters.

(1) Porosity

The degree of void density in soil is the ratio of void volume to particle volume, while the apparent porosity obtained by FESEM tests is the ratio of void area to particle area.

$$n = \frac{S_l}{S_0} \times 100\% \tag{D.2}$$

Where n is the apparent porosity of the soil, %, and S_l and S_0 are the areas of voids and particles, respectively, mm^2.

(2) the average area of pores

The image is composed of a series of pixels, which can be regarded as small squares or points. Therefore, the area is defined by the pixel number of a pore. The average area of pores S_{ave} is calculated as

$$S_{ave} = \frac{1}{n}\sum_{i=1}^{n} S_i \quad (i = 1, 2, \cdots, n) \tag{D.3}$$

Where *Si* is the area of pore *i*, and *n* is the total number of pores.

(3) the average perimeter of pores

The perimeter is usually defined as the summation length of boundary pixels, some optimization algorithm is used to reduce the overestimate of the perimeter (Liu et al., 2013). The average perimeter Cave is defined as

$$C_{ave} = \frac{1}{n}\sum_{i=1}^{n} C_i \quad (i = 1, 2, \cdots, n) \tag{D.4}$$

Where C_i is the area of pore *i*, and *n* is the total number of pores.

(4) Average form factor

Form factor (*ff*) is often used to describe the shape of features. It is defined by the perimeter (*C*) and area (*S*) as follows (Liu et al., 2011; Sezer et al., 2008; Soroushian and Elzafraney, 2005):

$$ff = 4 \cdot \pi \cdot S / C^2 \tag{D.5}$$

Form factor reflects the circularity and rough edges of pores. It is maximum at 1.0 for circles and 0.785 for squares. The complexity of pore boundary increases with decreasing form factor.

(5) fractal dimension

Fractal dimension concept is developed for describing a shape, a profile or a form in nature regardless of the complexity. Generally, fractal dimension gives the autocorrelation of the

profile or the rate of change in length (perimeter) in response to a change in the scale of measurement (area). Specifically, if the pore system follows the fractal characteristics, the relationship between area (S), perimeter (C) and fractal dimension (*Df*) can be expressed as:

$$\log(C) = Df / 2 \cdot \log(S) + c_1 \tag{D.6}$$

Where c_1 is a constant.

(6) uniformity coefficient

Calculating the coefficient of uniformity requires the information of grain diameters. The coefficient of uniformity, C_u is a crude shape parameter and is calculated using the following equation:

$$C_u = \frac{D_{60}}{D_{10}} \tag{D.7}$$

Where D_{60} is the grain diameter at 60% passing, and D_{10} is the grain diameter at 10% passing.

Appendix D Original FESEM images of clayey silt

D.1 Clayey silt samples

The original FESEM images of clayey silt samples with different stress and temperature history are presented in below. The Figure D.1 presents the FESEM images of initial sample at magnifications of 300×, 500× and 2000×. The Figure D.2 presents the FESEM images of sample after temperature freezing-thawing path at magnifications of 500×, 1000× and 2000×. The results of samples after stress path and stress-temperature path are shown in Figure D.3 and D.4, respectively. The detailed analysis of the microstructure changes during different stress and temperature history are interpreted in the main text of Chapter 6.

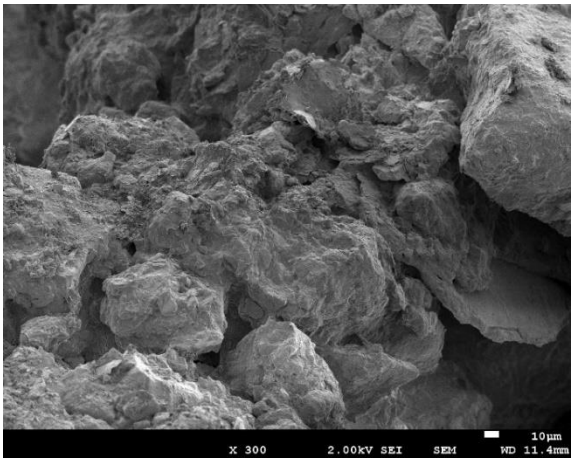

(a)

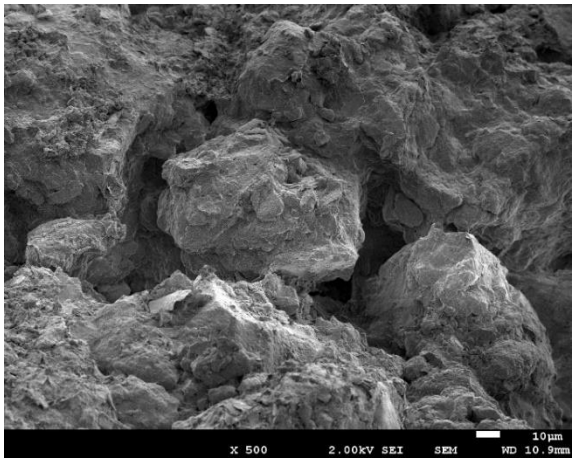

(b)

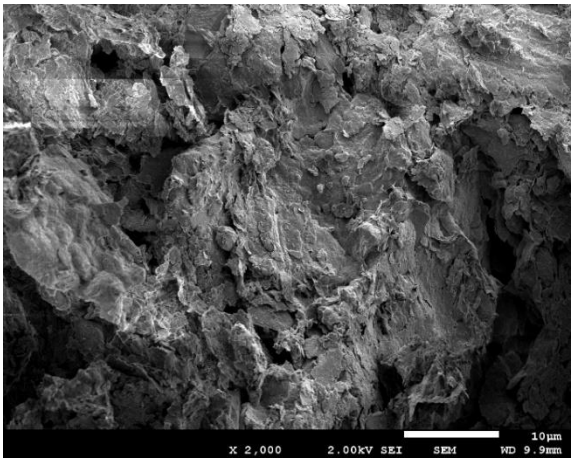

(c)

Figure D.1 FESEM images of initial clayey silt sample: (a) at a magnification of 300×; (b) at a magnification of 500×; (c) at a magnification of 2000×.

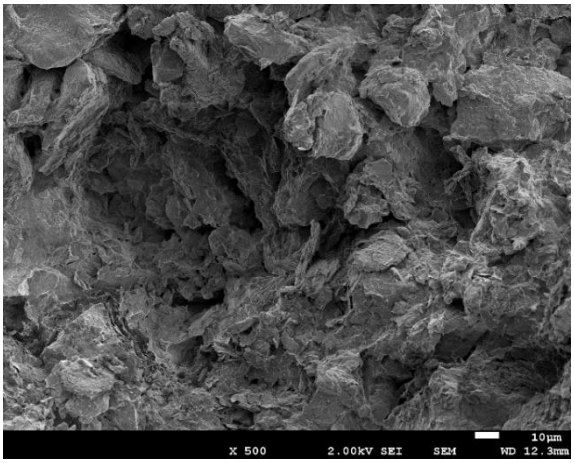

(a)

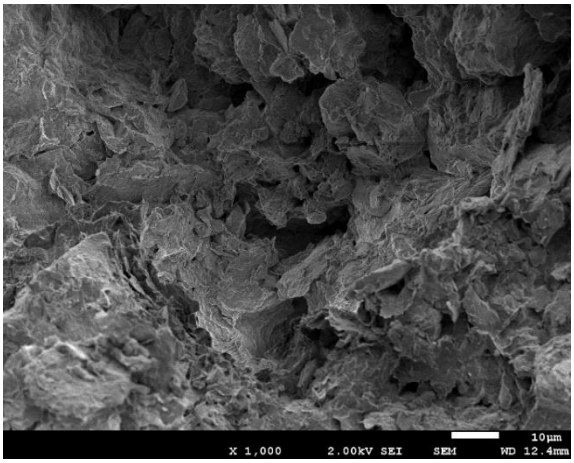

(b)

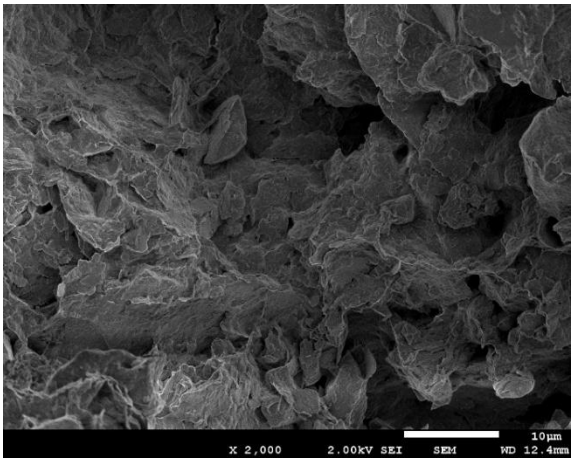

(c)

Figure D.2 FESEM images of clayey silt sample after temperature freezing and thawing path: (a) at a magnification of 500×; (b) at a magnification of 1000×; (c) at a magnification of 2000×.

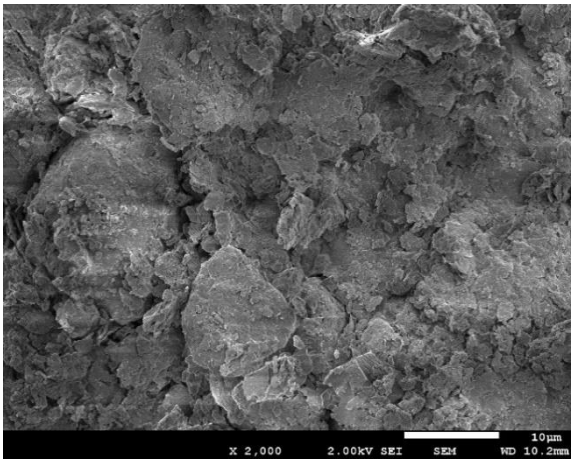

(a)

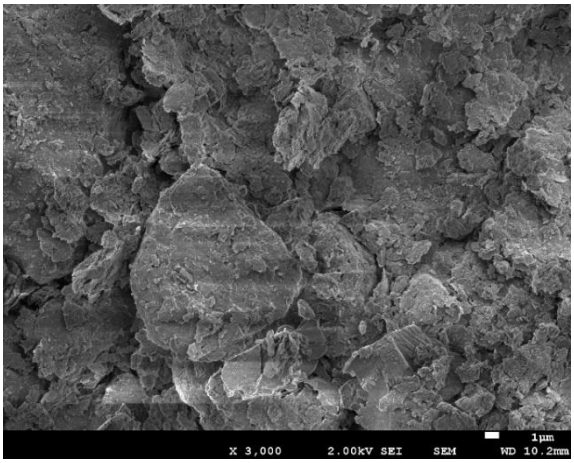

(b)

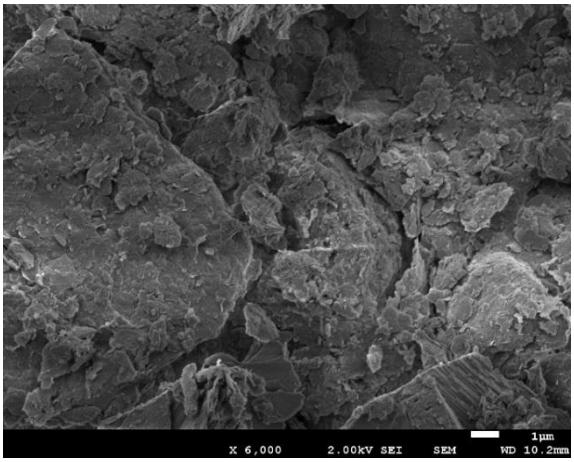

(c)

Figure D.3 FESEM images of clayey silt sample after stress loading unloading path: (a) at a magnification of 2000×; (b) at a magnification of 3000×; (c) at a magnification of 6000×.

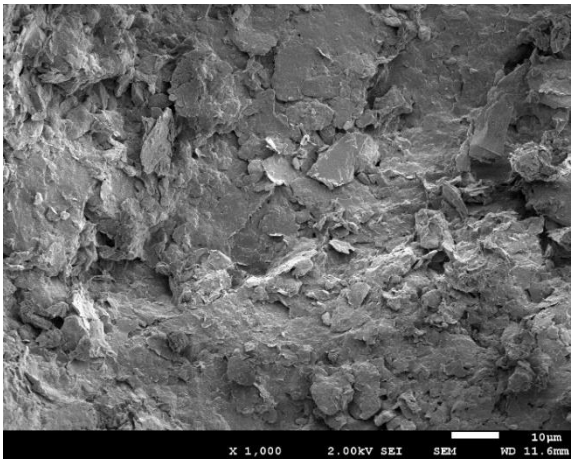

(a)

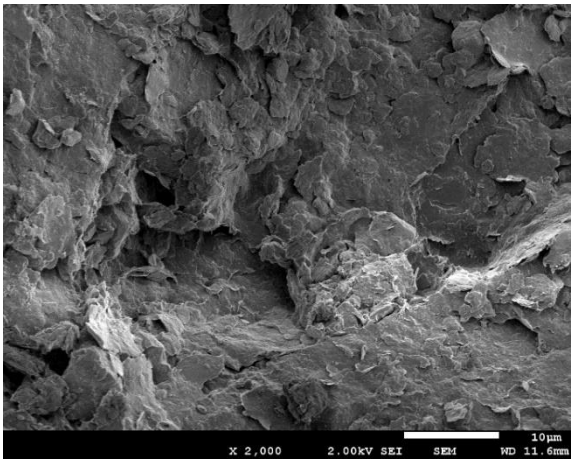

(b)

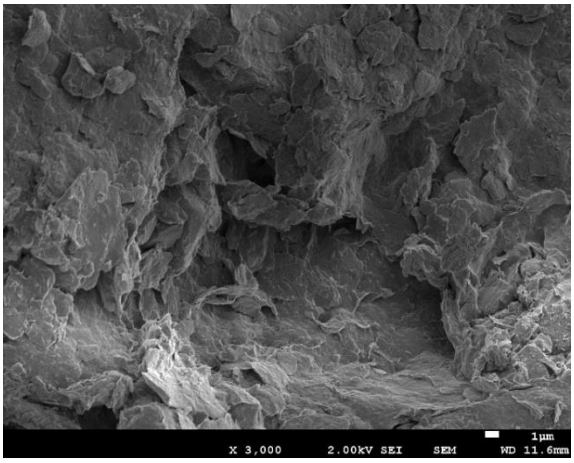

(c)

Figure D.4 FESEM images of clayey silt sample after stress loading-unloading and temperature freezing-thawing path: (a) at a magnification of 1000×; (b) at a magnification of 2000×; (c) at a magnification of 3000×.

D.2 Pozzolana samples

The original FESEM images of pozzolana samples before and after stress and temperature path at different magnifications are shown in Figure D.5 and D.6 separately.

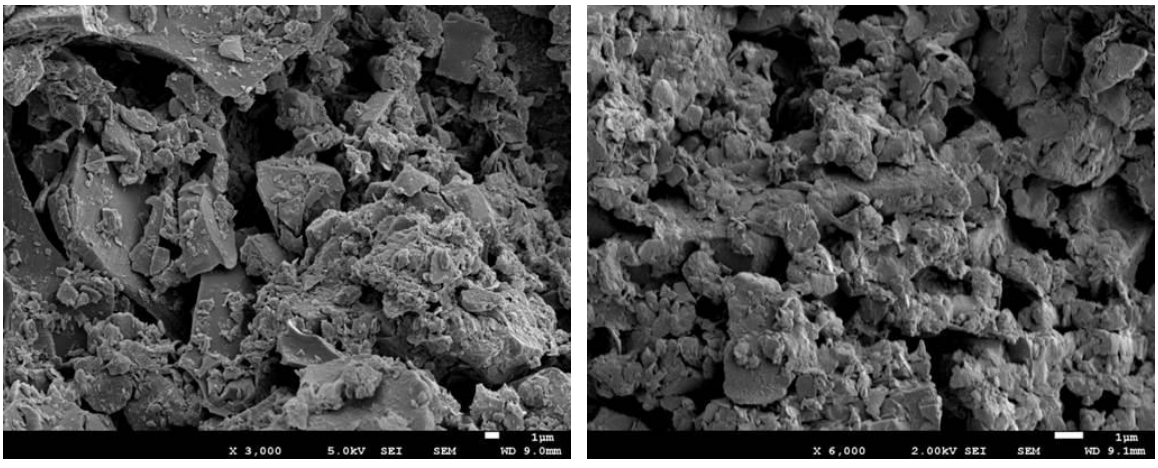

(a) (b)

Figure D.5 FESEM images of intact pozzolana sample: (a) at a magnification of 3000×; (b) at a magnification of 6000×.

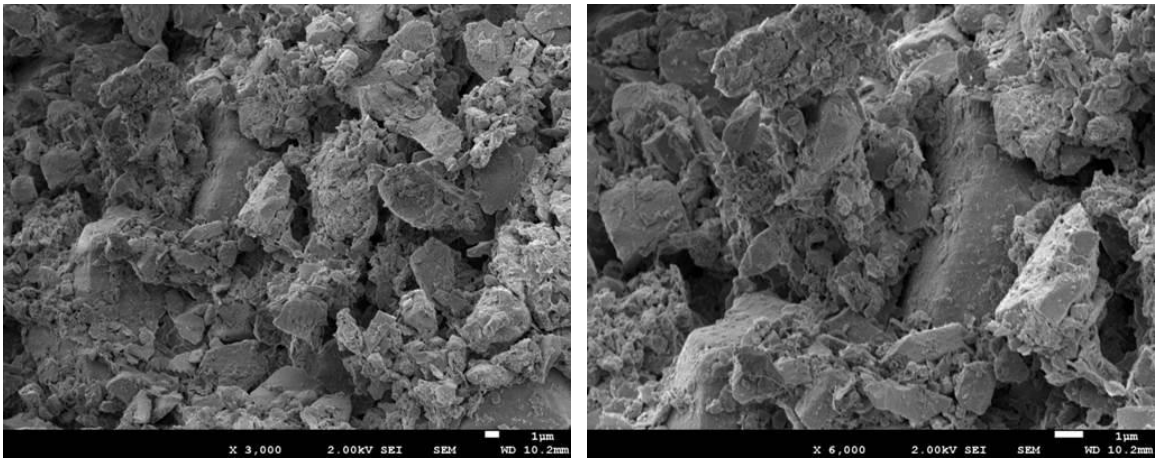

(a) (b)

Figure D.6 FESEM images of pozzolana samples after stress and temperature path: (a) at a magnification of 3000×; (b) at a magnification of 6000×.

D.3 Yellow tuff samples

The original FESEM images of yellow tuff samples before and after stress and temperature path at different magnifications are shown in Figure D.7 and D.8 separately.

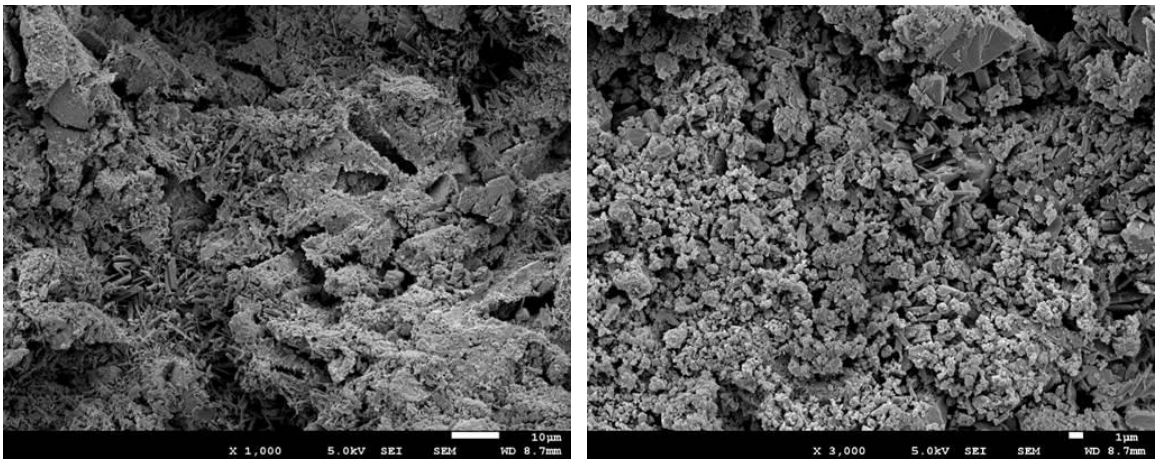

(a) (b)

Figure D.7 FESEM images of intact yellow tuff sample: (a) at a magnification of 1000×; (b) at a magnification of 3000×.

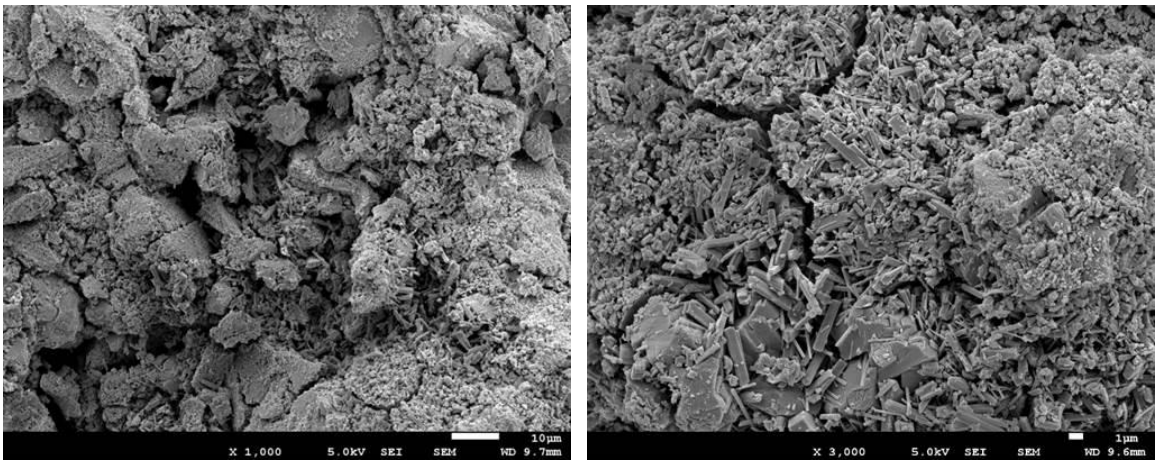

(a) (b)

Figure D.8 FESEM images of yellow tuff samples after stress and temperature path: (a) at a magnification of 1000×; (b) at a magnification of 3000×.